8-2023

High-Energy Storm Events and Their Impacts on Carbon Storage in Tidal Wetlands of South Carolina

Gavin Gleasman
ggleasm@clemson.edu

HIGH-ENERGY STORM EVENTS AND THEIR IMPACTS ON CARBON STORAGE IN TIDAL WETLANDS OF SOUTH CAROLINA

A Dissertation
Presented to
the Graduate School of
Clemson University

In Partial Fulfillment
of the Requirements for the Degree
Doctor of Philosophy.
Environmental Engineering and Earth Sciences

---

by
Gavin Gleasman
August 2023

Accepted by:
Dr. Kelly Best Lazar, Committee Chair
Dr. Alex Pullen
Dr. Cindy Lee
Dr. Timothy DeVol

ABSTRACT

Atmospheric carbon dioxide (CO_2) concentrations have been increasing at an accelerating rate for the past two centuries, profoundly impacting global climate change. Atmospheric CO_2 concentrations are influenced by the global carbon cycle through physical and biogeochemical pathways. Tidal wetland environments play a vital role in the global carbon cycle by offsetting atmospheric CO_2 concentrations through their natural physiochemical processes of high autotrophic productivity, allochthonous organic matter deposition, anoxic soils, and continuous accretion which promotes carbon sequestration with long-term storage at the land-ocean margin. The Intergovernmental Panel on Climate Change (IPCC) and United States Global Change Research Program (USGCRP) identify tidal wetlands to be important environments for regulating atmospheric CO_2 concentrations; however, these climate research governing bodies also identify current CO_2 flux datasets from tidal wetlands to be lacking expansive spatial and temporal monitoring. Furthermore, the role of hurricane disturbances on the productivity of CO_2 flux and carbon storage in tidal wetlands lacks scientific consensus.

This work produced a low-cost innovative CO_2 flux monitoring method and a unique continuous long-term dataset to yield insight into tidal wetlands' role in the carbon-climate feedback. Four key investigations of CO_2 flux in tidal wetlands were undertaken which included (1) the development and successful deployment of a low-cost, continuous long-term CO_2 flux monitoring method in a dynamic intertidal zone, (2) insight into near-annual CO_2 sequestration of 9.4 µmol m^{-2} s^{-1} in the North Inlet-Winyah Bay (NI-WB) tidal wetland system of SC and how the environmental conditions correlated to the CO_2 flux over the sampling period (August 2022 – May 2022), (3) a temporal determination of the 2022 Hurricane Ian's influence on CO_2 flux in the NI-WB tidal wetlands; with sequestration pre- and during-Hurricane Ian and net emission post-

Hurricane Ian, and (4) an identification of varying carbon accumulation rates (15.2-120.6 gC m^{-2} yr^{-1}) in NI-WB with historical correlation of high-energy deposits and carbon storage capacity.

The widespread adoption of the innovative CO_2 flux monitoring methodology presented within this dissertation and the continued identification of carbon storage via sediment cores in global tidal wetlands will produce a comprehensive synthesis of the role tidal wetlands play in carbon-climate feedback. The successful investigation of tidal wetlands' role in carbon-climate feedback will assist in refining ESM predictions of global climate change projections to ultimately inform tidal wetland management practices and climate policy.

DEDICATION

To my parents and brother, Doug, Lucia, and Cory, no words can describe my gratitude for you. The success I have achieved during my doctoral studies is not a feat accomplished alone. Dad, although data collection can be cumbersome and tedious, you made the experience enjoyable, and I cannot thank you enough for dropping off all other responsibilities and assisting me in the field. Mom, being a stellar proofreader, construction engineering brain, and a complete support system all in one package is rare. You were there for me every step of the way, regardless of the day of the week or time of the day. Cory, your graduate school tenure advice and general research guidance was vital in my progression through my graduate program and achieving my graduate study goals. I have always been inspired to follow in your footsteps and receive a higher education degree. I could not have achieved my goals without you all and I feel lucky for that you have been in my corner throughout my whole academic career.

To Ms. Hannah McHarris, thank you for understanding my dream to pursue a doctoral degree. Your support has made my life much easier and more enjoyable. You have grounded me during this process, and my dissertation would not be possible without you. I couldn’t be more grateful for your unwavering support. Thank you all for your continued love and for accompanying me on this journey. I hope to make you all just as proud in my next venture.

ACKNOWLEDGMENTS

I want to thank my colleagues, friends, and mentors for their sustained encouragement and support throughout my doctoral studies. I would first like to thank the entire faculty and staff in the Environmental Engineering and Earth Sciences Department at Clemson University for their support, guidance, and encouragement.

To my major advisor, Dr. Kelly Best Lazar, the journey throughout my doctoral work would not have been possible without you. Your sustained support is something I cherish more than you know. You have facilitated my development not only as a researcher and a scholar, but a person to view the world critically.

To Dr. Cindy Lee, you have been a constant supportive figure throughout my graduate coursework and research. Thank you for helping me grow as a technical writer and researcher. I thoroughly enjoyed your courses, and they will inspire throughout my academic career. To Dr. Timothy DeVol, your mentorship, lab space, and funding support made my project possible. As my sounding board for isotopic research queries, you helped me ground my research in appropriate methods and stay ‘happy’. To Dr. Alex Pullen, your courses have given me a strong foundation for climatology and research methods. I can confidently say I have more clarity in my career trajectory because of your advice and mentorship.

To Dr. Scott DeWolf, this dissertation and my growth as a researcher would be impossible without you. At each turn, you supported my work both technically and personally. From remote data acquisition to data management, your expertise and guidance aided in the completion of a successful research project. However, I have been more impacted and shaped by your genial disposition when working with a graduate student searching for answers and cannot thank you enough for your consistent availability at the ‘command center’. To Dr. Brian Powell, I appreciate you supporting my project's lab space and the analysis of isotopic samples. To Dr. Daniel Hitchcock, you were an integral part of establishing my research context, without your support and advocacy this project would not have been launched.

Thank you to The Clemson Baruch staff, NI-WB NOAA NERRS, and Hobcaw Barony Foundation Board Members for site access and the opportunity to pursue environmentally impactful research. Special thank you to the Geological Society of America Graduate Student Research Grant Program and Phi Kappa Phi Honor Society for the funding of my research project and the acquisition of invaluable data collection tools.

As a result of the connections and knowledge acquired during my tenure at Clemson University, I hope to continue to pursue my research agenda and make an environmental difference.

TABLE OF CONTENTS

LIST OF TABLES

LIST OF FIGURES

CHAPTER ONE

INTRODUCTION

BACKGROUND & PURPOSE

Atmospheric CO_2 Concentrations

Atmospheric carbon dioxide (CO_2) concentrations have been increasing at an accelerating rate for the past two centuries. The increase in atmospheric CO_2 concentrations is unequivocally due to anthropogenic emissions and land use changes (IPCC, 2021). The current atmospheric CO_2 concentrations reached a globally averaged high of ~415 parts per million (ppm) in 2021 which marks the highest atmospheric concentrations observed over the past 800,000 years (Fig. 1.1; Canadell et al., 2021; Lindsey, 2023). Since the beginning of the industrial revolution in 1750, global atmospheric CO_2 concentrations have increased by 47%, from ~277 ppm to the current level of ~415 ppm (Canadell et al., 2021; Friedlingstein et al., 2020). The 47% increase far exceeds atmospheric CO_2 concentration variations observed over the past 800,000 years during natural multimillennial glacial to interglacial warming periods (Fig. 1.1; Canadell et al., 2021; Lindsey, 2023). Additionally, the rate at which atmospheric CO_2 concentrations have increased from 1900-2021 is at least ten times faster than any other period over the same time period (Fig. 1.1; Canadell et al., 2021). The abundance of atmospheric CO_2 concentrations plays a significant role in determining Earth's radiative properties and influences global climate. Radiative forcing is a driving process affecting global climate change and is defined as a perturbation in Earth's energy budget due to modification in the atmosphere's net downward radiative flux (Mhyre et al., 2013). Carbon dioxide is a radiatively active gaseous compound in Earth's atmosphere and is identified as a long-lived greenhouse gas (GHG). Greenhouse gases contribute to increased radiative forcing

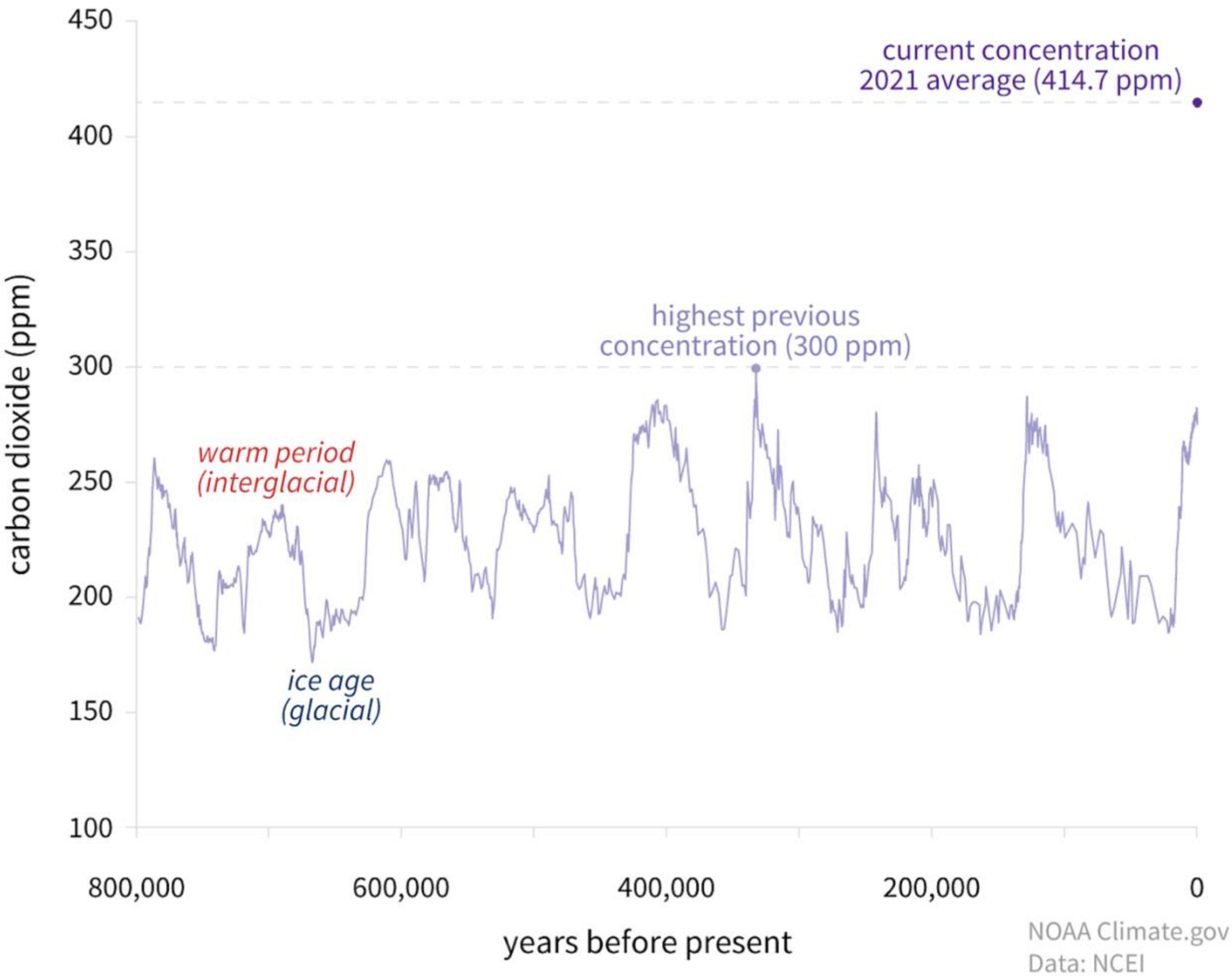

Figure 1.1 Atmospheric CO_2 concentrations from 800,000 years ago to 2021 (adapted from Lindsey, 2023).

by absorbing and trapping infrared radiation energy close to the Earth's surface, in a process known as the "Greenhouse Effect" (Mhyre et al., 2013). The increased flux of radiative energy to the Earth's surface from the Greenhouse Effect contributes to the elevation of surface temperatures, ultimately influencing global warming (Lindsey, 2013; Mhyre et al., 2013).

The Annual Greenhouse Gas Index (AGGI), developed by the National Oceanic and Atmospheric Administration (NOAA), demonstrates variation in Earth's radiative forcing due to changes in concentrations of atmospheric GHGs. The AGGI for all atmospheric GHGs has increased ~49% from 1990 to 2021 (Lindsey, 2013; Fig. 1.2). Over this period, CO_2 accounts for 66% of the change in AGGI (Lindsey, 2023). Therefore, global atmospheric CO_2 concentrations are significant contributors to the variation in radiative forcing in Earth's atmosphere, resulting in global climate change and the imbalance of heating on Earth's surface (IPCC, 2021).

Atmospheric CO_2 concentrations are regulated by the terrestrial and oceanic carbon cycle through physical and biogeochemical pathways (Canadell et al., 2021). The carbon cycle may amplify or suppress climate change by altering the rate at which atmospheric CO_2 concentrations are sequestered and stored in terrestrial and oceanic sinks or emitted as a source for atmospheric CO_2 (Canadell et al., 2021; Friedlingstein et al., 2020). The IPCC reports with high confidence that the evolution and efficiency of the carbon cycle-climate feedback will play a critical role in future climate change projections and climate policy (Canadell et al., 2021).

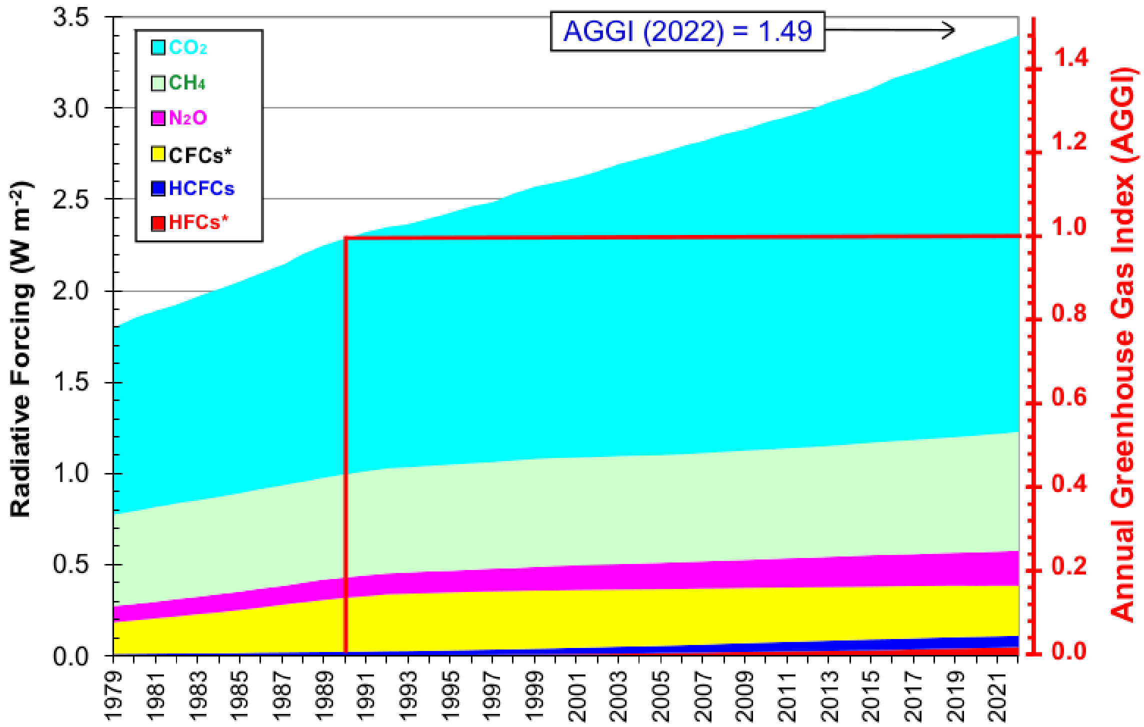

Figure 1.2. AGGI time-series comparison. Radiative forcing (y-axis left) and relative AGGI (y-axis right) conditions, calculated based on GHG concentrations from 1750 to the present. The dotted lines display the relative percent change in AGGI from 1990 to the present (adapted from NOAA Earth System Research Laboratories, n.d.).

Tidal Wetlands & Blue Carbon

Estuarine tidal wetlands are coastal environments located in intertidal zones and are characterized by brackish water conditions due to interaction between terrigenous and oceanic water inputs (Davidson Arnott et al., 2019; Greenberg et al., 2006). These dynamic coastal environments play an important role in the global carbon cycle and regulate atmospheric CO_2 concentrations by serving as natural hotspots for carbon sequestration and storage (Ouyang & Lee, 2020; Wang et al., 2019; Windham-Myers et al., 2018). The estuarine tidal wetland environment is a biogeochemical 'reactor' where physiochemical processes of high autotrophic productivity, allochthonous organic matter deposition, anoxic soils and continuous accretion promote carbon sequestration with long-term storage (Ouyang & Lee, 2020; Windham-Myers et al., 2018).

Despite their small spatial coverage, estuarine tidal wetlands are among the most efficient sequestering environments of atmospheric CO_2 and the strongest long-term storers of carbon (Windham-Myers et al., 2018). Tidal wetlands comprise only 2% of the ocean's spatial area on Earth's surface, but have been estimated to sequester over 50% of the annual carbon burial in oceans (Kirwan et al., 2023; Wang et al., 2019). Additionally, the average carbon accumulation rates in tidal wetlands are estimated to be 20-30 times higher than in terrestrial forest environments (Byun et al., 2019; Ouyang & Lee, 2020). Global tidal wetlands are estimated to effectively store ~116 Teragrams of carbon per year (Callaway et al., 2012; Wang et al., 2019), which equates to ~61 million pickup truck (3.6 liter V6 with 4,200 pound towing capacity) loads of carbon. The carbon concentrations sequestered and stored in tidal wetlands soils are commonly referred to as 'blue carbon' (Lovelock et al., 2017; Mcleod et al., 2011). The productive environments of tidal wetlands are vital proponents of the global carbon cycle due to their ability to efficiently sequester and store vast amounts of blue carbon, ultimately contributing to the mitigation of CO_2 concentration build-up in Earth's atmosphere (Nahlik & Fennessy, 2016).

Tidal Wetlands and Hurricane Activity

Hurricane activity serves as a source of periodic high-energy disturbances for coastal systems. High-energy activity includes elevated wind speed, excess precipitation, storm surge, and coastal flooding. Hurricanes are the largest drivers of economic coastal flood loss along the Eastern Coast of the United States, due to increased hurricane-induced precipitation rates and storm surges (Gori et al., 2022). The co-occurrence of storm surge and heavy precipitation (as overland flow or direct fluvial discharge) contributes to extreme compound flooding, resulting in substantial coastal economic loss (Gori et al., 2020; Wahl et al., 2015).

The IPCC reports an observed increase in the rapid intensification (wind speed increase of 46.3 km hr^{-1} within 24 hours) and a decrease in translation speed (forward motion) of hurricanes with a changing climate (Balaguru et al., 2018; Bhatia et al., 2019; IPCC, 2021; Kossin, 2018; Seneviratne et al., 2021). With continued climate change, the IPCC projects an increase in hurricane-induced precipitation rates (both peak and average), wind speeds (both peak and average), and storm surge (IPCC, 2021; Seneviratne et al., 2021). The transformation of hurricane activity with global climate change threatens coastal systems with extreme localized and regional flooding, due to the combination of rapid intensification and decreased translation speed with projected increases in precipitation rates, elevated wind speed, and intensified storm surge (Fig. 1.3; Emanuel, 2020; Hall & Kossin, 2019; IPCC, 2021; Kossin, 2018; Seneviratne et al., 2021; Peduzzi et al., 2012). The rapid intensification, decreased translation speed, storm surge, and heavy

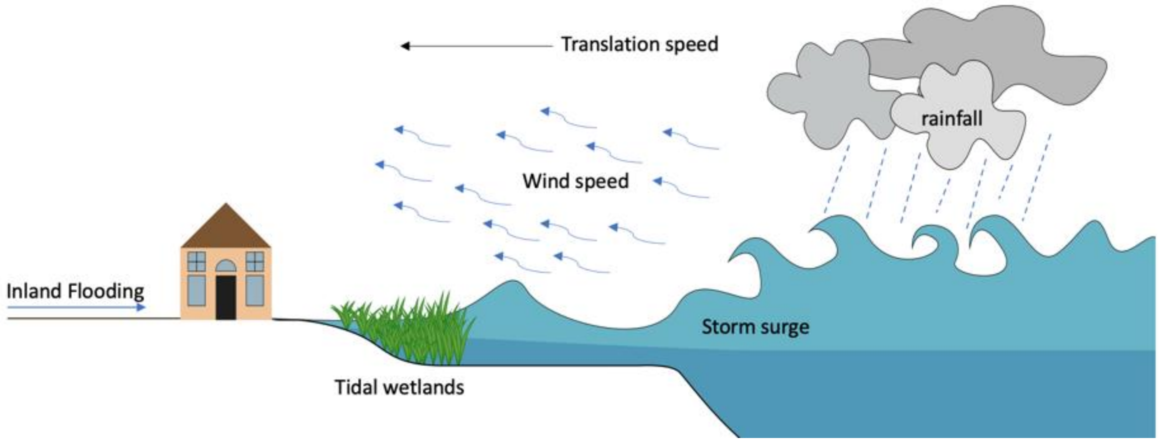

Figure 1.3. Conceptual model of hurricane effects on coastal systems tidal wetlands.

precipitation associated with the recent landfall of Hurricane Ian in the 2022 storm season led to regional coastal flooding (Bucci et al., 2023).

The coastal environments of tidal wetlands serve as an effective natural barrier to high-energy hurricanes (Al-Attabi et al., 2023; Ouyang & Lee, 2020; Sun & Carson, 2020). The low-lying tidal wetland basins introduce land-based friction to reduce storm wind speed, supply a horizontal barrier to minimize the extent of storm surge, and attenuate inland precipitation and storm surge flood waters within the environments fine-grained permeable sediment (Fig. 1.3; Costanza et al., 2008; Fairchild et al., 2021; Hu et al., 2015). The protective capabilities of tidal wetlands against tropical storms are valued to provide $1.8 million per kilometer of environmental services (Sun & Carson, 2020). However, the hurricane-induced influence on environmental service of carbon storage by tidal wetlands is largely unknown (Windham-Myers et al., 2018). The research agenda of this project was to develop continuous CO_2 flux datasets during a hurricane disturbance along the coast of South Carolina (SC) to provide insight to storm energy influence on tidal wetland carbon cycling.

Tidal Wetland CO_2 Flux and Storage during High-Energy Storm Events

The collection of continuous annual datasets for CO_2 flux in the intertidal zone of estuarine wetlands is lacking due to the difficulty of conducting fieldwork and long-term *in situ* monitoring in the diverse aquatic environment (Windham-Myers et al., 2018). The incomplete understanding of CO_2 flux during tidal mixing limits the understanding of the relative roles of estuarine tidal wetlands in carbon cycling at the critical land-ocean margin (Wang et al., 2019; Windham-Myers et al., 2018). Furthermore, the role of hurricane disturbances on CO_2 flux and carbon storage in tidal wetlands lacks scientific consensus (Najjar et al., 2018; Windham-Myers et al., 2018). Storm-induced precipitation and increased terrestrial overland flow promote the potential for periodic pulses of allochthonous organic matter into tidal wetland basins for deposition and long-term storage as blue carbon (Letourneau & Medeiros, 2019; Medeiros, 2022; Ward et al., 2017). High energy associated with hurricane storm surge also provides the potential to disrupt stored carbon with increased erosion to produce localized hotspots of CO_2 efflux (Lovelock et al., 2017; Mo et al., 2020; Najjar et al., 2018; Windham-Myers et al., 2018). Therefore, hurricanes events have the potential to either have positive carbon sequestration or negative carbon efflux impact on local carbon cycling in tidal wetlands.

The continuous long-term monitoring of CO_2 flux and carbon storage in tidal wetlands will contribute to the quantification of tidal wetlands' carbon budget and their role in regulating atmospheric CO_2 concentrations. The IPCC does not fully include CO_2 fluxes from wetlands in climatic modeling due to challenges associated with temporal data collection and spatial estimation (IPCC, 2021, Canadell et al., 2021). However, the IPCC recognizes with high confidence that carbon cycling in tidal wetlands is important to carbon-climate feedback and regulating atmospheric CO_2 concentrations (IPCC, 2021).

The limited analysis and understanding of variation in tidal wetland CO_2 flux induced by hurricanes led to the research objective of developing a method and collecting a dataset of long-term CO_2 flux in a SC wetland during a high-energy storm disturbance. The state of SC comprises ~1395 square kilometers (km^2) of tidal wetlands and has an ~80% chance of being impacted by a high energy storm each year, with a total landfall of 44 tropical cyclones from 1851 to 2021 (Mizzell et al., 2023; SCDNR, 2020). Therefore, SC's coastal system serves as a suitable location to conduct long-term carbon storage and CO_2 flux research in a tidal wetland during a high-energy event. The investigation of variation in tidal wetland carbon storage and CO_2 flux yields functional insights into tidal wetland-atmospheric CO_2 feedbacks (Fig. 1.4). The continuous monitoring of CO_2 flux and the analysis of soil carbon concentrations in a SC tidal wetland assists in determining the environment's ability to offset atmospheric CO_2 through sequestration and storage of carbon, or emit carbon back to the atmosphere (dotted line; Fig. 1.4). This dissertation conducted continuous CO_2 flux monitoring during the landfall of a hurricane to identify non-linear alteration in the tidal wetland-atmospheric CO_2 feedback. The investigation of the role of hurricane disturbances in the tidal wetland-atmospheric CO_2 feedback could potentially improve coastal carbon cycling estimates (Fig. 1.4). A comprehensive synthesis of tidal wetlands' role in regulating atmospheric CO_2 concentrations and increasing the quantity of CO_2 flux datasets will inform tidal wetland management practices and progress earth system models of climate-CO_2 concentration feedbacks within the global carbon cycle.

RESEARCH OBJECTIVE

Global climate change, coupled with high-energy storm activity, establishes an imminent influence on the coastal system's feedback mechanisms (Canadell et al., 2021; Vargas, 2012; Ye et al., 2020). However, a challenge persists in understanding long-term carbon cycling-climate feedbacks in estuarine tidal wetlands, especially during high-energy storm disturbances. The objectives of the research included

(1) The development of an innovative low-cost CO_2 flux monitoring system to collect continuous long-term datasets in the diverse aquatic conditions of tidal wetlands (Chapter 2). The innovative design will allow CO_2 flux monitoring during intertidal scenarios and

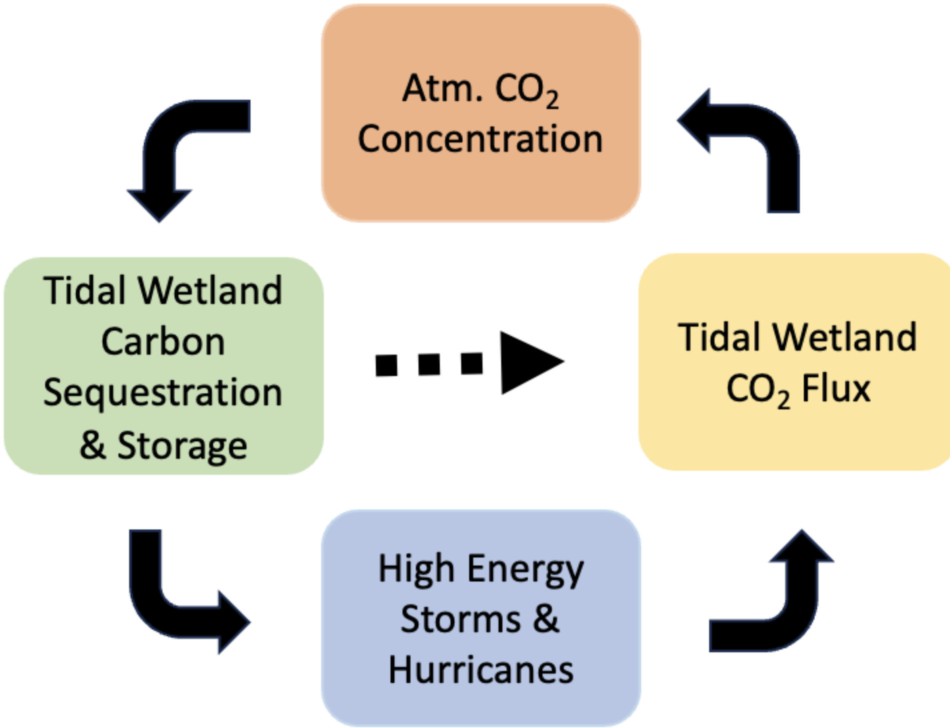

Figure 1.4. Tidal Wetland-Atmospheric CO_2 feedback loop. The development of tidal wetland carbon storage and long-term CO_2 flux datasets (dotted), including periods with high-energy storm disturbances, will improve the understanding of tidal wetlands' role in mitigating climate change.

unusually high water events (i.e., king tides and storm surges). The low-cost consideration of the design offsets the high-startup cost of current manufactured CO_2 flux equipment and allows for the distribution of more monitoring stations; ultimately improving the spatial and temporal monitoring of carbon sequestration and emission in tidal wetlands.

(2) The quantification of near-annual (ten months) carbon flux in the estuarine tidal wetlands of North Inlet-Winyah Bay (NI-WB), SC. The collection of the ten-month CO_2 concertation data is correlated to basic environmental conditions to identify an environmental influence on CO_2 flux. (Chapter 3).

(3) The determination of Hurricane Ian's influence on CO_2 flux in the NI-WB tidal wetlands (Chapter 4). Hurricane Ian made direct landfall at the NI-WB study location on September 30, 2022, as a category one hurricane. The monitoring of CO_2 flux persisted throughout the duration of the hurricane, which produced a novel dataset of CO_2 flux on varying temporal scales during a hurricane disturbance.

(4) The establishment of a historical correlation between carbon storage and high-energy events, as well as the identification of carbon accretion rates in varying locations of NI-WB (Chapter 5).

RESEARCH DESIGN

Tidal wetlands are capable of sequester autochthonous (e.g.., photosynthesis) and allochthonous (e.g., oceanic and terrestrial particulate organic matter/dCO_2) carbon for sequestration and storage with their high sedimentation rates and anoxic soils (Fig. 1.5). To develop long-term CO_2 flux datasets at the sediment interface in intertidal zones of coastal wetlands, an innovative soil gas flux design was deployed in two locations of North-Inlet Winyah

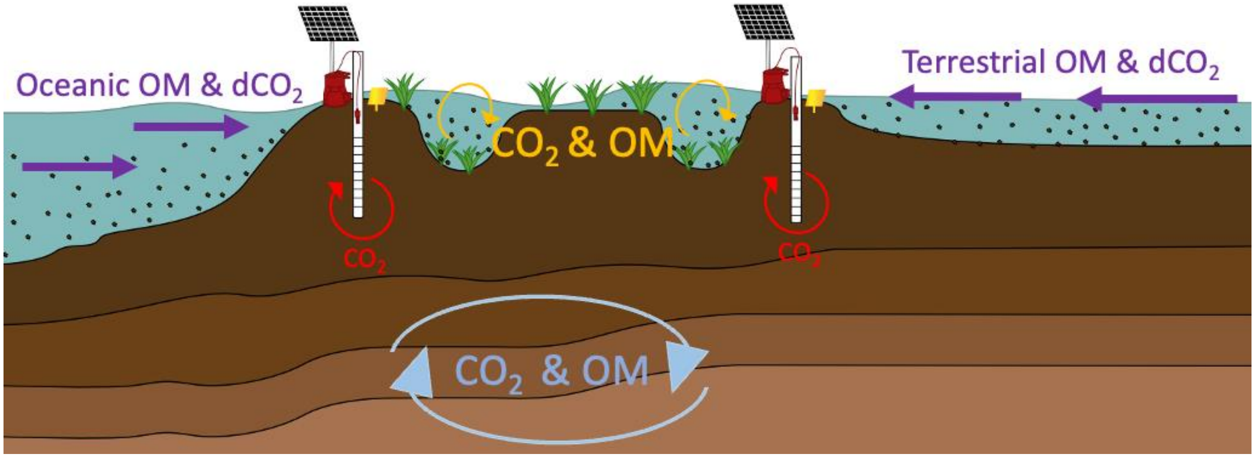

Figure 1.5. Conceptual model of the tidal wetland research site. Two CO_2 flux monitoring site collected concentrations of CO_2 for flux calculations (red). At the monitoring site, net sedimentation tiles were deployed, and soil cores are collected. The key processes of CO_2 flux and carbon storage within tidal wetlands are depicted with oceanic and terrestrial inputs (purple), ongoing sedimentation (yellow), and blue carbon storage in anoxic soils (blue).

Bay (Fig. 1.5). The monitoring stations collected concentrations of CO_2 in soil-gas well atmosphere to determine net sequestration or emission of CO_2 at the sediment interface (Chapter 2). The continuous long-term monitoring quantified NI-WB net flux behavior for a 10-month period, determining when the environment was a source or sink for atmospheric CO_2 concentrations (Chapter 3). Net sedimentation tiles were deployed at the CO_2 flux monitoring station to compare active sedimentation rates to carbon flux behavior (Chapter 3). The monitoring stations was developed to withstand high energy and allow for the collection of a comprehensive CO_2 flux dataset during a hurricane disturbance (Chapter 4). Sediment cores were collected at each monitoring station to determine carbon accumulation rates in NI-WB and correlate variation in blue carbon storage to historical storm events (Chapter 5).

REFERENCES

Al-Attabi, Z., Xu, Y., Tso, G., & Narayan, S. (2023). The impacts of tidal wetland loss and coastal development on storm surge damages to people and property: A Hurricane Ike case-study. *Scientific Reports*, *13*(1), 4620. https://doi.org/10.1038/s41598-023-31409-x

Balaguru, K., Foltz, G. R., & Leung, L. R. (2018). Increasing magnitude of hurricane rapid intensification in the central and eastern tropical Atlantic. *Geophysical Research Letters*, *45*(9), 4238–4247. https://doi.org/10.1029/2018GL077597

Bhatia, K. T., Vecchi, G. A., Knutson, T. R., Murakami, H., Kossin, J., Dixon, K. W., & Whitlock, C. E. (2019). Recent increases in tropical cyclone intensification rates. *Nature Communications*, *10*(1), 635. https://doi.org/10.1038/s41467-019-08471-z

Bucci, L., Alaka, L., Hagen, A., Delgado, S., & Beven, J., National Oceanic and Atmospheric Administration & National Weather Service. (2023) Hurricane Ian (AL092022). *National Hurricane Center Tropical Cyclone Report.* https://www.nhc.noaa.gov/data/tcr/AL092022_Ian.pdf

Byun, C., Lee, S.-H., & Kang, H. (2019). Estimation of carbon storage in coastal wetlands and comparison of different management schemes in South Korea. *Journal of Ecology and Environment*, *43*(1), 8. https://doi.org/10.1186/s41610-019-0106-7

Callaway, J. C., Borgnis, E. L., Turner, R. E., & Milan, C. S. (2012). Carbon sequestration and sediment accretion in San Francisco Bay tidal wetlands. *Estuaries and Coasts*, *35*(5), 1163–1181. https://doi.org/10.1007/s12237-012-9508-9

Canadell, J.G., P.M.S. Monteiro, M.H. Costa, L. Cotrim da Cunha, P.M. Cox, A.V. Eliseev, S. Henson, M. Ishii, S. Jaccard, C. Koven, A. Lohila, P.K. Patra, S. Piao, J. Rogelj, S. Syampungani, S. Zaehle, and K. Zickfeld, (2021). Global carbon and other biogeochemical cycles and feedbacks. In Climate change 2021: The physical science basis. Contribution of Working Group I to the Sixth Assessment Report of the Intergovernmental Panel on Climate Change [Masson-Delmotte, V., P. Zhai, A. Pirani, S.L. Connors, C. Péan, S. Berger, N. Caud, Y. Chen, L. Goldfarb, M.I. Gomis, M. Huang, K. Leitzell, E. Lonnoy, J.B.R. Matthews, T.K. Maycock, T. Waterfield, O. Yelekçi, R. Yu, and B. Zhou (eds.)]. Cambridge University Press, Cambridge, United Kingdom and New York, NY, USA, pp. 673–816, doi:10.1017/9781009157896.007.

Costanza, R., Pérez-Maqueo, O., Martinez, M. L., Sutton, P., Anderson, S. J., & Mulder, K. (2008). The value of coastal wetlands for hurricane protection. *AMBIO: A Journal of the Human Environment*, *37*(4), 241–248. https://doi.org/10.1579/0044-7447(2008)37[241:TVOCWF]2.0.CO;2

Davidson-Arnott, R., Bauer, B., & Houser, C. (2019). *Introduction to Coastal Processes and Geomorphology* (2nd ed.). Cambridge: Cambridge University Press. doi:10.1017/9781108546126

Emanuel, K. (2020). Evidence that hurricanes are getting stronger. *Proceedings of the National Academy of Sciences*, *117*(24), 13194–13195. https://doi.org/10.1073/pnas.2007742117

Fairchild, T. P., Bennett, W. G., Smith, G., Day, B., Skov, M. W., Möller, I., Beaumont, N., Karunarathna, H., & Griffin, J. N. (2021). Coastal wetlands mitigate storm flooding and associated costs in estuaries. *Environmental Research Letters*, *16*(7), 074034. https://doi.org/10.1088/1748-9326/ac0c45

Friedlingstein, P., O'Sullivan, M., Jones, M. W., Andrew, R. M., Hauck, J., Olsen, A., Peters, G. P., Peters, W., Pongratz, J., Sitch, S., Le Quéré, C., Canadell, J. G., Ciais, P., Jackson, R. B., Alin, S., Aragão, L. E. O. C., Arneth, A., Arora, V., Bates, N. R., … Zaehle, S.

(2020). Global carbon budget 2020. *Earth System Science Data*, *12*(4), 3269–3340. https://doi.org/10.5194/essd-12-3269-2020

Gori, A., Lin, N., & Smith, J. (2020). Assessing compound flooding from landfalling tropical cyclones on the North Carolina coast. *Water Resources Research*, *56*(4), e2019WR026788. https://doi.org/10.1029/2019WR026788

Gori, A., Lin, N., Xi, D., & Emanuel, K. (2022). Tropical cyclone climatology change greatly exacerbates US extreme rainfall–surge hazard. *Nature Climate Change*, *12*(2), 171–178. https://doi.org/10.1038/s41558-021-01272-7

Greenberg, R., Maldonado, J. E., Droege, S., & McDonald, M. V. (2006). Tidal Marshes: A global perspective on the evolution and conservation of their terrestrial vertebrates. *BioScience*, *56*(8), 675. https://doi.org/10.1641/0006-3568(2006)56[675:TMAGPO]2.0.CO;2

Hall, T. M., & Kossin, J. P. (2019). Hurricane stalling along the North American coast and implications for rainfall. *Npj Climate and Atmospheric Science*, *2*(1), 17. https://doi.org/10.1038/s41612-019-0074-8

Hu, K., Chen, Q., & Wang, H. (2015). A numerical study of vegetation impact on reducing storm surge by wetlands in a semi-enclosed estuary. *Coastal Engineering*, *95*, 66–76. https://doi.org/10.1016/j.coastaleng.2014.09.008

Intergovernmental Panel on Climate Change (IPCC). (2021). Climate change 2021: The physical science basis. Contribution of Working Group I to the Sixth Assessment Report of the Intergovernmental Panel on Climate Change [Masson Delmotte, V., P. Zhai, A. Pirani, S.L. Connors, C. Péan, S. Berger, N. Caud, Y. Chen, L. Goldfarb, M.I. Gomis, M. Huang, K. Leitzell, E. Lonnoy, J.B.R. Matthews, T.K. Maycock, T. Waterfield, O.

Yelekçi, R. Yu, and B. Zhou (eds.)]. Cambridge University Press, Cambridge, United Kingdom and New York, NY, USA, 2391 pp. doi:10.1017/9781009157896.

Kirwan, M. L., Megonigal, J. P., Noyce, G. L., & Smith, A. J. (2023). Geomorphic and ecological constraints on the coastal carbon sink. *Nature Reviews Earth & Environment*, *4*(6), 393–406. https://doi.org/10.1038/s43017-023-00429-6

Kossin, J. P. (2018). A global slowdown of tropical-cyclone translation speed. *Nature*, *558*(7708), 104–107. https://doi.org/10.1038/s41586-018-0158-3

Letourneau, M. L., & Medeiros, P. M. (2019). Dissolved organic matter composition in a marsh-dominated estuary: Response to seasonal forcing and to the passage of a hurricane. *Journal of Geophysical Research: Biogeosciences*, *124*(6), 1545–1559. https://doi.org/10.1029/2018JG004982

Lindsey, R. (2023, May 12). *Climate change: Atmospheric carbon dioxide*. National Atmospheric And Oceanic Administration. https://www.climate.gov/news-features/understanding-climate/climate-change-atmospheric-carbon-dioxide

Lovelock, C. E., Atwood, T., Baldock, J., Duarte, C. M., Hickey, S., Lavery, P. S., Masque, P., Macreadie, P. I., Ricart, A. M., Serrano, O., & Steven, A. (2017). Assessing the risk of carbon dioxide emissions from blue carbon ecosystems. *Frontiers in Ecology and the Environment*, *15*(5), 257–265. https://doi.org/10.1002/fee.1491

Mcleod, E., Chmura, G. L., Bouillon, S., Salm, R., Björk, M., Duarte, C. M., Lovelock, C. E., Schlesinger, W. H., & Silliman, B. R. (2011). A blueprint for blue carbon: Toward an improved understanding of the role of vegetated coastal habitats in sequestering CO_2. *Frontiers in Ecology and the Environment*, *9*(10), 552–560. https://doi.org/10.1890/110004

Medeiros, P. M. (2022). The effects of hurricanes and storms on the composition of dissolved organic matter in a southeastern U.S. estuary. *Frontiers in Marine Science, 9*. https://doi.org/10.3389/fmars.2022.855720

Mizzell, H., Griffin, M., Strait, F., (2023). S*C hurricanes comprehensive summary*. South Carolina Department of Natural Resources and Climatology Office. chrome-extension://efaidnbmnnnibpcajpcglclefindmkaj/https://www.dnr.sc.gov/climate/sco/hurricanes/pdfs/SCHurricanesExecutiveSummary.pdf

Mo, Y., Kearney, M. S., & Turner, R. E. (2020). The resilience of coastal marshes to hurricanes: The potential impact of excess nutrients. *Environment International*, *138*, 105409. https://doi.org/10.1016/j.envint.2019.105409

Myhre, G., D. Shindell, F.-M. Bréon, W. Collins, J. Fuglestvedt, J. Huang, D. Koch, J.-F. Lamarque, D. Lee, B. Mendoza, T. Nakajima, A. Robock, G. Stephens, T. Takemura and H. Zhang (2013). Anthropogenic and natural radiative forcing. In: Climate change 2013: The physical science basis. Contribution of Working Group I to the Fifth Assessment Report of the Intergovernmental Panel on Climate Change [Stocker, T.F., D. Qin, G.-K. Plattner, M. Tignor, S.K. Allen, J. Boschung, A. Nauels, Y. Xia, V. Bex and P.M. Midgley (eds.)]. Cambridge University Press, Cambridge, United Kingdom and New York, NY, USA

Nahlik, A. M., & Fennessy, M. S. (2016). Carbon storage in US wetlands. *Nature Communications*, *7*(1), 13835. https://doi.org/10.1038/ncomms13835

National Oceanic and Atmospheric Admiration Earth System Research Laboratories. (n.d.). *NOAA's annual greenhouse gas index*. https://gml.noaa.gov/aggi/

Najjar, R. G., Herrmann, M., Alexander, R., Boyer, E. W., Burdige, D. J., Butman, D., Cai, W.-J., Canuel, E. A., Chen, R. F., Friedrichs, M. A. M., Feagin, R. A., Griffith, P. C., Hinson, A. L., Holmquist, J. R., Hu, X., Kemp, W. M., Kroeger, K. D., Mannino, A., McCallister, S. L., … Zimmerman, R. C. (2018). Carbon budget of tidal wetlands, estuaries, and shelf waters of eastern North America. *Global Biogeochemical Cycles*, *32*(3), 389–416. https://doi.org/10.1002/2017GB005790

Ouyang, X., & Lee, S. Y. (2020). Improved estimates on global carbon stock and carbon pools in tidal wetlands. *Nature Communications*, *11*(1), 317. https://doi.org/10.1038/s41467-019-14120-2

Peduzzi, P., Chatenoux, B., Dao, H., De Bono, A., Herold, C., Kossin, J., Mouton, F., & Nordbeck, O. (2012). Global trends in tropical cyclone risk. *Nature Climate Change*, *2*(4), 289–294. https://doi.org/10.1038/nclimate1410

Seneviratne, S.I., X. Zhang, M. Adnan, W. Badi, C. Dereczynski, A. Di Luca, S. Ghosh, I. Iskandar, J. Kossin, S. Lewis, F. Otto, I. Pinto, M. Satoh, S.M. Vicente-Serrano, M. Wehner, and B. Zhou. (2021). Weather and climate extreme events in a changing climate. In climate change 2021: The physical science basis. Contribution of Working Group I to the Sixth Assessment Report of the Intergovernmental Panel on Climate Change [Masson-Delmotte, V., P. Zhai, A. Pirani, S.L. Connors, C. Péan, S. Berger, N. Caud, Y. Chen, L. Goldfarb, M.I. Gomis, M. Huang, K. Leitzell, E. Lonnoy, J.B.R. Matthews, T.K. Maycock, T. Waterfield, O. Yelekçi, R. Yu, and B. Zhou (eds.)]. Cambridge University Press, Cambridge, United Kingdom and New York, NY, USA, pp. 1513–1766, doi:10.1017/9781009157896.013

SCDNR. (2020). *Marine - salt marsh habitat*. South Carolina Department of Natural Resources. https://www.dnr.sc.gov/marine/habitat/saltmarsh.html

Sun, F., & Carson, R. T. (2020). Coastal wetlands reduce property damage during tropical cyclones. *Proceedings of the National Academy of Sciences*, *117*(11), 5719–5725. https://doi.org/10.1073/pnas.1915169117

Vargas, R. (2012). How a hurricane disturbance influences extreme CO_2 fluxes and variance in a tropical forest. *Environmental Research Letters, 7*(3), 035704. https://doi.org/10.1088/1748-9326/7/3/035704

Wahl, T., Jain, S., Bender, J., Meyers, S. D., & Luther, M. E. (2015). Increasing risk of compound flooding from storm surge and rainfall for major US cities. *Nature Climate Change*, *5*(12), 1093–1097. https://doi.org/10.1038/nclimate2736

Wang, F., Lu, X., Sanders, C. J., & Tang, J. (2019). Tidal wetland resilience to sea level rise increases their carbon sequestration capacity in United States. *Nature Communications, 10*(1), 5434. https://doi.org/10.1038/s41467-019-13294-z

Ward, N. D., Bianchi, T. S., Medeiros, P. M., Seidel, M., Richey, J. E., Keil, R. G., & Sawakuchi, H. O. (2017). Where carbon goes when water flows: Carbon cycling across the aquatic continuum. *Frontiers in Marine Science*, *4*, 7. https://doi.org/10.3389/fmars.2017.00007

Windham-Myers, L., Cai, W.-J., Alin, S., Andersson, A., Crosswell, J., Dunton, K.H., Hernandez-Ayon, J.M., Herrmann, M., Hinson, A.L., Hopkinson, C.S., Howard, J., Hu, X., Knox, S.H., Kroeger, K., Lagomasino, D., Megonigal, P., Najjar, R., Paulsen, M.-L., Peteet, D., Pidgeon, E., …P., Zhu, Z. (2018). Chapter 15: Tidal wetlands and estuaries.

Second state of the carbon cycle report. *U.S. Global Change Research Program*. https://doi.org/10.7930/SOCCR2.2018.Ch15

Ye, M., Wu, J., Liu, W., He, X., & Wang, C. (2020). Dependence of tropical cyclone damage on maximum wind speed and socioeconomic factors. *Environmental Research Letters*, *15*(9), 094061. https://doi.org/10.1088/1748-9326/ab9be2

CHAPTER TWO

LOW-COST METHODOLOGY FOR LONG-TERM MONITORING OF CARBON DIOXIDE SOIL GAS FLUX IN ESTUARINE TIDAL WETLAND ENVIRONMENTS

ABSTRACT

Tidal wetlands play a key role in the land-ocean-atmosphere carbon cycle by functioning as both a carbon sink and source. However, the estimates of carbon stocks and fluxes in tidal wetlands are unpredictable due to temporal and spatial *in situ* field sampling and diverse environmental challenges. A low-cost monitoring station was designed to enable easy deployment in local and regional wetlands, while collecting frequent measurements in complex and dynamic aquatic conditions. The monitoring station consisted of a well and floating power station. The well protected a non-dispersive infrared (NDIR) analyzer and provided a mechanism for collecting soil carbon dioxide (CO_2) concentrations. The floating power station housed a marine battery and solar panel to supply power during extended sampling periods to the NDIR analyzer and a cloud-connective data acquisition device which is Raspberry Pi-based. The in-situ collected concentrations were applied to a flux equation to determine net sequestration or emission. Enhanced spatial and temporal CO_2 flux sampling allowed by this novel monitoring station design will provide comprehensive insights to wetland-atmosphere carbon concentration feedbacks; hopefully influencing climate change projections and wetland management practices.

INTRODUCTION

Estuarine tidal wetland environments develop in intertidal zones of protected marine coasts and are characterized by brackish water conditions due to interactions between terrigenous and oceanic water sources (Davidson-Arnott et al., 2019; Greenberg et al., 2006). Despite occupying a small fraction of Earth's surface, these coastal environments play a key role in the land-ocean-atmosphere carbon cycle by functioning as both a carbon sink and source (Keller, 2011; Najjar et al., 2018; Villa and Bernal, 2018). Autochthonous (i.e., atmospheric CO_2 fixed by photosynthesis) and allochthonous (i.e., particulate organic matter produced offsite) carbon can be sequestered and stored within tidal wetland sediment (Windham-Myers et al., 2018). The sequestered carbon, known as 'blue carbon', experiences long-term storage in tidal wetlands due to slow decomposition rates and high sedimentation rates (Lovelock et al., 2017; Mcleod et al., 2011). Tidal wetlands also serve as a source of atmospheric CO_2 through releases of gaseous carbon from natural degradation and heterotrophic respiration (Lovelock et al., 2017).

The quantified role of tidal wetlands in the global carbon budget lacks scientific consensus (Wang et al., 2019). In the Second State of the Carbon Cycle Report, The United States Global Change Research Program identified knowledge gaps in the magnitude of annual carbon flux for intertidal and subtidal environments (Windham-Myers et al., 2018). The direct collection of gaseous carbon flux measurements from tidal wetland sediment is most commonly collected via chamber-based studies (Oertel et al., 2016). Methods for chamber-based analysis enable soil gas flux measurements to occur under near-natural conditions (Dossa et al., 2015). However, the active water level dynamics of tidal wetlands and current chamber-based methodology impose several challenges for measuring long-term soil gas flux in an estuarine setting. The limitations include high-startup cost, low spatial coverage, and infrequent sampling intervals (Hill and Vargas, 2022).

The technology of soil gas flux chambers generates substantial equipment expenses. Additionally, a single chamber's area represents only a small footprint in the environment and lacks wide-spread spatial resolution (Barba et al., 2018; Hill and Vargas, 2022). The high equipment cost may prohibit deployment of several chambers and further limit expansive spatial data collection. Additionally, the generally non-waterproof equipment requires most carbon flux studies to be completed during non-inundation periods, ensuing periodic and infrequent data collection (Cheng et al., 2021). The poor spatial and temporal resolution of current chamber-based methods presents a challenge for producing annual carbon flux data sets and forecasting the carbon cycle in tidal wetlands (Cueva et al., 2017; Lucas-Moffat et al., 2018).

The Intergovernmental Panel on Climate Change (IPCC), the leading body for assessing science related to climate, does not fully include CO_2 fluxes from wetlands in climatic modelling due to challenges associated with temporal data collection and spatial estimation (IPCC, 2021; Canadell et al., 2021). However, the IPCC does emphasize with high confidence that variations in the tidal wetland carbon cycle will alter atmospheric CO_2 concentrations (IPCC, 2021). The complex dynamics of tidal wetlands decrease the ability to collect continuous *in situ* soil gas flux measurements in these critical marginal marine carbon reservoirs. The purpose of this chapter is to address the temporal and spatial challenge of collecting estuarine carbon flux data by providing a design for a cost effective, long-term monitoring system, which collects soil gas flux measurements in highly dynamic estuarine tidal wetlands. The chapter includes a seven day dataset to provide a visualize representation of a continuous data set over an extended period within a dynamic tidal wetland environment. The wide-spread adoption of a low-cost CO_2 flux monitoring system will generate improved spatial and temporal datasets of annual CO_2 fluxes in tidal wetlands, hopefully contributing to an improved tidal wetland carbon budget and climate forecasting. This chapter was prepared for the submission to the Journal of Estuarine, Coastal, and Self Science.

MATERIALS & METHODS

Study Area

The deployment of soil gas flux monitoring stations occurred within the North Inlet – Winyah Bay (NI-WB) National Estuarine Research Reserve (NERR) near Georgetown, SC (Fig. 2.1). The NI-WB reserve comprises ~77 square kilometers (km^2) of pristine estuarine tidal wetlands which have been protected from development since 1992 by the Belle W. Baruch Foundation. The reserve consists of two connected estuarine environments, North Inlet and Winyah Bay. North Inlet is a small semidiurnal tidally-dominated estuary with an ~96 km^2 watershed, which receives freshwater hydrologic input from surrounding watersheds and northward flow from Winyah Bay (NI-WB NERRS, 2016). In contrast, Winyah Bay is a riverine-influenced estuary with a ~47,000 km^2 watershed (NI-WB NERRS, 2016). Winyah Bay experiences semidiurnal tide patterns, superimposed on unidirectional (riverine) flow to the Atlantic Ocean contributed by four main rivers: Pee Dee, Waccamaw, Black, and Swampit Rivers (NOAA, 1992).

CO_2 flux monitoring stations were constructed at inlet and outlet locations of NI-WB in No Man's Friend Creek and Town Creek (Fig. 2.1). No Man's Friend Creek receives freshwater flow from Winyah Bay. This area, known as Mud Bay, experiences high sediment loads and links Winyah Bay to North Inlet. Town Creek is dominated by oceanic influence due to its proximity to North Inlet.

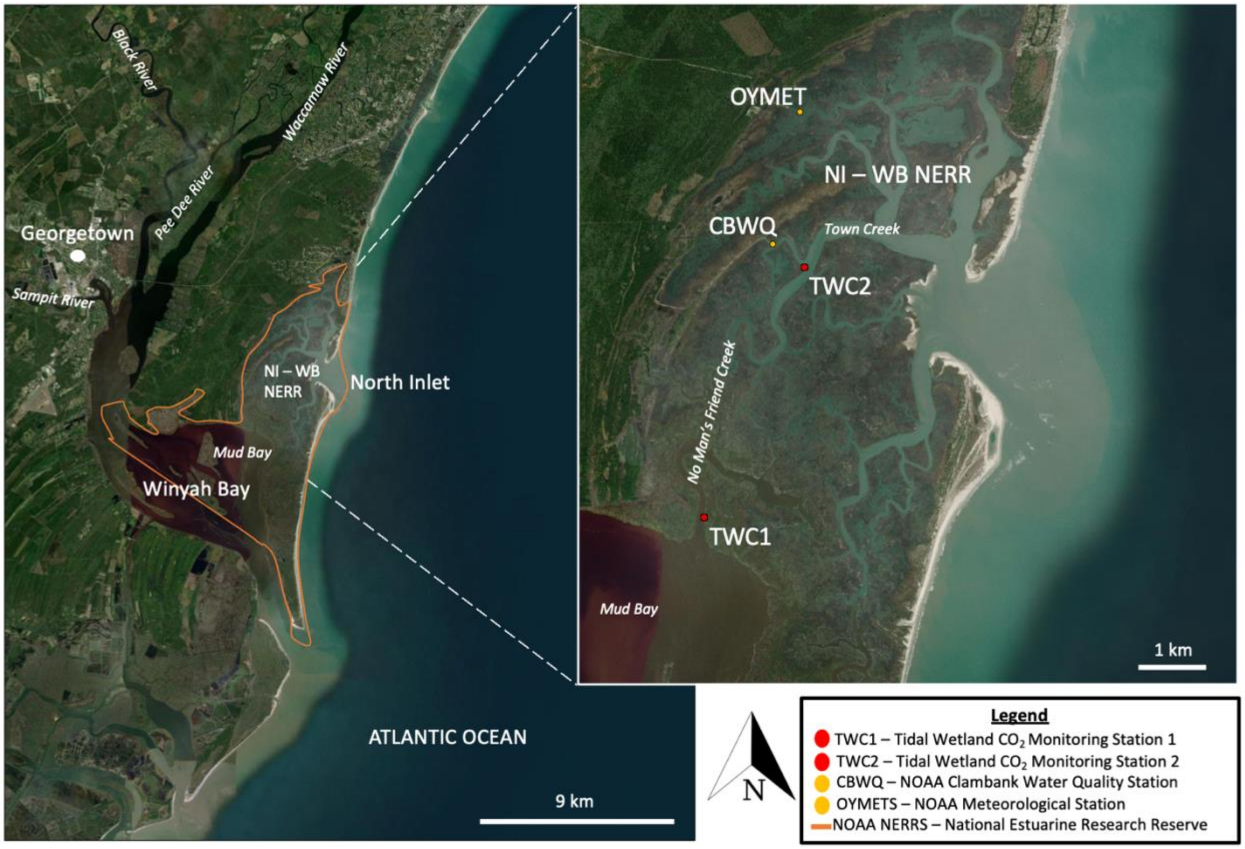

Figure 2.1. Study Area of North Inlet-Winyah Bay (NI-WB) National Estuarine Research Reserve (NERR) location in Georgetown, SC.

CO_2 Flux Monitoring Station Material

The designed CO_2 flux monitoring station was primarily comprised of a closed soil-gas well system and a floating power station to support data acquisition. The novel design and methodology described below permit the continuous collection of CO_2 flux in aquatic environments.

Collecting CO_2 Flux Measurements in Dynamic Coastal Environments: Soil-Gas Well

The well system mimics the closed dynamic chamber system method to measure gas flux at the sediment surface. A polyvinyl chloride (PVC) well was buried below ground and extends through the sediment-water-air interface to capture soil gas concentrations fluxing from the sediment surface (Fig. 2.2). A non-dispersive infrared (NDIR) gas analyzer (Vaisala GMP252) is housed at the top of the well system to quantify respired CO_2 concentrations. The buried portion of the well contains a screen which infills naturally with fine wetland sediment to replicate steady-state conditions. The well system extends above the water surface to protect the NDIR analyzer in the aquatic setting. A novel flotational backflow check valve is constructed within the PVC well to preserve the NDIR analyzer from unusually high tides and storm surges. The flotational check valve closes during rising water levels in high-water events due to a density differential between water and the air in the valve. The valve releases due to gravitational pull as water levels recede within the well. The well cap contains a one-way air and water flow valve to limit pressure build-up within the well (Clough et al., 2020). All features of the well above the ground surface are sealed with PVC cement and waterproof silicone to maintain a closed dynamic chamber system.

Accounting for Extreme Changes in Water Level: Floating Power Station

Electrical power is required for the collection of CO_2 concentration measurements via the NDIR analyzer and the data acquisition via a data logger. A Raspberry Pi Zero equipped with a universal serial bus (USB) hub that powers a RS485 Modbus converter and cellular modem serves as the systems data logger. The cellular connection supported continuous monitoring and acquisition of data in the remote locations of tidal wetlands. The NDIR analyzer's maximum power consumption was 0.5 watts (W). The Raspberry Pi's fully functioning power consumption was ~2 W. Based on these power needs, a 12.6 volt (V), 55 amp-hour deep cycle marine battery is used to power the system. The application of Watt's law ($Power = current \times voltage$) and Amp-hour formula ($Amp - hours = \frac{watts}{voltage} \times hours$) determines the NDIR analyzer, Raspberry Pi, and marine battery will function for ~11.5 days assuming no reserve (i.e., a perfect battery). To ensure continuous and long-term data collection beyond the 11.5 days, a waterproof 12 V, 55W solar panel is employed to trickle charge the marine battery.

The Raspberry Pi data logger and marine battery are housed within a National Electrical Manufactures Association (NEMA) 6P waterproof polycarbonate enclosure (Fig. 2.2). The electrical wire connection between the (1) Raspberry Pi-to-sensor and (2) marine battery-to-solar panel protrude through the enclosure via NEMA 6P wire glands; ensuring water protection of electrical equipment within the enclosure. The enclosure contains exterior heat tape and interior desiccant packets to limit moisture development.

The enclosure and solar panel are attached to the top of a commercially constructed floatation device comprised of expanded polystyrene (EPS) foam encased within polyethylene (PE) to allow electrical equipment to rise with unusually high waters (e.g., king tides, storm surge)

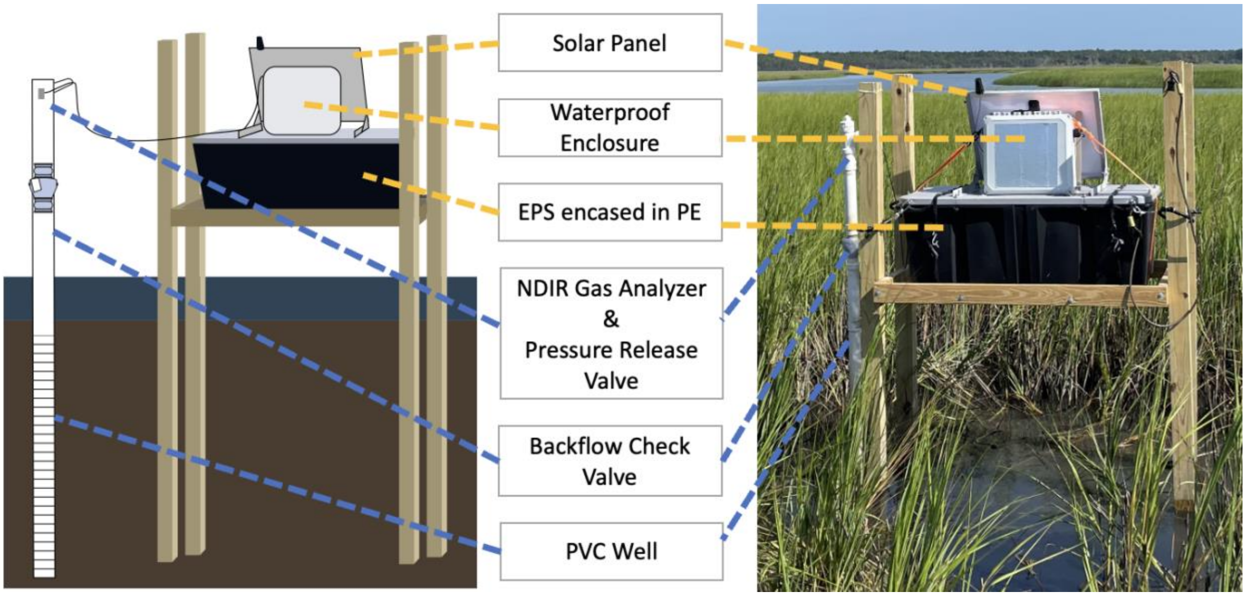

Figure 2.2. Complete monitoring station design with well system and floating power station. Blue lines indicate soil-gas well material (NDIR - Non-dispersive infrared gas analyzer; PVC – polyvinyl chloride). Yellow lines indicate floating power station (EPS – expanded polystyrene; PE – polyethylene).

and lower when waters recede. The encased EPS foam is fastened to a plastic base platform. The encased EPS foam is tethered to four lumber posts via stainless steel wire. The wire is looped around the posts via stainless steel rope clamps. To promote equipment longevity and limit weathering in the estuarine environment, material use includes stainless steel hardware, treated lumber, and PVC.

CO_2 Flux Monitoring Station Design and Deployment

Considering Environmental Conditions

Tidal wetlands are dynamic systems with varying hydrology, sediment transport, and local weather events. To conduct successful long-term CO_2 flux monitoring, the environmental dynamics of tidal wetlands must be considered to preserve electrical components, collect continuous data, and maintain integrity of the monitoring station. Local hydrologic flows of normal tides, higher than normal tides (king tides), and river discharges influence wetland inundation periods and water levels. Awareness of local water level maximums informed the construction of CO_2 flux monitoring systems in NI-WB to a height where equipment is protected from water damage. Furthermore, variation in hydrologic flows has the potential to impact sediment transport and accumulation rates within differing wetlands settings, ultimately influencing the burial processes of organic carbon for long-term storage (Hinson et al., 2019). The placement of monitoring stations and data analysis should be informed by natural sediment transport and accumulation patterns, as well as meteorological events such as high winds, storm surge, and flooding.

The present National Oceanic and Atmospheric Administration (NOAA) National Tidal Datum Epoch (NTDE; 1983-2001) was used to identify tidal ranges and water levels in NI-WB

(NOAA, 2022). The tidal range for NI-WB was 1.5 m. The mean tidal level (MTL) was ~1.6 m, with a mean high-water (MHW) level of ~2.5 m. Maximum tides peaked at 3 m (NOAA NERR, 2012). Since 2001, maximum water levels occurred during a king tide and peaked to ~3.3 m (NOAA NERR, 2012). During this period, Hurricane Matthew (2016) produced a maximum storm surge water level of ~3.2 m. Additionally, Hurricane Matthew produced the maximum wind speeds in North Inlet with measurements of at 33.6 meters per hour (m h^{-1}; NOAA NERRS, 2012). The consideration of environmental parameters and historical water levels of NI-WB was essential in the utility and longevity of a CO_2 flux monitoring station's soil-gas wells and floating power stations.

Monitoring Station Deployment

The soil-gas well and power station posts were deployed in boreholes at the water's edge at the monitoring station locations during the estimated MTL by the NOAA NERRS Clambank Water Quality Station (CBWQ; NOAA, 2022). The 5 cm diameter PVC well was buried 1.2 meters below ground and contains a 1-meter screen (1.27 cm screened openings at a 2.54 cm interval). The well extended 2 m above the ground surface, with the intent to exceed the maximum water levels. The backflow check valve was deployed at 1.4 m above the ground surface to protect the NDIR sensor from waters exceeding MHW (Fig. 2.3). The NDIR gas analyzer was secured in the center of the well's diameter. The wells were deployed and allowed to infill with sediment and reach steady state for at least one month prior to the initial collection of CO_2 flux measurements. The potential for subsidence of wells within fine grained sediment should be considered to ensure the design and construction accounts for NTDE water levels and warrants the aptitude of the NDIR

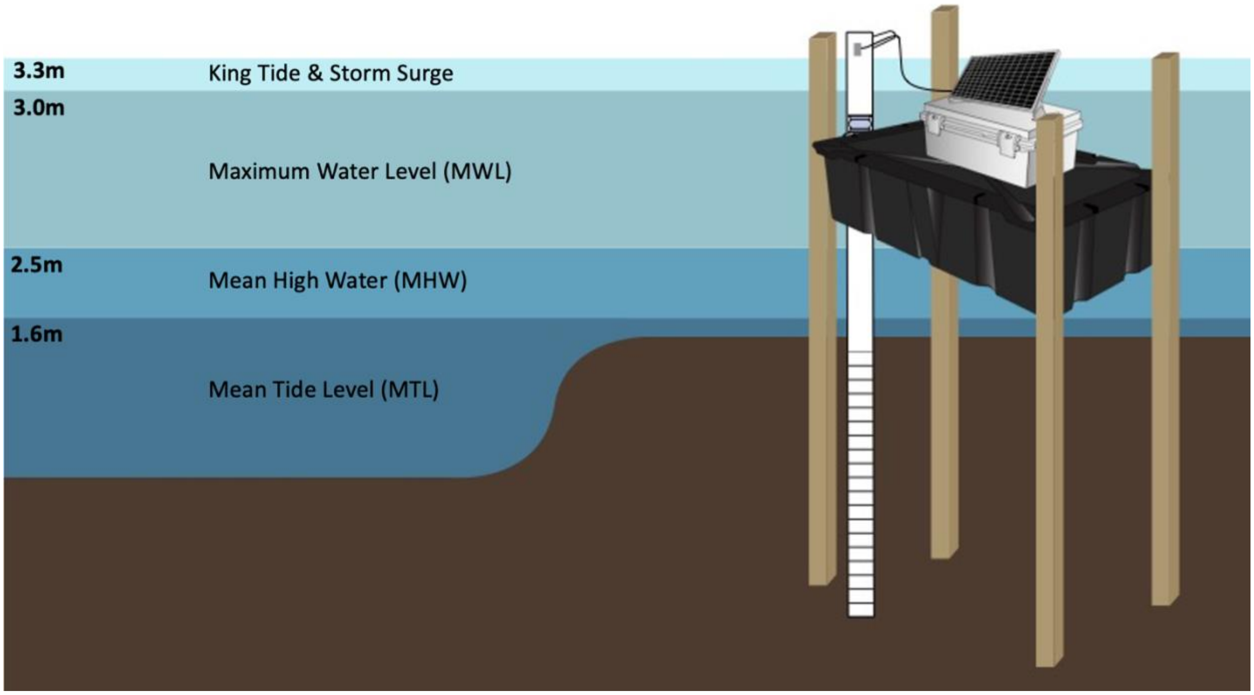

Figure 2.3. Soil-gas well and floating power station design associated with water levels of NI-WB. At the monitoring locations, the well system was deployed in boreholes created at the water's edge during the estimated time of mean tidal level (MTL) by the NOAA NERRS Clambank Water Quality Station (NOAA NERRS, 2012).

gas analyzer for long-term monitoring by protecting the electrical equipment from water damage in the aquatic setting. During routine equipment maintenance, the height of the PVC well and monitoring station's treated lumber posts were measured from the soil surface to the top of the well and posts to ensure subsidence did not occur.

The power station's 3 m treated lumber posts were deployed in boreholes at 1 m depth. The posts extended 2 m above the ground surface, exceeding historical maximum water levels. The base platform of the power station had dimensions of 1.4 m by 1 m and was 1.1 m above the ground surface. The encased EPS foam, waterproof enclosure, and solar panel extended 0.3 m above the platform. Therefore, the floating power station could rise, if necessary, to NTDE historical high-water levels to protect electrical equipment and promote continuous monitoring. Additionally, a stainless-steel cord was attached to the top of a lumber post and the encased EPS foam float for security purposes and to provide extra support in the case of unexpectedly high waters. All hardware used to construct the platform was stainless steel to avoid salt corrosion.

THEORY

Flux Calculation

The soil gas flux well was a closed dynamic chamber system above ground, with a naturally infilled screen below ground to mimic steady-state conditions and a one-way diaphragm pressure release valve. The one-way diaphragm pressure release valve (BBTUS 99502) has a cracking pressure of 20 millibars (mbar). Therefore, when 20 millibars of pressure built up in the well system, the diaphragm release valve cracked, to allow the pressure to release until the well atmosphere and surrounding atmosphere pressure were in equilibrium. The release of pressure may have cause flow through to occur, a characteristic of a closed dynamic chamber system. The stored carbon below ground must respire past the sediment interface over the area of the PVC well into the well's atmosphere. The NDIR analyzer measured CO_2 concentrations as parts per million (ppm) within the well's dynamically closed atmosphere. Assuming closed conditions during CO_2 concentrations measurements, the ideal gas law is incorporated into the flux equation as it governs gases in a closed system:

$$\mathrm{PV} = \mathrm{nRT} \qquad \textit{eqn. 1.1}$$

Where P is the standard atmospheric pressure (1,013.25 millibars [mbar]), V is the volume of an ideal gas at standard pressure (0.2241 cubic meters per mole [m^3 mol^{-1}], n is the number of moles of a gas, T is the standard temperature (273.15 Kelvin [K]), and R is the universal gas constant (0.83025 [mbar m^3 K^{-1} mol^{-1}]). The ideal gas law is applied to a flux equation:

$$\mathrm{Flux} = \frac{\Delta \mathrm{c}}{\Delta \mathrm{t}} \times \frac{\mathrm{PV}}{\mathrm{RT}} \times \frac{1}{\mathrm{A}} \qquad \textit{eqn. 1.2}$$

Where is $\frac{\Delta c}{\Delta t}$ is the change in measured CO_2 gas (c, [ppm]) over time (t, [s^{-1}]). Pressure in this application was the atmospheric pressure measured by an external weather station (P, millibars [mbar]; NOAA NERR, 2012). The volume (V, cubic meters [m^3]) of the gas was determined by subtracting the volume of the well (V_w, [m^3]) by the sampling volume (Vs, [m^3]) within the NDIR analyzer (Dossa et al., 2015).

$$\mathrm{V} = \mathrm{V_w} - \mathrm{V_s} \qquad \textit{eqn. 1.3}$$

The volume of the cylindrical well, with a 0.05 m diameter and 2 m height, was 3.93×10^{-3} m^3. The volume of the GMP 252 NDIR analyzer's sampling volume was 6.9×10^{-6} m^3. Therefore, the volume variable for this monitoring station was 3.92×10^{-3} m^3. Temperature was measured by the NDIR analyzer in Celsius and converted to Kelvin. The cross-sectional area of the cylindrical well was 1.96×10^{-3} m^2.

Parameter Functions

The GMP252 NDIR analyzer utilized built-in compensation of pressure and temperature to ensure precise measurements of CO_2 concentrations. The GMP252 NDIR analyzer was assumed to function properly for accurate concentration readings in this study due to successful calibration conducted by the NDIR sensor manufacturing company Vaisala (Appendix A). The flux equation is dependent upon pressure and temperature; therefore, if not measured by NDIR analyzer, it must be measured by an external sensor.

The pressure compensation was set for sea-level pressure (1,013.25 mbar) in this design, due to North Inlet's tidal wetland location at sea-level. Atmospheric pressure was measured via a nearby NOAA NERRs meteorological station (OYMET; Fig. 2.1). Well pressure was assumed to be equivalent to atmospheric pressure due to the one-way pressure release valve designed on the well that inhibits pressure build-up.

The GMP252 NDIR analyzer housed an on-board temperature sensor to compensate concentration measurements with real-time temperature readings. The temperature readings within the soil-gas wells were compared to atmospheric temperature readings collected via the nearby meteorological station (NOAA NERR, 2012). The comparison of the NDIR measured temperature and the atmospheric measured temperature, displayed a direct relationship between well temperature and atmospheric temperature (Fig. 2.4). Therefore, when the atmospheric temperature rises, well temperature rises, and vice versa. The comparison of the well temperature and

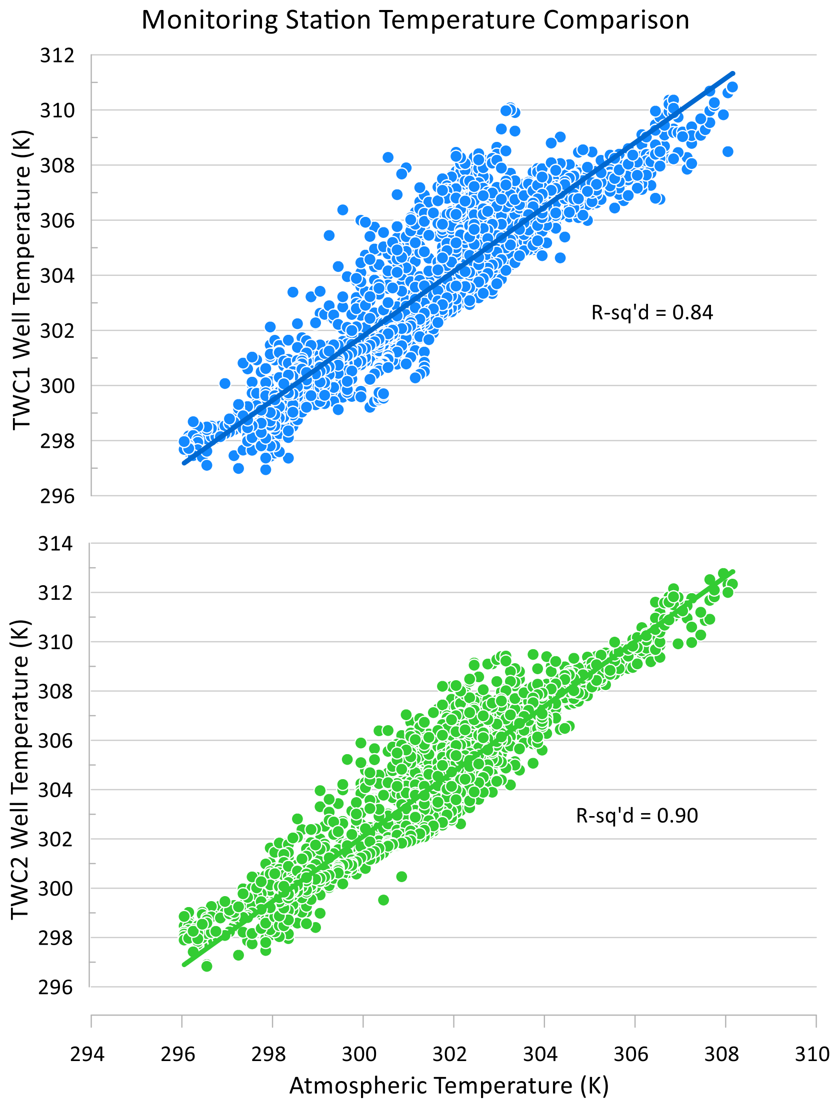

Figure 2.4. Well temperature vs. atmospheric temperature for TWC1 (blue; top) & TWC2 (green; bottom) monitoring station (4688 temperature measurements).

atmospheric temperature produced an R-squared value of ~0.84 for TWC1 and ~0.89 for TWC2, indicating well temperature to have a strong correlation to atmospheric temperature. The positive correlation and R-squared value of greater than ~0.84 between the well temperature versus atmospheric temperature ensured temperature imbalance does not occur within the soil-gas well design (Fig. 2.4).

Parameter estimation

Direct measurements of pressure and temperature are preferred to ensure an accurate description of the gas under analysis. In the absence of an internal and external pressure sensor, an estimation calculation using the barometric formula may provide a pressure variable for the flux calculation.

$$P(z) = P_0 \times e^{-\frac{p_0 \times g \times z}{p_0}} = P_0 \times e^{-\frac{z}{H}} \text{ ; where } H = \frac{RT}{g} \qquad \textit{eqn. 1.4}$$

$P(z)$ is the pressure estimated at the altitude of NDIR analyzer (z), P_0 is atmospheric pressure at sea level (1,013.25 mb), R is the universal gas constant (mbar m^3 K^{-1} mol^{-1}), T is measured temperature by the NDIR analyzer (K), and g is gravitational acceleration constant (9.18 m^2 s^{-1}; Lente and Ősz, 2020).

RESULTS

The well monitoring stations located in NI-WB collected data autonomously every five minutes. The autonomous data collection allowed for a continuous data set of CO_2 concentration readings within the well atmosphere (Fig. 2.5 & 2.6). The monitoring stations successfully collected and transmitted data within the intertidal zone of tidal wetlands and survived a high-energy event.

The continuous CO_2 concentration readings were then applied to the flux equation (eqn. 1.2) to determine the carbon exchange between the sediment interface and the overlying atmosphere. For the well monitoring station design, a negative flux indicated CO_2 concentrations being sequestered in the subsurface sediment. A positive flux, indicating CO_2 concentrations increasing in the well, was equivalent to an emission of CO_2 from the sediment interface.

Data sets with measurements every five minutes provided a high temporal resolution characterization of CO_2 flux during both inundated and non-inundated time periods. The high temporal resolution provided insight to CO_2 flux variation with abnormal pulses of high emission or sequestration, which can be observed with the peaks on 7/17/22. The establishment of multiple low-cost monitoring systems will identify spatial varying sequestration and emission of CO_2. For example, the TWC1 station experienced a higher variation of flux compared to the TWC2 station. The deployment of the stations in different locations, identifies varying carbon flux behavior across the tidal wetland. The application of increased spatial and temporal data sets offers high resolution CO_2 sequestration or emission analysis in additional global tidal wetlands.

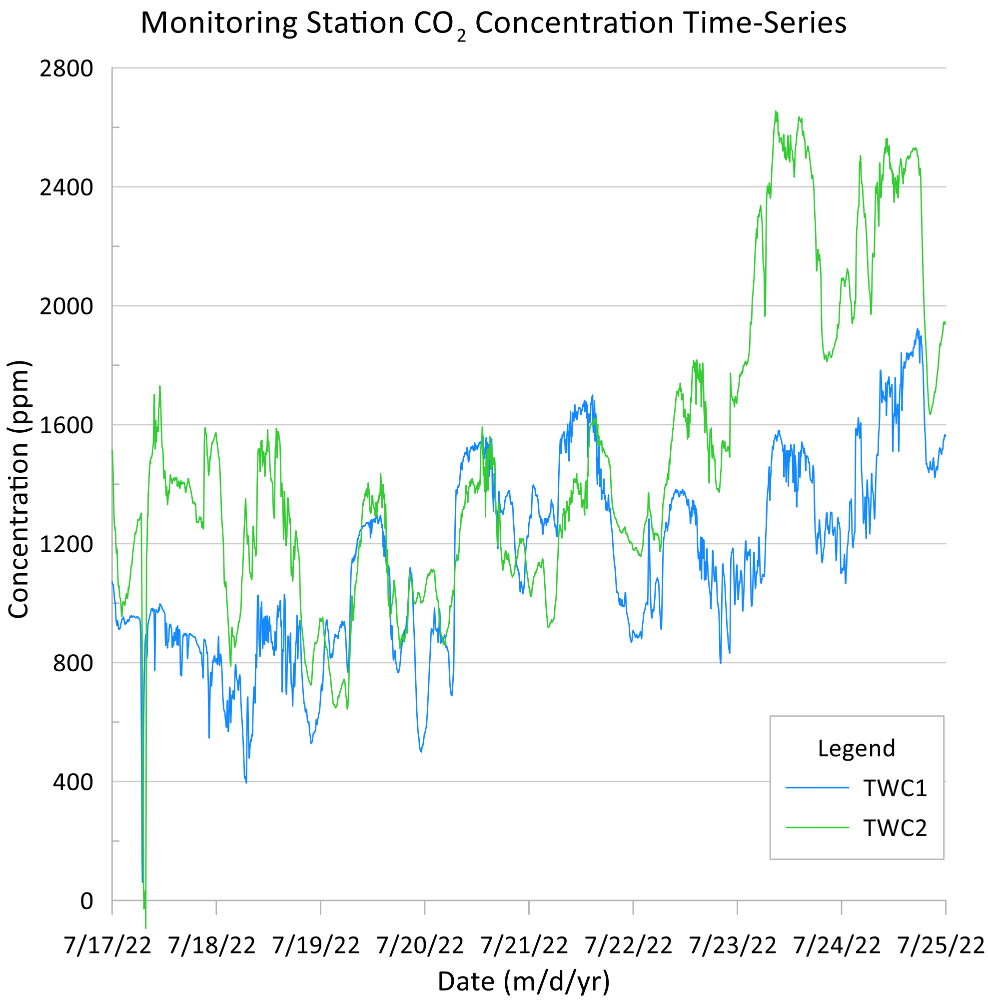

Figure 2.5. Concentration of CO_2 within the TWC1 and TWC2 well atmospheres over a one-week time interval.

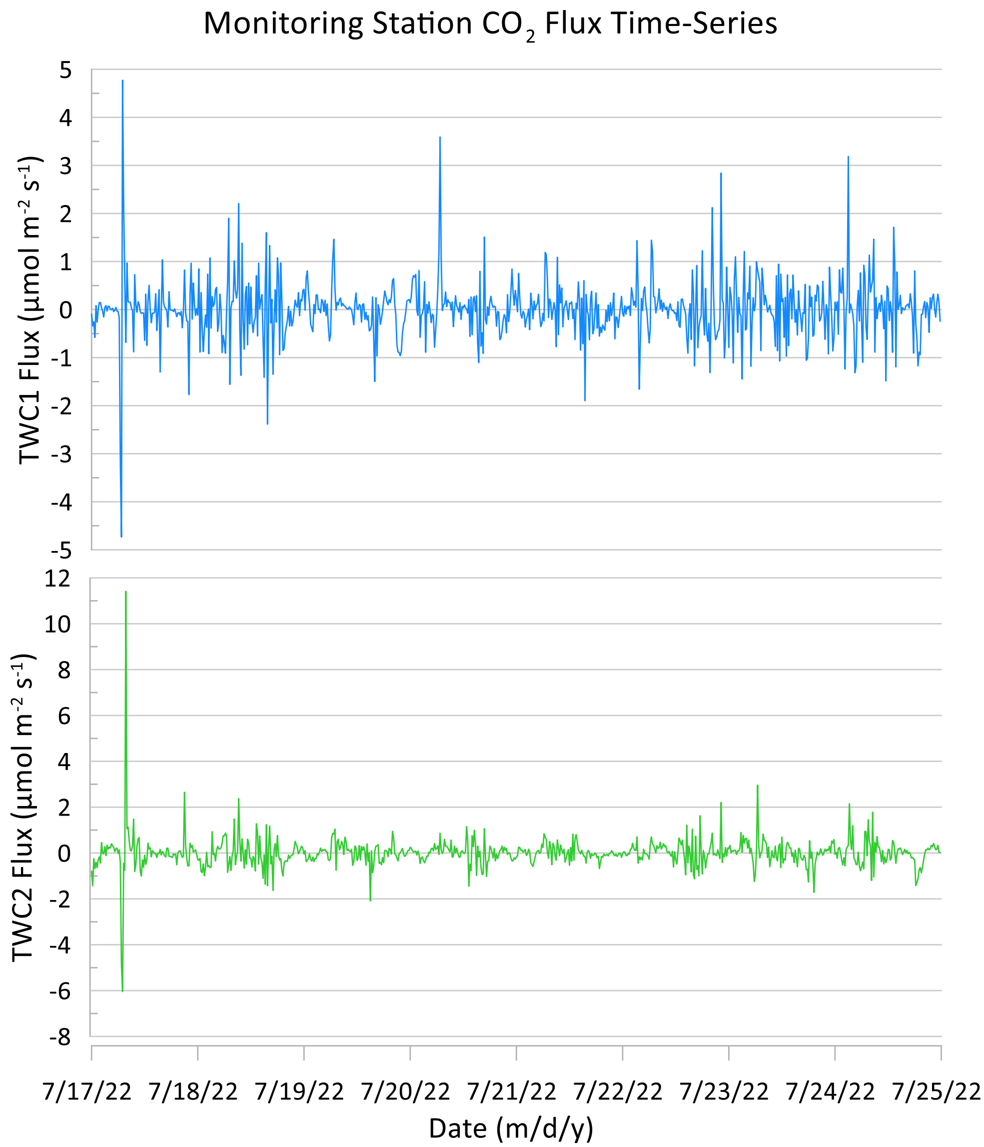

Figure 2.6. Flux measurements at TWC1 (top) and TWC2 (bottom) monitoring stations.

Resilience to Hurricane Energy

The CO_2 flux monitoring station design was developed to withstand high-energy conditions associated with coastal systems (e.g., gale winds, king tides, hurricanes). On September 30, 2022, Hurricane Ian made landfall over NI-WB NERR with a direct path between TWC1 (0.21 km from the eye) and TWC 2 (1.34 km from the eye; Figure 2.7). Hurricane Ian was designated as a Category 1 Hurricane upon landfall (Bucci et al., 2023). TWC1 remained fully functional throughout Hurricane Ian, with minor damages to the solar panel and wrack debris. TWC2 was overcome from high storm surge funneling into the North Inlet system, but collected data until the amalgamation with high tide and peak storm surge.

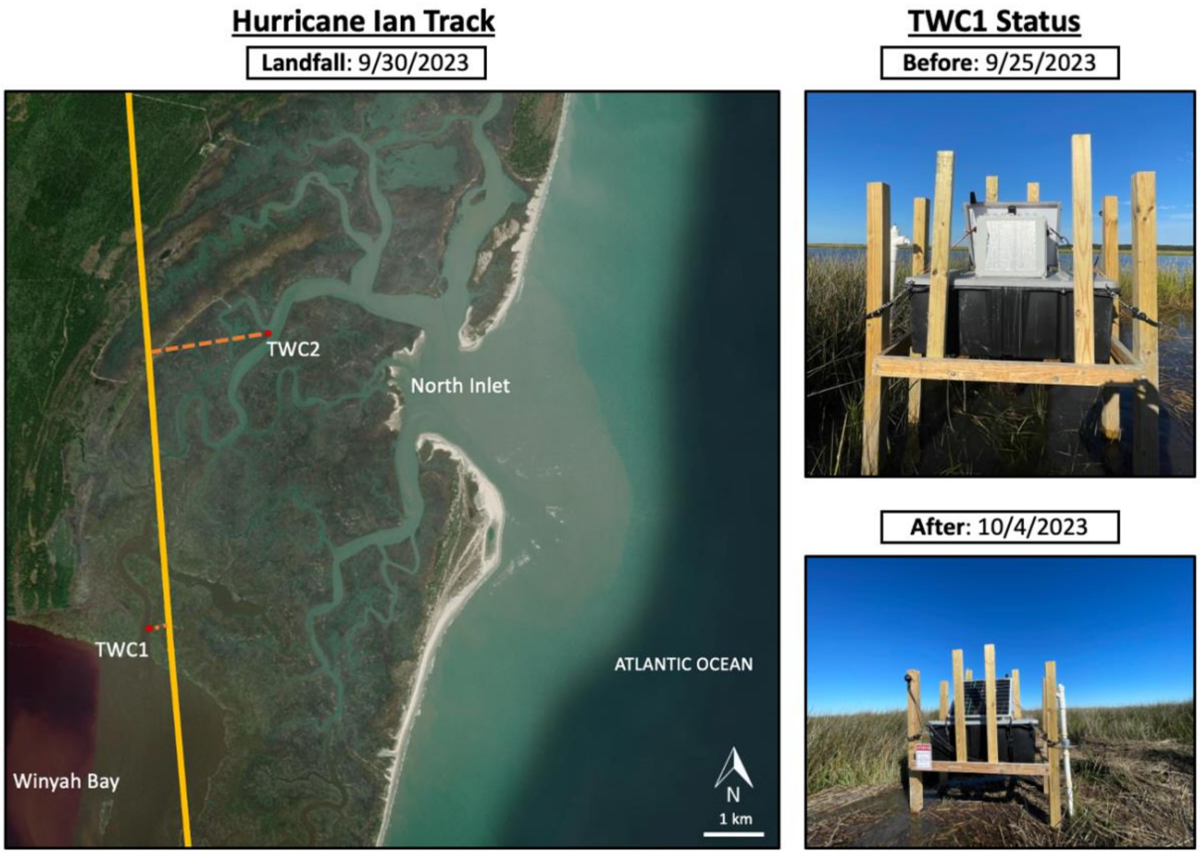

Figure 2.7. Hurricane Ian tack map through NOAA's NI-WB NERR and CO_2 flux monitoring stations. Before and after Hurricane Ian images of TWC1 Monitoring Station, with the inclusion of supplementary posts to support rise and fall of the flotational power station.

DISCUSSION

Method Applications

Greenhouse Gases of Concern

Estuarine tidal wetlands contribute to natural climate change mitigation by functioning as an efficient carbon reservoir. The described CO_2 monitoring station design and results identified CO_2 emission or sequestration in wetland environments through the application of the flux equation. The same methods may be applied to measure other GHGs of concern such as, methane (CH_4) and nitrous oxide (N_2O).

Methane is a short-lived, climate-forcing pollutant, with potent radiative forcing power (Mar et al., 2022). An NDIR CH_4 analyzer, or CH_4/CO_2 multigas NDIR analyzer (i.e., *Vaisala* MGP262), may be applied to the outlined design to quantify CH_4 fluxes in tidal wetlands. Saline conditions suppress methane emissions due to the presence of oceanic sulfate concentrations inhibiting methanogenesis (Poffenbarger et al., 2011). Therefore, within the salinity profile of tidal wetlands, CH_4 flux gradients across tidal wetlands systems may be analyzed with deployment of multiple monitoring stations. Furthermore, the trends of CH_4 flux due to sea-level rise and saltwater intrusion pulses may be measured by continuous analysis of CH_4 concentrations via a NDIR analyzer in the well monitoring station located in natural tidal wetland conditions for extended periods (He et al., 2022; Middelburg et al., 2002).

Nitrous oxide is a is a long-lived greenhouse gas which promotes destruction of ozone in the stratosphere of Earth's atmosphere (Montzka et al., 2011; Portmann et al., 2012). Nitrogen loads in estuarine wetland environments have been altered due to increased influence of wastewater discharge and agricultural fertilizer runoff (Murray et al., 2015). To identify *in situ* flux of N_2O in local tidal wetlands, a NDIR or Clark-type sensor (e.g., *Unisense* microsensor) may be equipped within the well monitoring station design. The monitoring station design enables the measurement of soil gas fluxes during varying water levels, offering the opportunity to conduct analysis of tidal rewetting on N_2O production (Emery et al., 2021). *In situ* measurements of N_2O flux may provide insight to the role of biological production of N_2O in estuarine tidal wetland sediment and the overall contribution to the global nitrogen cycle.

Design Manipulation

The monitoring station design may be altered based on environmental conditions at a given site. The soil-gas well height can vary depending on local tidal ranges and water level maxima. The well should be preferentially built to decrease volume of the well's atmosphere by minimizing the distance between sediment surface and NDIR analyzer. The flotational power station design may be manipulated depending on solar panel and battery use. The selection of the solar panel and battery is based on power consumption, as well as desired monitoring duration. The selected battery must account for NDIR analyzer and data acquisition power consumption. In addition to the power consumption, the efficiency rating of the solar panel wattage and battery amp-hour will determine the monitoring duration.

High wattage solar panels will ensure efficient tickle charging of the marine battery. The solar panel direction should be determined based on solar zenith and azimuth to maximize efficiency (Gardashov et al., 2020). Periodic cleaning of the solar panel may be required to warrant maximum solar collection efficiency. High amp-hour battery rating will ensure electrical system competency and data collection during low solar charging periods. It is recommended for long-term monitoring stations in remote tidal wetland locations, with difficult access, the solar panel efficiency and battery life amp-hour rating should be maximized.

Flotation of Powering Station Considerations

Expanded polystyrene (EPS) foam material was used as the flotational device within the monitoring station due to its buoyancy. The PE outer casing protects the EPS foam from exterior damages, such as saltwater corrosion. Other flotational devices may be applied to the outlined design to fit the spatial needs of subsequent research studies. Archimedes principle may be utilized to guarantee flotation of the auxiliary powering station. The volume of the flotational device may be multiplied by the density of water to determine the mass of the displaced water. The volume of the flotational device and density of the material (e.g., EPS foam) may be multiplied to determine the mass of the flotational device. If the mass of the flotational device is less than the mass of water, buoyant forces will allow the flotational device to stay above water.

In extreme high-water events, the NEMA 6P rating of the waterproof enclosure ensures the Raspberry Pi data logger and marine battery were protected during submersion conditions. The construction of the solar panel and waterproof enclosure should be balanced in the center of the flotational device to ensure the device is not imbalanced and overturned with high waters. If needed, supplementary posts may be added to the base platform to limit the loss of the powering station and guide the mobility during varying water levels. The addition of supplementary posts was added to the TWC1 and TWC2 monitoring stations prior to Hurricane Ian (Fig. 2.7).

Limitations and Solutions

The soil-gas well design aims to quantify the exchange of CO_2 concentration at the sediment and atmosphere interface. The wells are deployed in pre-dug boreholes and allowed to infill naturally with sediment to avoid compaction of soil surrounding the soil-gas well. It is recommended to allow at least one month for sediment to backfill the system and return to steady-state conditions before collecting measurements. For this study, the well system was deployed for 11 months to allow sediment to backfill into the system, however, complete backfilling was observed after one month. Additionally, it is essential to avoid compacting sediment during monitoring station maintenance. The limitation of soil compaction surrounding the soil-gas well will promote natural conditions for accurate interpretation of CO_2 gas diffusion within wetland sediments (Kühne et al., 2012).

The use of the one-way pressure release valve prevents the influence of a pressure gradient between the interior and exterior of the well system on CO_2 concentration measurements (Christiansen et al., 2011). If ambient-exterior atmospheric pressure is higher than well atmosphere pressure, the well atmosphere is assumed to equilibrate to ambient atmospheric pressure due to the proportional relationship between temperature and pressure within the ideal gas law. The well atmosphere temperature and ambient atmospheric temperature displayed a strong correlation (R-squared greater than 0.84; Fig. 2.4) over 15-minute sampling periods, contributing to the assumption that the increased temperature within the well would increase molecular kinetic energy, increasing the forces exerted on the well casing, and resulting in increased well atmosphere pressure which corresponds to ambient atmospheric pressure. The one-way nature of the release valve is required to minimize contamination of the well atmosphere due to the intake of external ambient CO_2 concentrations (Clough et al., 2020).

With elevated well atmosphere pressure compared to ambient-exterior atmospheric pressure, the one-way diaphragm pressure release valve is assumed to crack and allow pressure to release until equilibrium (pg. 34). During pressure release, the well becomes dynamic and experiences flow through, potentially altering the chamber CO_2 concentrations and flux calculations as steady- state conditions are assumed at the time of measurements (Dossa et al., 2015; Heinemeyer & McNarma, 2011). However, due to the long-term nature of the study, the pressure release valve was deployed because static closed chambers have a limitation to potentially cause an underestimation of CO_2 flux in long-term datasets from saturation and pressurization of the static chamber headspace (Dossa et al., 2015; Heinemeyer & McNarma, 2011). Additionally, a periodic depressurization of the well may occur due to air flow and wind inducing a Venturi effect over the vented one-way release valve. The depressurization of the well introduces a potential source for periodic sampling uncertainty. However, the overall benefits of a pressure release valve minimizes the prospective and episodic adverse results produced due to the Venturi effect (Clough et al., 2020).

An additional limitation to the reported design and measuring CO_2 flux in a tidal wetland is the presence of surface water impacting the volume of the well. The well atmosphere volume may be altered due to water levels within the well. As water levels are not measured within the well, the study assumes constant volume of the well, producing a tidal wetland environmental limitation to the flux equation. The implementation of a water level sensor within well system in future studies could produce the incorporation of varying volume within the flux equations.

A future study to compare the soil gas well and traditional closed chamber method would be beneficial to maximize the measurement of CO_2 flux in tidal wetland systems. The comparison between methods may be used to improve how CO_2 flux is measured within the intertidal zone of wetland systems, which currently does not exist in the literature.

CONCLUSION

Tidal wetlands are among the most productive environments within the carbon cycle due to their ability to efficiently store large amounts of organic carbon for long time periods. However, their natural ability to sequester and store large amounts organic carbon coupled with vulnerability of degradation due to climate change, may contribute a release of stored carbon as CO_2. High equipment cost, low spatial coverage, and infrequent sampling, along with complex environmental dynamics of tidal wetlands, impose several challenges for measuring in situ carbon field emissions and sequestration.

The CO_2 monitoring station offers a low-cost system to collect continuous, automated data in the harsh environmental conditions of tidal wetlands. The NDIR gas analyzer technology offers an inexpensive methodology to measure CO_2 gas concentrations within the well system's atmosphere. The well system provides the sensor protection and mimics steady state conditions with the presence of the naturally infilled screen and pressure release valve. The backflow check valve ensures preservation of the sensor during unusually high-water events, enabling the analysis of extreme environmental conditions. The floating power station's Raspberry Pi data logger and cellular connection allowed for cost effective collection of continuous CO_2 concentrations within remote locations of tidal wetlands. The mobility of the power station protects the electrical equipment during rising water events and permits data collection under hazardous conditions.

The soil-gas well design's cost is a third of the cost compared to current commercially manufactured CO_2 flux chambers. The low budget characteristics of the CO_2 flux monitoring station, coupled with easy manipulation of design dimensions based on local hydrological conditions, enables for the simple distribution of monitoring stations within regional and global wetlands. The dissemination of monitoring station construction and deployment will improve the temporal and spatial variability of measuring CO_2 gas flux. The structural integrity of the well system and power station allow for long-term carbon flux monitoring during diverse environmental conditions (e.g., weather, seasons, inundation intervals, tides, etc.). An increase in distribution of monitoring stations will also lead to insights of spatial variation in CO_2 flux based on localized environmental conditions (e.g., elevation, vegetation, climate, urbanization, etc.).

The continuous collection of CO_2 concentrations within the known dimensions of the well may be applied to a flux equation to determine net emission or sequestration of CO_2 in tidal wetlands. High frequency *in situ* measurements and uninterrupted CO_2 flux data sets will provide invaluable insight into the carbon cycle behavior and current state of annual CO_2 emissions in tidal wetlands. With enhanced observational *in situ* data sets, estimations of tidal wetland carbon stocks and atmospheric CO_2 concertation feedbacks can become more accurate, influencing climate change projections and wetland management practices.

REFERENCES

Barba, J., Cueva, A., Bahn, M., Barron-Gafford, G.A., Bond-Lamberty, B., Hanson, P.J., Jaimes, A., Kulmala, L., Pumpanen, J., Scott, R.L., Wohlfahrt, G., & Vargas, R. (2018). Comparing ecosystem and soil respiration: Review and key challenges of tower-based and soil measurements. *Agricultural and Forest Meteorology,* 249, 434–443. https://doi.org/10.1016/j.agrformet.2017.10.028

Bucci, L., Alaka, L., Hagen, A., Delgado, S., & Beven, J., National Oceanic and Atmospheric Administration, & National Weather Service. (2023) *Hurricane Ian (AL092022).* National Hurricane Center Tropical Cyclone Report. https://www.nhc.noaa.gov/data/tcr/AL092022_Ian.pdf

Canadell, J.G., P.M.S. Monteiro, M.H. Costa, L. Cotrim da Cunha, P.M. Cox, A.V. Eliseev, S. Henson, M. Ishii, S. Jaccard, C. Koven, A. Lohila, P.K. Patra, S. Piao, J. Rogelj, S. Syampungani, S. Zaehle, & K. Zickfeld, (2021). Global carbon and other Biogeochemical cycles and feedbacks. In Climate change 2021: The physical science basis. Contribution of Working Group I to the Sixth Assessment Report of the Intergovernmental Panel on Climate Change [Masson-Delmotte, V., P. Zhai, A. Pirani, S.L. Connors, C. Péan, S. Berger, N. Caud, Y. Chen, L. Goldfarb, M.I. Gomis, M. Huang, K. Leitzell, E. Lonnoy, J.B.R. Matthews, T.K. Maycock, T. Waterfield, O. Yelekçi, R. Yu, and B. Zhou (eds.)]. Cambridge University Press, Cambridge, United Kingdom and New York, NY, USA, pp. 673–816, doi:10.1017/9781009157896.007.

Cheng, Y., Zha, Y., Tong, C., Du, D., Chen, L., & Wei, G. (2021). Estimating the gaseous carbon budget of a degraded tidal wetland. *Ecological Engineering*, 160, 106147. https://doi.org/10.1016/j.ecoleng.2021.106147

Christiansen, J.R., Korhonen, J.F.J., Juszczak, R., Giebels, & M., Pihlatie, M. (2011). Assessing the effects of chamber placement, manual sampling and headspace mixing on CH_4 fluxes in a laboratory experiment. *Plant and Soil*, 343, 171–185. https://doi.org/10.1007/s11104-010-0701-y

Clough, T.J., Rochette, P., Thomas, S.M., Pihlatie, M., Christiansen, J.R., & Thorman, R.E. (2020). Global research alliance N_2O chamber methodology guidelines: Design considerations. *Journal of Environmental Quality*, 49, 1081–1091. https://doi.org/10.1002/jeq2.20117

Cueva, A., Bullock, S.H., López-Reyes, E., & Vargas, R. (2017). Potential bias of daily soil CO_2 efflux estimates due to sampling time. *Scientific Reports*, 7, 11925. https://doi.org/10.1038/s41598-017-11849-y

Davidson-Arnott, R., Bauer, B., & Houser, C. (2019). *Introduction to Coastal Processes and Geomorphology* (2nd ed.). Cambridge: Cambridge University Press. doi:10.1017/9781108546126

Dossa, G.G.O., Paudel, E., Wang, H., Cao, K., Schaefer, D., & Harrison, R.D. (2015). Correct calculation of CO_2 efflux using a closed-chamber linked to a non-dispersive infrared gas analyzer. *Methods in Ecology and Evolution*, 6, 1435–1442. https://doi.org/10.1111/2041-210X.12451

Emery, H.E., Angell, J.H., Tawade, A., & Fulweiler, R.W. (2021). Tidal rewetting in salt marshes triggers pulses of nitrous oxide emissions but slows carbon dioxide emission. Soil *Biology and Biochemistry*, 156, 108197. https://doi.org/10.1016/j.soilbio.2021.108197

Gardashov, R., Eminov, M., Kara, G., Emecen Kara, E.G., Mammadov, T., & Huseynova, X. (2020). The optimum daily direction of solar panels in the highlands, derived by an analytical method. *Renewable and Sustainable Energy Reviews*, 120, 109668. https://doi.org/10.1016/j.rser.2019.109668

Greenberg, R., Maldonado, J.E., Droege, S., & McDonald, M.V. (2006). Tidal marshes: A global gerspective on the evolution and conservation of their terrestrial vertebrates. *BioScience*, 56, 675. https://doi.org/10.1641/0006-3568(2006)56[675:TMAGPO]2.0.CO;2

He, L., She, C., Huang, J., Yang, P., Yu, H., & Tong, C. (2022). Effects of constant and fluctuating saltwater addition on CH_4 fluxes and methanogens of a tidal freshwater wetland: A mesocosm study. *Estuarine, Coastal and Shelf Science,* 277, 108076. https://doi.org/10.1016/j.ecss.2022.108076

Heinemeyer, A., & McNamara, N. P. (2011). Comparing the closed static versus the closed dynamic chamber flux methodology: Implications for soil respiration studies. *Plant and Soil*, *346*(1), 145–151. https://doi.org/10.1007/s11104-011-0804-0

Hill, A.C., & Vargas, R. (2022). Methane and carbon dioxide fluxes in a temperate tidal salt marsh: Comparisons between plot and ecosystem measurements. *JGR Biogeosciences*, 127. https://doi.org/10.1029/2022JG006943

Hinson, A.L., Feagin, R.A., & Eriksson, M. (2019). Environmental controls on the distribution of tidal wetland soil organic carbon in the continental United States. *Global Biogeochemical Cycles*, 33, 1408–1422. https://doi.org/10.1029/2019GB006179

Intergovernmental Panel on Climate Change (IPCC). (2021). Climate change 2021: The physical science basis. Contribution of Working Group I to the Sixth Assessment Report of the Intergovernmental Panel on Climate Change [Masson Delmotte, V., P. Zhai, A. Pirani, S.L. Connors, C. Péan, S. Berger, N. Caud, Y. Chen, L. Goldfarb, M.I. Gomis, M. Huang, K. Leitzell, E. Lonnoy, J.B.R. Matthews, T.K. Maycock, T. Waterfield, O. Yelekçi, R. Yu, and B. Zhou (eds.)]. Cambridge University Press, Cambridge, United Kingdom and New York, NY, USA, 2391 pp. doi:10.1017/9781009157896.

Keller, J.K. (2011). Wetlands and the global carbon cycle: What might the simulated past tell us about the future? *New Phytologist*, 192, 789–792. https://doi.org/10.1111/j.1469-8137.2011.03954.x

Kühne, A., Schack-Kirchner, H., Hildebrand, E.E. (2012). Gas diffusivity in soils compared to ideal isotropic porous media. *Journal of Plant Nutrition and Soil Science*, 175, 34–45. https://doi.org/10.1002/jpln.201000438

Lente, G., & Ősz, K. (2020). Barometric formulas: Various derivations and comparisons to environmentally relevant observations. *ChemTexts*, 6, 13. https://doi.org/10.1007/s40828-020-0111-6

Lovelock, C.E., Atwood, T., Baldock, J., Duarte, C.M., Hickey, S., Lavery, P.S., Masque, P., Macreadie, P.I., Ricart, A.M., Serrano, & O., Steven, A. (2017). Assessing the risk of carbon dioxide emissions from blue carbon ecosystems. *Frontiers in Ecology and the Environment*, 15, 257–265. https://doi.org/10.1002/fee.1491

Lucas-Moffat, A.M., Huth, V., Augustin, J., Brümmer, C., Herbst, M., & Kutsch, W.L. (2018) Towards pairing plot and field scale measurements in managed ecosystems: Using eddy covariance to cross-validate CO_2 fluxes modeled from manual chamber campaigns. *Agricultural and Forest Meteorology*, 256–257, 362–378. https://doi.org/10.1016/j.agrformet.2018.01.023

Mar, K.A., Unger, C., Walderdorff, L., Butler, & T. (2022). Beyond CO_2 equivalence: The impacts of methane on climate, ecosystems, and health. *Environmental Science & Policy*, 134, 127–136. https://doi.org/10.1016/j.envsci.2022.03.027

Mcleod, E., Chmura, G.L., Bouillon, S., Salm, R., Björk, M., Duarte, C.M., Lovelock, C.E., Schlesinger, W.H., & Silliman, B.R. (2011). A blueprint for blue carbon: Toward an improved understanding of the role of vegetated coastal habitats in sequestering CO_2. *Frontiers in Ecology and the Environment*, 9, 552–560. https://doi.org/10.1890/110004

Middelburg, J.J., Nieuwenhuize, J., Iversen, N., Høgh, N., de Wilde, H., Helder, W., Seifert, R., & Christof, O. (2002). Methane distribution in European tidal estuaries. *Biogeochemistry*, 59, 95–119. https://doi.org/10.1023/A:1015515130419

Montzka, S.A., Dlugokencky, E.J., & Butler, J.H. (2011). Non-CO_2 greenhouse gases and climate change. *Nature*, 476, 43–50. https://doi.org/10.1038/nature10322

Murray, R.H., Erler, D.V., Eyre, B.D., 2015. Nitrous oxide fluxes in estuarine environments: Response to global change. *Global Change Biology*, 21, 3219–3245. https://doi.org/10.1111/gcb.12923

Najjar, R. G., Herrmann, M., Alexander, R., Boyer, E. W., Burdige, D. J., Butman, D., Cai, W.-J., Canuel, E. A., Chen, R. F., Friedrichs, M. A. M., Feagin, R. A., Griffith, P. C., Hinson, A. L., Holmquist, J. R., Hu, X., Kemp, W. M., Kroeger, K. D., Mannino, A., McCallister, S. L., … Zimmerman, R. C. (2018). Carbon budget of tidal wetlands, estuaries, and shelf waters of eastern North America. *Global Biogeochemical Cycles*, *32*(3), 389–416. https://doi.org/10.1002/2017GB005790

National Estuarine Research Reserve System (NOAA NERRS). (2012). *System-wide Monitoring Program*. Data accessed from the NOAA NERRS Centralized Data Management Office. http://www.nerrsdata.org

National Oceanic and Atmospheric Administration (NOAA), National Ocean Service (NOS), Belle W. Baruch Institute of the University of South Carolina, & South Carolina Coastal Council. (1992) *Final Management plan, North Inlet/Winyah Bay National Estuarine Research Reserve*. National Ocean Service. https://repository.library.noaa.gov/view/noaa/2461.

National Oceanic and Atmospheric Administration (NOAA). (2022). *Tides & Currents: Datums for 8662299, Clambank Cree Dock, Goat Island, SC*. NOAA. https://tidesandcurrents.noaa.gov/datums.html?id=8662299

North Inlet – Winyah Bay National Estuarine Research Reserve (NI-WB NERR). (2016). *Management Plan. North Inlet – Winyah Bay National Estuarine Research Reserve*. https://northinlet.sc.edu/

Oertel, C., Matschullat, J., Zurba, K., Zimmermann, F., & Erasmi, S. (2016). Greenhouse gas emissions from soils—A review. *Geochemistry*, 76, 327–352. https://doi.org/10.1016/j.chemer.2016.04.002

Poffenbarger, H.J., Needelman, B.A., & Megonigal, J.P. (2011). Salinity influence on methane emissions from tidal marshes. *Wetlands*, 31, 831–842. https://doi.org/10.1007/s13157-011-0197-0

Portmann, R.W., Daniel, J.S., & Ravishankara, A.R. (2012). Stratospheric ozone depletion due to nitrous oxide: influences of other gases. P*hilosophical Transactions of the Royal Society B: Biological Sciences*, 367, 1256–1264. https://doi.org/10.1098/rstb.2011.0377

Villa, J.A., & Bernal, B. (2018). Carbon sequestration in wetlands, from science to practice: An overview of the biogeochemical process, measurement methods, and policy framework. *Ecological Engineering*, 114, 115–128. https://doi.org/10.1016/j.ecoleng.2017.06.037

Wang, F., Lu, X., Sanders, C.J., & Tang, J. (2019). Tidal wetland resilience to sea level rise increases their carbon sequestration capacity in United States. *Nature Communications*, 10, 5434. https://doi.org/10.1038/s41467-019-13294-z

Windham-Myers, L., Cai, W.-J., Alin, S., Andersson, A., Crosswell, J., Dunton, K. H., Hernandez-Ayon, J. M., Herrmann, M., Hinson, A. L., Hopkinson, C. S., Howard, J., Hu, X., Knox, S. H., Kroeger, K., Lagomasino, D., Megonigal, P., Najjar, R., Paulsen, M.-L., Peteet, D., … Zhu, Z. (2018). *Chapter 15: Tidal Wetlands and Estuaries. Second State of the Carbon Cycle Report*. U.S. Global Change Research Program. https://doi.org/10.7930/SOCCR2.2018.Ch15

CHAPTER THREE

CHARACTERIZATION OF CARBON DIOXIDE (CO_2) FLUX IN ESTUARINE TIDAL WETLANDS OF NORTH INLET-WINYAH BAY, SOUTH CAROLINA

ABSTRACT

An innovative carbon dioxide (CO_2) flux monitoring station was deployed for sampling over a ten-month period from August 2022 to May 2023 at No Man's Friend Creek, a tidal creek adjacent to Mud Bay within the North Inlet-Winyah Bay estuarine system. During the sampling period, monthly variation of net CO_2 flux occurred, with the highest sequestration in the summer months, low net sequestration in the winter months, and net emission in the spring months. The TWC1 monitoring station experienced a ten-month net sequestration of 9.385µmol m^{-2} s^{-1}. Basic water quality and meteorological parameters of NI-WB all significantly correlated to CO_2 concentration measurements in the well atmosphere, except for wind speed. An increase in accumulation of sediment within NI-WB was accompanied by an increase in net CO_2 sequestration.

INTRODUCTION

Carbon dioxide (CO_2) is a climactically important greenhouse gas which contributes significantly to radiative forcing and global warming (IPCC, 2021; Etminan et al., 2016). Global atmospheric CO_2 concentrations have increased by ~ 47% since the pre-Industrial Era, reaching concentrations greater than 410 parts per million (ppm) in 2019 (IPCC, 2021). Tidal wetland environments account for a small portion of the Earth's surface, but are essential in modulating atmospheric CO_2 concentrations due to their ability to naturally sequester and store carbon (Hopkinson et al., 2012; Najjar et al., 2018; Song et al., 2009; Xu et al., 2014). Therefore, quantifying the magnitude of CO_2 flux (sequestration/emission) in tidal wetland systems is critical for identifying global carbon budgets, projecting future climate models, and developing environmental management strategies (Najjar et al., 2018; Yang et al., 2018).

The quantified role of tidal wetlands within the global carbon budget lacks scientific consensus (Hill & Vargas, 2022; Wang et al., 2019; Windham-Myers et al., 2018). In the Second State of the Carbon Cycle Report (SOCCR2), The United States Global Change Research Program identified knowledge gaps in the magnitude of long-term carbon flux data sets, limiting the understanding of the relative roles of estuarine tidal wetlands in carbon cycling (Windham-Myers et al., 2018). Specifically, the SOCCR2 described the carbon exchange data set for the Atlantic coast as "limited" and identified high variation among study sites (Windham-Myers et al., 2018). With a limiting dataset and high variation among monitoring locations, the driving factors and mechanisms which promote carbon sequestration or emission are unclear (Peng et al., 2022). An increase in the density of long-term observations of CO_2 flux in tidal wetlands will enable the analysis of seasonal and interannual variability of atmospheric-wetland carbon exchange, ultimately improving coastal carbon budgets (Song et al., 2009; Benway et al., 2016; Windham-Myers et al., 2018).

The purpose of this study is to identify the net CO_2 flux at the sediment surface interface in a coastal wetland and investigate the relationship between monitored carbon concentrations and environmental parameters. The continuous long-term monitoring of CO_2 concentrations and calculations of net flux resulted in determining the magnitude of CO_2 exchange over a ten-month period (August 2022 to May 2023) in a tidal wetland environment which has little anthropogenic influence. The correlation of the continuous data set of CO_2 concentrations to various water quality and meteorological parameters provided comprehensive insights into near-annual mechanisms impacting CO_2 exchange to fill the gaps in climate change research. This chapter is being prepared for submission to the Frontiers: Earth Science Journal.

METHODS

Study Site

Carbon dioxide flux monitoring occurred within the tidal wetlands of NI-WB located near Georgetown, SC (Fig. 3.1). The tidal wetlands of NI-WB are a part of the National Oceanic and Atmospheric Administration's (NOAA) National Estuarine Research Reserve (NERR) network. The NOAA NERRs network is made up of 30 estuarine systems around the United States, which are protected from anthropogenic development and designated for coastal research by the Coastal Zone Management Act. The monitoring of anthropogenic influence on tidal wetland systems is beneficial to inform coastal community management practices; however protected sites, such as the NERRS locations, serve as a successful location to monitor minimally influenced natural tidal wetland system behavior. The benefit of NERRS location is the associated long-term environmental monitoring network of meteorological and water quality data to supplement research efforts. The NI-WB NERR was designated in 1992, protecting ~ 77 square kilometers (km^2) of pristine estuarine tidal wetlands from anthropogenic development (Li et al., 2022). The reserve is located within two differing but interconnected estuarine systems: (1) the North Inlet Estuary and (2) the Winyah Bay Estuary (NOAA, 1992). North Inlet is an oceanic-dominated estuary with a ~96 km^2 watershed, while Winyah Bay is a riverine-influenced estuary comprising ~47,000 km^2 of watershed (NI-WB NERRS, 2016). The North Inlet system is tidally dominated with a semidiurnal tidal pattern which receives freshwater inputs from the surrounding watershed and northward flow from the Winyah Bay system. Winyah Bay experiences a strong unidirectional riverine flow from four surrounding rivers (Pee Dee, Waccamaw, Black, and Swampit Rivers), which is superimposed by a semidiurnal tidal pattern. The tidal range within NI-WB systems is 1.5 m (NI-WB NERRS, 2016). The dominant vegetation within the NI-WB estuary is *Spartina alterniflora* (smooth cordgrass), with small subsections of dominant *Juncus roemerianus* (needle rush; Gardner et al., 2006; H. Li et al., 2022).

The NOAA NERRS system manages an active water quality (CBWQ) and metrological station (OYMET) within NI-WB (Fig. 3.1). The monitoring stations collect continuous measurements for long-term monitoring of environmental characteristics in NI-WB. The CBWQ station collects standard water quality parameters (depth, temperature, specific conductivity, salinity, DO, pH, and turbidity) every 15 minutes. The OYMET station measures standard meteorological measurements (temperature, relative humidity, barometric pressure, total precipitation, and wind speed) every five seconds and is reported as 15-minute averages (NOAA NERRS, 2012).

Soil Gas Flux Monitoring Station & Instrumentation

A CO_2 soil gas flux monitoring station (TWC1; Fig. 3.1) was deployed on the streambank of No Man's Friend Creek at the confluence between the North Inlet and Winyah Bay estuaries (Chapter 2). The transition zone between North Inlet and Winyah Bay, known as Mud Bay, is characterized by high sediment loads, accretion rates, and riverine inputs from the extensive Winyah Bay watershed (Buzzelli et al., 2004; Patchineelam & Kjerfve, 2004). The placement of TWC1 CO_2 soil gas flux monitoring station at No Man's Friend Creek near Mud Bay was assumed to experience inputs from the North Inlet watershed and Winyah Bay watershed, which is the third largest watershed on the East Coast (NI-WB NERRS, 2016).

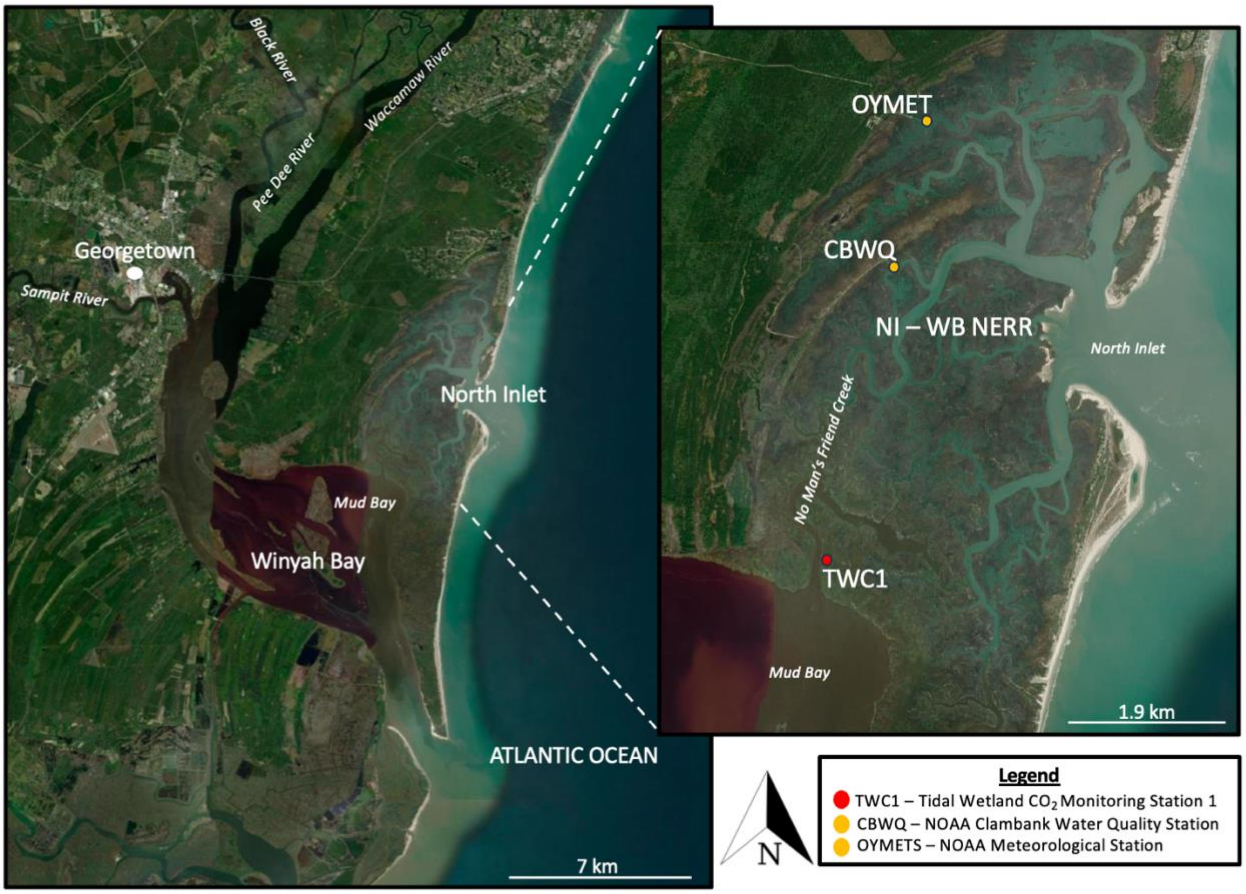

Figure 3.1. The study area of North Inlet-Winyah Bay National Estuarine Research Reserve located near Georgetown, SC.

The CO_2 soil gas flux monitoring station design consisted of a soil-gas well and a flotational power station (Chapter 2, Fig. 2.2). The innovative monitoring station design allowed for continuous long-term CO_2 flux monitoring by accounting for the dynamic environmental conditions (high-energy storms, king tides, gale winds, salt corrosion, etc.) of estuarine tidal wetlands. This study included CO_2 flux data collected at TWC1 from August 2022 to May 2023.

Soil-gas well

The soil-gas well station permitted CO_2 flux analysis by deploying a non-dispersive infrared (NDIR) gas analyzer (Vaisala GMP252) within a polyvinyl chloride (PVC) well to measure CO_2 concentrations (ppm). The design assumed a measurable CO_2 exchange across the sediment surface, resulting in the variation of CO_2 concentrations within the well atmosphere. The change in concentrations was applied to a flux equation to determine the emission or sequestration of CO_2 from the tidal wetland soils.

The PVC well was a 3.2 m long well and had a 5 cm diameter (Chapter 2, Fig. 2.2, pg.42). The well system extended 1.2 m below ground, with a one-meter screen interval (1.27 cm screened slots with 2.54 cm spacing). The screened interval permitted surrounding sediment to infill into the well, ultimately resulting in the anchoring of the well system and replicating near natural conditions for soil gas flux. The remaining 2 m of the well system extended above the ground surface, exceeding maximum historical water levels in North Inlet produced by higher than normal tides (king tides) and storm surges (1.7 m above mean tidal level; NOAA NERRS, 2012; NOAA, 2022). The 2 m height above maximum historical water levels protected the NDIR gas analyzer's electrical components. To further protect the NDIR analyzer against unusually high water, a backflow check valve was deployed within the PVC well at the maximum historical tidal levels

(1.4 m above the ground surface). A one-way pressure release valve was located atop the soil-gas well to ensure pressure equilibrium between the well atmosphere and the surrounding natural atmosphere.

Flotational Power Station

The CO_2 flux monitoring system was supplied power via an external floating power source (Chapter 2, Fig. 2.2). The flotational power source enabled continuous long-term monitoring of CO_2 flux with varying water levels. The electrical data acquisition equipment was fixed to a commercial flotational device made up of expanded polystyrene foam encased within polyethylene. The commercial flotational device allowed the electrical equipment to rise with high waters and recede when water levels decrease.

The data acquisition equipment included a Raspberry Pi-base data logger, marine battery, and solar panel. A Raspberry Pi Zero equipped with an RS485 Modbus converter and cellular modem via a USB hub comprised the data logger. The cellular connection to the Raspberry Pi-based data logger allowed for the automated collection and transmission of CO_2 concentration measurements in the remote location of NI-WB. The NDIR analyzer and Raspberry Pi-base data logger were powered via a 12.6 volt (V), 55 amp-hour deep cycle marine battery.

The commercial flotational device and data acquisition equipment was attached to four treated lumber posts via stainless steel wire loops to guide equipment oscillation in varying water levels. All hardware was made up of stainless steel and plastic to avoid salt corrosion damage. The flotational capability of the monitoring station enabled long-term monitoring and high-resolution identification of CO_2 flux. (Further description of the CO_2 flux monitoring station is described in Chapter 2).

CO_2 Flux and Net Flux Calculations

CO_2 Flux Equation

The concentration (c) of CO_2 within the well atmosphere was collected every 900 seconds (s). The concentrations were applied to a flux equation to determine sequestration (negative flux) or emission (positive flux) across the area (A; m^2) of the sediment interface in the well (1.96×10^{-3} m^2) over time (t; seconds; eqn. 2.1).

$$Flux = \frac{\Delta c}{\Delta t} \times \frac{PV}{RT} \times \frac{1}{A} \qquad \textit{eqn. 2.1}$$

The flux equation incorporated the ideal gas law (PV=nRT) by applying the universal gas constant to the (R; 0.83025 [mabr m^3 K^{-1} mol^{-1}) governing equation. The universal gas constant was calculated with standard atmospheric pressure (P_i; 1,013.25 mbar), the volume of an ideal gas as standard pressure (V_i; 0.2241 m^3 mol^{-1}), and standard temperature (T_i; 273.15 Kelvin [K]).

The pressure (P; mbar) values used within the governing equation were derived from a nearby NOAA weather station (OYMET) within NI-WB. The volume (V; m^3) variable in the governing equation was calculated by subtracting the volume of the well (3.9×10^{-3} m^3) by the NDIR gas analyzer's sampling volume (6.9×10^{-6} m^3), resulting in a fixed volume (3.92×10^{-3} m^3; Dossa et al., 2015). The temperature variable (T; K) was determined by *in situ* measurements of the NDIR gas analyzer.

Net Flux Calculation

The resulting flux calculations µmol m^{-2} s^{-1} identified sequestration or emission of CO_2 through the sediment surface interface. The continuous nature of the CO_2 concentration monitoring permits net flux calculations conducted at TWC1. The flux measurements were summed over a specific period to identify a net sequestration (negative flux) or emission (positive flux) of CO_2 from NI-WB sediment. Net flux calculations were conducted monthly and for the complete duration of the sampling period. The number of measurements (*n*) differed from month to month due to the varying number of days for each month and periodic equipment maintenance (Table 3.1). The total net flux, calculated for August 2022 to May 2023 was based on a total of 26,801 measurements.

Rank Order Correlation Methods

Spearman and Kendall tau-b rank-order correlation methods were conducted to measure the strength and direction of association existing between CO_2 concentrations and flux to meteorological and water quality environmental parameters. The CO_2 concentration and environmental parameter dataset was nonparametric and nonlinear, prompting the use of the Spearman and Kendall tau-b correlation analysis. The Spearman correlation assumptions include that (1) variables are ordinal, interval, ratio scale, or continuous in nature, (2) the variables represent paired observations, and (3) a monotonic relationship exists between the variables (Schober et al., 2018). The Kendall statistical correlation analysis to adjusts for tied ranks, which is the Kendall-tau b correlation, assumes that (1) variables are ordinal or continuous in nature, (2) the variables represent paired observations, and (3) a monotonic relationship improves correlation accuracy but is not a strict assumption (Kendall, 1938). The correlation analysis was conducted via Statistical Package for the Social Sciences (SPSS) software for both Spearman and Kendall tau-b correlations. The Spearman method and Kendall tau-b method were both conducted to avoid impartial biases from a single statistical method. The Spearman method commonly produces correlation coefficients with larger magnitudes than Kendall tau-b. However, the two tests are used to support one another by producing similar trends in the strength and direction of a relationship between variables, leading to more robust findings.

Net Accumulation Rate

Allochthonous sediment import and accretion promote carbon sequestration through burial and long-term storage in tidal wetlands (Callaway et al., 2012). Active sedimentation rates were determined using net sedimentation tiles (NST). The NST consisted of an eight-by-eight-inch ceramic tile which was anchored flush to the ground surface via a buried metal conduit (Fig. 3.2). The NSTs were deployed in a cleared vegetative area (at least 15 cm from vegetation) to allow the development of a borehole to anchor the tiles and permit *in situ* measurement. Therefore, vegetative induced sediment deposition was limited at the location of the sediment tile. The accretion of sediment was quantified by the extent of accumulation upon the NST tile. The extent of accumulation from the tile surface to the deposited sediment surface above the tile was measured using a digital micrometer. If vegetation was present on the tile surface, the extent of accumulation was measured from the tile surface to the deposited sediment surface above the tile, as well as the tile surface to the top of the deposited vegetation for total accumulation. After accumulation was measured, the tile was cleared to allow new deposition during the next sampling period. Accretion was monitored approximately every four to eight weeks, as recommended by Pasternack (2002).

Figure 3.2. Conceptual design of the Net Sedimentation Tile (top) and infield photo of the Net Sedimentation tile deployed at TWC1 CO_2 gas flux monitoring station (bottom).

Sampling of the NST occurred over seven sampling periods from August 20, 2022, to May 25, 2023 (sampling periods identified in Table 3.2). The accumulation rates during the sampling periods were considered constant due to the technique of collecting periodic measurements. The accumulation rate was compared to net flux, which occurred over the same sampling period to provide insight into the relationship between carbon flux and accumulation.

RESULTS

3.1 Annual and Monthly CO_2 Flux

The ten month flux calculations include CO_2 concentration measurements conducted at TWC1 from August 2022 to May 2023 (Fig. 3.3 & 3.4). The net flux during this period was -9.385 µmol m^{-2} s^{-1} (Table 3.1). Therefore, over the ten-month period, the area of TWC1 at No Man's Friend Creek near Mud Bay showed a net sequestering (negative flux) of carbon.

The TWC1 monitoring station recorded net emission for only three out of the ten months. Net emission occurred for October (2.649 µmol m^{-2} s^{-1}), March (1.156 µmol m^{-2} s^{-1}), and April (6.906 µmol m^{-2} s^{-1}). Net sequestration occurred for the remaining months of sampling (Table 3.1). Net sequestration greater the 2.0 µmol m^{-2} s^{-1} occurred over August (-2.767 µmol m^{-2} s^{-1}), September (-5.964 µmol m^{-2} s^{-1}), December (-2.326 µmol m^{-2} s^{-1}), and May (-4.543 µmol m^{-2} s^{-1}). Net sequestration less than 2.0 µmol m^{-2} s^{-1} occurred through November (-1.559 µmol m^{-2} s^{-1}), January (-0.655 µmol m^{-2} s^{-1}), and February (-1.372 µmol m^{-2} s^{-1}; Fig. 3.3 & 3.4). Sampling maintenance produced no data collection between October 24, 2022 to December 8, 2022, and January 15, 2023 to January 20, 2023.

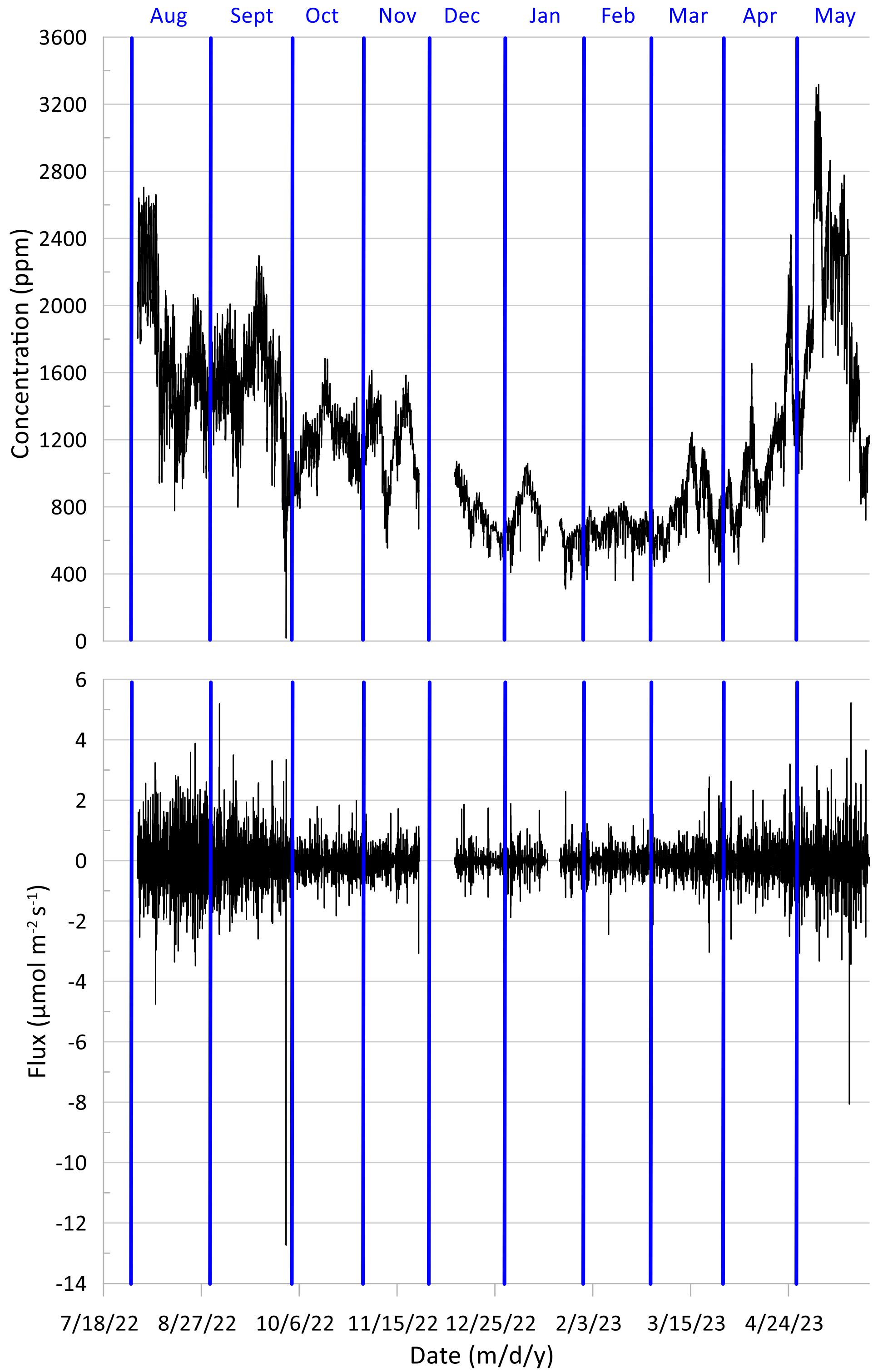

Figure 3.3. Time series plot for CO_2 concertation measurements in ppm (top) and CO_2 flux in $\mu mol\ m^{-2}\ s^{-1}$ (bottom) conducted for the TWC1 monitoring station in NI-WB. Data collection did not occur from 11/24/22 -12/8/22 and 1/15/23-1/20/23.

Monthly Net Flux										
Year	2022					2023				
Month	Aug	Sept	Oct	Nov	Dec.	Jan	Feb	Mar	Apr	May
n	2976	2880	2976	2223	2257	2514	2688	2976	2880	2431
Net Flux ($\mu mol\ m^{-2}\ s^{-1}$)	-2.767	-5.964	2.649	-1.559	-3.236	-0.655	-1.372	1.156	6.906	-4.543
Standard deviation (σ; $\mu mol\ m^{-2}\ s^{-1}$)	0.671	0.593	0.267	0.261	0.188	0.211	0.202	0.297	0.392	0.570
Emission (E)/ Sequestration (S)	S	S	E	S	S	S	S	E	E	S
Total Net Flux ($\mu mol\ m^{-2}\ s^{-1}$)	Aug 2022 – May 2023 *n* =26801	-9.385								

Table 3.1. Monthly net CO_2 flux from August 2022 to May 2023. The total number of measurements is represented by the variable (n).

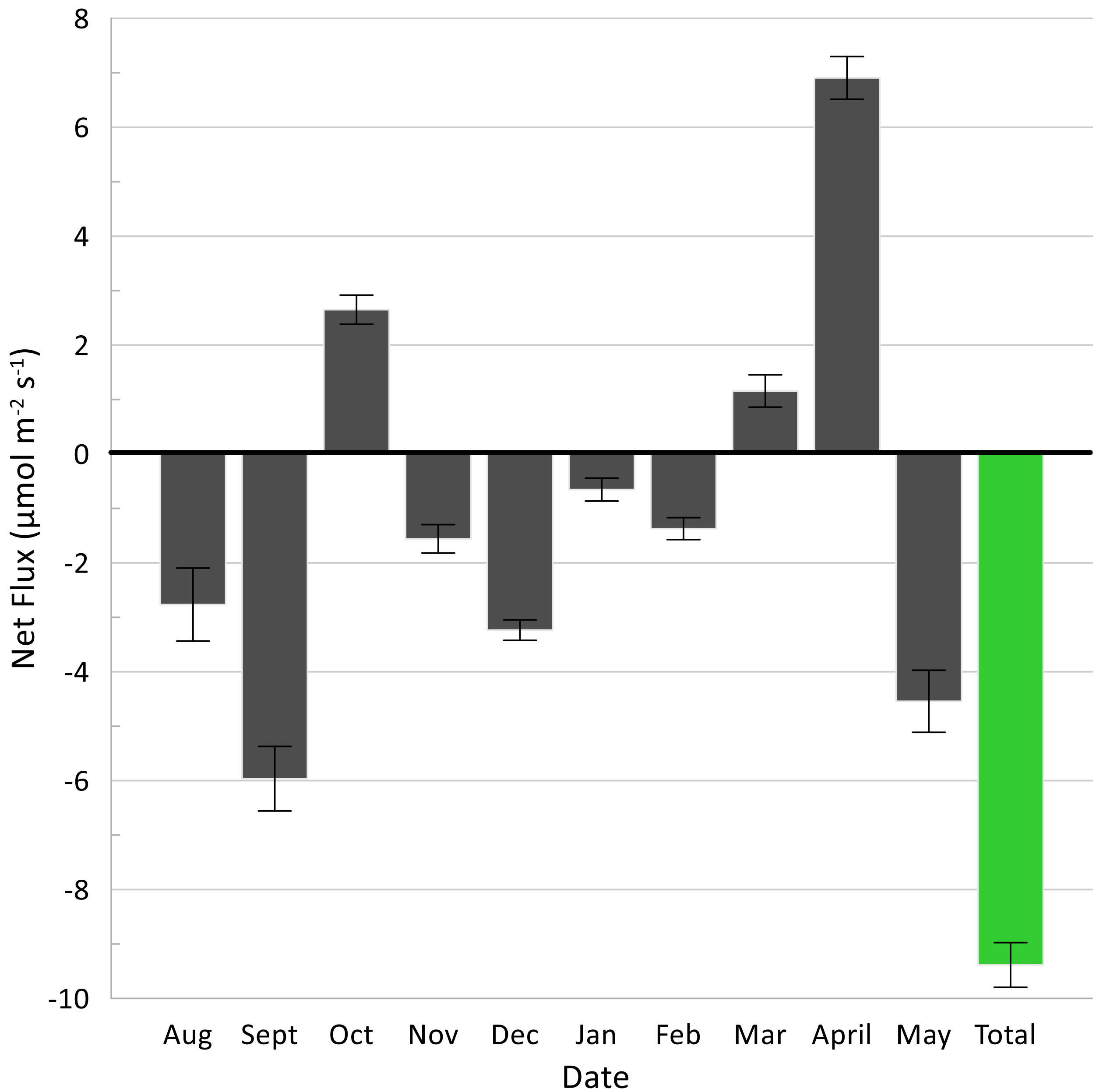

Figure 3.4. Bar chart displaying monthly net flux calculation results (black) from August 2022 to May 2023 and total net flux during this period (green). The error bars represent standard deviation of flux calculations.

Spearman Correlation and Kendall tau-b Correlation Matrix

The strength of correlation for the Spearman and Kendall tau- b correlation coefficient ranges on a scale from -1 to +1. The complete correlation between two variables is expressed by either -1 or +1. The strength of correlation among variables is determined based on proximity from complete correlation of either -1 or +1. The positive or negative attribute of the correlation coefficient indicates whether the variables display a direct or inverse relationship (Kendall, 1938; Schober et al., 2018; Fig. 3.5).

Based on both the Spearman and Kendall tau-b correlation method, CO_2 concentrations within the well atmosphere directly correlate with the water parameters of depth, temperature, specific conductivity, salinity, and turbidity, while the CO_2 concentrations within the well atmosphere have an inverse relationship with dissolved oxygen and pH. The Spearman and Kendall tau-b methods report the following strength of relationship (proximity from perfect correlation of -1 or +1) to CO_2 concentration within the well atmosphere from strongest to weakest correlation: (1) water temperature, (2) dissolved oxygen (DO), (3) pH, (4) turbidity, (5) salinity, (6) specific conductivity, and (7) depth.

The Spearman and Kendall tau-b correlation methods indicated a direct relationship between CO_2 concentrations in the well atmosphere to the meteorological parameters of well atmosphere temperature and surrounding atmospheric temperature; however, the CO_2 concentrations within the well atmosphere have an inverse relationship with the meteorological parameters of relative humidity, barometric pressure, and total precipitation. The strength of the relationship (proximity from perfect correlation of -1 or +1) between CO_2 concentrations in the well atmosphere and meteorological parameters was reported from strongest to weakest correlation as: (1) well atmosphere temperature, (2) surrounding atmospheric temperature, (3) barometric

Water Quality & CO2 Concentration			
Spearman Correaltion		Kendall tau-b Correaltion	
	CO2 Conc		CO2 Conc
CO2 Conc	---	CO2 Conc	---
Depth	0.130	Depth	0.087
Water Temp	0.778	Water Temp	0.565
SpCond	0.260	SpCond	0.177
Salinity	0.268	Salinity	0.182
DO	-0.553	DO	-0.383
pH	-0.292	pH	-0.213
Turbidity	0.283	Turbidity	0.199

Meteorology & CO2 Concentration			
Spearman Correaltion		Kendall tau-b Correaltion	
	CO2 Conc		CO2 Conc
CO2 Conc	---	CO2 Conc	---
Well Temp	0.595	Well Temp	0.415
Atm Temp	0.586	Atm Temp	0.408
Relative H	-0.106	Relative H	-0.072
Bar Pressure	-0.106	Bar Pressure	-0.075
Total Precip	-0.045	Total Precip	-0.037
Wind Spd	---	Wind Spd	---

Scale
1.00
0.50
0.00
-0.50
-1.00

Figure 3.5. Correlation matrix for water quality parameters and CO_2 concentrations (a & b) and meteorological parameters and CO_2 concentrations (c & d). Spearman (a &c) and Kendall tau-b (b & d) correlation methods were used to develop the matrices. The matrix scale ranges from maximum positive correlation of +1 (red) to maximum negative correlation of -1 (blue; SPSS output found in Appendix B).

pressure, (4) relative humidity, and (5) total precipitation. The meteorological parameter of wind speed did not have a significant correlation with CO_2 concentrations within the well atmosphere (Fig. 3.5).

Accretion Rate and Net CO_2 Flux

The sediment accretion rates varied throughout the sampling period (Fig. 3.6; Table 3.2). For three sampling periods, the sediment and total (vegetation + sediment accretion) accretion rates were less than or equal to 0.008 millimeters per day (mm d^{-1}). Table 3.2 shows these results for the sampling collection dates of 12/8/22, 4/2/23, and 5/25/23. During these low accretion rate sampling periods, the net CO_2 sequestration was less than 1.5 µmol m^{-2} s^{-1} or emission was less than 0.5 µmol m^{-2} s^{-1}. The sampling period of 12/9/2022 - 1/7/2023 resulted in a sediment and total accretion rates of 0.020 mm d^{-1}, accompanied by a net sequestration of 0.409 µmol m^{-2} s^{-1}. The sampling period of 1/8/2023 - 2/8/2023 resulted in a sediment and total accretion rate of 0.027 mm d^{-1}, which was higher than the previous and subsequent sampling periods in 2023. The net sequestration for this period was 2.944 µmol m^{-2} s^{-1}, which was higher compared to the net flux calculations during the previous and subsequent sampling periods in 2023. The 9/19/2022 - 11/8/2022 sampling period resulted in the highest accretion rates of 0.053 mm d^{-1} sediment accretion and 0.2446 mm d^{-1} total accretion. Along with the highest accretion rates, this period experienced the highest net sequestration rates of -8.550 µmol m^{-2} s^{-1}. The sampling period of 8/20/2022 – 9/18/2022 resulted in a sediment accretion rate of 0.032 and total accretion rate of 0.777 mm d^{-1}, accompanied by the highest observed emission of the 10 month sampling period of 4.911 µmol m^{-2} s^{-1}.

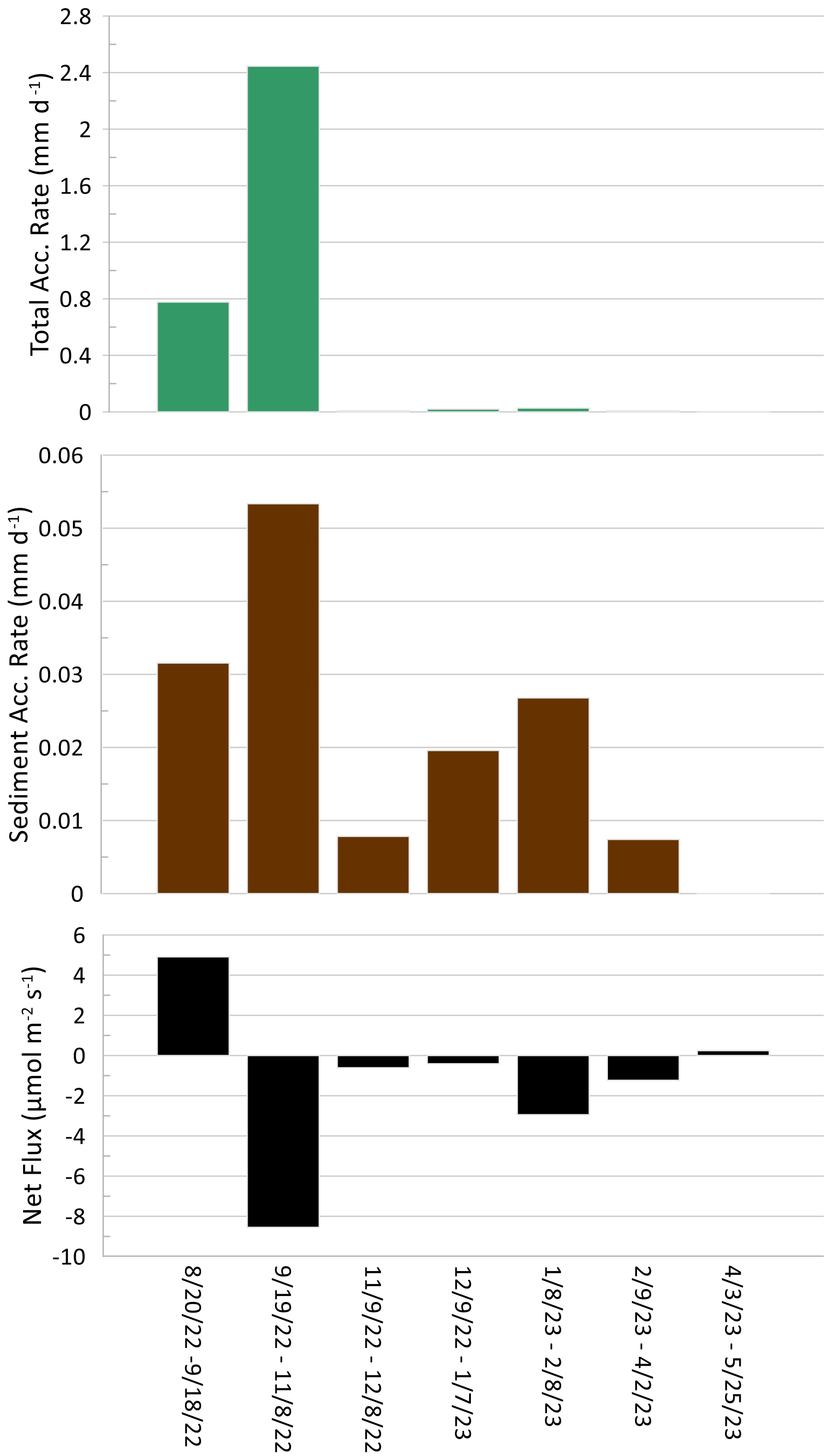

Figure 3.6. Time series plots of total accretion rates (top; green; sediment and vegetation), sediment accretion rates (middle; brown), and net flux (bottom; black). See Table 3.2 for values.

Accumulation Rates at TWC1								
Year	2022				2023			
Date	8/20	9/18	11/8	12/8	1/7	2/8	4/2	5/25
Days	0	29	51	30	29	32	53	57
Accumulation sediment (mm)	n/a	0.915	2.721	0.235	0.568	0.857	0.393	<0.001
Accumulation vegetation (mm)	n/a	21.614	122.0	0.0	0.0	0.0	0.0	0.0
Accumulation rate for sediment (mm day^{-1})	n/a	0.032	0.053	0.008	0.020	0.027	0.007	<0.001
Total Accumulation rate for sediment and vegetation (mm day^{-1})	n/a	0.777	2.446	0.008	0.020	0.027	0.007	<0.001

Net CO_2 Flux for Accumulation Rate Sampling Periods at TWC1							
Year	2022			2022-2023	2023		
Sampling period	8/20-9/18	9/19-11/8	11/9-12/8	12/9-1/7	1/8-2/8	2/9-4/2	4/3-5/25
Net Flux (μmol m^{-2} s^{-1})	4.911	-8.550	-0.608	-0.409	-2.944	-1.233	0.244
Standard Deviation (μmol m^{-2} s^{-1})	0.625	0.381	0.257	0.196	0.196	0.266	0.493
n	2880	4896	1504	2880	2601	5013	5047

Table 3.2. Accumulation rate sampling data (top) and net CO_2 flux calculations for the accumulation rate sampling periods (bottom). The total number of measurements is identified with the variable (n).

DISCUSSION

Net Flux in NI-WB

Annual and Monthly CO_2 Flux Variation in NI-WB

The TWC1 monitoring station at No Man's Friend Creek experienced net sequestration at the sediment surface interface for a ten-month period. The collection is planned to be continued until December of 2023. Within the ten month data set, the late summer months (August/September) experienced high sequestration (>3.5 µmol m^{-2} s^{-1}) compared to other months in different seasons. The Fall month of October experienced net emission. However, Hurricane Ian made direct landfall on September 30, 2022, producing a large-scale disturbance in NI-WB (discussed in detail in Chapter 4). At the end of the Fall season, net sequestration returned in November and was maintained through the winter months of December, January, and February. The net sequestration during this period was generally low (<2 µmol m^{-2} s^{-1}) compared to other months, apart from December (<3.5 µmol m^{-2} s^{-1}). The gap in data in December, due to equipment maintenance, should be noted as potential periods of net emission or sequestration but were not included in the current calculation. Net emission dominated the early spring months of March and April, shifting back to net sequestration in May. Seasonal variation significantly impacts atmospheric CO_2 concentrations, due to variation in biogenic activity and organic watershed inputs into tidal wetlands (Canuel et al., 2012; Tian et al., 2015). The dataset of CO_2 exchange at NI-WB displayed monthly variability of net CO_2 flux calculations, indicating the potential for seasonal biogenic activity and organic watershed inputs to influence net CO_2 flux in the NI-WB tidal wetlands.

Net Flux Calculations Limitations and Recommendations

The net flux calculation from this study identified the overall CO_2 exchange occurring within the footprint of the well system on No Man's Friend Creek. For a more representative characterization of CO_2 flux for the extent of the NI-WB, the spatial distribution of CO_2 soil gas flux monitoring stations should be increased. This will help identify inter-wetland variation in CO_2 exchange and accurately characterize the overall magnitude of source or sink behavior of NI-WB, a calculation which has not been included here due to the lack of understanding of spatial variability.

An alternative approach to measuring CO_2 flux for a long temporal scale is the eddy covariance method, which measures CO_2 concentrations at an elevated height on a tower system above the tidal wetland surface. An important description of the eddy covariance method includes the assumption of surface homogeneity, even atmosphere turbulence, and the collection of net ecosystem exchange (NEE), which limits the individual identification of soil, water, or sediment contribution to CO_2 flux (Hill & Vargas, 2022; Li et al., 2020). The CO_2 soil gas flux monitoring well identifies soil-to-atmosphere vertical exchange of CO_2, while calculating net flux in varying water levels and diverse wetland conditions for extended time periods. The ideal development of spatially and temporally accurate net CO_2 exchange in tidal wetlands would include the combined utilization of the eddy covariance and soil-gas well methods.

Well Atmosphere CO_2 Concentration Relation to Environmental Parameters

Tidal wetlands are dynamic environments, experiencing a range of water quality and meteorological conditions (Neubauer & Megonigal, 2021). The Spearman and Kendall tau-b correlations matrices suggested the interconnectedness of environmental parameters within the wetland environments. For both correlation methods, the environmental parameters significantly correlated to one another, as well as CO_2 concentrations in the well atmosphere (except for wind speed). The Kendall tau-b correlation method generally provided smaller correlation coefficients compared to the Spearman correlation method. The Spearman correlation is much more sensitive to discrepancies and errors in data sets (Schober et al., 2018); however, the similar trends in correlation coefficients led to similar interpretation and inferences of relationships between environmental parameters and CO_2 concentrations.

Estuarine tidal wetland environments are referred to as “biogeochemical reactors” where terrestrial, oceanic, and atmospheric conditions meet and interact (Windham-Myers et al., 2018). The correlation matrices indicated all standard water quality and most meteorological parameters influenced CO_2 flux within the NI-WB tidal wetlands; signifying the environment's physiochemical factors to be fundamental attributes which impact wetlands’ ability to sequester or emit CO_2. In summation of the correlation results, I hypothesize the parameters of water temperature, salinity, specific conductivity, and atmospheric temperature to have the potential to alter CO_2 solubility with a direct correlation. Increased water temperature, salinity, specific conductivity, and atmospheric temperature, decreases solubility of CO_2, resulting in an increase of CO_2 concentrations within the well atmosphere. I surmise pressure to have the potential to alter CO_2 solubility with an inverse correlation. An increase in pressure causes CO_2 to become more soluble, resulting in CO_2 concentrations to readily exit the well atmosphere. As CO_2 becomes more soluble and exists the well atmosphere, the pH of water decreases. This study identifies CO_2 concentrations to have a direct relationship with water depth, turbidity, and humidity, while having an indirect relationship with dissolved oxygen and precipitation; however, further research is required to understand the influence between CO_2 concentrations and these parameters. The further analysis of dissolved CO_2 concentration at the monitoring sites, cross-spectral analysis, and magnitude squared coherence calculations (estimation of the similarities between two frequencies or signals) may provide further insight into the concomitant relationship between CO_2 concentrations and environmental characteristics of NI-WB.

Accumulation Rates and Net CO_2 Flux

Accumulation rates were the highest at TWC1 on No Man's Friend Creek during the sampling periods of 9/19/2022 - 11/8/2022 and 1/8/2023 - 2/8/2023. Hurricane Ian occurred on 9/30/2022; the elevated accumulation rates from 9/19/2022 - 11/8/2022 may be due to increased sediment input from hydraulic flows associated with Hurricane Ian. The high energy of hurricane systems transport increased sediment loads to tidal wetland environments in other areas (Browning et al., 2019; Smith et al., 2015). Since sampling did not occur directly before and after the landfall of Hurricane Ian on 9/30/2022, the immediate influence of accumulation rates from Hurricane Ian could not be determined. However, in this study, elevated accumulation rates at TWC1 were accompanied by elevated net sequestration during two sampling intervals (9/19/2022 - 11/8/2022 and 1/8/2023 - 2/8/2023). Increased sedimentation and burial of carbon are believed to enhance tidal wetland CO_2 sequestration and carbon storage (Morris et al., 2016). However, the initial sampling period from 8/20/22 – 9/18/22 resulted in elevated sedimentation compared the other sampling intervals and a net emission. Therefore, sediment accumulation rates may influence CO_2 sequestration, but do not solely determine net CO_2 flux behavior in tidal wetlands.

Isotopic analysis of the sediment cores at the location of the NST measurements determined historical sedimentation rates to be 0.024 mm d^{-1} (described in detail in Chapter 5). The average sediment accumulation rates, determined by the active NST measurements, were 0.021 mm d^{-1}.

Therefore, the NST tile measurements prove to be similar to historically identified sediment accumulation rates while providing vital insight into specific periods of elevated sedimentation.

CONCLUSION

The area of No Man's Friend Creek, near Mud Bay of NI-WB, experienced monthly variations in CO_2 flux. However, TWC1 was ultimately dominated by net sequestration of CO_2 over a ten-month period (August 2022 – May 2023). The basic biogeochemical conditions (water quality and meteorological parameters) of NI-WB interact to contribute to the net sequestration of CO_2 concentrations. Specifically, the increase in accumulation (total and sediment) for two periods (9/19/2022 - 11/8/2022 and 1/8/2023 - 2/8/2023) was paired with net CO_2 sequestration, inferring the transport and deposition of carbon with increased sediment input to NI-WB. The increased deployment and enhanced spatial distribution of CO_2 monitoring stations in NI-WB would provide an ecosystem-wide characterization of CO_2 flux and overall carbon cycling. Furthermore, the increase in the global distribution of soil gas flux monitoring stations would develop a comprehensive net CO_2 exchange data set for different environments, either acting as a CO_2 source contributing to global warming or offsetting global warming by sequestering atmospheric CO_2. The development of more comprehensive datasets will not only determine the future CO_2 flux outlook, but provide informed carbon budget knowledge for future tidal wetland management practices.

REFERENCES

Benway, H., Alin, S., Boyer, E., W.-J. Cai, W.-J., Coble, P., Cross, J., Friedrichs, M., Goñi, M., Griffith, P., Herrmann, M., Lohrenz, S., Mathis, J., McKinley, G., Najjar, R., Pilskaln, C., Siedlecki, S., and Smith, R. L. (2016). A science plan for carbon cycle Research in North American coastal waters. Report of the coastal carbon synthesis (CCARS) community workshop. *Ocean Carbon and Biogeochemistry Program and North American Carbon Program.* https://www.us-ocb.org/coastal-carbon-synthesis-ccars/.

Browning, T. N., Sawyer, D. E., Brooks, G. R., Larson, R. A., Ramos-Scharrón, C. E., & Canals-Silander, M. (2019). Widespread Deposition in a Coastal Bay Following Three Major 2017 Hurricanes (Irma, Jose, and Maria). *Scientific Reports*, *9*(1), 7101. https://doi.org/10.1038/s41598-019-43062-4

Buzzelli, C., Akman, O., Buck, T., Koepfler, E., Morris, J., & Lewitus, A. (2004). Relationships among water-quality parameters from the North Inlet–Winyah Bay National Estuarine Research Reserve, South Carolina. *Journal of Coastal Research*, *2009*(10045), 59–74. https://doi.org/10.2112/SI45-059.1

Callaway, J. C., Borgnis, E. L., Turner, R. E., & Milan, C. S. (2012). Carbon sequestration and sediment accretion in San Francisco Bay tidal wetlands. *Estuaries and Coasts*, *35*(5), 1163–1181. https://doi.org/10.1007/s12237-012-9508-9

Canuel, E. A., Cammer, S. S., McIntosh, H. A., & Pondell, C. R. (2012). Climate change impacts on the organic carbon cycle at the land-ocean interface. *Annual Review of Earth and Planetary Sciences*, *40*(1), 685–711. https://doi.org/10.1146/annurev-earth-042711-105511

Dossa, G. G. O., Paudel, E., Wang, H., Cao, K., Schaefer, D., & Harrison, R. D. (2015). Correct calculation of CO_2 efflux using a closed-chamber linked to a non-dispersive infrared gas analyzer. *Methods in Ecology and Evolution*, *6*(12), 1435–1442. https://doi.org/10.1111/2041-210X.12451

Etminan, M., Myhre, G., Highwood, E. J., & Shine, K. P. (2016). Radiative forcing of carbon dioxide, methane, and nitrous oxide: A significant revision of the methane radiative forcing. *Geophysical Research Letters*, *43*(24), 12,614-12,623. https://doi.org/10.1002/2016GL071930

Gardner, L. R., Kjerfve, B., & Petrecca, D. M. (2006). Tidal fluxes of dissolved oxygen at the North Inlet-Winyah Bay National Estuarine Research Reserve. *Estuarine, Coastal and Shelf Science*, *67*(3), 450–460. https://doi.org/10.1016/j.ecss.2005.12.002

Hill, A. C., & Vargas, R. (2022). Methane and carbon dioxide Fluxes in a temperate tidal salt marsh: Comparisons between plot and ecosystem measurements. *Journal of Geophysical Research: Biogeosciences*, *127*(7). https://doi.org/10.1029/2022JG006943

Hopkinson, C. S., Cai, W.-J., & Hu, X. (2012). Carbon sequestration in wetland dominated coastal systems—A global sink of rapidly diminishing magnitude. *Current Opinion in Environmental Sustainability*, *4*(2), 186–194. https://doi.org/10.1016/j.cosust.2012.03.005

Intergovernmental Panel on Climate Change (IPCC). (2021) Climate change 2021: The physical science Basis. Contribution of Working Group I to the Sixth Assessment Report of the Intergovernmental Panel on Climate Change [Masson Delmotte, V., P. Zhai, A. Pirani, S.L. Connors, C. Péan, S. Berger, N. Caud, Y. Chen, L. Goldfarb, M.I. Gomis, M. Huang, K. Leitzell, E. Lonnoy, J.B.R. Matthews, T.K. Maycock, T. Waterfield, O.

Yelekçi, R. Yu, and B. Zhou (eds.)]. Cambridge University Press, Cambridge, United Kingdom and New York, NY, USA, 2391 pp. doi:10.1017/9781009157896

Kendall, M. G. (1938). A new measure of rank correlation. *Biometrika*, *30*(1/2), 81–93. JSTOR. https://doi.org/10.2307/2332226

Li, H., Wang, C., Yu, Q., & Smith, E. (2022). Spatiotemporal assessment of potential drivers of salt marsh dieback in the North Inlet-Winyah Bay estuary, South Carolina (1990–2019). *Journal of Environmental Management*, *313*, 114907. https://doi.org/10.1016/j.jenvman.2022.114907

Li, X., Wahlroos, O., Haapanala, S., Pumpanen, J., Vasander, H., Ojala, A., Vesala, T., & Mammarella, I. (2020). Carbon dioxide and methane fluxes from different surface types in a created urban wetland. *Biogeosciences*, *17*(13), 3409–3425. https://doi.org/10.5194/bg-17-3409-2020

Morris, J. T., Barber, D. C., Callaway, J. C., Chambers, R., Hagen, S. C., Hopkinson, C. S., Johnson, B. J., Megonigal, P., Neubauer, S. C., Troxler, T., & Wigand, C. (2016). Contributions of organic and inorganic matter to sediment volume and accretion in tidal wetlands at steady state. *Earth's Future*, *4*(4), 110–121. https://doi.org/10.1002/2015EF000334

National Estuarine Research Reserve System (NOAA NERRS). (2012). *System-wide Monitoring Program.* Data accessed from the NOAA NERRS Centralized Data Management Office. http://www.nerrsdata.org

National Oceanic and Atmospheric Administration (NOAA), National Ocean Service (NOS), Belle W. Baruch Institute of the University of South Carolina, South Carolina Coastal Council. (1992). *Final Management plan, North Inlet/Winyah Bay National Estuarine*

Research Reserve. National Ocean Service. https://repository.library.noaa.gov/view/noaa/2461

National Oceanic and Atmospheric Administration (NOAA). (2022). *Tides & Currents: Datums for 8662299, Clambank Cree Dock, Goat Island, SC*. NOAA. https://tidesandcurrents.noaa.gov/datums.html?id=8662299

North Inlet – Winyah Bay National Estuarine Research Reserve (NI-WB NERR). (2016). *Management Plan. North Inlet – Winyah Bay National Estuarine Research Reserve.* https://northinlet.sc.edu/

Najjar, R. G., Herrmann, M., Alexander, R., Boyer, E. W., Burdige, D. J., Butman, D., Cai, W.-J., Canuel, E. A., Chen, R. F., Friedrichs, M. A. M., Feagin, R. A., Griffith, P. C., Hinson, A. L., Holmquist, J. R., Hu, X., Kemp, W. M., Kroeger, K. D., Mannino, A., McCallister, S. L., … Zimmerman, R. C. (2018). Carbon budget of tidal wetlands, estuaries, and shelf waters of eastern North America. *Global Biogeochemical Cycles*, *32*(3), 389–416. https://doi.org/10.1002/2017GB005790

Neubauer, S. C., & Megonigal, J. P. (2021). Biogeochemistry of wetland carbon preservation and flux. In *Wetland Carbon and Environmental Management* (pp. 33–71). American Geophysical Union (AGU). https://doi.org/10.1002/9781119639305.ch3

Patchineelam, S. M., & Kjerfve, B. (2004). Suspended sediment variability on seasonal and tidal time scales in the Winyah Bay estuary, South Carolina, USA. *Estuarine, Coastal and Shelf Science*, *59*(2), 307–318. https://doi.org/10.1016/j.ecss.2003.09.011

Peng, Y., Zhou, C., Jin, Q., Ji, M., Wang, F., Lai, Q., Shi, R., Xu, X., Chen, L., & Wang, G. (2022). Tidal variation and litter decomposition co-affect carbon emissions in estuarine wetlands. *Science of The Total Environment*, *839*, 156357. https://doi.org/10.1016/j.scitotenv.2022.156357

Schober, P., Boer, C., & Schwarte, L. A. (2018). Correlation coefficients: Appropriate use and interpretation. *Anesthesia & Analgesia*, *126*(5). https://journals.lww.com/anesthesia-analgesia/Fulltext/2018/05000/Correlation_Coefficients__Appropriate_Use_and.50.aspx

Smith, J. E., Bentley, S. J., Snedden, G. A., & White, C. (2015). What role do hurricanes play in sediment delivery to subsiding river deltas? *Scientific Reports*, *5*(1), 17582. https://doi.org/10.1038/srep17582

Song, C., XU, X., Tian, H., & Wang, Y. (2009). Ecosystem–atmosphere exchange of CH_4 and N_2O and ecosystem respiration in wetlands in the Sanjiang Plain, Northeastern China. *Global Change Biology*, *15*(3), 692–705. https://doi.org/10.1111/j.1365-2486.2008.01821.x

Tian, H., Ren, W., Yang, J., Tao, B., Cai, W.-J., Lohrenz, S. E., Hopkinson, C. S., Liu, M., Yang, Q., Lu, C., Zhang, B., Banger, K., Pan, S., He, R., & Xue, Z. (2015). Climate extremes dominating seasonal and interannual variations in carbon export from the Mississippi River Basin. *Global Biogeochemical Cycles*, *29*(9), 1333–1347. https://doi.org/10.1002/2014GB005068

Wang, F., Lu, X., Sanders, C. J., & Tang, J. (2019). Tidal wetland resilience to sea level rise increases their carbon sequestration capacity in United States. *Nature Communications*, *10*(1), 5434. https://doi.org/10.1038/s41467-019-13294-z

Windham-Myers, L., Cai, W.-J., Alin, S., Andersson, A., Crosswell, J., Dunton, K. H., Hernandez-Ayon, J. M., Herrmann, M., Hinson, A. L., Hopkinson, C. S., Howard, J., Hu, X., Knox, S. H., Kroeger, K., Lagomasino, D., Megonigal, P., Najjar, R., Paulsen, M.-L., Peteet, D., … Zhu, Z. (2018). *Chapter 15: Tidal Wetlands and Estuaries. Second State of the Carbon Cycle Report*. U.S. Global Change Research Program. https://doi.org/10.7930/SOCCR2.2018.Ch15

https://doi.org/10.7930/SOCCR2.2018.Ch15

Xu, X., Zou, X., Cao, L., Zhamangulova, N., Zhao, Y., Tang, D., & Liu, D. (2014). Seasonal and spatial dynamics of greenhouse gas emissions under various vegetation covers in a coastal saline wetland in southeast China. *Ecological Engineering*, *73*, 469–477. https://doi.org/10.1016/j.ecoleng.2014.09.087

Yang, P., Lai, D. Y. F., Huang, J. F., Zhang, L. H., & Tong, C. (2018). Temporal variations and temperature sensitivity of ecosystem respiration in three brackish marsh communities in the Min River Estuary, southeast China. *Geoderma*, *327*, 138–150. https://doi.org/10.1016/j.geoderma.2018.05.005

CHAPTER FOUR

IMPACT OF HURRICANE IAN (2022) ON CARBON DIOXIDE (CO_2) FLUX IN TIDAL WETLANDS OF NORTH INLET-WINYAH BAY, SOUTH CAROLINA

ABSTRACT

Hurricane Ian made landfall as a Category 1 hurricane on September 30, 2022, over the North Inlet-Winyah Bay tidal wetlands. The subsequent CO_2 changes were captured by an innovative, low-cost carbon monitoring station located less than 1.5 km from the eye of Hurricane Ian. The wetlands experienced a net CO_2 sequestration four weeks prior to Hurricane Ian (-2.632 μmol m^{-2} s^{-1}), a net CO_2 sequestration over the 24-hour period of Hurricane Ian's landfall (-3.902 μmol m^{-2} s^{-1}), and a net CO_2 emission for four weeks after Hurricane Ian (3.155 μmol m^{-2} s^{-1}). As Hurricane Ian made direct landfall, NI-WB experienced net CO_2 emission and transitioned to net CO_2 sequestration as the hurricane's eye passed the tidal wetlands. After Hurricane Ian's landfall, the NI-WB tidal wetlands experienced a brief (<12 hours) period of elevated CO_2 sequestration, followed by longer periods of net emission. This study represents one of the first to capture the continuous patterns of CO_2 flux in tidal wetlands throughout the immediate passage of a hurricane, providing insight into the effects of high-energy events on net carbon sequestration in estuarine wetland environments.

INTRODUCTION

Tropical cyclones are extreme weather events consisting of large rotational air masses which develop in oceanic waters between latitudes of 30 °N and 30 °S. The extreme weather events form due to (1) warm oceanic water, (2) rapid vertical cooling of sea surface temperatures, (3) presence of moisture-laden air masses, (4) significant Coriolis force, (5) well-developed low-pressure vorticity, and (6) low vertical wind shear (Shultz et al., 2014). In the Atlantic Ocean basin, established tropical cyclones are commonly known as hurricanes. Atlantic hurricanes are categorized within the Saffir-Simpson scale. The scale classifies hurricane strength within a series of energy levels based on maintained wind speed and ranges from Category 1 through 5. A Category 1 hurricane begins with minimum wind speeds reaching 33 meters per second (m s^{-1}), progressing through the Saffir-Simpson scale, to a maximum level of a Category 5 hurricane with minimum wind speeds of 70 m s^{-1} (Camelo & Mayo, 2021).

In addition to powerful wind speeds, coastal systems are threatened by storm surge and precipitation flooding due to hurricane disturbances. Hurricanes are the most significant drivers of coastal flood loss along the Atlantic coast, dominating the upper tail distribution (> 50-year return period) for storm surge and precipitation-induced flooding (Gori et al., 2022). The coupling of hurricane-induced storm surge and precipitation also contributes to extreme compound flooding within coastal systems (Gori et al., 2020; Wahl et al., 2015).

The Intergovernmental Panel on Climate Change (IPCC) reported in the Sixth Assessment Report: The Physical Science Basis (2021), an observed increase in rapid intensification (wind speed increase of 46.3 km hr^{-1} within 24 hours) and decrease in translation speed (forward motion) of hurricanes with a changing climate (Balaguru et al., 2018; Bhatia et al., 2019; Kossin, 2018). Additionally, the IPCC projected an increase in both average and peak hurricane precipitation rates and wind speeds with global climate change (IPCC, 2021). The combination of hurricane-induced rapid intensification, decreased translation speed, increased precipitation rates, and increased wind speed presents an ever-increasing threat to coastal systems (IPCC, 2021; Emanuel, 2020; Hall & Kossin, 2019; Kossin, 2018; Peduzzi et al., 2012).

Coastal tidal wetlands serve as an effective natural defense against high-energy hurricanes (Al-Attabi et al., 2023; Ouyang & Lee, 2020; Sun & Carson, 2020). The characteristics of tidal wetland environments introduce land-based friction to reduce storm wind speed, supply a natural permeable horizontal barrier to minimize the extent of storm surge, and attenuate flood waters within the low elevation of wetland basins (Fairchild et al., 2021; Hu et al., 2015). Coastal tidal wetlands are also known to serve as a long-term natural sink for global carbon, storing what is known as blue carbon (Gao et al., 2016; Najjar et al., 2018; Ouyang & Lee, 2020). The tidal wetland processes of high primary productivity, ongoing sedimentation, and slow decomposition rates in anoxic soils effectively store ~116 teragrams of blue carbon per year (Callaway et al., 2012; Wang et al., 2019). The efficient carbon sequestration and storage in tidal wetlands assist in offsetting atmospheric carbon dioxide (CO_2) concentrations and mitigating global climate change (Villa & Bernal, 2018).

The current state of hurricane activity and projected increase in storm intensity imposes the potential for periodic high-energy perturbations in known natural wetland processes and coastal carbon cycling (Najjar et al., 2018; Windham-Myers et al., 2018). Precipitation associated with hurricanes has the potential to induce extreme hydrologic events on inland watersheds and pulse organic matter from headwater streams to tidal wetland sinks for deposition (Medeiros, 2022; Ward et al., 2017). High energy associated with hurricane storm surge also provides the potential to disrupt stored carbon with increased erosion to promote CO_2 efflux (Lovelock et al., 2017; Mo et al., 2020; Najjar et al., 2018; Windham-Myers et al., 2018). My study aimed to identify the influence a hurricane has on CO_2 flux at the sediment interface in a tidal wetland of SC across several intervals before and after the hurricane event. The quantification of carbon exchange during the localized high-energy event characterized hurricane energy impact on tidal wetlands net carbon budget, ultimately improving known wetland carbon cycling and wetland-atmosphere exchanges for climate projections. This chapter is being prepared for submission to Nature Communications.

METHODS

Study site

Site Location

North Inlet-Winyah Bay (NI-WB), located in Georgetown, SC, is a National Oceanic and Atmospheric Administration (NOAA) designated National Estuarine Research Reserve (NERR; Fig. 4.1). The NI-WB reserve was designated in 1992, encompassing ~77 square kilometers (km^2) of pristine estuarine tidal wetlands with high water quality and little anthropogenic development (Li et al., 2022). The reserve includes two interconnected estuarine systems of North Inlet and Winyah Bay. North Inlet is an oceanic-dominated estuary with an ~96 km^2 watershed (NI-WB NERRS, 2016). Winyah Bay is a riverine-influenced estuary comprising ~47,000 km^2 of watershed, making it the third largest watershed on the East Coast (NI-WB NERRS, 2016). Hydraulic circulation in North Inlet is tidally dominated, with a semidiurnal tidal pattern which receives freshwater inputs from surrounding watersheds and northward flow from Winyah Bay. The Winyah Bay estuarine environment experiences semidiurnal tide patterns, which are superimposed on riverine unidirectional flow to the Atlantic Ocean from the Pee Dee, Waccamaw, Black, and Swampit Rivers (NOAA, 1992). The average tidal range for NI-WB was ~1.5 m. Peak tidal currents within the North Inlet system reach 1.4 m s^{-1}, while peak Winyah Bay tidal currents are greater than 2.0 m s^{-1} (Gardner et al., 2006; Patchineelam & Kjerfve, 2004) *Spartina alterniflora* (smooth cordgrass) was the dominant vegetation throughout NI-WB,

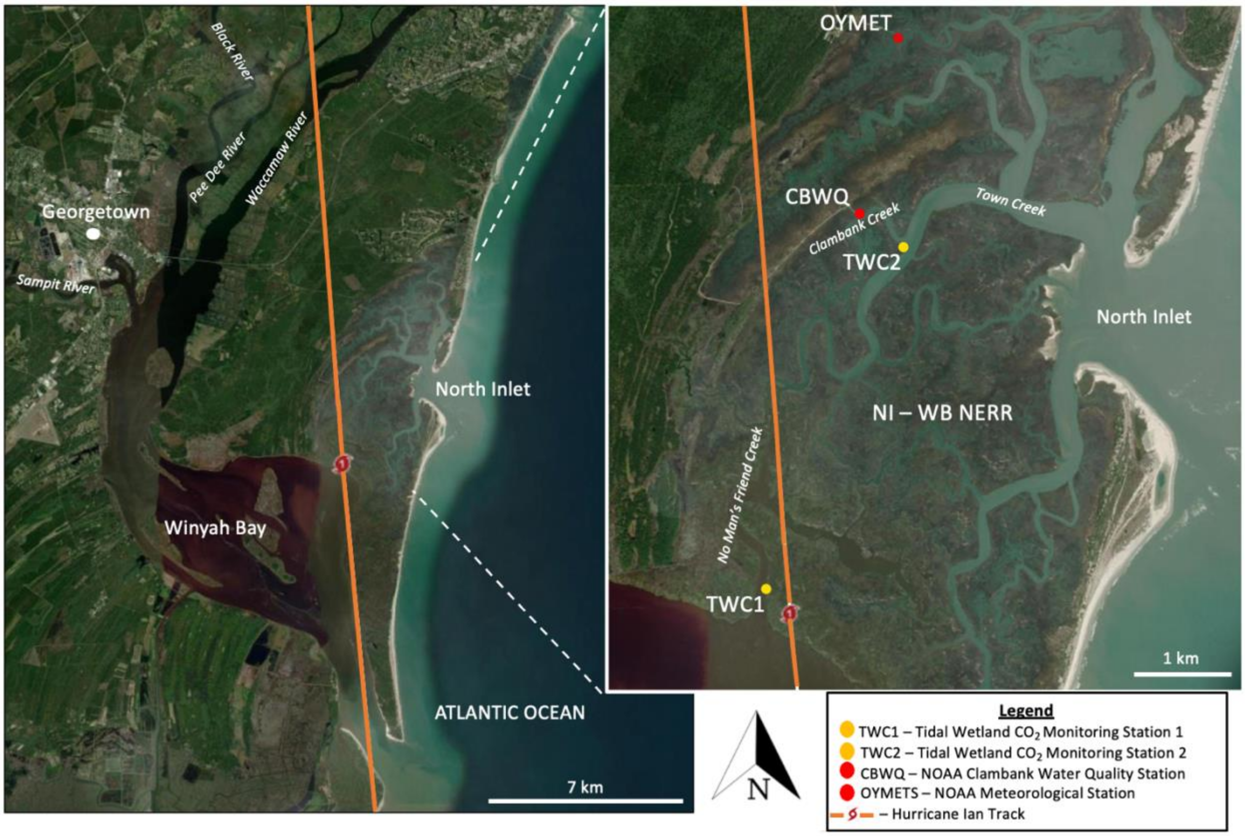

Figure 4.1. Hurricane Ian track and site location map within the study area of North Inlet-Winyah Bay (NI-WB) National Estuarine Research Reserve (NERR), located in Georgetown, SC.

with the presence of *Juncus roemerianus* (needle rush) in the northern territory of the North Inlet system (Gardner et al., 2006; Li et al., 2022).

Carbon dioxide flux monitoring stations were deployed in two locations of North Inlet (Fig. 4.1). The first CO_2 flux monitoring station (TWC1) was located on No Man's Friend Creek at the convergence of the North Inlet and Winyah Bay systems, in an area known as Mud Bay. The location of Mud Bay makes up a shallow portion of Winyah Bay with high sediment loads, accretion rates, and freshwater inputs from the expansive Winyah Bay watershed (Buzzelli et al., 2004; Patchineelam et al., 1999). The second CO_2 flux monitoring station (TWC2) was located at the convergence of Town Creek and Clambank Creek within the North Inlet system. Town Creek was dominated by oceanic influence due to its proximity to the inlet of the North Inlet estuary. Further description of the monitoring station and data collection can be found in Chapter 2 and below in the instrumentation section.

Active and historical meteorological and water quality data was continuously collected by the NOAA NERRS system within North Inlet (Fig. 4.1). Meteorological parameters (temperature & barometric pressure) were measured at the Oyster Landing Station (OYMET) every five seconds and collected as 15-minute averages (NOAA NERRS, 2012). Water quality parameters (water level, water temperature, turbidity, pH, etc.) were collected at the Clambank Station (CBWQ) every 15 minutes (NOAA NERRS, 2012).

Hurricane Ian

A robust tropical wave, moving west from the African Coast on September 14-15, 2022, was responsible for the origin of Hurricane Ian (Bucci et al., 2023). The wave slowly traveled through the Atlantic Ocean within the monsoon trough and Inter-tropical Convergence Zone (Bucci et al., 2023). The wave reached the Windward Islands on September 21, 2022 (Bucci et al., 2023). Despite moderate-to-strong wind shear the storm's convective activity increased and was determined to be a tropical depression via satellite imagery by the National Weather Service (Bucci et al., 2023). The tropical depression was located ~209 km north of Aruba at 01:00 Eastern Standard Time (EST; Bucci et al., 2023). At 19:00 EST on September 23, 2022, the system reached tropical storm status ~539 km southeast of Jamaica (Fig. 4.2; Bucci et al., 2023). The subtropical ridge pushed the tropical storm northwestward, where convection began to experience rapid intensification. At 01:00 EST on September 26, 2022, the storm developed into a hurricane system as its passed ~160 km south-southwest of the Grand Cayman Islands (Bucci et al., 2023). The warm waters and low vertical wind shear allowed the hurricane to continue to rapidly intensify as it approached the coast of Cuba, becoming a major Category 3 hurricane with ~57 m s^{-1} winds (Bucci et al., 2023). Hurricane Ian made landfall within the Pinar del Rio Province of Cuba at 03:30 EST on September 27, 2022 (Bucci et al., 2023).

Hurricane Ian entered the southeastern Gulf of Mexico at 09:00 EST on September 27, 2022, with only a slight decrease in energy (Fig. 4.2; Bucci et al., 2023). The hurricane continued to travel over the Gulf of Mexico, making landfall at 21:00 EST on September 27, 2022, at the Dry Tortuga Islands with ~57 m s^{-1} winds as a Category 3 (Bucci et al., 2023). Hurricane Ian grew in strength as it traveled through the Gulf of Mexico, before making initial landfall on Cayo Costa, FL, as a Category 4 hurricane with ~67 m s^{-1} winds at 14:05 EST on September 28, 2022 (Bucci et al., 2023). The eye of Hurricane Ian made landfall in Punta Gorda, FL, at 15:35 EST with a wind intensity of ~67 m s^{-1}, equivalent to a Category 4 hurricane (Bucci et al., 2023). The storm surge reached levels of 3 to 4.5 m above ground level along the southwest coast of FL (Bucci et al.,

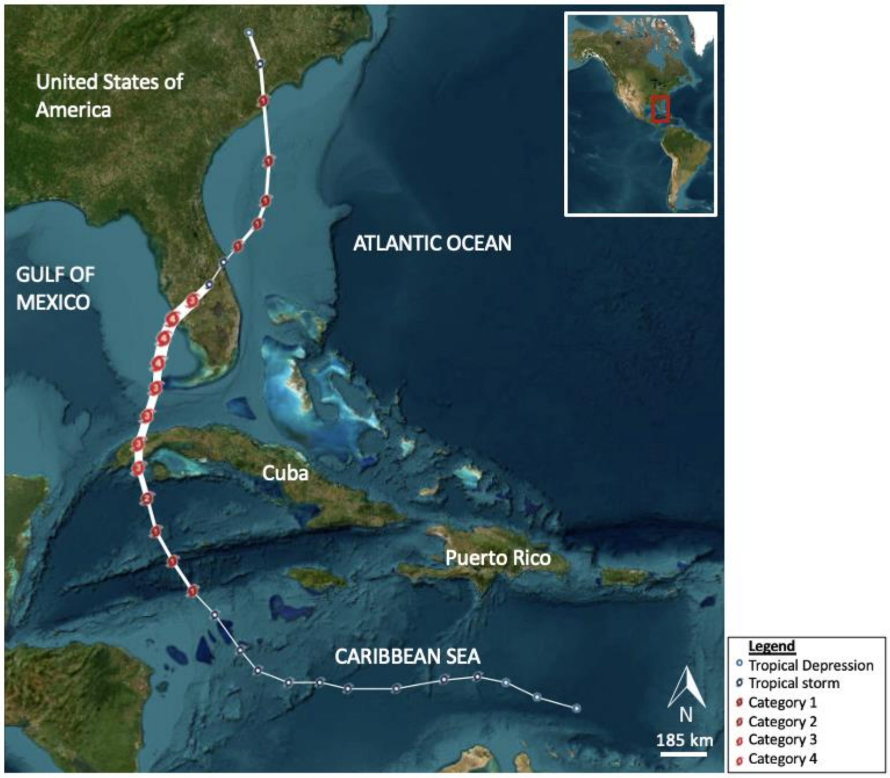

Figure 4.2. Hurricane Ian track map including intensities. The storm's intensity is represented by a red roundel for a hurricane (1-4 Category grade on the Saffir-Simpson Scale), a dark blue roundel for a tropical storm, and a light blue dot for a tropical depression (NOAA & NHC, 2022).

2023). Hurricane Ian lost significant energy as it traveled northeast over the FL peninsula, resulting in the dissipation to a tropical storm which emerged into the Atlantic Ocean near Cape Canaveral, FL at 07:00 EST on September 29, 2022, with winds of ~31 m s^{-1} (Bucci et al., 2023).

Once in the western Atlantic Ocean, the storm increased in energy to become a Category 1 hurricane at 13:00 EST on September 29, 2022. The hurricane began traveling north to the Carolina coast with winds of ~33 m s^{-1} (Fig. 4.2). Hurricane Ian made its final landfall around 13:05 EST near Georgetown, SC as a Category 1 hurricane with ~36 m s^{-1} winds (Bucci et al., 2023).

The path of Hurricane Ian traveled directly through the NI-WB NEERS, passing through the study sites monitoring stations on September 30, 2022 (Fig. 4.1). The Oyster Landing Meteorological Station (OYMET) in North Inlet recorded peak wind speeds of ~50 m s^{-1} at 11:15 EST. Peak precipitation at OYMET occurred between 11:00-11:45 EST, with a total of 29 millimeters (mm). The minimum barometric pressure from the eye of Hurricane Ian, 981 millibars (mbar), occurred at OYMET from 13:15-14:15 EST. The peak water level in North Inlet was measured to be ~3 m at the Clambank Water Quality Station Datum (NOAA NERRS, 2012).

Instrumentation

An innovative CO_2 flux monitoring station was utilized to collect continuous CO_2 concentration measurements within the dynamic environmental conditions of the NI-WB tidal wetland system (Chapter 2). The monitoring station was similar in concept to the closed dynamic chamber system method to measure soil gas flux at the sediment surface by applying a non-dispersive infrared (NDIR) gas analyzer (Vaisala GMP252) within a soil-gas well (Fig. 4.3). The NDIR analyzer measured CO_2 concentrations within the well atmosphere. Temporal variation

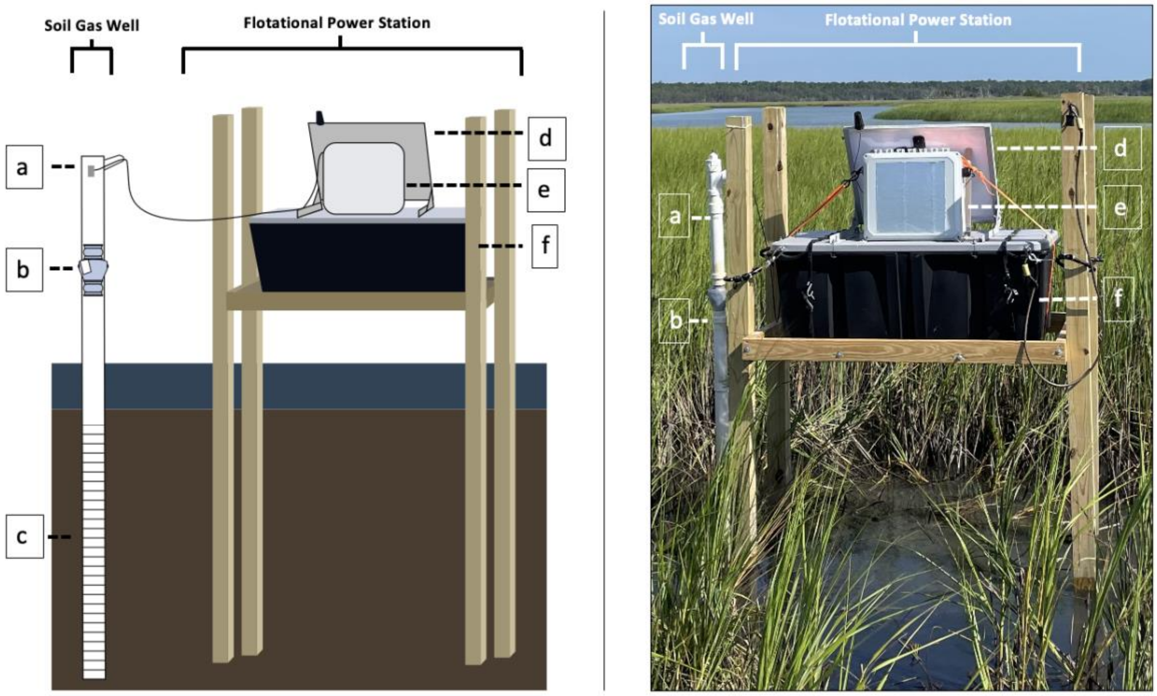

Figure 4.3. CO_2 Flux Monitoring Station conceptual diagram (left) and field image (right). Soil-gas well components include a) NDIR gas analyzer & pressure release valve, b) backflow check well, and c) PVC well screen. The flotational power station components include d) solar panel, e) waterproof enclosure, and f) EPS encased in PE.

within the CO_2 measurements was applied to the flux equation (2.3.1 Carbon Dioxide Flux; eqn. 2.1) to determine emission or sequestration across the sediment surface. The soil-gas well and floating power station (Fig. 4.3) enable measurements to occur under high-energy conditions.

The soil-gas well consisted of a 3.2 m long polyvinyl chloride (PVC) well with a 5 cm diameter. The PVC well was buried 1.2 m below ground with a 1-m long screen interval (1.27 cm screened slots with 2.54 cm spacing) to allow sediment to infill the well and replicate near natural conditions (Fig. 4.3; c). The well system extended 2 m above the ground surface, exceeding maximum historical water levels in North Inlet caused by king tides and storm surges (1.7 m above mean tidal level; NOAA NERRS, 2012; NOAA, 2022). At the maximum tidal level in North Inlet (1.4 m), a backflow check valve was deployed to close with rising waters within the well system and protect the NDIR analyzer during extreme events (Fig. 4.3; b). The NDIR analyzer was secured at the top of the well system, measuring the CO_2 concentrations in parts per million (ppm) of the well's atmosphere (Fig. 4.3; a). To limit pressure build-up within the well atmosphere, a one-way pressure release valve was fitted to the top of the well to ensure equivalent well pressure to atmospheric pressure for natural sampling conditions (Fig. 4.3; a).

The NDIR analyzer was powered via an external floating power source (Fig. 4.3). The implementation of a flotational power station enabled continuous measurements during extreme high-water events. A commercial flotational device, made of expanded polystyrene (EPS) foam encased within polyethylene (PE), enabled the electrical data acquisition equipment to rise with increasing water levels and descend with lowering water levels (Fig. 4.3; f). The electrical data acquisition equipment included a Raspberry Pi-base data logger, marine battery, and solar panel. The data logger consisted of a Raspberry Pi Zero equipped with an RS485 Modbus converter and cellular modem via a USB hub which permitted automated collection and transmission of CO_2 concentration measurements in the remote location of North Inlet. A 12.6 volt (V), 55 amp-hour deep cycle marine battery supplied power to the NDIR analyzer and data logger. The data logger and marine battery were housed atop the flotational device within a waterproof enclosure with a National Electrical Manufacturers Association (NEMA) 6p rating (Fig. 4.3; e). To accommodate long-term monitoring and sustain a complete power source, a 12 V, 55-Watt solar panel was also secured to the flotational device to continually trickle charge the deep cycle marine battery (Fig. 4.3; d). The complete flotational power source was attached to four treated lumber posts via stainless steel wired loop to guide oscillation during varying water levels.

The use of the soil-gas well and the protection of the electrical equipment within the CO_2 flux monitoring station design allowed the successful collection of CO_2 flux measurements in high-energy events with no interruption. Measurements of CO_2 concentrations were collected every five minutes within the well system throughout the duration of Hurricane Ian at one monitoring site. The uninterrupted data provided a comprehensive insight into CO_2 flux during high-energy hurricane conditions.

Data Analysis

Carbon Dioxide Flux

The measured CO_2 concentrations (c; ppm) within the well atmosphere are applied to a flux equation to determine sequestration or emission across a known area (A; m^2) of the sediment interface for a specific amount of time (t; seconds [s]) within the North Inlet estuary (eqn. 3.1):

$$Flux = \frac{\Delta c}{\Delta t} \times \frac{PV}{RT} \times \frac{1}{A} \qquad \textit{eqn. 3.1}$$

The carbon concentrations were measured via the NDIR analyzer. Measurements of CO_2 occurred every 300 s for detailed identification of CO_2 concentration variation. Within the flux equation, CO_2 concentrations of 900 s intervals were applied to correspond with the NOAA NERRS standard measurement collection of 15 minutes.

The soil-gas well represents a closed dynamic chamber system, resulting in the incorporation of ideal gas law ($P_iV_i=nRT_i$) within the governing flux equation by implementing the universal gas constant (R; 0.83025 mbar m^3 K^{-1} mol^{-1}). The universal gas constant was calculated using standard atmospheric pressure (P_i; 1,013.25 mbar), volume of an ideal gas as standard pressure (Vi; 0.2241 cubic meters per mole [m3 mol^{-1}]), and standard temperature (Ti; 273.15 Kelvin [K]).

Pressure (P; mbar) values were derived as atmospheric pressure from a nearby weather station (OYMET). The application of the one-way release value within the soil-gas well permitted the assumption for atmospheric pressure to be equivalent to the pressure of the well atmosphere. The volume (V; cubic meters [m^3]) of gas being analyzed was determined by subtracting the volume of the well (3.93×10^{-3} m^3) by the NDIR gas analyzer's sampling volume 6.9×10^{-6} m^3, resulting in a fixed volume variable of 3.92×10^{-3} m^3 (Chapter 2; Dossa et al., 2015). The NDIR analyzer collected *in situ* temperature values (T; K).

The fluctuation of CO_2 concentrations within the soil-gas well occurred across the sediment surface. The cross-sectional area (A) of the cylindrical PVC well was 1.96×10^{-3} m^2. The resulting flux measurements (μmol m^{-2} s^{-1}) determine emission or sequestration of CO_2 across the soil-gas well's cross-sectional area.

Net Flux

A net exchange of CO_2 was determined at the monitoring station environment due to the collection of continuous measurements. The sum of CO_2 flux measurements indicated either a net sequestration (negative) or emission (positive). Net flux calculations were conducted for varying time intervals to determine CO_2 exchange before and after the disturbance of Hurricane Ian (Table 4.1 & Table 4.3).

Net flux was calculated daily with the sum of 96 measurements (every 15 minutes) for a 24-hour period. Daily flux calculations included the day of Hurricane Ian's landfall in SC (September 30, 2022). The daily flux calculations were compared at intervals of one week (672 measurements), two weeks (1,344 measurements), three weeks (2,016 measurements), and four weeks (2,688 measurements) pre- and post-hurricane Ian (Fig. 4.4 – 4.8). The weekly net flux calculations aid in determining the overall flux behavior of the monitoring stations within the tidal wetlands for an extended period pre- and post- Hurricane Ian.

To consider the immediate effects of Hurricane Ian, net flux was calculated throughout the progression of Hurricane Ian (Fig. 4.9 – 4.13). For my study, Hurricane Ian's impact on the coastal system was determined based on atmospheric pressure and water level variations measurements collected from the NOAA NERRS Central Data Management long-term monitoring system (NOAA NERRS, 2012). Hurricanes are commonly identified by decreases in atmospheric pressure due to their low-pressure system (Shultz et al., 2014). Hurricane also impact water levels due to wind energy producing a storm surge to elevate coastal waters (Familkhalili et al., 2020). A detailed description of CO_2 flux variation was identified for pre-, during, and post-hurricane landfall by calculating net flux over the extreme hurricane-induced pressure and water level variation for the purpose of this study.

Prior to Hurricane Ian, the North Inlet system did not experience an atmospheric pressure lower than 1005 mbar during the 2022 Hurricane Season (June 1 – September 30; NOAA NERRS, 2012). Therefore, net flux calculations for Hurricane Ian began at the initial drop in pressure below 1005 mbar (04:30 EST, 9/30/22), to the eye of the low-pressure system at 981 mbar (13:45 EST, 9/30/22), and the return to a 1005 mbar pressure (02:15 EST, 10/1/22) over NI-WB (OYMET; NOAA NERRS, 2012). Hurricane Ian made landfall in conjunction with rising tides in the NI-WB tidal sequences. Net flux was calculated from the initial rise in local water levels from 1.57 m (05:15 EST, 9/30/22), peak water level of 3.93 m (12:30 EST, 9/30/22), and return to low water level at 1.3 m (20:00 EST, 9/30/22).

Additionally, net flux was determined from the start of Hurricane Ian based on atmospheric pressure change (1005 mbar; 04:30 EST on 9/30/22) and the return to initial net sequestration behavior (positive to negative flux). The same calculation was completed for the start of Hurricane Ian based on water level (1.57 m; 05:15 EST on 9/30/22) to first net sequestration behavior. The calculation of net flux during this time determined the period of transition from net emission (positive flux) following the high-energy disturbance to net sequestration (negative flux) within the tidal wetland environment.

Kruskal – Wallis Test

A Kruskal–Wallis test was used to identify significant differences between CO_2 concentrations in the well atmosphere and CO_2 flux pre-, during, and post-Hurricane Ian, providing a temporal analysis of alterations in CO_2 transport due to the storm disturbance. The Kruskal – Wallis Test compared pre-, during, and post-measurements to assess whether mean ranks differed. The mean rank within the Kruskal-Wallace test refers to the average of the ranks for all observations within a sampling period (Kruskal & Wallis, 1952). The time series included 24 hr (*n* =96), 48 hr (*n*=192), 72 hr (*n*=288), one week (*n*=672), two weeks (*n*=1,344), three weeks (*n* = 2,016), and four weeks (*n*=2,688) pre- and post-Hurricane Ian. The Hurricane Ian time interval always represented the 24 hr period of September 30, 2022 (*n*=96). The pre- and post-hurricane time series, along with the Hurricane Ian time series, were summed to determine total measurements within the Kruskal-Wallis analysis (*n*). The CO_2 flux data were non-parametric and met the Kruskal Wallis test assumptions: (1) observations of the data set were mutually independent, (2) the measurement scale was categorical, ordinal, or continuous in nature, (3) the analysis compared more than two categorical independent groups, and (4) mean rank comparison was true regardless of variability (Kruskal & Wallis, 1952).

RESULTS

Long-Term Net Flux Intervals

TWC1 Monitoring Station

The trends of CO_2 gas concentrations in the soil-gas well atmosphere, and the application of the concentrations to a flux equation, showed gas exchange at the sediment surface interface. From September 2, 2022, to October 28, 2022, daily flux calculations experienced varying sequestration to emission (Fig. 4.5). Prior to Hurricane Ian, TWC1 generally experienced higher CO_2 concentrations in the well system and a net sequestration behavior compared to the 72-hour period before and after the hurricane. During Hurricane Ian, TWC1 experienced low CO_2 concentrations and net sequestration (-3.902 µmol m^{-2} s^{-1}). Following Hurricane Ian, TWC1 experienced low CO_2 concentrations and net emission. (Fig. 4.4 – 4.5; Table 4.1).

The mean ranks of the CO_2 concentrations in the well atmosphere were significantly different across three-time intervals: four weeks prior to Hurricane Ian (9/2/22-9/29/22), the 24-hour period on the day of Hurricane Ian (9/30/22), and four weeks post-Hurricane Ian (10/1/22-10/28/22; Kruskal-Wallis test; $H(2)$ =2,613.9, $p = 0$). The mean rank of the flux during the four weeks prior to, during, and post Hurricane Ian were not statically significant (Kruskal-Wallis; $H (2) = 4.256$, $p = 0.119$). However, four weeks prior to Hurricane Ian (9/2/22-9/29/22), TWC1 experienced net sequestration of -2.632 µmol m^{-2} s^{-1}. For four weeks post-Hurricane Ian, TWC1 experienced net emission of 3.155 µmol m^{-2} s^{-1} (Fig. 4.4 – 4.6; Table 4.1 – 4.2).

The mean rank of CO_2 concentrations for three weeks prior to Hurricane Ian (9/9/22-9/28/22), Hurricane Ian (9/330/22), and three weeks post-hurricane (10/1/22- 10/21/22) were found to be statistically different (Kruskal Wallis – $H (2) = 1856.029$, $p = 0$). The difference in mean rank of CO_2 flux for the three-week periods pre- and post-, along with Hurricane Ian, were not statically significant (Kruskal Wallis; $H (2) = 3.91$ H, $p = 0.119$). During the three weeks prior to Hurricane Ian, TWC1 experienced net emission of 0.918 µmol m^{-2} s^{-1}. TWC1 produced 3.458 µmol m^{-2} s^{-1} of net emission for three weeks post-Hurricane Ian (Fig. 4.4 – 4.6; Table 4.1 – 4.2).

During the two-week period prior to Hurricane Ian (9/16/22-9/29/22), Hurricane Ian (9/30/22), and post-Hurricane Ian (10/1/22-14/22), TWC1 experienced significant differing mean rank of CO_2 concentrations within the well atmosphere (Kruskal-Wallis; $H (2) = 1582.416$, $p = 0$) and a non-significant difference of mean ranked CO_2 flux (Kruskal-Wallis; $H (2) = 4.196$ H, $p = 0.124$). TWC1 displayed net sequestration of -3.333 µmol m^{-2} s^{-1} two weeks prior to Hurricane Ian. Two weeks post-Hurricane Ian, TWC1 experienced net emission of 4.508 µmol m^{-2} s^{-1} (Fig. 4.4 – 4.6; Table 4.1 – 4.2).

Across all the hurricane stages of one week prior to (9/23/22-9/29/22), during (9/30/22), and one-week post-Hurricane Ian (10/1/22-10/7/22), TWC1 experienced significant differing mean ranks of CO_2 concentrations within the well atmosphere (Kruskal-Wallis; H (2) = 723.453, p = <0.001) and non-significant CO_2 flux mean ranks (Kruskal-Wallis; H (2) 5.428, p = 0.066). For one week prior to Hurricane Ian, TWC1 produced net sequestration of -0.603 µmol m^{-2} s^{-1}. For one week after Hurricane Ian, TWC1 experienced net emission of 3.733 µmol m^{-2} s^{-1} (Fig. 4.4 – 4.6; Table 4.1 – 4.2).

For the time series of 72 hr (Kruskal-Wallis; H (2) = 237.419, p = <0.001), 48 hr (Kruskal-Wallis; H (2) = 109., p = <0.001), and 24 hr (Kruskal-Wallis; H (2) = 13.322, p = <0.001), all three storm stages of pre-, during, and post-Hurricane Ian experienced significantly different mean ranks of CO_2 concentrations and non-significant differences in CO_2 flux (Fig. 4.5). The 72 hr and 48 hr time series prior to Hurricane Ian experienced a net sequestration, while the 72 hr and 48 hr time series post-hurricane had net emission. The 24-hour period pre- and post-Hurricane Ian experienced net emissions (Fig. 4.4 – 4.6; Table 4.1 – 4.2).

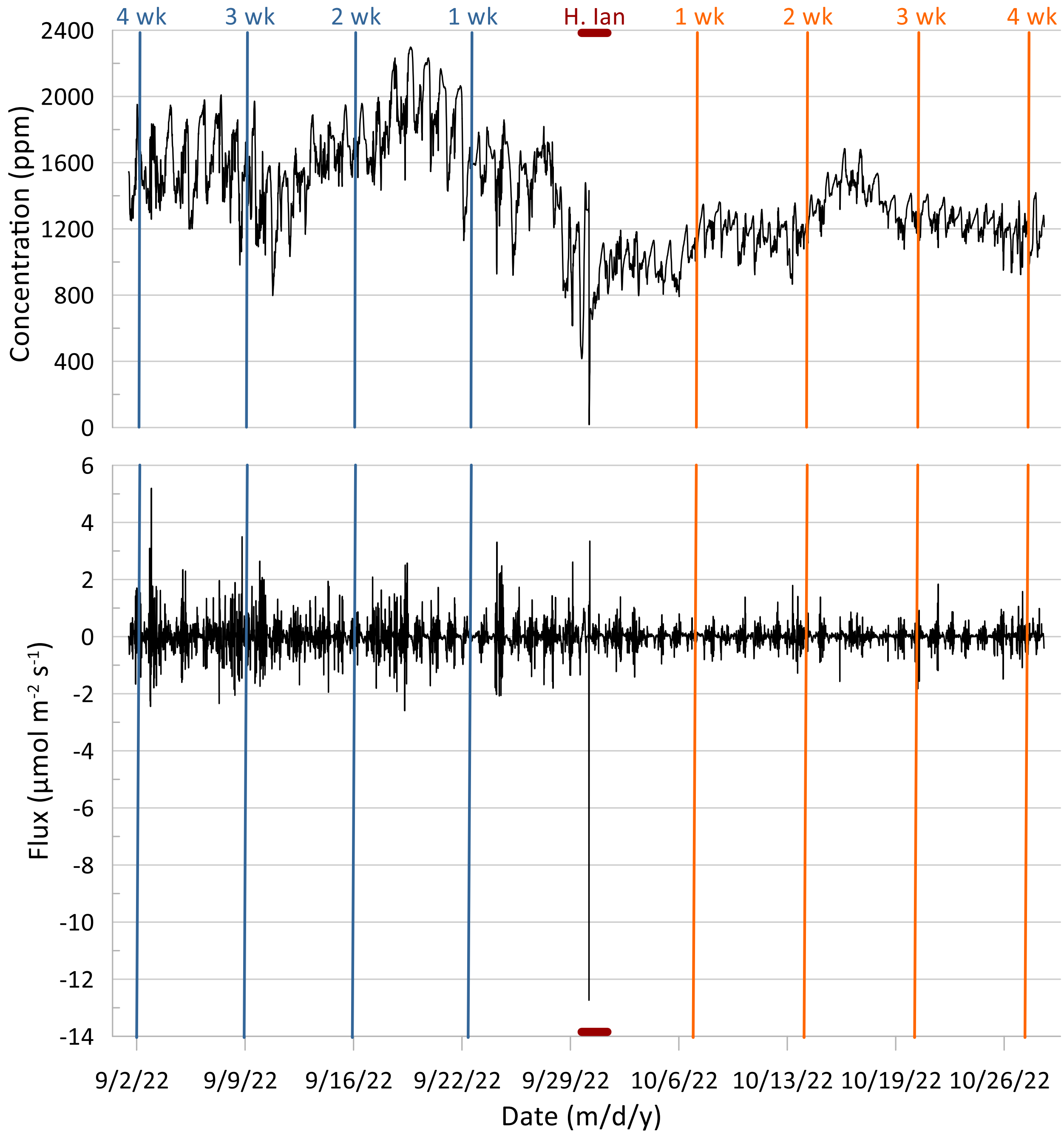

Figure 4.4. TWC1 weekly time series line plot of well atmosphere CO2 concentration vs. time (top) and flux calculation vs. time (bottom) for up to 4 weeks pre- and post-Hurricane Ian. Blue lines indicate the pre-Hurricane Ian time series, the maroon marker represents the Hurricane Ian time series, and orange lines indicate the post-Hurricane Ian time series.

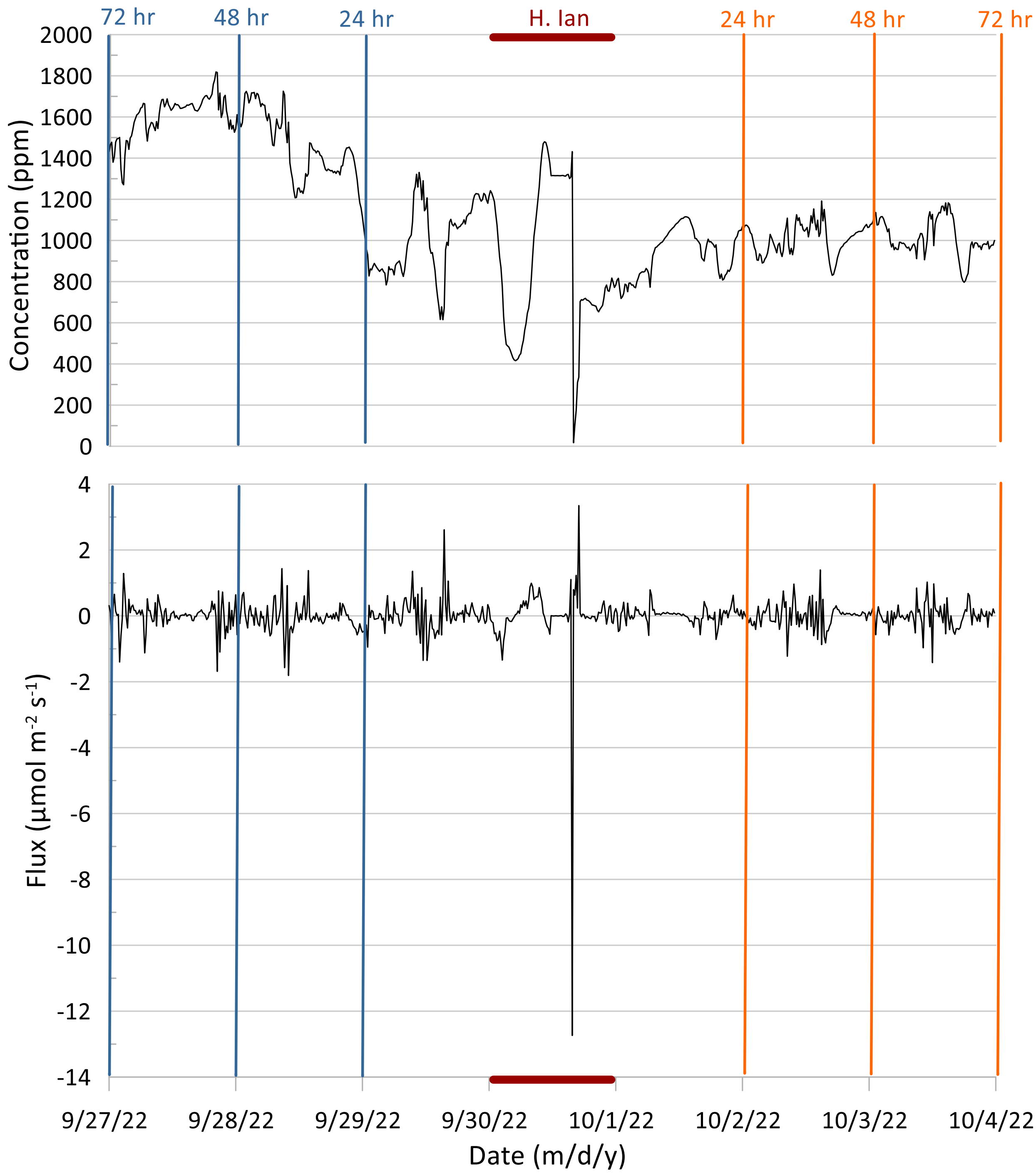

Figure 4.5. TWC1 hourly time series line plot of well atmosphere CO_2 concentration vs. time (top) and flux calculation vs. time (bottom) for up to 72 hours pre- and post-Hurricane Ian. Blue lines indicate the pre-Hurricane Ian time series, the maroon marker represents the Hurricane Ian time series, and orange lines indicate the post-Hurricane Ian time series.

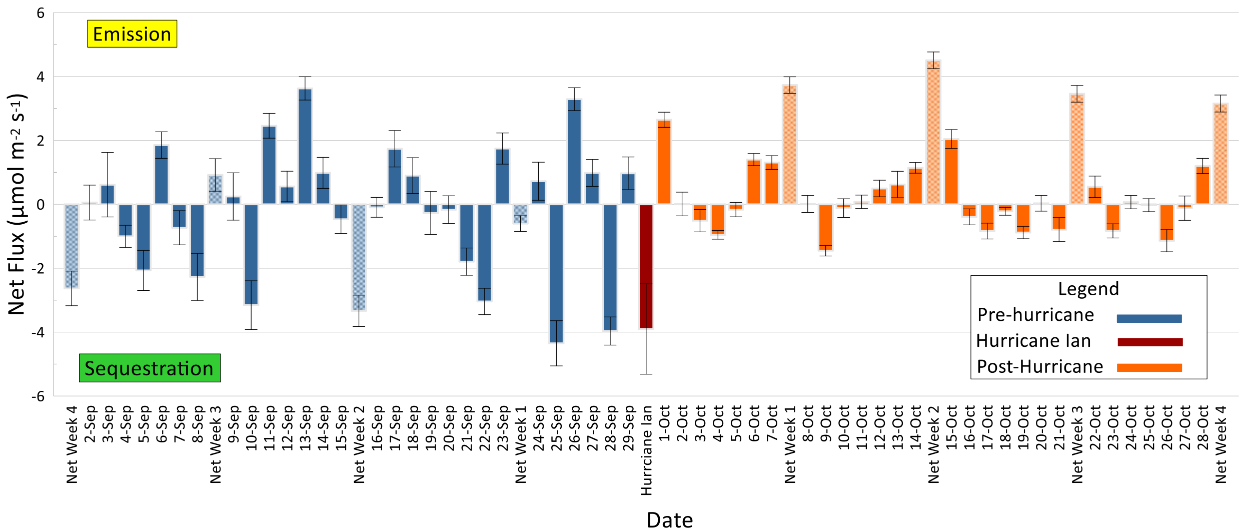

Figure 4.6. TWC1 24-hour net flux calculation for every day pre- (blue), during (maroon), and post-Hurricane Ian (orange) for up to 4 weeks. Negative values represent sequestration, and positive values represent emission. Net calculations for one, two, three, and four weeks are textured to display dominate emission or sequestration behavior at TWC1.

TWC1 - Pre-Hurricane Ian				
n measurements	Interval	Net CO_2 Flux ($\mu mol\ m^{-2}\ s^{-1}$)	Std. Dev. (σ) ($\mu mol\ m^{-2}\ s^{-1}$)	Sequestration / Emission
96	24 hr.	0.970	0.513	Emission
192	48 hr.	-2.996	0.477	Sequestration
288	72 hr.	-2.013	0.458	Sequestration
672	1 wk.	-0.603	0.488	Sequestration
1,344	2 wk.	-3.333	0.491	Sequestration
2,016	3 wk.	0.918	0.508	Emission
2,688	4 wk.	-2.632	0.542	Sequestration

TWC1 - Hurricane Ian				
n measurements	Interval	Net CO_2 Flux ($\mu mol\ m^{-2}\ s^{-1}$)	Std. Dev. (σ) ($\mu mol\ m^{-2}\ s^{-1}$)	Sequestration / Emission
96	24 hours	-3.902	1.41	Sequestration

TWC1 - Post-Hurricane Ian				
n measurements	Interval	Net CO_2 Flux ($\mu mol\ m^{-2}\ s^{-1}$)	Std. Dev. (σ) ($\mu mol\ m^{-2}\ s^{-1}$)	Sequestration / Emission
96	24 hr.	2.646	0.236	Emission
192	48 hr.	2.656	0.311	Emission
288	72 hr.	2.144	0.325	Emission
672	1 wk.	3.733	0.258	Emission
1,344	2 wk.	4.508	0.261	Emission
2,016	3 wk.	3.458	0.260	Emission
2,688	4 wk.	3.155	0.266	Emission

Table 4.1. Net Flux calculations for pre-, during, and post-Hurricane Ian at TWC1 (Detailed SPSS outputs are shown in Appendix C).

Kruskal Wallace Test Statistics for TWC1 CO_2 Concentrations						
Total *n* measurements	Interval (2022)	Time Series	KW H	df	Significance	Null Hypothesis
288	9/29-10/1	24 hr.	13.322	2	0.001	Reject
480	9/28-10/2	48 hr.	109.300	2	<0.001	Reject
672	9/27-10/3	72 hr.	237.419	2	<0.001	Reject
1440	9/23-10/7	1 wk.	723.453	2	<0.001	Reject
2784	9/16-10/14	2 wk.	1582.416	2	0.000	Reject
4218	9/9-10/21	3 wk.	1856.029	2	0.000	Reject
5472	9/2-10/28	4 wk.	2613.932	2	0.000	Reject

Kruskal Wallace Test Statistics for TWC1 Net Flux						
Total *n* measurements	Interval (2022)	Time series	KW H	df	Significance	Null hypothesis
288	9/29-10/1	24 hr.	0.672	2	0.672	Retain
480	9/28-10/2	48 hr.	3.960	2	0.138	Retain
672	9/27-10/3	72 hr.	1.085	2	0.581	Retain
1440	9/23-10/7	1 wk.	5.428	2	0.066	Retain
2784	9/16-10/14	2 wk.	4.169	2	0.124	Retain
4218	9/9-10/21	3 wk.	3.910	2	0.142	Retain
5472	9/2-10/28	4 wk.	4.256	2	0.119	Retain

Table 4.2. Kruskal-Wallis Test conducted via SPSS hypothesis states the distribution of flux and concentration are the same across the categories of pre-, during, and post-Hurricane Ian. The significance level was 0.05 (Detailed SPSS outputs are shown in Appendix C).

TWC2 Monitoring Station

The TWC2 monitoring station was overcome by the storm surge of Hurricane Ian entering the North Inlet system. Data was collected continuously for one month prior to Hurricane Ian and up to 09:45 EST on the day of Hurricane Ian's landfall. Similar to TWC1, the TWC2 monitoring station experienced varying net daily fluxes of sequestration and emission (Fig. 4.7– 4.9). Prior to Hurricane Ian, the net flux calculations for four weeks (9/2/22-9/29/22), three weeks (9/9/22-9/29/22), two weeks (9/16/22-9/29/22), one week (9/23/22-9/29/22), 72 hrs (9/27/22-9/27/22), 48 hrs (9/28/22-9/29/22), and 24 hrs (9/29/22) were dominantly characterized by sequestration. On the day of hurricane Ian (9/30/22), TWC2 experienced net emission of 0.030 µmol m^{-2} s^{-1} from 00:00 EST to 09:45 EST (Fig. 4.7– 4.9; Table 4.3). During the time series intervals, net sequestration varied, but was dominated by sequestration behavior (Table 4.4). As time approached the landfall of Hurricane Ian, the overall CO_2 concentrations within the well atmosphere decreased (Fig. 4.7– 4.9).

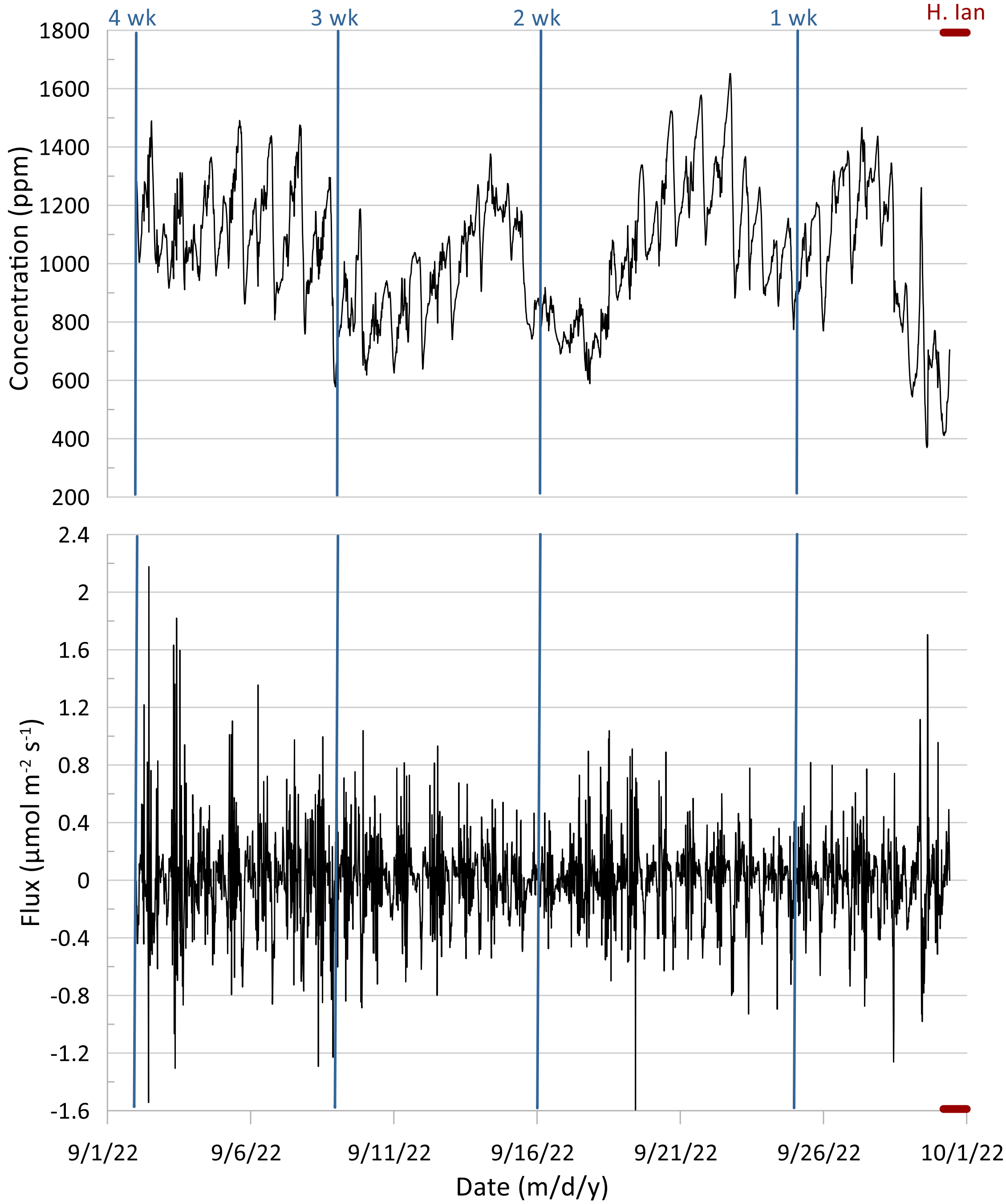

Figure 4.7. TWC2 weekly time series plot of well atmosphere CO2 concentration vs. time (top) and Flux calculation vs. time (bottom) for up to four weeks pre-Hurricane Ian. Blue lines indicate the pre-Hurricane Ian time series, maroon marker represents the Hurricane Ian time series.

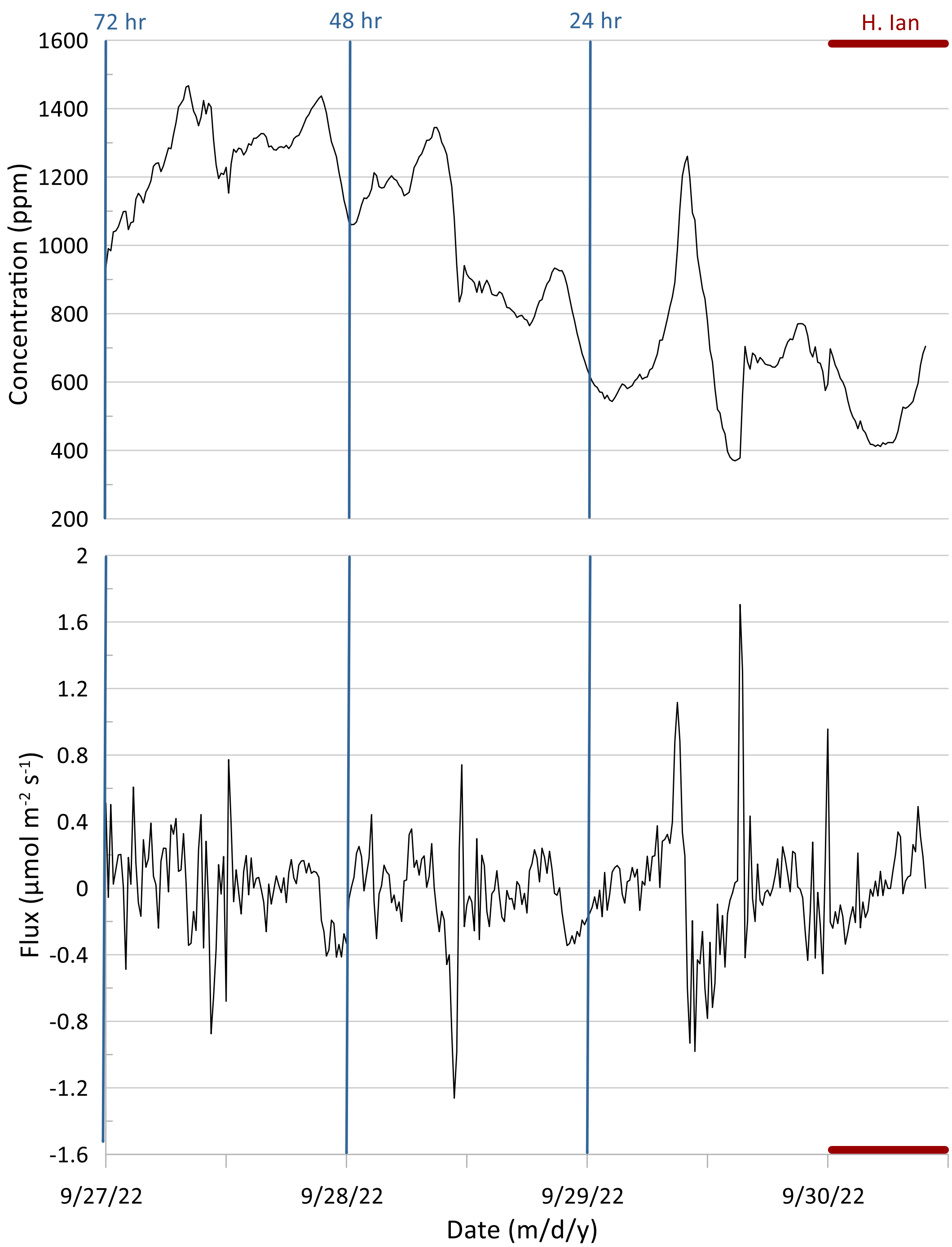

Figure 4.8. TWC2 hourly time series line plot of well atmosphere CO_2 concentration vs. time (top) and Flux calculation vs. time (bottom) for up to 72 hours pre-Hurricane Ian. Blue lines indicate the time series pre-Hurricane Ian, maroon marker represents the Hurricane Ian time series.

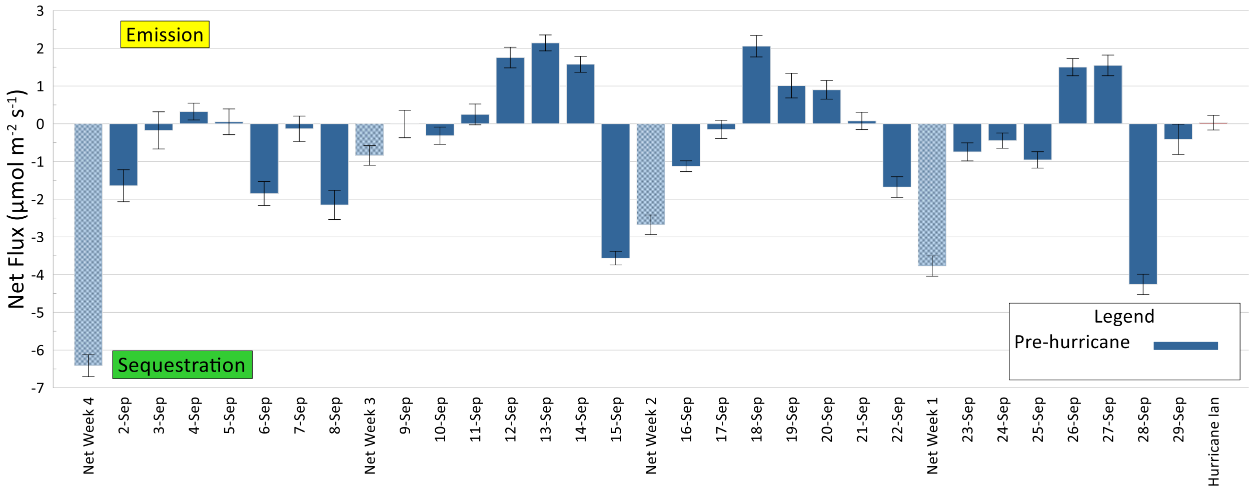

Figure 4.9. TWC2 24-hour net flux calculation for every day pre- (blue) and during (maroon) Hurricane Ian for up to four weeks. Negative values represent sequestration and positive values represent emission. Net calculations for one, two, three, and four weeks are textured to display dominate emission or sequestration behavior at TWC2.

TWC2 – Pre-Hurricane Ian				
n measurements	Interval	Net CO_2 Flux ($\mu mol\ m^{-2}\ s^{-1}$)	Std. Dev. (σ) ($\mu mol\ m^{-2}\ s^{-1}$)	Sequestration / Emission
96	24 hr.	-0.411	0.400	Sequestration
192	48 hr.	-4.670	0.342	Sequestration
288	72 hr.	-3.122	0.321	Sequestration
672	1 wk.	-3.027	0.268	Sequestration
1,344	2 wk.	-2.680	0.261	Sequestration
2,016	3 wk.	-0.840	0.259	Sequestration
2,688	4 wk.	-6.414	0.290	Sequestration

TWC2 – Hurricane Ian				
n measurements	Interval	Net CO_2 Flux ($\mu mol\ m^{-2}\ s^{-1}$)	Std. Dev. (σ) ($\mu mol\ m^{-2}\ s^{-1}$)	Sequestration / Emission
37	24 hours	0.030	0.195	Emission

Table 4.3. Net flux calculations for pre-, during, and post-Hurricane Ian at TWC2.

Net Flux during Hurricane Ian

The analysis of the net flux through variations in atmospheric pressure and water level assisted in identifying the immediate impact of hurricane energy on CO_2 flux throughout the extent of the disturbance. For both hurricane-induced atmospheric pressure and water level change, TWC1 experienced net emission (Fig. 4.10-4.13; Table 4.4). As the hurricane entered the North Inlet system, the atmospheric pressure decreased, water level increased, and net emission occurred. After the eye of the hurricane passed, the atmospheric pressure began to rise, water level dropped, and net sequestration occurred (Fig. 4.10-4.13).

The soil-gas well system included a backflow check valve to protect the NDIR analyzer against unusually high-water levels. At approximately 10:15 EST to 14:45 EST, water levels reached a height greater than 3 m on Clambank Creek (CBWQ; Fig. 4.1), which likely resulted in the closing of the backflow check valve (Fig. 4.11-4.12). TWC1 was located on No Man's Friend Creek which was characterized by higher topographic elevations than the Clambank Creek. From 11:45 EST to 14:00 EST, the TWC1 atmosphere was reading a near-constant CO_2 concertation within the well atmosphere (+/- 0.6 ppm).

Assuming water levels reached a height to close the backflow check valve in TWC1 on No Man's Friend Creek during this time, the CO_2 sensor was reading the same closed dynamic chamber system atmosphere from 11:45 EST to 14:00 EST. Net flux calculations were conducted for atmospheric pressure and water level change with both the complete dataset and closed valve assumption. Although the backflow check valve decreased the number of measurements conducted during Hurricane Ian, the difference in net flux calculation was only (<0.1 μmol m^{-2} s^{-1}) and the NDIR analyzer was protected to continually collect measurements as Hurricane Ian passed.

As atmospheric pressure decreased from 04:30 EST until the eye of the hurricane arrived at 13:45 EST on September 30, 2022, a net flux of 8.127 µmol m^{-2} s^{-1} was emitted. From 13:45 EST on September 30, 2022, to 02:15 EST on October 1, 2022, a net flux of 4.630 µmol m^{-2} s^{-1} of CO_2 was sequestered as atmospheric pressure increased. Throughout the complete pressure variation due to Hurricane Ian, a net flux of 3.497 µmol m^{-2} s^{-1} of CO_2 was emitted (Fig. 4.10-4.13; Table 4.4).

With rising water levels from 05:15 EST to 12:30 EST, a net flux of 8.222 µmol m^{-2} s^{-1} was emitted. As water levels decreased following the passing of the eye of Hurricane Ian, a net flux of 4.630 µmol m^{-2} s^{-1} was sequestered. Throughout this period of water level variation associated with Hurricane Ian, a net flux of 2.564 µmol m^{-2} s^{-1} was emitted (Fig. 4.10-4.13; Table 4.4).

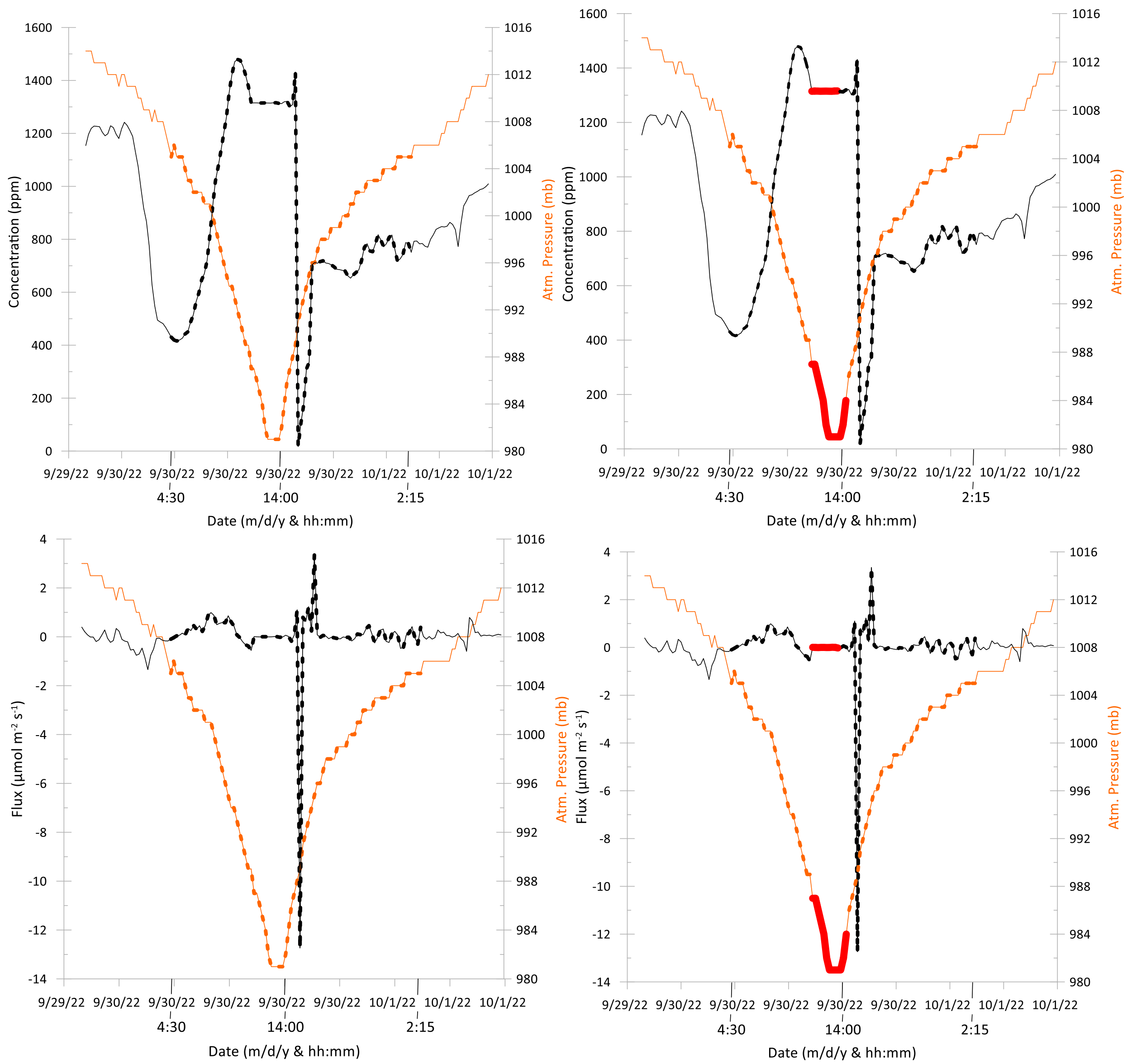

Figure 4.10. Hurricane Ian time series plots of CO_2 concentration vs. time (top) and CO_2 flux vs. time (bottom), over the course of Hurricane Ian landfall from 9/30/2022 to 10/1/2022. Black lines represent CO_2 concentration/flux. Orange lines represent atmospheric pressure. Unprocessed data (left) and closed valve considerations (right) are represented via the same time series. Dotted lines indicate data representing the direct influence of Hurricane Ian. Red lines indicate data not used in net flux calculations.

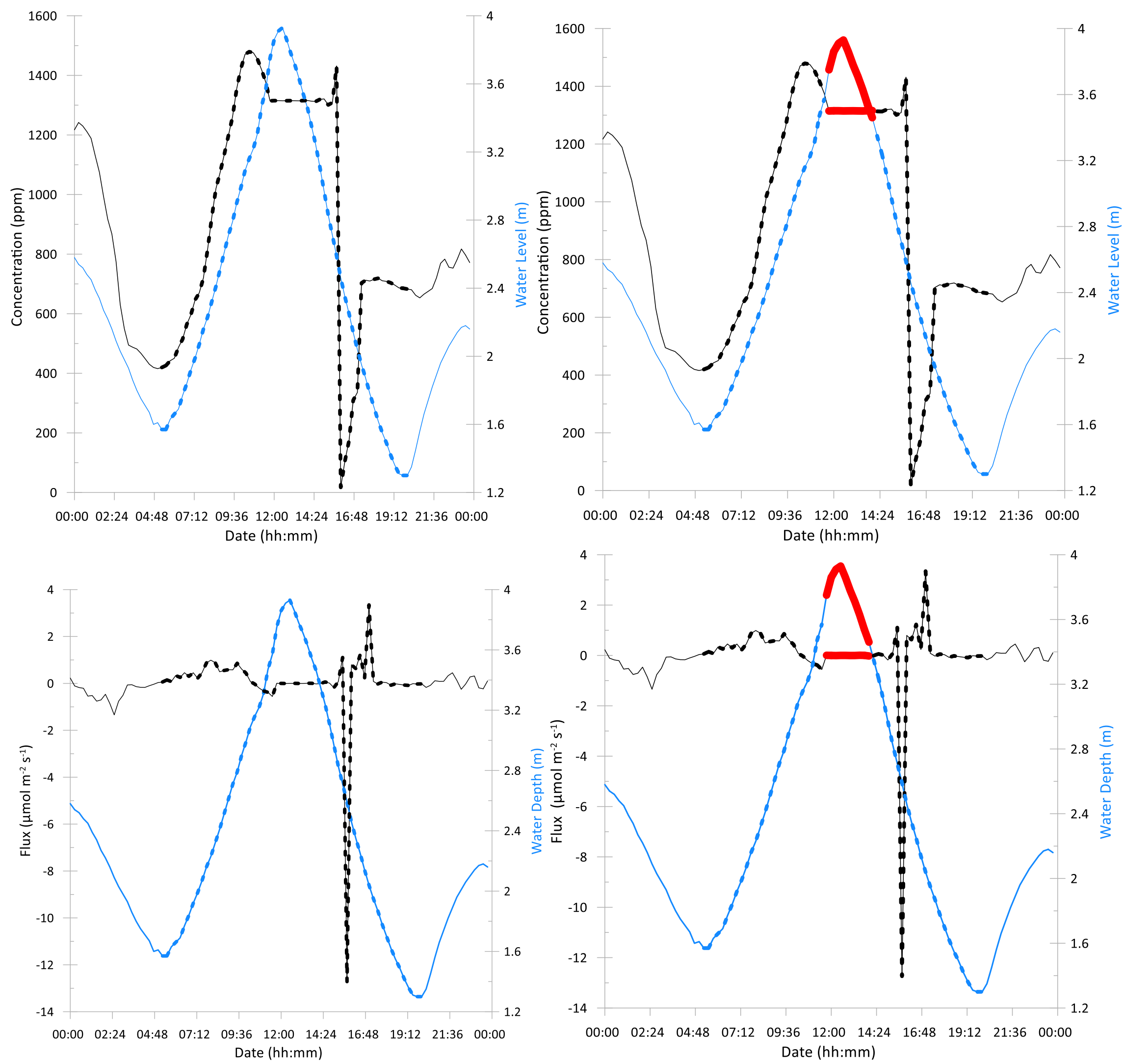

Figure 4.11. Hurricane Ian time series plots of CO_2 concentration vs. time (top) and CO_2 flux vs. time (bottom), over the course of Hurricane Ian landfall on 9/30/2022. Black lines represent CO_2 concentration/flux. Blue lines represent the water level. Unprocessed data (left) and closed valve considerations (right) are represented via the same time series. Dotted lines indicate data representing the direct influence of Hurricane Ian. Red lines indicate data not used in net flux calculations.

TWC1 – Hurricane Ian								
Date	*n*	Interval (EST)	Action	Net CO_2 Flux (µmol m-2 s-1)	Std. Dev. (σ) (µmol m^{-2} s^{-1})	Net CO_2 Flux (valve close) (µmol m-2 s-1)	Std. Dev. (σ) (µmol m^{-2} s^{-1})	Seq/ Emis.
9/30	37	04:30-13:45	Pressure falling	8.127	0.367	8.120	0.395	Emis.
9/30 - 10/1	51	13:45-2:15	Pressure rising	-4.630	1.890	-4.612	1.929	Seq.
9/30 - 10/1	88	04:30-2:15	Pressure Rise & Fall	3.497	1.460	3.508	1.552	Emis.
9/30	30	05:15-12:30	Water rising	8.222	0.389	8.219	0.402	Emis.
9/30	30	12:45-20:00	Water falling	-5.658	2.465	-5.644	2.766	Seq.
9/30	60	05:15-20:00	Water Rise & Fall	2.564	1.765	2.575	1.937	Emis.

Table 4.4. Net Flux calculations for pre-, during, and post-landfall of Hurricane Ian at TWC1. Sequestration = Seq. and Emission = Emis.

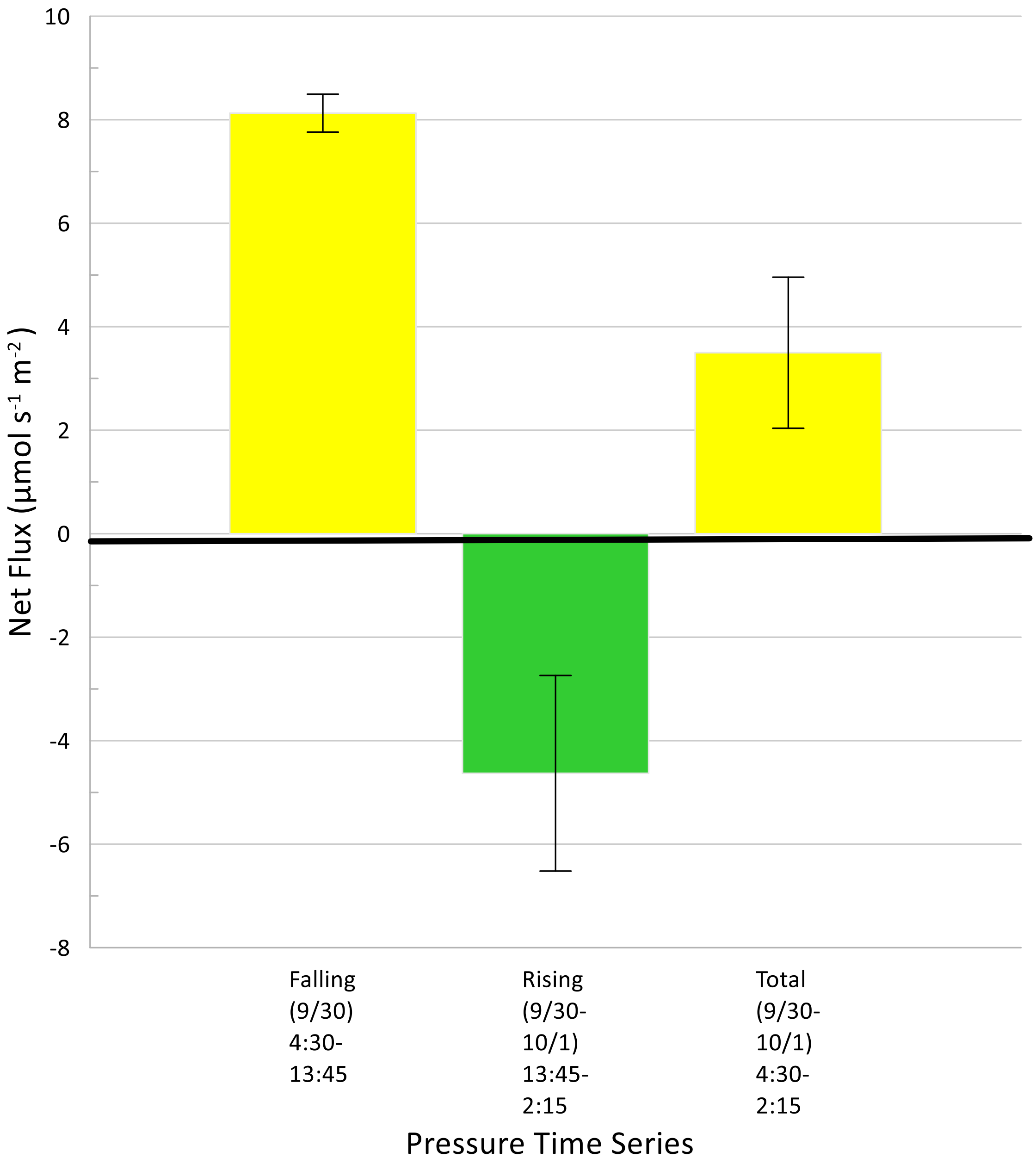

Figure 4.12. Net flux bar chart at falling atmospheric pressure, rising atmospheric pressure, and the total throughout the atmospheric pressure oscillation. Green bars indicate sequestration and yellow bars indicate emission. Error bars represent standard deviation of flux calculations.

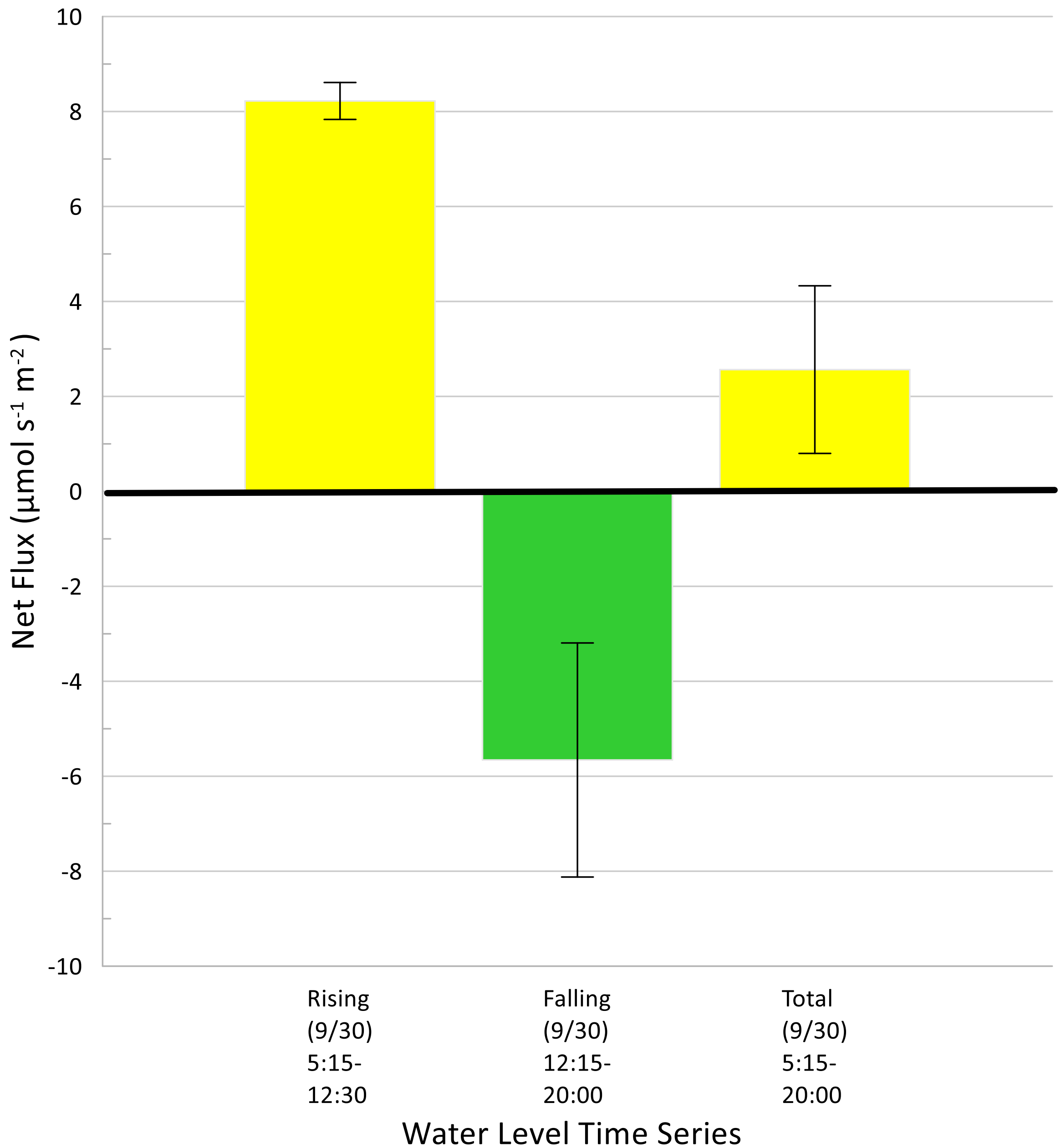

Figure 4.13. Net flux bar chart at rising water levels, falling water levels, and throughout the water level oscillation (total). Green bars indicate sequestration and yellow bars indicate emission. Error bars represent standard deviation of flux calculations.

Return to Net Flux Following Hurricane Ian Disruption

The pattern of change displayed by the net flux of CO_2 closely tracked the arrival of Hurricane Ian and resulted in net sequestration for September 30, 2022. The net flux calculation was used to identify the time in which the environment returned to a net sequestration following the Hurricane Ian disturbance. At the start of the hurricane, the NI-WB coastal systems started to experience a change in pressure below 1005 mbar at 04:30 EST on September 30, 2022. The water level began to rise in NI-WB at 05:15 EST on September 30, 2022. Net flux calculations were started at 04:30 EST and 05:15 EST on September 30, 2022. The net flux calculations were dominated by sequestration (negative flux value) following the passing of Hurricane Ian on the evening of September 30th (Fig. 4.14). However, after September 30, 2022, the net flux did not reach overall net CO_2 sequestration until 21:00 EST on December 12, 2022 (83 days later; Fig. 4.14). Within this time interval, equipment malfunction and maintenance produced an approximately two-week gap in data. Measurements within this time interval may have altered the quantification of the period of return to sequestration after Hurricane Ian; however, the time was determined with the best available data set.

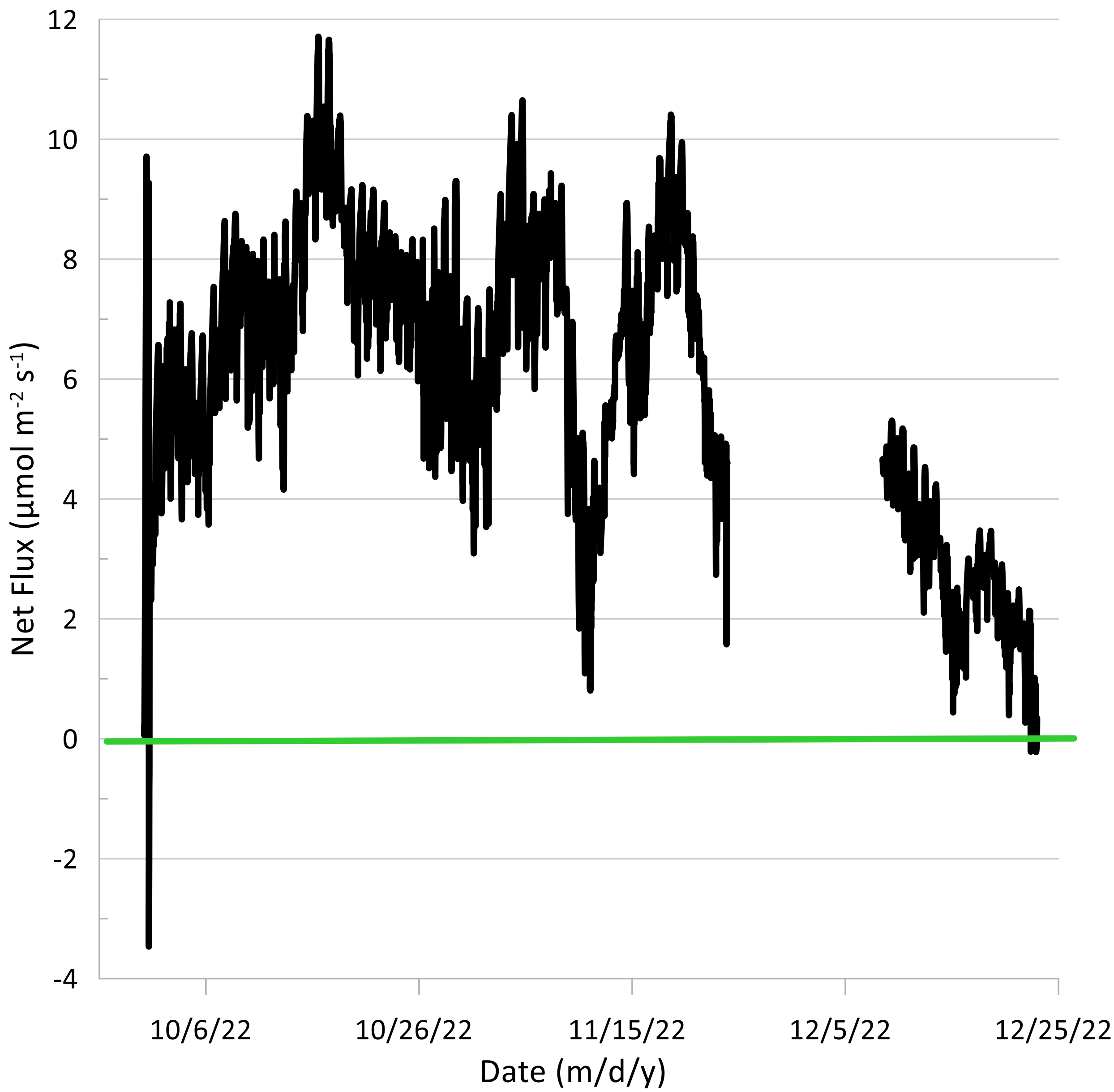

Figure 4.14. Time series plot from the initial start of Hurricane Ian determined by pressure decrease and return of the system to a net sequestration of CO2 (black line). Below green line represent sequestration. The net flux calculation from the initial water level increase due to Hurricane Ian and the return of the system to net sequestration of CO2 was imperceptible to the pressure plot above.

DISCUSSION

Net CO_2 Flux characteristic Pre-, During, and Post-Hurricane Ian

For a month prior to and on the day of Hurricane Ian's landfall, the NI-WB tidal wetland was (net) sequestering CO_2 concentrations. Following Hurricane Ian, the NI-WB system was (net) emitting CO_2. Therefore, within an eight-week period, the NI-WB tidal wetlands underwent a transition from net sequestering of atmospheric CO_2 concentrations to net emission following the high-energy hurricane disturbance.

The landfall of Hurricane Ian in September falls on the transition from summer to winter. A previous study has identified tidal wetlands to experience a decrease in CO_2 emissions during the late fall to winter season (Salimi et al., 2021). Likely, the NI-WB system typically experiences a decline in CO2 sequestration during late fall to winter as vegetation dies back (or undergoes senescence) with the change in season (Chapter 2); however, the Hurricane Ian disturbance in the 2022 hurricane season caused NI-WB to shift to net emission behavior immediately. Therefore, the natural timing of the Atlantic hurricane season, and potential hurricane landfall, may have alter seasonal CO_2 flux behavior. The specific altering of summer and fall seasons, which are known for high net sequestration behavior, will impact coastal carbon budgets (Salimi et al., 2021).

Immediate impacts of Hurricane Ian on CO_2 Flux

As hurricanes approach coastal systems, high-energy hydrodynamic processes (e.g., storm surge, flooding, erosion) are introduced to tidal wetlands (Plant & Stockdon, 2012). Tidal wetlands act as a natural barrier to high-energy storm systems and help to dissipate coastal flooding and erosion (Al-Attabi et al., 2023). As the high energy from Hurricane Ian was initially introduced to the NI-WB tidal wetlands (i.e., pressure decrease and water level rise), net emission of CO_2 occurred for an ~10-hour period. After the eye of Hurricane Ian passed the NI-WB tidal wetlands, net sequestration occurred for an ~10-hour period. Throughout varying atmospheric pressure and water level associated with Hurricane Ian (~20 hours), the tidal wetlands system experienced a net emission. Therefore, the disturbance of Hurricane Ian caused direct and immediate net emission of CO_2 flux in NI-WB. For future carbon cycling modeling and carbon budget projections, the consideration of hurricane activity should be accounted for, as Hurricane Ian altered NI-WB carbon flux behavior.

Lasting impacts on CO_2 behavior following Hurricane Ian

Variation in Net Flux

The NI-WB tidal wetlands experienced elevated CO_2 sequestration during the 24-hour period of Hurricane Ian's landfall and increased net sequestration occurred less than 12 hours after Hurricane Ian's initial landfall (Fig. 4.14). However, the net CO_2 flux calculations post-Hurricane Ian's landfall resulted in net emission until December 22, 2022. The net sequestration following Hurricane Ian may have been a result of atmospheric pressure increasing as the eye of Hurricane Ian moved inland, increasing CO_2 solubility to promote net sequestration. Additionally, a study conducted by Medeiros (2022) identified terrigenous dissolved organic carbon concentrations to increase in a tidal following a hurricane event. The increased availability of dissolved organic carbon following Hurricane Ian could have promoted net sequestration behavior. The extended period of emission following Hurricane Ian may have been provoked by a decrease in above and below ground biomass due to the high-energy disturbance of Hurricane Ian effecting biogenic activity (Mo et al., 2020). For future consideration of hurricane impact on wetlands' ability to store carbon during high energy events, management plans should focus on the long-term influence hurricanes have on wetland environments. NI-WB experienced dominant net emission in the long term (4 weeks), shortly after the disturbance (<12 hours), followed by extended emission.

Well atmosphere CO_2 Concentration Variation

The Kruskal – Wallis mean rank analysis of CO_2 flux was not statistically significant (Kruskal Wallis; $p > 0.05$; Table 4.2) for pre-, during, and post-Hurricane Ian; which may be a result of the complexity of flux calculation data which incorporates multiple variables (temperature, pressure, concentrations, etc.). The Kruskal – Wallis mean rank analysis of CO_2 concentrations within the well atmosphere for all periods pre-, during, and post-Hurricane Ian were statistically different (Kruskal Wallis; $p < 0.05$; Table 4.2); indicating an influence of Hurricane Ian on CO_2 concentrations within the well atmosphere. A Dunn-Bonferroni post hoc analysis further identified a statistical relationship between individual time periods pre-, during, and post-Hurricane Ian (Table 4.5). The pairwise comparison for well atmosphere CO_2 concentrations pre-hurricane Ian (24/48/72 hr), during (24 hr), and post- Hurricane Ian (24/48/72 hr) were all statistically different (significance <0.05), further indicating an immediate impact of Hurricane Ian energy to CO_2 exchange in the NI-WB tidal wetlands. The periods of pre- and post-hurricane Ian (24/48/72 hr) were compared with each other, as well as the 24-hour period during Hurricane Ian's landfall. The pairwise comparisons for CO_2 concentrations during and post-hurricane Ian (24/48/72 hr) were the only time intervals not significantly different from one another (significance >0.05). Ultimately, the well atmosphere CO_2 concentrations decreased during Hurricane Ian and did not recover to previous concentrations until at least three days after the high energy event.

Dunn-Bonferroni Post Hoc Method for Kruskal-Wallis Method					
Time series	Pairwise comparison	Test statistic	Standard error	Standard test statistic	Significance
24 hr	Pre- & During	43.115	12.021	3.587	<0.001
24 hr	During & Post-	-14.51	12.021	-1.207	0.227*
24 hr	Pre- & Post-	28.604	12.021	2.38	0.017
48 hr	Pre- & During	151.385	17.339	8.731	0.000
48 hr	During & Post-	-26.609	17.339	-1.535	0.125*
48 hr	Pre- & Post-	124.776	14.157	8.814	0.000
72 hr	Pre- & During	261.948	22.879	11.449	0.000
72 hr	During & Post-	-40.413	22.879	-1.766	0.077*
72 hr	Pre- & Post-	221.535	16.178	13.694	0.000

Table 4.5. Post hoc pairwise comparison of pre-, during, and post-Hurricane Ian periods. The asterisk (*) indicates not statistically significant values (SPSS output found in Appendix C).

CONCLUSION

Coastal systems face increasing threats due to the high energy associated with hurricane events under a changing climate (Mo et al., 2020). This study has demonstrated that hurricane events can disrupt carbon flux in tidal wetlands. Hurricane Ian promoted brief net CO_2 sequestration in NI-WB within the 24-hour period of landfall. The NI-WB tidal wetland then shifted to be predominantly net-emitting CO_2.

Hurricane Ian exerted a short-lived and unpredictable influence on carbon flux behavior within NI-WB. The landfall of Hurricane Ian produced a localized hotspot for alterations in CO_2 flux at the TWC1 monitoring station, providing a foundational insight to the understudied influence of carbon flux and storage in tidal wetlands. Further analysis of varying category hurricane grades may help predict the response of carbon cycling in tidal wetlands to low-frequency, high-magnitude disturbances. The direct landfall of a higher category hurricane may induce a higher influence of CO_2 emissions; however, the data collected for this study showed that a category one storm introduced enough energy to alter the CO_2 exchange relatively dramatically during landfall.

As hurricane intensity characteristics are altered with a changing climate, identifying the risk of coastal CO_2 flux becomes important for producing accurate tidal wetland blue carbon budgets. The decrease in sequestration of blue carbon or emission of stored CO_2 from tidal wetlands may contribute to increased atmospheric CO_2 concertation, influencing global warming. The further sampling of extreme events will aid in defining, balancing, and predicting hurricanes' impact on tidal wetlands' carbon budgets. Tidal wetlands already combat climate change with the threat of inundation from sea-level rise. Tidal wetlands must avoid degradation from rising sea-levels through increased accretion to continue to sequester and store atmospheric CO_2 (Najjar et al., 2018). The quantification of tidal wetlands' role in coastal CO_2 cycling during high-energy disturbances will support efforts to further protect these beneficial environments in a changing climate.

REFERENCES

Al-Attabi, Z., Xu, Y., Tso, G., & Narayan, S. (2023). The impacts of tidal wetland loss and coastal development on storm surge damages to people and property: A Hurricane Ike case-study. *Scientific Reports*, *13*(1), 4620. https://doi.org/10.1038/s41598-023-31409-x

Balaguru, K., Foltz, G. R., & Leung, L. R. (2018). Increasing magnitude of hurricane rapid intensification in the central and eastern Tropical Atlantic. *Geophysical Research Letters*, *45*(9), 4238–4247. https://doi.org/10.1029/2018GL077597

Bhatia, K. T., Vecchi, G. A., Knutson, T. R., Murakami, H., Kossin, J., Dixon, K. W., & Whitlock, C. E. (2019). Recent increases in tropical cyclone intensification rates. *Nature Communications*, *10*(1), 635. https://doi.org/10.1038/s41467-019-08471-z

Bucci, L., Alaka, L., Hagen, A., Delgado, S., & Beven, J., National Oceanic and Atmospheric Administration & National Weather Service. (2023) *Hurricane Ian (AL092022)*. National Hurricane Center Tropical Cyclone Report. https://www.nhc.noaa.gov/data/tcr/AL092022_Ian.pdf

Buzzelli, C., Akman, O., Buck, T., Koepfler, E., Morris, J., & Lewitus, A. (2004). Relationships among Water-Quality Parameters from the North Inlet–Winyah Bay National Estuarine Research Reserve, South Carolina. *Journal of Coastal Research*, *2009*(10045), 59–74. https://doi.org/10.2112/SI45-059.1

Callaway, J. C., Borgnis, E. L., Turner, R. E., & Milan, C. S. (2012). Carbon Sequestration and Sediment Accretion in San Francisco Bay Tidal Wetlands. *Estuaries and Coasts*, *35*(5), 1163–1181. https://doi.org/10.1007/s12237-012-9508-9

Camelo, J., & Mayo, T. (2021). The lasting impacts of the Saffir-Simpson Hurricane Wind Scale on storm surge risk communication: The need for multidisciplinary research in addressing a multidisciplinary challenge. *Weather and Climate Extremes*, *33*, 100335. https://doi.org/10.1016/j.wace.2021.100335

Dossa, G. G. O., Paudel, E., Wang, H., Cao, K., Schaefer, D., & Harrison, R. D. (2015). Correct calculation of CO_2 efflux using a closed-chamber linked to a non-dispersive infrared gas analyzer. *Methods in Ecology and Evolution*, *6*(12), 1435–1442. https://doi.org/10.1111/2041-210X.12451

Emanuel, K. (2020). Evidence that hurricanes are getting stronger. *Proceedings of the National Academy of Sciences*, *117*(24), 13194–13195. https://doi.org/10.1073/pnas.2007742117

Fairchild, T. P., Bennett, W. G., Smith, G., Day, B., Skov, M. W., Möller, I., Beaumont, N., Karunarathna, H., & Griffin, J. N. (2021). Coastal wetlands mitigate storm flooding and associated costs in estuaries. *Environmental Research Letters*, *16*(7), 074034. https://doi.org/10.1088/1748-9326/ac0c45

Familkhalili, R., Talke, S. A., & Jay, D. A. (2020). Tide-Storm surge interactions in highly altered estuaries: How channel deepening increases surge vulnerability. *Journal of Geophysical Research: Oceans*, *125*(4), e2019JC015286. https://doi.org/10.1029/2019JC015286

Gao, Y., Yu, G., Yang, T., Jia, Y., He, N., & Zhuang, J. (2016). New insight into global blue carbon estimation under human activity in land-sea interaction area: A case study of China. *Earth-Science Reviews*, *159,* 36–46. https://doi.org/10.1016/j.earscirev.2016.05.003

Gardner, L. R., Kjerfve, B., & Petrecca, D. M. (2006). Tidal fluxes of dissolved oxygen at the North Inlet-Winyah Bay National Estuarine Research Reserve. *Estuarine, Coastal and Shelf Science*, *67*(3), 450–460. https://doi.org/10.1016/j.ecss.2005.12.002

Gori, A., Lin, N., & Smith, J. (2020). Assessing compound flooding from landfalling tropical cyclones on the North Carolina coast. *Water Resources Research*, *56*(4), e2019WR026788. https://doi.org/10.1029/2019WR026788

Gori, A., Lin, N., Xi, D., & Emanuel, K. (2022). Tropical cyclone climatology change greatly exacerbates US extreme rainfall–surge hazard. *Nature Climate Change*, *12*(2), 171–178. https://doi.org/10.1038/s41558-021-01272-7

Hall, T. M., & Kossin, J. P. (2019). Hurricane stalling along the North American coast and implications for rainfall. *Npj Climate and Atmospheric Science*, *2*(1), 17. https://doi.org/10.1038/s41612-019-0074-8

Hu, K., Chen, Q., & Wang, H. (2015). A numerical study of vegetation impact on reducing storm surge by wetlands in a semi-enclosed estuary. *Coastal Engineering*, *95*, 66–76. https://doi.org/10.1016/j.coastaleng.2014.09.008

Intergovernmental panel on Climate Change (IPCC). (2021). Climate change 2021: The physical science basis. Contribution of Working Group I to the Sixth Assessment Report of the Intergovernmental Panel on Climate Change [Masson Delmotte, V., P. Zhai, A. Pirani, S.L. Connors, C. Péan, S. Berger, N. Caud, Y. Chen, L. Goldfarb, M.I. Gomis, M. Huang, K. Leitzell, E. Lonnoy, J.B.R. Matthews, T.K. Maycock, T. Waterfield, O. Yelekçi, R. Yu, and B. Zhou (eds.)]. Cambridge University Press, Cambridge, United Kingdom and New York, NY, USA, 2391 pp. doi:10.1017/9781009157896.

Kossin, J. P. (2018). A global slowdown of tropical-cyclone translation speed. *Nature*, *558*(7708), 104–107. https://doi.org/10.1038/s41586-018-0158-3

Kruskal, W. H., & Wallis, W. A. (1952). Use of ranks in one-criterion variance analysis. *Journal of the American Statistical Association*, *47*(260), 583–621. JSTOR. https://doi.org/10.2307/2280779

Li, H., Wang, C., Yu, Q., & Smith, E. (2022). Spatiotemporal assessment of potential drivers of salt marsh dieback in the North Inlet-Winyah Bay estuary, South Carolina (1990–2019). *Journal of Environmental Management*, *313*, 114907. https://doi.org/10.1016/j.jenvman.2022.114907

Lovelock, C. E., Atwood, T., Baldock, J., Duarte, C. M., Hickey, S., Lavery, P. S., Masque, P., Macreadie, P. I., Ricart, A. M., Serrano, O., & Steven, A. (2017). Assessing the risk of carbon dioxide emissions from blue carbon ecosystems. *Frontiers in Ecology and the Environment*, *15*(5), 257–265. https://doi.org/10.1002/fee.1491

Medeiros, P. M. (2022). The effects of hurricanes and storms on the composition of dissolved Organic Matter in a Southeastern U.S. Estuary. *Frontiers in Marine Science*, *9*. https://doi.org/10.3389/fmars.2022.855720

Mo, Y., Kearney, M. S., & Turner, R. E. (2020). The resilience of coastal marshes to hurricanes: The potential impact of excess nutrients. *Environment International*, *138*, 105409. https://doi.org/10.1016/j.envint.2019.105409

National Estuarine Research Reserve System (NOAA NERRS). (2012). *System-wide Monitoring Program*. Data accessed from the NOAA NERRS Centralized Data Management Office. http://www.nerrsdata.org

National Oceanic and Atmospheric Administration (NOAA), National Ocean Service (NOS), Belle W. Baruch Institute of the University of South Carolina, South Carolina Coastal Council. (1992). *Final Management plan, North Inlet/Winyah Bay National Estuarine*

Research Reserve. National Ocean Service. https://repository.library.noaa.gov/view/noaa/2461.

National Oceanic and Atmospheric Administration (NOAA). (2022). *Tides & Currents: Datums for 8662299, Clambank Cree Dock, Goat Island, SC*. NOAA. https://tidesandcurrents.noaa.gov/datums.html?id=8662299

National Oceanic and Atmospheric Administration & National Hurricane Center. (2022) *Tropical cyclone best track for Hurricane Ian 2022* [Data set]. https://services2.arcgis.com/C8EMgrsFcRFL6LrL/arcgis/rest/services/Hurricane_Ian_Track/FeatureServer.

North Inlet – Winyah Bay National Estuarine Research Reserve (NI-WB NERR). (2016). *Management Plan. North Inlet – Winyah Bay National Estuarine Research Reserve*. https://northinlet.sc.edu/

Najjar, R. G., Herrmann, M., Alexander, R., Boyer, E. W., Burdige, D. J., Butman, D., Cai, W.-J., Canuel, E. A., Chen, R. F., Friedrichs, M. A. M., Feagin, R. A., Griffith, P. C., Hinson, A. L., Holmquist, J. R., Hu, X., Kemp, W. M., Kroeger, K. D., Mannino, A., McCallister, S. L., … Zimmerman, R. C. (2018). Carbon budget of tidal wetlands, estuaries, and shelf waters of eastern North America. *Global Biogeochemical Cycles*, *32*(3), 389–416. https://doi.org/10.1002/2017GB005790

Ouyang, X., & Lee, S. Y. (2020). Improved estimates on global carbon stock and carbon pools in tidal wetlands. *Nature Communications*, *11*(1), 317. https://doi.org/10.1038/s41467-019-14120-2

Patchineelam, S. M., & Kjerfve, B. (2004). Suspended sediment variability on seasonal and tidal time scales in the Winyah Bay estuary, South Carolina, USA. *Estuarine, Coastal and Shelf Science*, *59*(2), 307–318. https://doi.org/10.1016/j.ecss.2003.09.011

Patchineelam, S. M., Kjerfve, B., & Gardner, L. R. (1999). A preliminary sediment budget for the Winyah Bay estuary, South Carolina, USA. *Marine Geology*, *162*(1), 133–144. https://doi.org/10.1016/S0025-3227(99)00059-6

Peduzzi, P., Chatenoux, B., Dao, H., De Bono, A., Herold, C., Kossin, J., Mouton, F., & Nordbeck, O. (2012). Global trends in tropical cyclone risk. *Nature Climate Change*, *2*(4), 289–294. https://doi.org/10.1038/nclimate1410

Plant, N. G., & Stockdon, H. F. (2012). Probabilistic prediction of barrier-island response to hurricanes. *Journal of Geophysical Research: Earth Surface*, *117*(F3). https://doi.org/10.1029/2011JF002326

Salimi, S., Almuktar, S. A. A. A. N., & Scholz, M. (2021). Impact of climate change on wetland ecosystems: A critical review of experimental wetlands. *Journal of Environmental Management*, *286*, 112160. https://doi.org/10.1016/j.jenvman.2021.112160

Shultz, J. M., Shepherd, J. M., Bagrodia, R., & Espinel, Z. (2014). Tropical cyclones in a year of rising global temperatures and a strengthening El Niño. *Disaster Health*, *2*(3–4), 151–162. https://doi.org/10.1080/21665044.2014.1111722

Sun, F., & Carson, R. T. (2020). Coastal wetlands reduce property damage during tropical cyclones. *Proceedings of the National Academy of Sciences*, *117*(11), 5719–5725. https://doi.org/10.1073/pnas.1915169117

Villa, J. A., & Bernal, B. (2018). Carbon sequestration in wetlands, from science to practice: An overview of the biogeochemical process, measurement methods, and policy framework. *Ecological Engineering*, *114*, 115–128. https://doi.org/10.1016/j.ecoleng.2017.06.037

Wahl, T., Jain, S., Bender, J., Meyers, S. D., & Luther, M. E. (2015). Increasing risk of compound flooding from storm surge and rainfall for major US cities. *Nature Climate Change*, *5*(12), 1093–1097. https://doi.org/10.1038/nclimate2736

Wang, F., Lu, X., Sanders, C. J., & Tang, J. (2019). Tidal wetland resilience to sea level rise increases their carbon sequestration capacity in United States. *Nature Communications*, *10*(1), 5434. https://doi.org/10.1038/s41467-019-13294-z

Ward, N. D., Bianchi, T. S., Medeiros, P. M., Seidel, M., Richey, J. E., Keil, R. G., & Sawakuchi, H. O. (2017). Where carbon goes when water flows: Carbon cycling across the aquatic continuum. *Frontiers in Marine Science*, *4*, 7. https://doi.org/10.3389/fmars.2017.00007

Windham-Myers, L., Cai, W.-J., Alin, S., Andersson, A., Crosswell, J., Dunton, K. H., Hernandez-Ayon, J. M., Herrmann, M., Hinson, A. L., Hopkinson, C. S., Howard, J., Hu, X., Knox, S. H., Kroeger, K., Lagomasino, D., Megonigal, P., Najjar, R., Paulsen, M.-L., Peteet, D., … Zhu, Z. (2018). *Chapter 15: Tidal wetlands and estuaries. Second state of the carbon cycle report*. U.S. Global Change Research Program. https://doi.org/10.7930/SOCCR2.2018.Ch15

CHAPTER FIVE

CARBON STORAGE AND HIGH-ENERGY EVENTS IN NORTH INLET-WINYAH BAY, SOUTH CAROLINA: A COMPLEX HISTORICAL RELATIONSHIP

ABSTRACT

The objective of this study was to determine the spatial distribution of carbon storage in a tidal wetland of SC through elemental and isotopic analysis of sediment cores. The study also aimed to identify high-energy events influence on historical carbon storage using elemental analysis and paleotempestological methods of grain size analysis. The spatial distribution of stored carbon in the North Inlet-Winyah Bay (NI-WB) of estuarine system of SC was found to be heterogenous. Within NI-WB, the No Man's Friend Creek sampling location contained a total of 25.74 g of carbon within the upper 100 cm and a carbon accumulation rate of 120.60 gC m^{-2} yr^{-1}. Town Creek stored 13.55 g of carbon in the upper 100 cm of sediment and experienced a carbon accumulation rate of 15.21 gC m^{-2} yr^{-1}. The spatial variation in stored carbon may be due to differing hydraulic flows and watershed inputs in the NI-WB system. In their respected sediment cores, No Man's Friend Creek and Town Creek were also found to possess correlated variations in sediment grain size and percent carbon, indicating the potential for high-energy hydraulic flows to impact carbon storage.

INTRODUCTION

The objective of this study was to determine spatial carbon storage capacity in the North Inlet-Winyah Bay (NI-WB) tidal wetlands of SC and apply paleotempestology methods to identify potential influence of high-energy events on preserved carbon concentrations. The determination of spatial heterogeneity in historical carbon accumulation identified the importance of expanding sediment core collection in wetland systems to determine carbon stock allotments. A historical record of natural variation in stored carbon concentrations associated with high-energy hydraulic flows could provide valuable insights into the interaction of future high-energy events and coastal carbon cycling.

Tidal wetland systems are characterized as low-lying coastal basin with fine-grained permeable sediments and rich vegetation which serve as a natural sponge for coastal flood waters (Duarte et al., 2013; Gedan et al., 2011; Reents et al., 2021; Sun & Carson, 2020; Van Coppenolle & Temmerman, 2019). The high-energy flood disturbances are vital processes to the geomorphic structure of tidal wetlands by promoting sediment accretion (Thorne et al., 2022). The flood-induced high-energy hydraulic conditions increase riverine carrying capacity and discharges to tidal wetlands, depositing allochthonous sediment which assists in tidal wetland accretion (Thorne et al., 2022; Voulgaris & Meyers, 2004). Corresponding to the transport of allochthonous sediment to tidal wetlands, high-energy hydraulic flows also promote the mobilization of allochthonous organic material into tidal wetland basins for deposition. The mobilized terrestrial carbon is transported from headwaters to the wetland basin in periodic pulses from high-energy induced hydraulic flows, and is commonly described as the Pulse Shunt Concept (Raymond et al., 2016; Ward et al., 2017). Therefore, high-energy disturbances have the potential to alter sediment deposition and carbon storage in tidal wetlands.

Tropical cyclones, commonly known as hurricanes in the Atlantic Basin, are large high-energy disturbances which profoundly impact coastal water levels due to storm surge and excess precipitation (Chuang et al., 2019; Marsooli et al., 2019; Morton & Barras, 2011; Patrick et al., 2020). Tidal wetlands serve as the first line of defense against hurricanes by attenuating the storm-induced flood waters (Al-Attabi et al., 2023; Fairchild et al., 2021; Highfield et al., 2018). The occurrence of hurricane events presents the potential for periodic elevated transport of allochthonous coarse grained sediment and carbon to tidal wetland basins for deposition.

The high-energy storm surge from hurricanes transport and deposit coarse-grained allochthonous sediment into tidal wetlands (Fig. 5.1; Bregy et al., 2018; Castagno, et al., 2021; Hawkes & Horton, 2012; Morton & Barras, 2011; Scott et al., 2003). Hurricanes induce an increase in precipitation rates, which increases overland flow and promotes the transportation of coarse-grained terrestrial material to be deposited in tidal wetlands (Fig. 5.1; Fuller et al., 2018; Hawkes & Horton, 2012; Zhu et al., 2020). Following the high-energy storm surge or precipitation event, conventional sedimentation may bury the coarse-grained deposits, preserving the influence of the high-energy event stratigraphically within the wetland sediment record (Castagno et al., 2021).

Additionally, the hydraulic flows of hurricanes (i.e., storm surge and precipitation-induced flooding) contribute to the mobilization of stored carbon in coastal watersheds (Fig. 5.1; Letourneau & Medeiros, 2019; Medeiros, 2022; Yan et al., 2017). Recent studies reported extreme events could represent between 20 to 70 percent (%) of the annual flux of organic carbon to tidal wetlands (Medeiros, 2022; Osburn et al., 2019; Yan et al., 2020). Therefore, hurricane events have the potential to disrupt known coastal carbon cycling and promote carbon storage in tidal wetlands (Windham-Myers et al., 2018).

Paleotempestology is the study of historical storms which use geological proxies to reconstruct high-energy activity within the sediment record (Walsh et al., 2016). Paleotempestology methods identify the preservation of coarse sediment deposits in fine-grained dominated environments. The presence of coarse grained deposits in tidal wetlands sediment cores indicates increased hydraulic flows to allow the mobilization of coarse-grained material in the

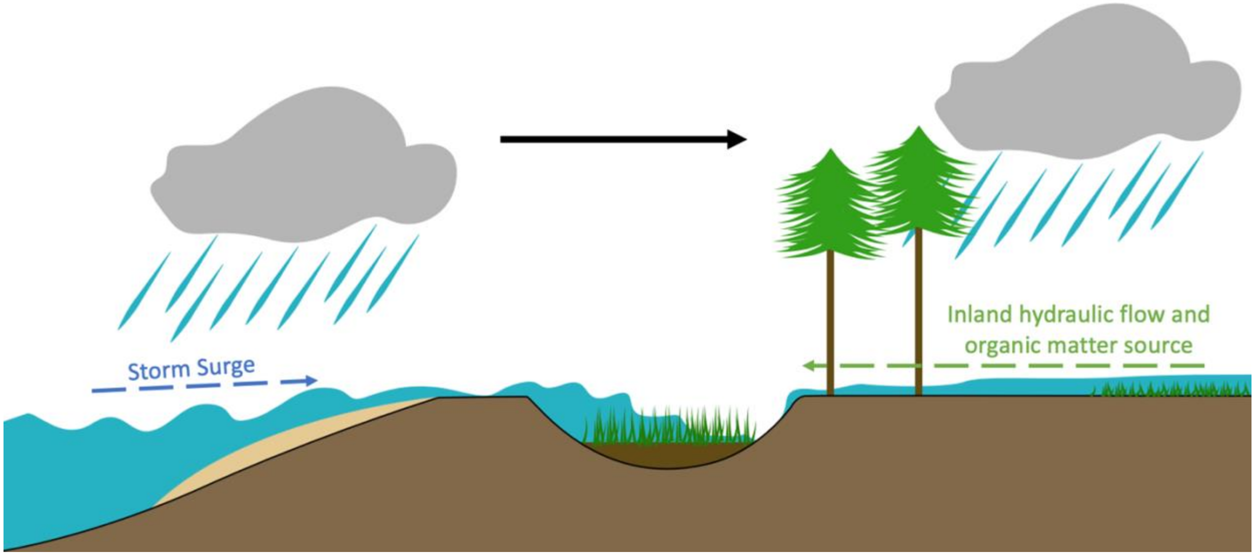

Figure 5.1. Conceptual diagram of storm surge and inland hydraulic transport of allochthonous sediment and organic matter input to tidal wetlands due to storm activity. Adapted from Bregy et al., 2018; Wallace et al., 2014.

fine-grain dominated environments (Bregy et al., 2018; Dietz et al., 2021; Fuller et al., 2018). The concurrent identification of increased stored carbon with coarse grained deposits may link historical alteration to carbon storage due to increased hydraulic flows.

Hurricane-induced storm surge and precipitation dominate the upper tail distribution (>50-year return period) for flooding events and are the main contributors to coastal flood loss on the Atlantic Coast (Gori et al., 2022; Wahl et al., 2015). Additionally, the Intergovernmental Panel on Climate Change (IPCC) projects proliferation in local and coastal flooding due to an increase in (1) normal precipitation intensity and frequency, (2) peak hurricane precipitation rates, and (3) storm surge (IPCC, 2021; Seneviratne, 2021). As climate change continues to amplify precipitation rates and hurricane intensity, the identification of how carbon storage was historically altered in tidal wetlands due to high-energy hydraulic flows will assist in determining the environments' role in future coastal carbon cycle. This chapter was prepared for submission to the journal *Geology*.

METHODS

Study Site

Two sediment cores were collected in the NI-WB estuarine tidal wetland (Fig. 5.2). The NI-WB estuarine environment was a designated National Oceanic and Atmospheric Administration (NOAA) National Estuarine Research Reserve (NERR). The NI-WB NERR encompasses ~77 square kilometers (km^2) of pristine estuarine tidal wetlands with high water quality and little anthropogenic development (Li et al., 2022). The North Inlet and Winyah Bay estuarine systems are made up of two differing environments. The North Inlet estuary was oceanic-dominated, with a watershed of ~96 km^2 which receives a majority of its freshwater input from the surrounding watershed and precipitation events (NI-WB NERRS, 2016). In contrast, the Winyah

Bay estuarine system was riverine-influenced and comprises ~47,000 km^2 of watershed, making it the third largest watershed on the East Coast of the United States (NI-WB NERRS, 2016). The Winyah Bay system receives freshwater inputs from 4 major rivers: the Pee Dee, Waccamaw, Black, and Swampit Rivers (NOAA, 1992). Both estuarine systems experience semi-diurnal tidal patterns.

The NI-WB tidal wetlands are geologically located in the coastal plain of SC, which is principally described as Tertiary and Quaternary sediment deposited in the marine shelf setting (Patchineelam et al., 1999) . The North Inlet marsh basin was bounded by modern barrier islands to the east and regressive relict beach ridges to the west (Gardner & Porter, 2001). The relict beach ridges were developed ~147,000 to 86,000 years before present (BP; Patchineelam et al., 1999). Approximately 4000 years B.P., during the late Holocene sea level rise, relict beach ridges were flooded, eroded, and buried by fine-grained deposition to make up the current marsh conditions of North Inlet (Patchineelam et al., 1999). Therefore, the North Inlet basin was dominated with Holocene aged sediment (Gardner & Porter, 2001).

Sediment cores were collected in two locations in North Inlet, Town Creek (TownC) and No Man's Friend Creek (NMFC; Fig. 5.2). Town Creek was dominated by oceanic influence due to its proximity to North Inlet and experienced tidally-dominated hydraulic circulation. No Man's Friend Creek was located at the convergence of North Inlet and Winyah Bay, at a location known as Mud Bay. The Winyah Bay system experiences unidirectional riverine flow superimposed by a tidally-influenced current. The two sampling locations represent differing environmental conditions and hydraulic influence within the NI-WB estuarine tidal wetland system.

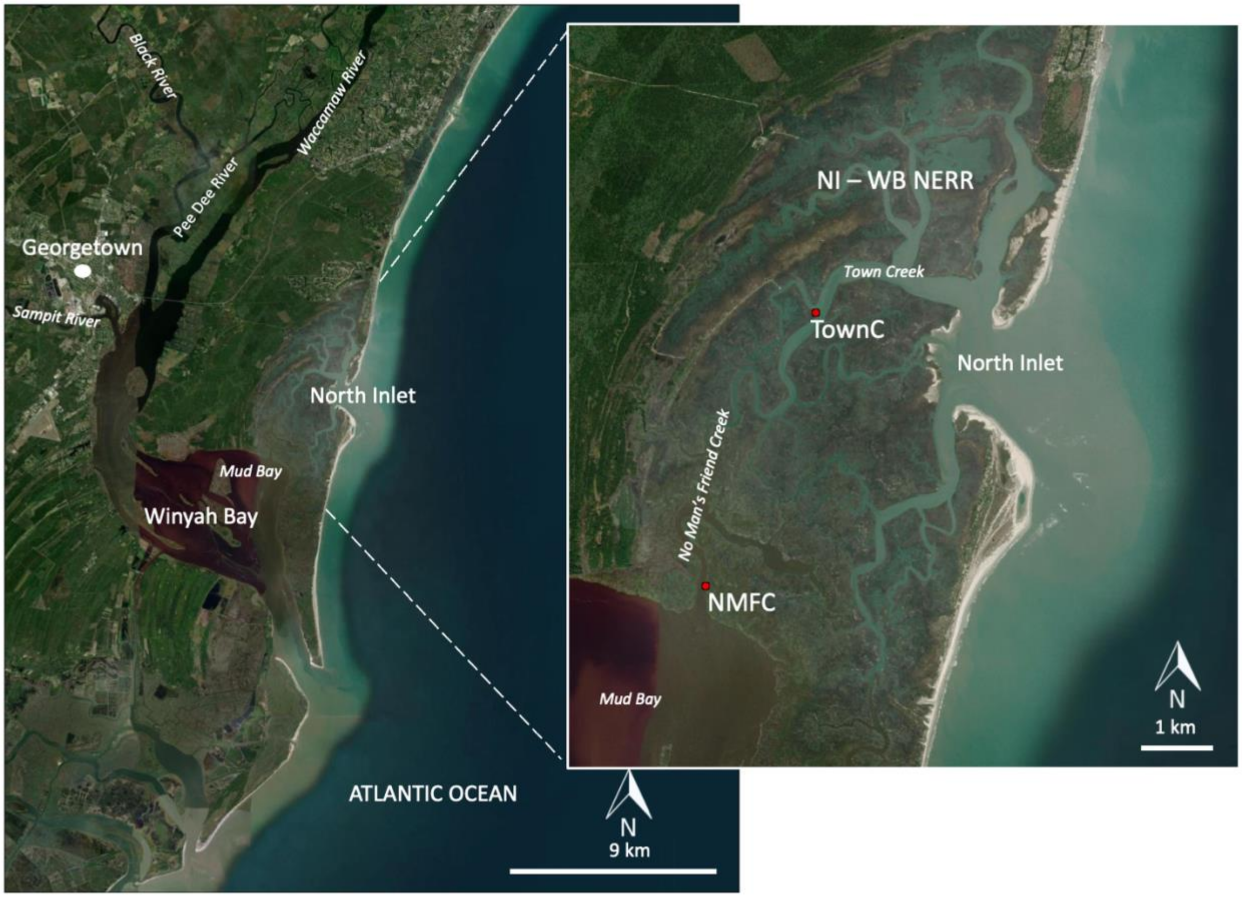

Figure 5.2. The study site of North Inlet-Winyah Bay National Estuarine Research Reserve near Georgetown, South Carolina. Red circles represent locations of sediment core collections near No Man's Friend Creek (NMFC) and Town Creek (TownC).

Sediment Core Field Collection

Two sediment cores were collected in NI-WB. The location of Town Creek (UTM: 17N 668617 3689504) was selected for sediment core collection to identify carbon storage in a location dominated by oceanic influence. The location of No Man's Friend Creek (UTM: 17N 670239 3687263) was selected for sediment core collection to identify carbon storage in a location dominated by riverine influence. The sediment cores were collected in Town Creek and No Man's Friend Creek with a Russian peat borer at the location used to deploy CO_2 Flux monitoring station (further explained in Chapter 1). The Russian peat borer collects 50-centimeter (cm) long cores with minimal compaction to sediment (Smeaton et al., 2020). Two core pushes were conducted in the same borehole to reach a total depth of approximately 100 cm (1 m). Duplicate cores were collected at the same location to have sufficient sample mass for laboratory analysis. The intact sediment cores were transported back to the laboratory (Clemson University – Clemson, SC) within a protective sheath.

Laboratory Analysis

Core Sectioning

The intact cores were imaged radiographically to conduct a density analysis. Then, the sediment cores were sectioned every two centimeters through the whole 100 cm core. The sectioned sediment intervals were weighed, dried at 85 °C for 72 hours, and weighed again to determine a dry sediment weight and bulk density. One of the duplicate cores was sectioned for total elemental carbon concentration and grain size analysis. The other duplicate core was used for isotopic analysis. The analytical methods to determine carbon concentration, grain size, isotopic age dates, and radiographically derived densities are described below.

Carbon Concentration

The total elemental carbon concentration of the tidal wetland sediment was determined using a CHNS (carbon, hydrogen, nitrogen, sulfur) Elemental Analyzer (ThermoScientific FlashSmart). The dried sediment samples were powdered by mortar and pestle to create a homogenous sample. Approximately 0.7-1.5 micrograms of sediment were placed within a tin capsule and ignited at 950 °C to determine CO_2 concentrations during CHNS analysis. Before operation, the CHNS analyzer sufficiently performed a hot and cold gas leak test. A calibration curve (K-Factor 203433) for the instrument was determined using four standard samples of 2,5-bis(5-tert-butyl-benzoxazol-2-yl)thiophene BBOT ($C_{26}H_{26}N_2O_2S$; 72.540 % Carbon; purchased from ThermoScientific). A BBOT check standard was processed every ten samples to determine a percent error ($\frac{|observed-expected|}{expected} \times 100$) between the known percent carbon in BBOT and percent carbon output of the Elemental Analyzer. Triplicate samples were processed every ten samples during analysis to determine relative standard deviation ($\frac{|population\ standard\ devaition|}{population\ mean} \times 100$) between triplicate percent carbon results. The CHNS analysis assumes the samples were representative of the complete core section and underwent complete combustion during ignition within the CHNS analyzer's quartz chamber. Since the dry sediment mass for each core interval was known, the percent carbon was applied to the total mass of the sediment interval to determine the distribution of stored carbon downcore.

Particle Size Analysis

The particle size analysis was conducted using a Beckman Coulter LS13-320 Laser Diffraction Particle Size Analyzer. Prior to analysis, sediment samples were treated with 6% sodium hexametaphosphate solution [$Na(PO_3)_6$] to ensure the deflocculation of material.

Additionally, the samples were sonicated for 10 minutes before analysis for further disaggregation, ensuring deflocculated material was measured (Fuller et al., 2018). All samples were processed under an obscuration level of 9-12% within the particle size analyzer.

The particle size analyzer determined the distribution of grain size for each sample. The grain size distribution was sorted into statistical bins based on the percentile of the particle's diameters within the sample: D_{10} (<10%), D_{25} (<25%), D_{50} (<50%), D_{75} (<75%), and D_{90} (<90%). This study aimed to identify coarse-grained deposits; therefore, the D_{90} value was used as it represents the maximum grain size transported due to high-energy flows (Bregy et al., 2018). The D_{90} value was compared between 2-cm intervals for the complete core 100 cm core. A duplicate sample was processed every five samples during analysis. Duplicate samples were processed every 5 samples for relative percent difference ($\frac{|sample-duplicate|}{\frac{sample+duplicate}{2}} \times 100$). The laser particle size analyzer method pertained the assumption that the analyzed material was representative of the whole 2-cm interval section.

Isotopic Analysis

The sediment age was determined by detecting lead-210 (^{210}Pb) activity within the 2-cm intervals of the sediment core. Lead-210 is a naturally occurring radionuclide with a 22.3-year half-life and is a daughter product of the uranium-238 (^{238}U) decay series. Within the subsurface, ^{283}U goes through a series of decays until it reaches a gaseous daughter product of radon-222 (^{222}Rn). The gaseous state of ^{222}Rn either remains deposited in the subsurface or releases to the atmosphere. The decay of ^{238}U to ^{222}Rn to ^{210}Pb in the subsurface produces what is known as, "supported" ^{210}Pb (Arias-Ortiz et al., 2018). When ^{222}Rn diffuses to the atmosphere and decays to ^{210}Pb, it can experience fallout to be deposited at Earth's surface due to precipitation or wind. The deposition of ^{210}Pb is known as "unsupported" ^{210}Pb, and was used to age-date distinct stratigraphic layers within the sediment core (Arias-Ortiz et al., 2018).

Dried sediment samples were powered and stored in a sealed three-inch plastic petrie dish to preserve the mass of the sample and conduct lead-214 (^{214}Pb) energy analysis for an indirect determination of ^{226}Ra activity which was assumed to be in equilibrium. Samples consisted of 2.5 grams (g), 5 g, and 10 g, depending on available dry sediment mass within the core. The samples were analyzed in a high purity germanium (HPGe) detector to determine gamma emission from the sediment. Gamma emissions were counted for a 24-hour period for the detection at the total ^{210}Pb detection energy of 46.5 kiloelectron volt (keV). The samples were then counted again 30 days later for a gamma emission energy of 295 and 352 keV to determine levels of ^{214}Pb activity in the sediment to produce a supported ^{210}Pb activity. The difference of the total ^{210}Pb and supported ^{210}Pb activities produces an "unsupported" ^{210}Pb activity which was used for age dating.

Blank samples of pure silica were also analyzed in the HPGe detector to determine the background noise in the instrument. The efficiency of the detector was determined by counting the gamma emission from a known ^{210}Pb standard. The efficiency of the detector for ^{214}Pb was determined by counting the gamma emission from a known europium-152 (^{152}Eu) standard. The net counts of ^{210}Pb and ^{214}Pb, background noise, and chamber efficiency were used to identify the activity per dry mass for the sediment samples. The ^{210}Pb activity of the sediment and known half-life of ^{210}Pb (~22 years) can be applied to the decay equation to determine the age of the sediment being analyzed (Arias-Ortiz et al., 2018; Bonczyk, 2013).

Radiographic Imagery

Radiographic imagining was utilized as a grain size proxy to indicate dense sand layers downcore (Boldt et al., 2010; Castagno, et al., 2021; Fig. 5.3). The radiographic imaging was conducted with a Pinnacle Platinum 40 kilowatt (kW) Overhead Tube Crane (OTC) diagnostic radiographic imaging machine with a wireless digital radiography (DR) image receptor. The high-resolution images (~200 micrometers) were collected with a 68 kilovolt (kV) energy, at 10 milliamperes second (mAs), and source to digital image distance (SID) of 137 cm. The Hounsfield (HU) scale is a semiquantitative method of determining variation in sediment core material density by measuring X-ray attenuation. The HU scale ranges from -10000 to +10000, with water having a HU of 0 (HU = ([density of material–density of water]/[density of water]) × 1000). The radiographic imaging machine software produced HU density calculations every 2 mm downcore for each sediment core (two 50 cm borehole pushes; Fig. 5.3). The diagnostic radiographic imaging machine software determined a discretized HU density reading across the width of the core (Fig. 5.3; *blue lines*) and the software produced a standard deviation output for the determination of each HU measurement (Appendix D). Additionally, I then independently calculated the standard deviation for all HU results reported from the HU radiographic imaging machine for each 100 cm core at No Man's Friend Creek and Town Creek. An elevated HU indicated a higher density of the sediment core material being imaged. The higher density material appeared more white within the radiographic image, with less dense material appearing more black. Coarse grained sand layers were interpreted by elevated HU units (white in appearance).

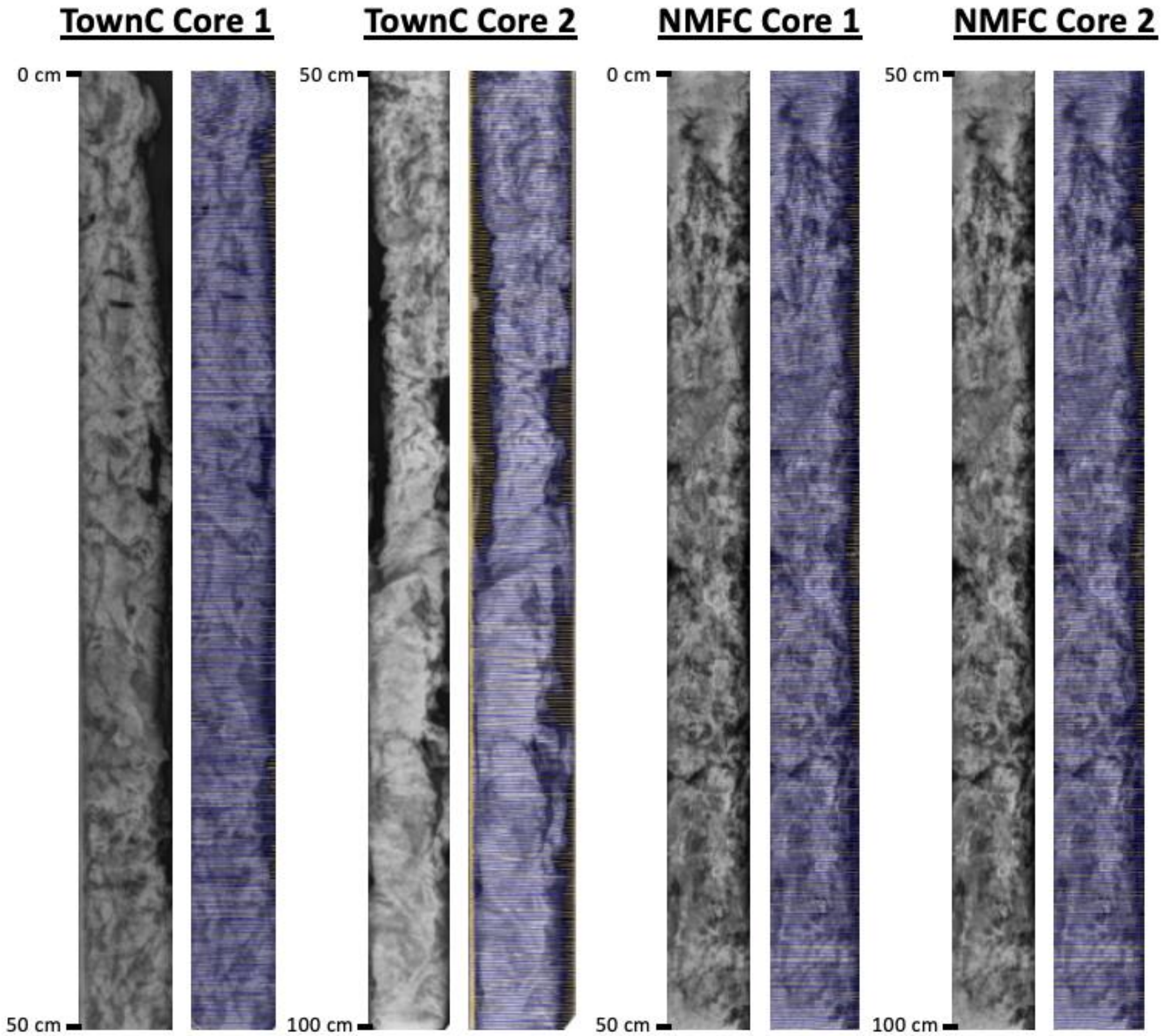

Figure 5.3. Radiographic images (left in grayscale) with Hounsfield density measurements (right with blue density reading lines) of each sediment core push (50 cm) with the respected borehole locations in Town Creek (TownC) and No Man's Friend Creek (NMFC) in NI-WB. Within the radiographic images more dense material was represented by greater brightness (white) on the radiograph while less dense material appears darker (black) because there was less X-ray attenuation (absorption).

RESULTS

Carbon Storage

The locations of Town Creek and No Man's Friend Creek were found to have different carbon storage within the upper 100 cm of sediment as determined by the CHNS elemental analysis (Table 5.1). The total carbon measured in the 100 cm core at Town Creek was 13.55 g, while the total carbon measurement for the No Man's Friend Creek was 25.74 g. Town Creek and No Man's Friend Creek additionally were found to experience different sediment accumulation rates. Based on isotopic analysis of unsupported ^{210}Pb activity, the age of the sediment at 40 cm depth below ground surface was ~188 years before present at TownC and ~45 years before present at NMFC (Fig 5.4.). Therefore, the sediment accumulation rate at Town Creek was 0.21 centimeters per year (cm yr^{-1}) The accumulation rate at No Man's Friend Creek was 0.89 cm yr^{-1}. With the measured age dates at 40 cm, as well as a known radius of the sediment core, the carbon accumulation rate was calculated using the total grams of carbon in the upper 40 cm of the Town Creek (5.62 g) and No Man's Friend Creek (10.68 g) cores. The calculations showed a carbon accumulation rate of 15.21 grams of carbon per square meter for one year (gC m^{-2} yr^{-1}) and 1260.60 gC m^{-2} yr^{-1} for the No Man's Friend Creek Core.

Parameter	**Town Creek**	**No Man's Friend Creek**
Total Carbon in upper 100 cm (g)	13.55	25.74
Sediment Accumulation Rate (cm yr^{-1})	0.21	0.89
Carbon Accumulation Rate (gC m^{-2} yr^{-1})	15.21	120.60

Table 5.1. Carbon storage parameters for Town Creek and No Man's Friend Creek.

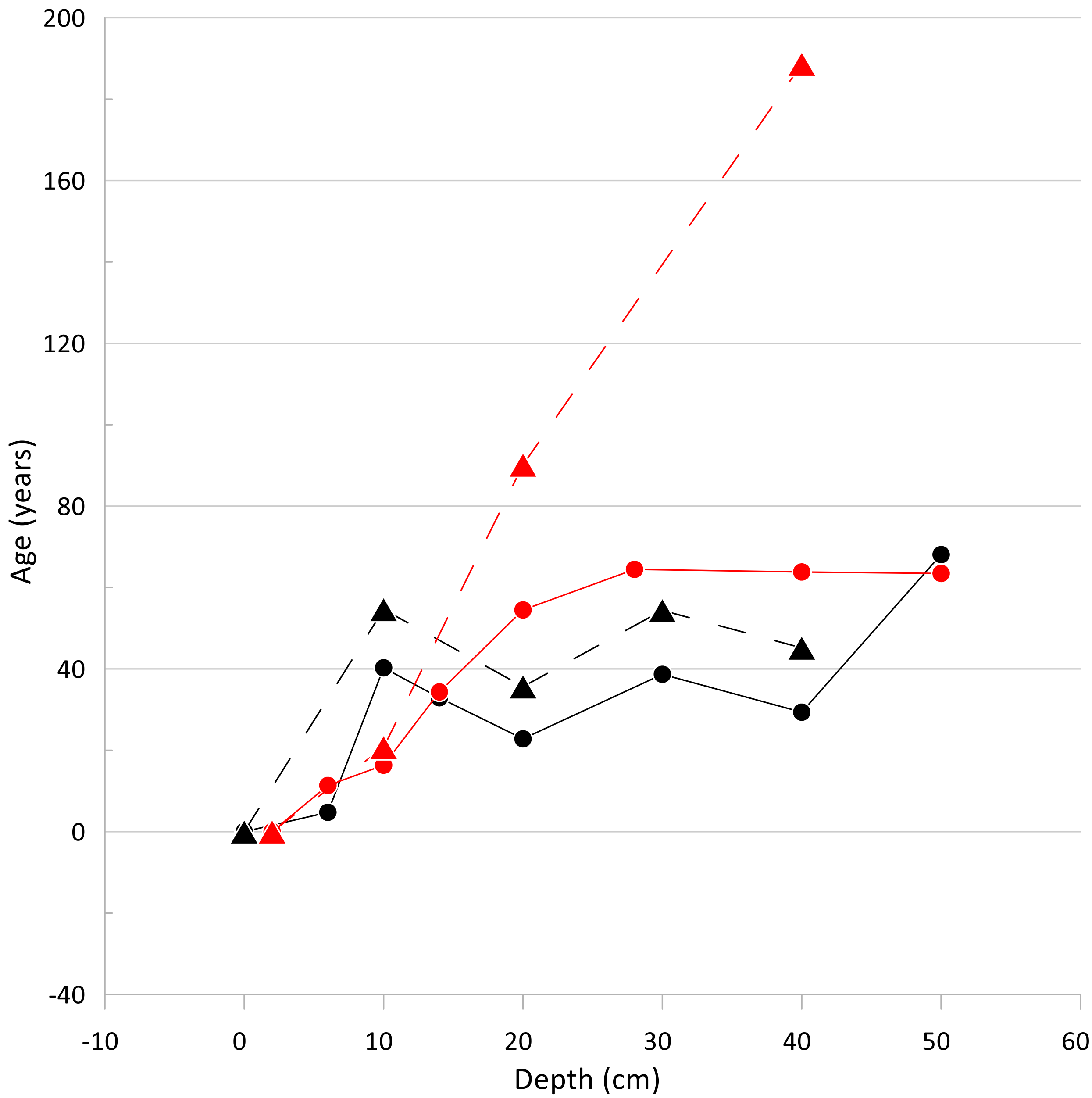

Figure 5.4. Isotopic analysis results for Town Creek (red) and No Man's Friend Creek (black). The solid lines and circular data points at depth represent total ^{210}Pb age dates with supported influence. The dotted lines and triangular data points at depth represent ^{210}Pb unsupported age dates.

Hypothesized Historical High-Energy and Carbon Variation

The percent carbon, sediment grain size, and Hounsfield density were compared for Town Creek and No Man's Friend Creek sediment cores (Fig. 5.5 & 5.6; Appendix D). The percent carbon range for Town Creek was between 1.42% to 13.81% and had an average of 3.21% (Fig. 5.5). The relative standard deviation (RSD) of triplicate samples in the Town Creek core was averaged, resulting in 11.74%. The percent error of the check standard samples for Town Creek was all lower than 1%. The range of percent carbon in the No Man's Friend Creek sediment core ranged from 4.12% to 19.97%, with an average of 10.75% (Fig. 5.6). The No Man's Friend Creek relative standard deviation average for triplicate samples was 5.41%, and the percent error for the check standard samples was all less than 1%.

The maximum grain size, D_{90} value, for Town Creek, was 857.70 micrometers (coarse sand), and the minimum was 76.27 µmeters (very fine sand; Fig. 5.5). The average D_{90} value was 265.09 µmeters (medium sand). The average relative percent difference for the duplicate samples was 13.56%. The maximum D_{90} value for No Man's Friend Creek was 493.7 µmeters (medium sand), while the minimum was 116.7 µmeters (very fine sand; Fig. 5.6). The average D_{90} for No Man's Friend Creek was 276.35 µmeters (medium sand). The average relative percent difference for the No Man's Friend Creek duplicate samples was 11.23%.

The radiographic analysis of density spanned a range of 917 HU to 3040 HU for Town Creek and 970 HU to 2665 HU for No Man's Friend Creek (Fig. 5.5 & 5.6). The average Hounsfield density for Town Creek was 1623.22 HU with a standard deviation of 357.63 HU. The average Hounsfield density for No Man's Friend Creek was 1582.89 HU with a standard deviation of 262.31 HU.

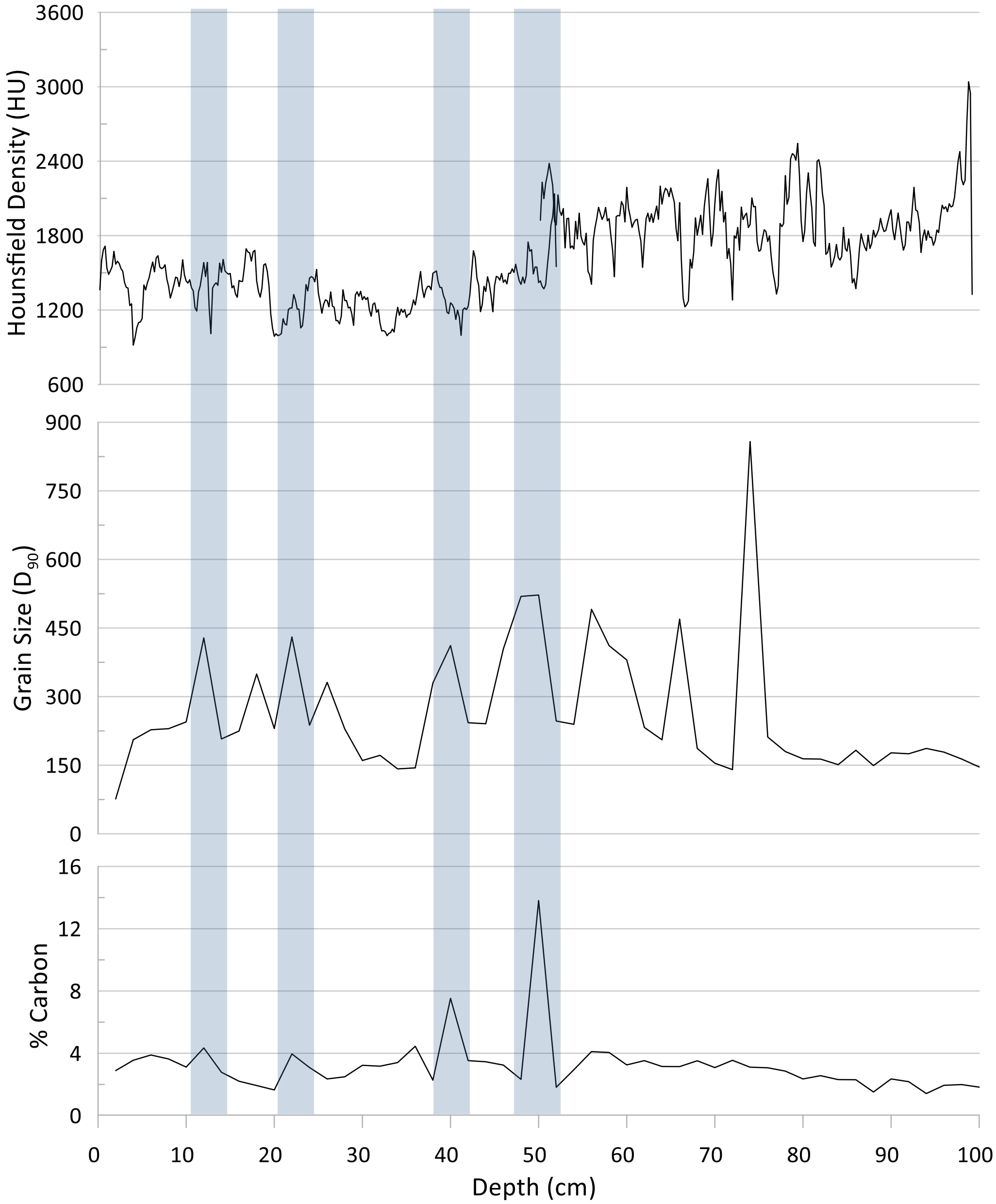

Figure 5.5. Town Creek down core distribution of percent carbon, grain size, and Hounsfield unit. The shaded area identifies the correlation of all proxies. Increased HU density and D90 values indicated presence of larger grains. Increased percent carbon values indicated the presence of more carbon. The overlap in radiographic data was due to the disintegration of the bottom a borehole core push, causing measurements to exceed 50cm.

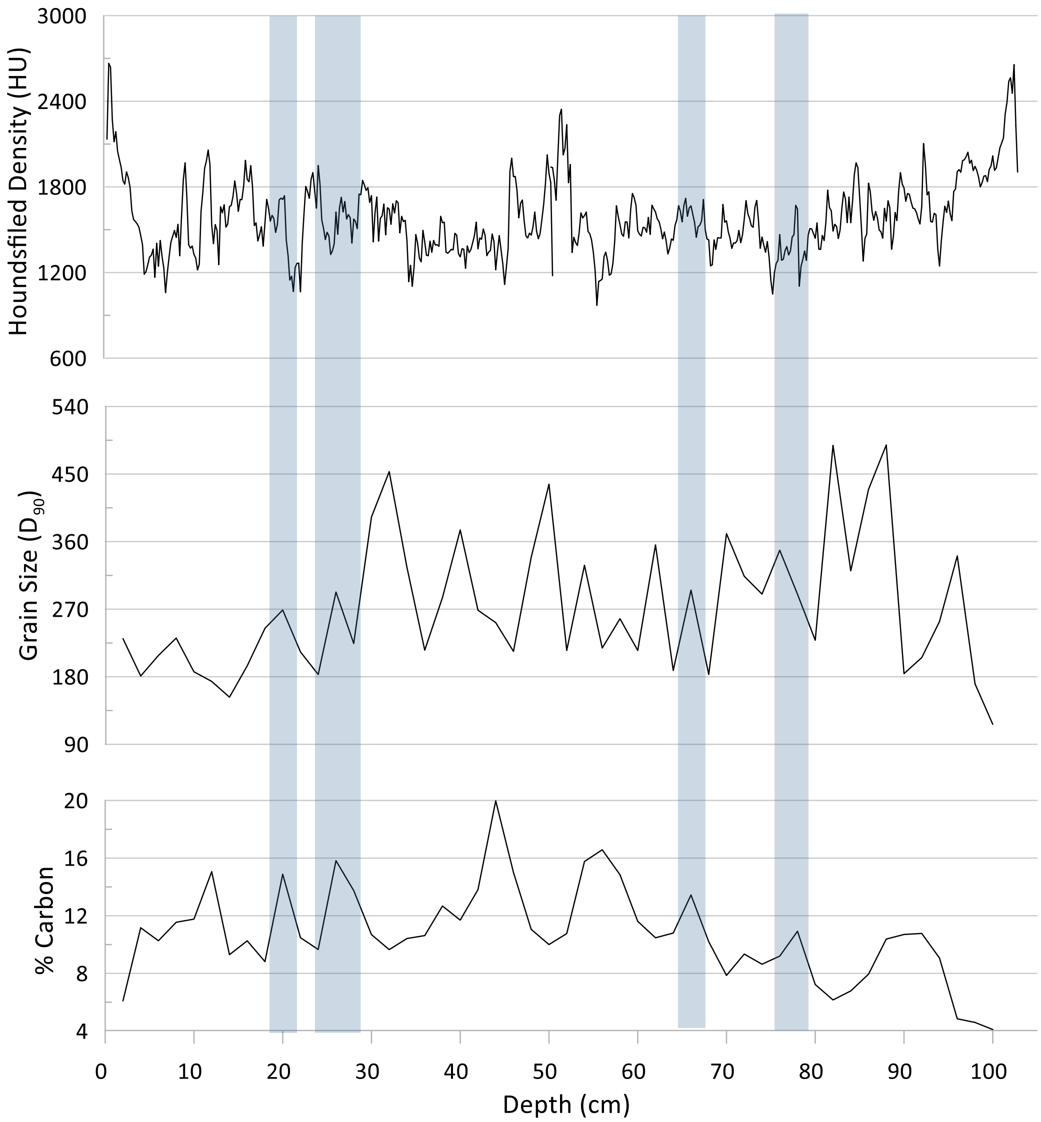

Figure 5.6. No Man's Friend Creek down core distribution of percent carbon, grain size, and Hounsfield unit. The shaded area identifies the correlation of all proxies. Increased HU density and D90 values indicated presence of larger grains. Increased percent carbon values indicated the presence of more carbon.

Potential storm events were identified by using large grain size (D_{90}) as a proxy for high hydraulic flow. High-energy hydraulic events produced increased stream discharge and carrying capacity to transport larger grained material to fine-grained wetlands (Bregy et al., 2018; Dietz et al., 2021; Fuller et al., 2018). The presence of peaks in grain size and HU density were then compared to peaks of percent carbon to determine preserved evidence for potential increase in stored carbon concentration associated with potential high-energy events. The HU density results were not visually discerning and not included in the identification of a high-energy hydraulic flow (further explained in Discussion: Historical Storm Influence on Carbon Storage). The elevated D_{90} grain size, accompanied by increased percent carbon at the same depth was interpreted as a preserved event with high-energy and increased carbon concentrations (Fig. 5.5; Fig. 5.6). The Town Creek core displayed a correlation between D_{90} and percent carbon peaks for four potential events (12 cm, 22 cm, 40 cm, and 50 cm) within the top 50 cm of the core (Fig. 5.5). The No Man's Friend Creek core also showed a correlation of four peaks between D_{90} and percent carbon (20 cm, 26 cm, 66 cm, and 78 cm) within the upper 80 cm of the core (Fig. 5.6).

DISCUSSION

Sediment and Carbon Accumulation Variation in NI-WB

The stored carbon and accumulation rates differed between the two locations of Town Creek and No Man's Friend Creek. The sediment core from the area of No Man's Friend Creek had nearly double the carbon in the top 100 cm of sediment compared to the Town Creek area. Additionally, the sediment accumulation rate at No Man's Friend Creek was more than half the sediment accumulation rate at Town Creek.

The location of the sediment core collected in No Man's Friend Creek was in proximity to the Mud Bay area of the Winyah Bay system, which has been estimated to receive 4.3×10^5 tons of suspended sediment per year from its large watershed (Patchineelam et al., 1999). Patchineelam et al. (1999) reported the four main rivers which provide fine-grained sediment input to Winyah Bay preferentially contribute to accretion in the shallow area of Mud Bay (Patchineelam et al., 1999).

The results of this study identified Mud Bay, specifically No Man's Friend Creek, to have a high accretion rate compared to the surrounding wetland area of Town Creek. The increased sediment input from the Winyah Bay watershed may be responsible for the elevated carbon concentration in the top 100 cm of sediment in No Man's Friend Creek when compared to Town Creek. The river continuum theory suggests the carbon concentration should vary systemically downstream, with the mouth of the river basin experiencing high organic matter concentrations (Ward et al., 2017). In alignment with the river continuum theory, the expansive Winyah Bay watershed likely promoted the transport of stored organic matter across the terrestrial aquatic continuum for deposition at No Man's Friend Creek; compared to the North Inlet watershed which had a more limited carbon reservoir given the much smaller area of the watershed resulting in lower overland transport and deposition of organic matter.

The variation in carbon deposition between the two sites was exhibited by the difference in carbon accumulation rates. Tidal wetlands along the East Coast of the United States have been estimated to have an average carbon accretion rate ranging from 25 to 155 gC m^{-2} yr^{-1} (Weston et al., 2023). The Town Creek carbon accumulation rate was below the East Coast average with 15.21 gC m^{-2} yr^{-1}. However, the radiometric age date used for this calculation at a 40 cm depth was 188 years old, which was just outside the seven half-lives of ^{210}Pb (~150 years), introducing some expected uncertainty due to long-term equilibrium of ^{226}Ra and ^{210}Pb in sediment after seven half-lives (Jia et al., 2018). The carbon accumulation of No Man's Friend Creek was on the high end of the estimated East Coast range with 120.60 gC m^{-2} yr^{-1}. The distance between the Town Creek and No Man's Friend Creek sampling location was 3.4 km, suggesting considerable spatial variation of carbon storage in NI-WB. Chen et al. (2016) reported surface (1-2 cm) carbon concentration distribution to vary on a 10 – 100 m spatial scale over a 0.5 km^2 intertidal island in North Inlet, and identified a knowledge gap in spatial distribution of carbon concentration at depth across the complete tidal wetlands of North Inlet (77 km^2). The displayed heterogeneity in carbon storage between the No Man's Friend Creek and Town Creek cores highlighted spatial variation in carbon concentrations at depth between the two NI-WB locations and the importance of hydraulic settings on vertical carbon sequestration in NI-WB. The identification of the extent of inter-wetland heterogeneity of carbon storage in tidal wetlands should be conducted through the collection and analysis of a spatially representative transect of sediment cores. The representative transect of soil cores across the complete extent of the wetland environment would enhance carbon stock allotment for tidal wetland systems.

Historical Storm Influence on Carbon Storage

The alignment of percent carbon and grain size (D_{90}) served as a proxy for high-energy flow, including hurricanes (Boldt et al., 2010; Castagno, et al., 2021). High energy flows have increased discharge and carrying capacity, allowing for the deposition of large grains in the normally fine-grained dominated tidal wetland (Thorne et al., 2022; Voulgaris & Meyers, 2004). Town Creek and No Man's Friend Creek experienced alignments of the data for elevated grain size and percent carbon. The individual alignment of the peaks within each core indicated potential for high-energy storms to impact carbon storage in tidal wetlands, by specifically transporting stored terrestrial carbon to the coastal basin.

The core from No Man's Friend Creek experienced more peaks of percent carbon and grain size compared to the core collected at Town Creek. The variation in the quantity of percent carbon and grain size peaks indicated No Man's Friend Creek was influenced more consistently by pulses of high energy flow compared to Town Creek, based on the pulse shunt theory. The more consistent high energy flow and vast inputs of organic material from the Winyah Bay watershed resulted in higher carbon accumulation. The Town Creek sediment core experiences low variation in percent carbon distribution down core, signaling potential steady input of carbon from oceanic sources with less dynamic inputs from the terrestrial system.

Each correlated peak indicated a period of increased hydraulic flow; however, the peaks may not conclusively represent a hurricane event. Hurricanes, heavy storm precipitation, and the release of constructed dam across the Winyah Bay watershed rivers could all increase riverine discharge and alter normal hydraulic conditions. To provide more evidence of a hurricane event, a foraminiferal analysis could be conducted. The identification of offshore foraminiferal assemblages within hypothesized storm deposits, interbedded with marsh dominating foraminiferal assemblages assists with the justification of a hurricane deposit (Bregy et al., 2018; Hippensteel & Martin, 1999; Pilarczyk et al., 2014).

The correlation between increased grain size events and percent carbon to HU density was inconclusive. The maximum D_{90} and HU values for Town Creek are both higher than the No Man's Friend Creek D_{90} and HU values. The minimum D_{90} and HU values for Town Creek are both lower than the NMFC D_{90} and HU values. However, the peak distribution correlation was inconclusive. The correlation of the increases in Hounsfield peaks were not highly visually discerning compared to the grain size and carbon concentration correlations for the four potential high-energy events in each collected core. The radiographically derived densities may be inconclusive due to disintegration during transportation and a result of desiccation. Therefore, when utilizing radiographic imaging to determine sediment density, the cores should be transported in tightly confining sheaths to ensure integrity of the sediment structure and imaged on the day of collection. If timely and tightly intact core imaging is conducted, radiographic imaging may serve as a beneficial non-destructive practice to gain an initial perspective of the general grain size distribution throughout the extent of the core.

Additionally, increased resolution of age dating at the one-centimeter scale could assist with identifying distinct variations in carbon accretion rates occurring during identified storm events. However, when using radiological dating-derived rates of marsh accretion, caution must be followed as wetland systems commonly experience sediment mixing, compaction, diagenetic processes, and flood deposition to alter uniform age distribution with depth (Weston et al., 2023). These sources of uncertainty may allow for ^{210}Pb activity to potentially serve as a future storm proxy because flood events transport terrigenous material for deposition to tidal wetlands, impacting the ^{210}Pb activity distribution downcore and potentially altering uniform age distribution with depth (Arias-Ortiz et al., 2018).

CONCLUSION

The NI-WB estuarine system experiences a spatial distribution of stored carbon in the upper 100 cm of sediment in the two locations of sediment core collection in NI-WB. The marginal environments between North Inlet and Winyah Bay experience high rates of carbon storage compared to the inner North Inlet environment. The large contrast of carbon storage between the two locations of NI-WB can be attributed to the varying hydraulic conditions within the tidal wetland system. Additionally, the sediment cores experienced location specific correlation in the variation of downcore carbon concentration and coarse-grained deposits, inferring the potential for high-energy flows to alter carbon storage. The natural variation in environmental conditions within NI-WB made it difficult to determine the high energy flows of distinct hurricane events or common storm events. Further foraminiferal assemblage identification could aid in the determination of hurricane storm deposits. A record of high-energy impacts on carbon storage potential is essential to aid in the prediction of coastal carbon cycling with future increased precipitation, hurricanes, and watershed flooding due to global warming.

REFERENCES

Al-Attabi, Z., Xu, Y., Tso, G., & Narayan, S. (2023). The impacts of tidal wetland loss and coastal development on storm surge damages to people and property: A Hurricane Ike case-study. *Scientific Reports*, *13*(1), 4620. https://doi.org/10.1038/s41598-023-31409-x

Arias-Ortiz, A., Masqué, P., Garcia-Orellana, J., Serrano, O., Mazarrasa, I., Marbà, N., Lovelock, C. E., Lavery, P. S., & Duarte, C. M. (2018). Reviews and syntheses: Pb-derived sediment and carbon accumulation rates in vegetated coastal ecosystems – setting the record straight. *Biogeosciences*, *15*(22), 6791–6818. https://doi.org/10.5194/bg-15-6791-2018

Boldt, K. V., Lane, P., Woodruff, J. D., & Donnelly, J. P. (2010). Calibrating a sedimentary record of overwash from southeastern New England using modeled historic hurricane surges. *Marine Geology*, *275*(1), 127–139. https://doi.org/10.1016/j.margeo.2010.05.002

Bonczyk, M. (2013). A determination of the concentration level of ^{210}PB isotope in solid samples for the assessment of radiation risk occurring in coal mines. *Journal of Sustainable Mining*, *12*(2), 1–7. https://doi.org/10.7424/jsm130201

Bregy, J. C., Wallace, D. J., Totten, R. L., & Cruz, V. J. (2018). 2500-year paleotempestological record of intense storms for the northern Gulf of Mexico, United States. *Geological Records of Extreme Wave Events*, *396*, 26–42. https://doi.org/10.1016/j.margeo.2017.09.009

Castagno, K. A., Donnelly, J. P., & Woodruff, J. D. (2021). Grain-size analysis of hurricane-induced event beds in a New England salt marsh, Massachusetts, USA. *Journal of Coastal Research*, *37*(2), 326–335. https://doi.org/10.2112/JCOASTRES-D-19-00159.1

Chen, S., Torres, R., & Goñi, M. A. (2016). The role of salt marsh structure in the distribution of surface sedimentary organic matter. *Estuaries and Coasts*, *39*(1), 108–122. https://doi.org/10.1007/s12237-015-9957-z

Chuang, W.-C., Eason, T., Garmestani, A., & Roberts, C. (2019). Impact of Hurricane Katrina on the Coastal Systems of Southern Louisiana. *Frontiers in Environmental Science*, *7*. https://doi.org/10.3389/fenvs.2019.00068

Dietz, M. E., Liu, K., Bianchette, T. A., & Smith, D. (2021). Differentiating hurricane deposits in coastal sedimentary records: Two storms, one layer, but different processes. *Environmental Research Communications*, *3*(10), 101001. https://doi.org/10.1088/2515-7620/ac26dd

Duarte, C. M., Losada, I. J., Hendriks, I. E., Mazarrasa, I., & Marbà, N. (2013). The role of coastal plant communities for climate change mitigation and adaptation. *Nature Climate Change*, *3*(11), 961–968. https://doi.org/10.1038/nclimate1970

Fairchild, T. P., Bennett, W. G., Smith, G., Day, B., Skov, M. W., Möller, I., Beaumont, N., Karunarathna, H., & Griffin, J. N. (2021). Coastal wetlands mitigate storm flooding and associated costs in estuaries. *Environmental Research Letters*, *16*(7), 074034. https://doi.org/10.1088/1748-9326/ac0c45

Fuller, I. C., Macklin, M. G., Toonen, W. H. J., & Holt, K. A. (2018). Storm-generated Holocene and historical floods in the Manawatu River, New Zealand. *Geomorphology*, *310*, 102–124. https://doi.org/10.1016/j.geomorph.2018.03.010

Gardner, L. R., & Porter, D. E. (2001). Stratigraphy and geologic history of a southeastern salt marsh basin, North Inlet, South Carolina, USA. *Wetlands Ecology and Management*, *9*(5), 371–385. https://doi.org/10.1023/A:1012060408387

Gedan, K. B., Kirwan, M. L., Wolanski, E., Barbier, E. B., & Silliman, B. R. (2011). The present and future role of coastal wetland vegetation in protecting shorelines: Answering recent challenges to the paradigm. *Climatic Change*, *106*(1), 7–29. https://doi.org/10.1007/s10584-010-0003-7

Gori, A., Lin, N., Xi, D., & Emanuel, K. (2022). Tropical cyclone climatology change greatly exacerbates US extreme rainfall–surge hazard. *Nature Climate Change*, *12*(2), 171–178. https://doi.org/10.1038/s41558-021-01272-7

Hawkes, A. D., & Horton, B. P. (2012). Sedimentary record of storm deposits from Hurricane Ike, Galveston and San Luis Islands, Texas. *Geomorphology*, *171–172*, 180–189. https://doi.org/10.1016/j.geomorph.2012.05.017

Highfield, W. E., Brody, S. D., & Shepard, C. (2018). The effects of estuarine wetlands on flood losses associated with storm surge. *Ocean & Coastal Management*, *157*, 50–55. https://doi.org/10.1016/j.ocecoaman.2018.02.017

Hippensteel, S. P., & Martin, R. E. (1999). Foraminifera as an indicator of overwash deposits, Barrier Island sediment supply, and Barrier Island evolution: Folly Island, South Carolina. *Palaeogeography Palaeoclimatology Palaeoecology*, *149*(1–4), 115–125. https://doi.org/10.1016/S0031-0182(98)00196-5

Jia, J., Yang, Y., Cai, T., Gao, J., Xia, X., Li, Y., & Gao, S. (2018). On the sediment age estimated by 210Pb dating: Probably misleading “prolonging” and multiple-factor-caused "loss." *Acta Oceanologica Sinica*, *37*(6), 30–39. https://doi.org/10.1007/s13131-018-1214-4

Letourneau, M. L., & Medeiros, P. M. (2019). Dissolved organic matter composition in a marsh-dominated estuary: Response to seasonal forcing and to the passage of a hurricane. *Journal of Geophysical Research: Biogeosciences*, *124*(6), 1545–1559. https://doi.org/10.1029/2018JG004982

Li, H., Wang, C., Yu, Q., & Smith, E. (2022). Spatiotemporal assessment of potential drivers of salt marsh dieback in the North Inlet-Winyah Bay estuary, South Carolina (1990–2019). *Journal of Environmental Management*, *313*, 114907. https://doi.org/10.1016/j.jenvman.2022.114907

Marsooli, R., Lin, N., Emanuel, K., & Feng, K. (2019). Climate change exacerbates hurricane flood hazards along US Atlantic and Gulf Coasts in spatially varying patterns. *Nature Communications*, *10*(1), 3785. https://doi.org/10.1038/s41467-019-11755-z

Medeiros, P. M. (2022). The Effects of hurricanes and storms on the composition of dissolved organic matter in a southeastern U.S. estuary. *Frontiers in Marine Science*, *9*. https://doi.org/10.3389/fmars.2022.855720

Morton, R.A. & Barras, J. A. (2011). Hurricane impacts on coastal wetlands: A half-century record of storm-generated features from southern Louisiana. *Journal of Coastal Research*, *27*(6A), 27–43. https://doi.org/10.2112/JCOASTRES-D-10-00185.1

National Oceanic and Atmospheric Administration (NOAA), National Ocean Service (NOS), Belle W. Baruch Institute of the University of South Carolina, South Carolina Coastal Council. (1992). *Final Management plan, North Inlet/Winyah Bay National Estuarine*

Research Reserve. National Ocean Service. https://repository.library.noaa.gov/view/noaa/2461.

North Inlet – Winyah Bay National Estuarine Research Reserve (NI-WB NERR). (2016). *Management Plan. North Inlet – Winyah Bay National Estuarine Research Reserve.* https://northinlet.sc.edu/

Osburn, C. L., Rudolph, J. C., Paerl, H. W., Hounshell, A. G., & Van Dam, B. R. (2019). Lingering carbon cycle effects of Hurricane Matthew in North Carolina's coastal waters. *Geophysical Research Letters*, *46*(5), 2654–2661. https://doi.org/10.1029/2019GL082014

Patchineelam, S. M., Kjerfve, B., & Gardner, L. R. (1999). A preliminary sediment budget for the Winyah Bay estuary, South Carolina, USA. *Marine Geology*, *162*(1), 133–144. https://doi.org/10.1016/S0025-3227(99)00059-6

Patrick, C. J., Yeager, L., Armitage, A. R., Carvallo, F., Congdon, V. M., Dunton, K. H., Fisher, M., Hardison, A. K., Hogan, J. D., Hosen, J., Hu, X., Kiel Reese, B., Kinard, S., Kominoski, J. S., Lin, X., Liu, Z., Montagna, P. A., Pennings, S. C., Walker, L., … Wetz, M. (2020). A system level analysis of coastal ecosystem responses to hurricane impacts. *Estuaries and Coasts*, *43*(5), 943–959. https://doi.org/10.1007/s12237-019-00690-3

Pilarczyk, J. E., Dura, T., Horton, B. P., Engelhart, S. E., Kemp, A. C., & Sawai, Y. (2014). Microfossils from coastal environments as indicators of paleo-earthquakes, tsunamis and storms. *Palaeogeography, Palaeoclimatology, Palaeoecology*, *413,* 144–157. https://doi.org/10.1016/j.palaeo.2014.06.033

Raymond, P. A., Saiers, J. E., & Sobczak, W. V. (2016). Hydrological and biogeochemical controls on watershed dissolved organic matter transport: Pulse-shunt concept. *Ecology*, *97*(1), 5–16. https://doi.org/10.1890/14-1684.1

Reents, S., Mueller, P., Tang, H., Jensen, K., & Nolte, S. (2021). Plant genotype determines biomass response to flooding frequency in tidal wetlands. *Biogeosciences*, *18*(2), 403–411. https://doi.org/10.5194/bg-18-403-2021

Scott, D. B., Collins, E. S., Gayes, P. T., & Wright, E. (2003). Records of prehistoric hurricanes on the South Carolina coast based on micropaleontological and sedimentological evidence, with comparison to other Atlantic Coast records. *GSA Bulletin*, *115*(9), 1027–1039. https://doi.org/10.1130/B25011.1

Smeaton, C., Barlow, N. L. M., & Austin, W. E. N. (2020). Coring and compaction: Best practice in blue carbon stock and burial estimations. *Geoderma*, *364*, 114180. https://doi.org/10.1016/j.geoderma.2020.114180

Sun, F., & Carson, R. T. (2020). Coastal wetlands reduce property damage during tropical cyclones. *Proceedings of the National Academy of Sciences*, *117*(11), 5719–5725. https://doi.org/10.1073/pnas.1915169117

Thorne, K., Jones, S., Freeman, C., Buffington, K., Janousek, C., & Guntenspergen, G. (2022). atmospheric river storm flooding influences tidal marsh elevation building processes. *Journal of Geophysical Research: Biogeosciences*, *127*(3), e2021JG006592. https://doi.org/10.1029/2021JG006592

Van Coppenolle, R., & Temmerman, S. (2019). A global exploration of tidal wetland creation for nature-based flood risk mitigation in coastal cities. *Estuarine, Coastal and Shelf Science*, *226*, 106262. https://doi.org/10.1016/j.ecss.2019.106262

Voulgaris, G., & Meyers, S. T. (2004). Net effect of rainfall activity on salt-marsh sediment distribution. *Marine Geology*, *207*(1), 115–129. https://doi.org/10.1016/j.margeo.2004.03.009

Wahl, T., Jain, S., Bender, J., Meyers, S. D., & Luther, M. E. (2015). Increasing risk of compound flooding from storm surge and rainfall for major US cities. *Nature Climate Change*, *5*(12), 1093–1097. https://doi.org/10.1038/nclimate2736

Wallace Davin J., Woodruff Jonathan D., Anderson John B., & Donnelly Jeffrey P. (2014). Palaeohurricane reconstructions from sedimentary archives along the Gulf of Mexico, Caribbean Sea and western North Atlantic Ocean margins. *Geological Society, London, Special Publications*, *388*(1), 481–501. https://doi.org/10.1144/SP388.12

Walsh, K. J. E., McBride, J. L., Klotzbach, P. J., Balachandran, S., Camargo, S. J., Holland, G., Knutson, T. R., Kossin, J. P., Lee, T., Sobel, A., & Sugi, M. (2016). Tropical cyclones and climate change. *WIREs Climate Change*, *7*(1), 65–89. https://doi.org/10.1002/wcc.371

Ward, N. D., Bianchi, T. S., Medeiros, P. M., Seidel, M., Richey, J. E., Keil, R. G., & Sawakuchi, H. O. (2017). Where carbon goes when water flows: Carbon cycling across the aquatic continuum. *Frontiers in Marine Science*, *4*, 7. https://doi.org/10.3389/fmars.2017.00007

Weston, N. B., Rodriguez, E., Donnelly, B., Solohin, E., Jezycki, K., Demberger, S., Sutter, L. A., Morris, J. T., Neubauer, S. C., & Craft, C. B. (2023). Recent acceleration of wetland accretion and carbon accumulation along the U.S. east coast. *Earth's Future*, *11*(3), e2022EF003037. https://doi.org/10.1029/2022EF003037

Windham-Myers, L., Cai, W.-J., Alin, S., Andersson, A., Crosswell, J., Dunton, K. H., Hernandez-Ayon, J. M., Herrmann, M., Hinson, A. L., Hopkinson, C. S., Howard, J., Hu, X., Knox, S. H., Kroeger, K., Lagomasino, D., Megonigal, P., Najjar, R., Paulsen, M.-L., Peteet, D., … Zhu, Z. (2018). *Chapter 15: Tidal wetlands and estuaries. Second state of* *the carbon cycle report*. U.S. Global Change Research Program. https://doi.org/10.7930/SOCCR2.2018.Ch15

Yan, G., Labonté, J. M., Quigg, A., & Kaiser, K. (2020). Hurricanes accelerate dissolved organic carbon cycling in coastal ecosystems. *Frontiers in Marine Science*, *7*, 248. https://doi.org/10.3389/fmars.2020.00248

Yan, X., Zhang, R., & Knutson, T. R. (2017). The role of Atlantic overturning circulation in the recent decline of Atlantic major hurricane frequency. *Nature Communications*, *8*(1), 1695. https://doi.org/10.1038/s41467-017-01377-8

Zhu, Z., Vuik, V., Visser, P. J., Soens, T., van Wesenbeeck, B., van de Koppel, J., Jonkman, S. N., Temmerman, S., & Bouma, T. J. (2020). Historic storms and the hidden value of coastal wetlands for nature-based flood defence. *Nature Sustainability*, *3*(10), 853–862. https://doi.org/10.1038/s41893-020-0556-z

CHAPTER SIX

CONCLUSION

KEY FINDINGS

The research objective of this study was to investigate carbon dioxide (CO_2) flux and carbon storage in North Inlet-Winyah Bay (NI-WB), SC. Specifically, this study aimed to identify and comprehend the influence high energy systems have on CO_2 flux and historical carbon storage in tidal wetlands. The following key findings were established.

(1) An innovative low-cost CO_2 gas flux design incorporating a soil well and non-dispersive infrared analyzer was developed to monitor vertical CO_2 flux at the sediment interface. The CO_2 soil gas flux design allowed for continuous long-term monitoring in intertidal environments with varying water levels and during extreme high-energy events (i.e., king tides and hurricanes). The design included a long-term regenerative power source with a cellular connection to ensure continuous data collection in remote tidal wetlands. The innovative design resulted in continuous monitoring in the aquatic environment while costing approximately one-third of a comparable commercially manufactured CO_2 flux chamber (total cost for CO_2 gas flux design was ~1,800 US dollars in 2022 for one station). The widespread adoption of the cost-effective, long-term CO_2 flux monitoring station system will generate improved spatial and temporal datasets of CO_2 fluxes in tidal wetlands.

(2) No Man's Friend Creek, located near Mud Bay within the NI-WB system, experienced monthly variation in CO_2 flux, but was dominated by near-annual net CO_2 sequestration of 9.4 $\mu mol\ m^{-2}\ s^{-1}$. The meteorological and water quality conditions (i.e., temperature, pressure, relative

humidity, precipitation, specific conductivity, salinity, dissolved oxygen, pH, and turbidity) of NI-WB actively interacted through physiochemical processes to contribute to carbon sequestration in the tidal wetlands and offset atmospheric CO_2 concentrations. An increase in active sedimentation was also identified to correspond with net CO_2 sequestration in NI-WB.

(3) Hurricane Ian made landfall at NI-WB as a category one storm on September 30, 2022, at 13:45 EST. The continuous monitoring throughout the hurricane identified temporal variation in CO_2 flux due to the high-energy disturbance. Prior to Hurricane Ian, CO_2 flux at the innovative monitoring station at No Man's Friend Creek in NI-WB was dominated by net sequestration of CO_2. On September 30, net emissions dominated the period leading up to the direct landfall of Hurricane Ian. As the eye of Hurricane Ian moved inland, net sequestration persisted for the remainder of the day on September 30, resulting in a net sequestration of 3.9 µmol m^{-2} s^{-1} of CO_2 for the 24-hour period. The net CO_2 sequestration behavior in NI-WB transitioned to net emission that dominated for at least one month post-Hurricane Ian.

(4) Based on sediment cores collected from No Man's Friend Creek and Town Creek in NI-WB, the spatial distribution of stored carbon showed large heterogenous distribution within the estuarine system. The marginal wetland environment located on No Man's Friend Creek at the transition between North Inlet and Winyah Bay estuaries contained a total of 25.74 g of carbon within the upper 100 cm and a carbon accumulation rate of 120.60 gC m^{-2} yr^{-1}. The inner North Inlet environment of Town Creek had 13.55 g of carbon in the upper 100 cm of sediment and an accumulation rate of 15.21 gC m^{-2} yr^{-1}. The spatial variation in stored carbon reflected differing hydraulic flows and watershed inputs within the NI-WB system. The identification of historical

high-energy hydraulic flows, using paleotempestological methods of grain size distribution, concurrently suggested four events with increased carbon concentration indicating the potential for historical high-energy events to impact carbon storage.

IMPLICATIONS FOR RESEARCH

Tidal wetlands are biogeochemical 'reactors' which experience dynamic temporal and spatial environmental conditions. The tidal wetland carbon cycle is influenced by the physiochemical process occurring in the atmosphere, water, and sediment. If additional carbon cycling analysis is conducted going further, the monitoring of CO_2 flux at the sediment interface by the soil-gas well should be accompanied by CO_2 flux measurements in the atmosphere via an eddy covariance tower and in the aquatic setting via continuous water quality, dissolved CO_2, and grab sample analysis. The continuous long-term analysis of carbon flux in the atmosphere, sediment interface, and aquatic setting will aid in determining the residence time of carbon in tidal wetlands and identify the various pathways for CO_2 flux across the subsurface-marine-atmosphere continuum. Additionally, increasing the number of CO_2 flux monitoring stations will identify lateral spatial variation of carbon flux at the sediment surface interface by deploying CO_2 flux monitoring stations in a representative transect throughout the extent of tidal wetland systems. The TWC1 CO_2 flux monitoring station identified net sequestration on No Man's Friend Creek near Mud Bay. However, as the collected sediment cores displayed (Chapter 5), the environmental conditions influenced spatial variation in carbon storage in the North Inlet tidal wetland system. A transect of CO_2 flux monitoring stations will produce a representative quantifiable net sequestration value across the extent of tidal wetland surface areas.

The widespread adoption of the CO_2 flux monitoring methods outlined in this study will generate improved spatial and temporal datasets of carbon cycling in tidal wetlands. The expanded extent of CO_2 flux monitoring will aid in identifying how various high energy disturbances (i.e., Category 1-5 Hurricane, tropical storm, tropical depression, etc.) impact CO_2 flux in tidal wetlands with space and time. The accumulation of supplemental continuous CO_2 flux datasets for tidal wetlands, both long-term and during high-energy events, will contribute to synthesizing tidal wetlands' role in regulating atmospheric CO_2 concentrations.

Furthermore, this study identified a correlation between historical high-energy hydraulic events and increased carbon storage. The high-energy hydraulic events were determined based on paleotempestology proxies of grain size and sediment density within a sediment core. The identification transition in foraminiferal assemblages across the inferred high-energy deposits would justify the genesis of the deposits from an offshore storm event. Further identification of historical storm events and variation in percent carbon of sediment will provide insights to post-storm carbon residence time in tidal wetlands. A historical record of periodic storm pulses of carbon into wetlands will provide insight to how future storms will affect carbon storage in tidal wetland basins.

SUMMARY

The Intergovernmental Panel on Climate Change (IPCC) and the U.S Global Change Research Program (USGCRP) identified carbon cycling and CO_2 flux datasets of tidal wetlands to be limiting on both a temporal and spatial scale. The current limitation of comprehensive carbon cycling and CO_2 flux datasets results in low confidence projections of tidal wetlands' role in carbon-climate feedback. The limited datasets and low confident projections often lead to the exclusion of tidal wetlands from earth systems models (ESM), which predict future atmospheric CO_2 concentrations and the magnitude of global climate change. This research study produced a low-cost innovative CO_2 flux monitoring method and a unique long-term dataset to supplement IPCC and USGCRP efforts to predicting future carbon cycling. Specifically, this study successfully investigated continuous long-term CO_2 flux of an intertidal zone, quantified annual net sequestration in No Man's Friend Creek, determined hurricane-induced variation in CO_2 flux due to high-energy conditions, and identified a variation in historical tidal wetland carbon storage correlated to high-energy hydraulic flows. The integration of methods and findings from this study conducted in NI-WB, with supplemental CO_2 flux analysis (eddy covariance towers and aquatic dCO_2/particulate OM) and further paleotempestology findings in global tidal wetlands, will produce a comprehensive synthesis of the role tidal wetlands play in carbon-climate feedbacks; ultimately refining ESM predictions of global climate change. The improved projection of carbon cycling in tidal wetlands will aid in the development of informed wetland management practices and climate policy.

APPENDICES

APPENDIX A

<u>Soil Gas Flux Monitoring Station Material List</u>

Cost of all material for one monitoring station in 2022 – $1,882

Soil gas well:

- Vaisala GMP252 NDIR CO_2 Sensor
    - CO_2 measurements. Placed at the top of the PVC casing.

- Plastic Drain strainer
    - Cut with diameter equal to GMP252 CO_2 sensor and PVC glued to the inside of the main well casing to hold the sensor secure within the center of the well casing diameter.
    - Image:

- 10’ 2” PVC Pipe
    - Serves as the main well casing with 1.27 cm screened openings at a 2.54 cm interval for the lower 1-meter of the well. The screen is cut with a chop saw.
    - Image

- Pool noodle float
    - Cut into circular pieces to be attached to the backflow check valve with hot glue and PVC glue.

- 2” PVC Quiet Check Backflow Valve
    - A rotary Dremel tool was used to cut off the backflow check valve spring, allowing the valve to open with gravitational force.
    - Image:

- 2” PVC Coupling
    - Attached via PVC glue between main PVC well casing and the backflow check valve.

- 2” PVC DWV Combo Wye with Screw Cleanout Plug
    - Placed at the top of the main PVC casing. The cleanout plugs are drilled to create a hole in the center of the plugs. The top plug contains a one-way pressure release valve. The other plug hole allowed the wiring of the data logger to enter the PVC casing to connect to the GMP252 sensor.
    - Image:

- One-way Water Non-Return Pressure Release Valve
    - Placed at the top of DWV Combo Wye with Screw Cleanout Plug with PVC glue.
    - Image:

Power Station:
- Serial to Cellular Raspberry Pi based Connection Box
    - Cellular cloud connection to the GMP252 sensor. Box consists of raspberry pi, RS485 Modbus Converter, antenna, and wiring.
    - Image:

- 12V 55Ah Deep Cycle Marine Battery
  - o Deep cycle marine battery to allow trickle charger in an aquatic setting.
  - o Image:

- 12V 50 Watt Waterproof Trickle Charger Solar Panel
  - o Long-term trickle charging of the marine battery.
  - o Image:

- Polycarbonate NEMA 6P Screw Close Waterproof Enclosure
  - o Waterproof protection of electrical equipment.
  - o Image:

- NEMA 6P Wire Glands
  - Dill holes created with a step drill bit. The wire glands allow wires to protrude an enclosure, while keeping it waterproof.
  - Image:

- Heat Barrier Tape
  - Placed on NEMA 6P enclosure to limit heat buildup of electrical equipment.
  - Image:

- Desiccant Packets
  - Placed within the NEMA 6P enclosure to limit moisture buildup.
  - Image:

- TaylorMade Dock Float (24x48x16 inch)
  - o With weight capacity equivalent to your electrical equipment weight
  - o Image:

- Costco Folding Table (24x48 inch)
  - o Placed atop the Taylor Made dock flow. The dock float cannot be drilled into, as that would impact the integrity of the float’s buoyancy. The table is attached via lug bolts and plastic tie downs. The table is drilled into, to secure equipment with to the floating station via lug bolts.
  - o Image:

- 2 – 6’x2”x4” treated lumber
  - o Cut in half using a chop saw for the edge of the stationary base.
  - o Image:

- 1 – 10’x2”x4” treated lumber
    - Cut in half using a chop saw for the edge of the stationary base.
    - Image: See above

- 2 – 8’x2”x4” treated lumber
    - Cut in half by chop saw to be vertical guides attached to the stationary base. The vertical guides do not allow flotational equipment to flip on its side.
    - Image:

- 4 – 12’x4”x4” treated lumber
    - Stationary base attached to the posts via stainless steel deck screws.
    - Image:

- Stainless Steel Wire Clamps
  - Used as the loops to attach the float/Costco table to the treated lumber posts.
  - Image:

- Security Padlock and Security Cable
  - Attached from the top of the post and float/table to protect from theft.
  - Image:

Equipment:

- PVC Glue
- Hot Glue
- Chop Saw
- Rotary Dremel Tool
- Electric Drill
- Step Drill Bit
- Tie Downs
- Stainless Steel & Galvanized Lug Bolts, Washers, and Screws

Monitoring Station TWC1 GMP252 Calibration Certificate

VAISALA

Vaisala is ISO 9001, ISO 14001 and AQAP 2110 certified company.

CALIBRATION CERTIFICATE

This certificate may only be reproduced in full, except with the prior written permission by the issuing laboratory

Certificate Number: H90-21340341

Instrument	Carbon Dioxide Probe GMP252
Configuration code	50C0A5N1
Serial number	T3470053
Manufacturer	Vaisala Oyj, Finland
Calibration date	29 August 2021

The adjustment data of the carbon dioxide probe was measured by using accurate bottled carbon dioxide gas concentrations. After adjustment, observed values were obtained from the probe. Pressure and temperature compensation was made by using the compensation algorithm of the probe and by using actual pressure and temperature readings of reference temperature and pressure transmitters. At the time of shipment, the probe met its operating specifications.

For the CO_2 calibration, an accurate mixture of nitrogen and carbon dioxide traceable to Dutch Metrology Institute (VSL) was used. The reference temperature and pressure transmitters are calibrated at Vaisala Measurement Standards Laboratory (MSL), an ISO/IEC 17025 accredited calibration laboratory (FINAS), by using working standards traceable to the international system of units (SI) through national metrology institutes (NIST USA, MIKES Finland, or equivalent) or accredited calibration laboratories.

CO_2 calibration results

Reference ppm CO_2	Observed ppm CO_2	Difference ppm CO_2	Permissible difference ppm CO_2	Measurement uncertainty ppm CO_2
2000	2000	0	± 40	± 31
9990	9990	0	± 200	± 105

Uncertainties (95 % confidence level, k=2)

Ambient conditions: Humidity 45 ± 5 %RH, Temperature 23 ± 1 °C, Pressure 1015 ± 20 hPa.

Equipment used in calibration

Type	Serial number	Calibration date	Certificate number
PTU307	16784	2020-10-05	K008-D03611
PTU30T	17636	2021-05-24	K008-E02291

Gas cylinders used in calibration

Type	CO_2 concentration (ppm)	Cylinder number	Reference number
Carbon dioxide mixture (accuracy of ±0.5%)	2000	7523112231489	100615623
Carbon dioxide mixture (accuracy of ±0.5%)	9990	7523112296450	100615838

Digitally signed by: Julia Sotnikova
Date: 2021-09-13 13:15:36 (+03:00)
Location: Vaisala Oyj, Finland

Technician

DOC247068-B

Vaisala Oyj | PO Box 26, FI-00421 Helsinki, Finland
Phone +358 9 894 91 | Fax +358 9 8949 2227
Email helpdesk@vaisala.com | www.vaisala.com
Domicile Vantaa, Finland | VAT FI01244162 | Business ID 0124416-2

Monitoring Station TWC2 GMP252 Calibration Certificate

VAISALA

Vaisala is ISO 9001, ISO 14001 and AQAP 2110 certified company.

CALIBRATION CERTIFICATE

This certificate may only be reproduced in full, except with the prior written permission by the issuing laboratory

Certificate Number: H90-21340348

Instrument	Carbon Dioxide Probe GMP252
Configuration code	50C0A5N1
Serial number	T3470045
Manufacturer	Vaisala Oyj, Finland
Calibration date	29 August 2021

The adjustment data of the carbon dioxide probe was measured by using accurate bottled carbon dioxide gas concentrations. After adjustment, observed values were obtained from the probe. Pressure and temperature compensation was made by using the compensation algorithm of the probe and by using actual pressure and temperature readings of reference temperature and pressure transmitters. At the time of shipment, the probe met its operating specifications.

For the CO_2 calibration, an accurate mixture of nitrogen and carbon dioxide traceable to Dutch Metrology Institute (VSL) was used. The reference temperature and pressure transmitters are calibrated at Vaisala Measurement Standards Laboratory (MSL), an ISO/IEC 17025 accredited calibration laboratory (FINAS), by using working standards traceable to the international system of units (SI) through national metrology institutes (NIST USA, MIKES Finland, or equivalent) or accredited calibration laboratories.

CO_2 calibration results

Reference ppm CO_2	Observed ppm CO_2	Difference ppm CO_2	Permissible difference ppm CO_2	Measurement uncertainty ppm CO_2
2000	2000	0	± 40	± 31
9990	9990	0	± 200	± 105

Uncertainties (95 % confidence level, k=2)

Ambient conditions: Humidity 45 ± 5 %RH, Temperature 23 ± 1 °C, Pressure 1015 ± 20 hPa.

Equipment used in calibration

Type	Serial number	Calibration date	Certificate number
PTU307	16784	2020-10-05	K008-D03611
PTU30T	17636	2021-05-24	K008-E02291

Gas cylinders used in calibration

Type	CO_2 concentration (ppm)	Cylinder number	Reference number
Carbon dioxide mixture (accuracy of ±0.5%)	2000	7523112231489	100615623
Carbon dioxide mixture (accuracy of ±0.5%)	9990	7523112296450	100615838

Digitally signed by: Julia Sotnikova
Date: 2021-09-13 13:23:31 (+03:00)
Location: Vaisala Oyj, Finland

Technician

DOC247068-B

Vaisala Oyj | PO Box 26, FI-00421 Helsinki, Finland
Phone +358 9 894 91 | Fax +358 9 8949 2227
Email helpdesk@vaisala.com | www.vaisala.com
Domicile Vantaa, Finland | VAT FI01244162 | Business ID 0124416-2

APPENDIX B

Spearman and Kendall tau-b Correlation Matrix SPSS Output

* The correlation matrices have parameters on both the x and y axis of table. The x parameters are correlated against the environmental parameter on the y axis. For example, the first parameter on the x axis and y axis is CO_2 concertation, and the correlation is 100 percent since it is same parameter, therefore it is not given a correlation coefficient. The correlation coefficient is reported, along with the significance and n (total measurements).

a.)

1 -Year: Water Quality & CO2 Concentration Spearman Correlation								
CO2 Conc	---							
Depth	0.130	---						
Water Temp	0.778	0.043	---					
SpCond	0.260	0.385	0.101	---				
Salinity	0.268	0.400	0.110	0.997	---			
DO	-0.553	0.325	-0.738	0.032	0.023	---		
pH	-0.292	0.635	-0.511	0.298	0.299	0.835	---	
Turbidity	0.283	0.036	0.521	-0.141	-0.131	-0.36	-0.336	---
	CO2 Conc	Depth	Water Temp	SpCond	Salinity	DO	pH	Turbidity

b.)

1 - Year: Water Quality & CO2 Concentration Kendall Tau-b Correlation								
CO2 Flux	---							
Depth	0.087	---						
Water Temp	0.565	0.029	---					
SpCond	0.177	0.268	0.065	---				
Salinity	0.182	0.280	0.070	0.971	---			
DO	-0.383	0.222	-0.543	0.024	0.018	---		
pH	-0.213	0.479	-0.376	0.216	0.218	0.683	---	
Turbidity	0.199	0.025	0.379	-0.098	-0.092	-0.252	-0.250	---
	CO2 Flux	Depth	Water Temp	SpCond	Salinity	DO	pH	Turbidity

c.)

1 -Year: Meteorology & CO2 Concentration Spearman Correlation							
CO2 Conc	---						
Well Temp	0.595	---					
Atm Temp	0.586	0.875	---				
Relative H	-0.106	-0.093	---	---			
Bar Pressure	-0.106	-0.256	-0.383	-0.065	---		
Total Precip	-0.045	-0.075	-0.040	0.192	-0.073	---	
Wind Spd	---	0.178	0.180	-0.382	-0.169	0.090	---
	CO2 Conc	Well Temp	Atm Temp	Relative H	Bar Pressure	Total Precip	Wind Spd

d.)

1 -Year: Meteorology & CO2 Concentration Kendall Tau-b Flux Correlation							
CO2 Conc	---						
Well Temp	0.415	---					
Atm Temp	0.408	0.748	---				
Relative H	-0.072	-0.069	-0.011	---			
Bar Pressure	-0.075	-0.174	-0.264	-0.045	---		
Total Precip	-0.037	-0.060	-0.033	0.157	-0.061	---	
Wind Spd	---	0.119	0.120	-0.261	-0.118	0.073	---
	CO2 Conc	Well Temp	Atm Temp	Relative H	Bar Pressure	Total Precip	Wind Spd

Scale
1.00
0.50
0.00
-0.50
-1.00

1-Year: Water Quality & CO2 Concentration Spearman Correlation

		TWC1 CO2	Depth	Water Temp	SpCond	Salinity	DO_mgl	pH	Turbidity
TWC1 CO2	Correlation Coefficient	--							
	Sig. (2-tailed)	.							
	N	26646							
Depth	Correlation Coefficient	.130**	--						
	Sig. (2-tailed)	<.001	.						
	N	26552	28399						
Water Temp	Correlation Coefficient	.778**	.043**	--					
	Sig. (2-tailed)	.000	<.001	.					
	N	26629	28399	28476					
SpCond	Correlation Coefficient	.260**	.385**	.101**	--				
	Sig. (2-tailed)	.000	.000	<.001	.				
	N	26628	28399	28475	28475				
Salinity	Correlation Coefficient	.268**	.400**	.110**	.997**	--			
	Sig. (2-tailed)	.000	.000	<.001	.000	.			
	N	26628	28399	28475	28475	28475			
DO_mgl	Correlation Coefficient	-.553**	.325**	-.738**	.032**	.023**	--		
	Sig. (2-tailed)	.000	.000	.000	<.001	<.001	.		
	N	26628	28399	28475	28475	28475	28475		
pH	Correlation Coefficient	-.292**	.635**	-.511**	.298**	.299**	.835**	--	
	Sig. (2-tailed)	.000	.000	.000	.000	.000	.000	.	
	N	26628	28399	28475	28475	28475	28475	28475	
Turbidity	Correlation Coefficient	.283**	.036**	.521**	-.141**	-.131**	-.360**	-.336**	--
	Sig. (2-tailed)	.000	<.001	.000	<.001	<.001	.000	.000	.
	N	26621	28384	28460	28460	28460	28460	28460	28460

1-Year: Meteorology & CO_2 Concentration Spearman Correlation

		ATM TWC1 CO2	TWC1 Well Temp	Atm Temp	Relative H	Bar. Pressure	Total Precip	Wind Spd
ATM TWC1 CO2	Correlation Coefficient	--						
	Sig. (2-tailed)	.						
	N	26885						
TWC1 Well Temp	Correlation Coefficient	.595**	--					
	Sig. (2-tailed)	.000	.					
	N	26885	28723					
Atm Temp	Correlation Coefficient	.586**	.875**	--				
	Sig. (2-tailed)	.000	.000	.				
	N	26885	28723	28723				
Relative H	Correlation Coefficient	-.106**	-.093**	-.004	--			
	Sig. (2-tailed)	<.001	<.001	.488	.			
	N	26873	28711	28711	28711			
Bar. Pressure	Correlation Coefficient	-.106**	-.256**	-.383**	-.065**	--		
	Sig. (2-tailed)	<.001	.000	.000	<.001	.		
	N	26873	28711	28711	28711	28711		
Total Precip	Correlation Coefficient	-.045**	-.075**	-.040**	.192**	-.073**	--	
	Sig. (2-tailed)	<.001	<.001	<.001	<.001	<.001	.	
	N	26872	28710	28710	28710	28710	28710	
Wind Spd	Correlation Coefficient	.006	.178**	.180**	-.382**	-.169**	.090**	--
	Sig. (2-tailed)	.364	<.001	<.001	.000	<.001	<.001	.
	N	26873	28711	28711	28710	28710	28710	28711

1-Year: Water and CO2 Concentration Correlation Kendall tau

		TWC1 CO2	Depth	Water Temp	SpCond	Salinity	DO_mgl	pH	Turbidity
TWC1 CO2	Correlation Coefficient	--							
	Sig. (2-tailed)	.							
	N	26646							
Depth	Correlation Coefficient	.087**	--						
	Sig. (2-tailed)	<.001	.						
	N	26552	28399						
Water Temp	Correlation Coefficient	.565**	.029**	--					
	Sig. (2-tailed)	.000	<.001	.					
	N	26629	28399	28476					
SpCond	Correlation Coefficient	.177**	.268**	.065**	--				
	Sig. (2-tailed)	.000	.000	<.001	.				
	N	26628	28399	28475	28475				
Salinity	Correlation Coefficient	.182**	.280**	.070**	.971**	--			
	Sig. (2-tailed)	.000	.000	<.001	.000	.			
	N	26628	28399	28475	28475	28475			
DO_mgl	Correlation Coefficient	-.383**	.222**	-.543**	.024**	.018**	--		
	Sig. (2-tailed)	.000	.000	.000	<.001	<.001	.		
	N	26628	28399	28475	28475	28475	28475		
pH	Correlation Coefficient	-.213**	.479**	-.376**	.216**	.218**	.683**	--	
	Sig. (2-tailed)	.000	.000	.000	.000	.000	.000		
	N	26628	28399	28475	28475	28475	28475	28475	
Turbidity	Correlation Coefficient	.199**	.025**	.379**	-.098**	-.092**	-.252**	-.250**	--
	Sig. (2-tailed)	.000	<.001	.000	<.001	<.001	.000	.000	
	N	26621	28384	28460	28460	28460	28460	28460	28460

1 – Year: Meteorology & CO_2 Concentration Kendall tau-b Flux Correlation

		ATM TWC1 CO2	TWC1 Well Temp	Atm Temp	Relative H	Bar. Pressure	Total Precip	Wind Spd
ATM TWC1 CO2	Correlation Coefficient	--						
	Sig. (2-tailed)	.						
	N	26885						
TWC1 Well Temp	Correlation Coefficient	.415**	--					
	Sig. (2-tailed)	.000	.					
	N	26885	28723					
Atm Temp	Correlation Coefficient	.408**	.748**	--				
	Sig. (2-tailed)	.000	.000	.				
	N	26885	28723	28723				
Relative H	Correlation Coefficient	-.072**	-.069**	-.011**	--			
	Sig. (2-tailed)	<.001	<.001	.007	.			
	N	26873	28711	28711	28711			
Bar. Pressure	Correlation Coefficient	-.075**	-.174**	-.264**	-.045**	--		
	Sig. (2-tailed)	<.001	.000	.000	<.001	.		
	N	26873	28711	28711	28711	28711		
Total Precip	Correlation Coefficient	-.037**	-.060**	-.033**	.157**	-.061**	--	
	Sig. (2-tailed)	<.001	<.001	<.001	<.001	<.001	.	
	N	26872	28710	28710	28710	28710	28710	
Wind Spd	Correlation Coefficient	.004	.119**	.120**	-.261**	-.118**	.073**	--
	Sig. (2-tailed)	.306	<.001	<.001	.000	<.001	<.001	.
	N	26873	28711	28711	28710	28710	28710	28711

APPENDIX C

Kruskal-Wallis SPSS Output

4 Week KW SPSS Output - Flux

Hypothesis Test Summary

	Null Hypothesis	Test	Sig.[a,b]	Decision
1	The distribution of Flux is the same across categories of Storm Stage.	Independent-Samples Kruskal-Wallis Test	.119	Retain the null hypothesis.

a. The significance level is .050.

b. Asymptotic significance is displayed.

Independent-Samples Kruskal-Wallis Test Summary

Total N	5472
Test Statistic	4.256[a]
Degree Of Freedom	2
Asymptotic Sig.(2-sided test)	.119

a. The test statistic is adjusted for ties.

Pairwise Comparisons of Storm Stage

Sample 1-Sample 2	Test Statistic	Std. Error	Std. Test Statistic	Sig.	Adj. Sig.[a]
1-3	-78.029	43.092	-1.811	.070	.211
1-2	-199.783	164.089	-1.218	.223	.670
3-2	121.754	164.089	.742	.458	1.000

Each row tests the null hypothesis that the Sample 1 and Sample 2 distributions are the same.

Asymptotic significances (2-sided tests) are displayed. The significance level is .050.

a. Significance values have been adjusted by the Bonferroni correction for multiple tests.

4 Week KW SPSS Output - Concentration

Hypothesis Test Summary

	Null Hypothesis	Test	Sig.[a,b]	Decision
1	The distribution of TWC1 CO_2 is the same across categories of Storm Stage.	Independent-Samples Kruskal-Wallis Test	.000	Reject the null hypothesis.

a. The significance level is .050.

b. Asymptotic significance is displayed.

Independent-Samples Kruskal-Wallis Test Summary

Total N	5472
Test Statistic	2613.932[a]
Degree Of Freedom	2
Asymptotic Sig.(2-sided test)	.000

a. The test statistic is adjusted for ties.

Pairwise Comparisons of Storm Stage

Sample 1-Sample 2	Test Statistic	Std. Error	Std. Test Statistic	Sig.	Adj. Sig.[a]
2-3	-786.087	164.089	-4.791	<.001	.000
2-1	2933.439	164.089	17.877	.000	.000
3-1	2147.352	43.092	49.832	.000	.000

Each row tests the null hypothesis that the Sample 1 and Sample 2 distributions are the same.

Asymptotic significances (2-sided tests) are displayed. The significance level is .050.

a. Significance values have been adjusted by the Bonferroni correction for multiple tests.

3 Week KW SPSS Output - Flux

Hypothesis Test Summary

	Null Hypothesis	Test	Sig.[a,b]	Decision
1	The distribution of Flux is the same across categories of Storm Stage.	Independent-Samples Kruskal-Wallis Test	.142	Retain the null hypothesis.

a. The significance level is .050.

b. Asymptotic significance is displayed.

Independent-Samples Kruskal-Wallis Test Summary

Total N	4128
Test Statistic	3.910[a]
Degree Of Freedom	2
Asymptotic Sig.(2-sided test)	.142

a. The test statistic is adjusted for ties.

Pairwise Comparisons of Storm Stage

Sample 1-Sample 2	Test Statistic	Std. Error	Std. Test Statistic	Sig.	Adj. Sig.[a]
1-3	-65.016	37.538	-1.732	.083	.250
1-2	-149.937	124.500	-1.204	.228	.685
3-2	84.921	124.500	.682	.495	1.000

Each row tests the null hypothesis that the Sample 1 and Sample 2 distributions are the same.

Asymptotic significances (2-sided tests) are displayed. The significance level is .050.

a. Significance values have been adjusted by the Bonferroni correction for multiple tests.

3 Week KW SPSS Output - Concentration

Hypothesis Test Summary

	Null Hypothesis	Test	Sig.[a,b]	Decision
1	The distribution of TWC1 CO_2 is the same across categories of storm stage.	Independent-Samples Kruskal-Wallis Test	.000	Reject the null hypothesis.

a. The significance level is .050.

b. Asymptotic significance is displayed.

Independent-Samples Kruskal-Wallis Test Summary

Total N	4128
Test Statistic	1856.029[a]
Degree Of Freedom	2
Asymptotic Sig.(2-sided test)	.000

a. The test statistic is adjusted for ties.

Pairwise Comparisons of storm stage

Sample 1-Sample 2	Test Statistic	Std. Error	Std. Test Statistic	Sig.	Adj. Sig.[a]
2-3	-623.801	124.500	-5.010	<.001	.000
2-1	2183.314	124.500	17.537	.000	.000
3-1	1559.514	37.538	41.545	.000	.000

Each row tests the null hypothesis that the Sample 1 and Sample 2 distributions are the same.

Asymptotic significances (2-sided tests) are displayed. The significance level is .050.

a. Significance values have been adjusted by the Bonferroni correction for multiple tests.

2 Week KW SPSS Output - Flux

Hypothesis Test Summary

	Null Hypothesis	Test	Sig.[a,b]	Decision
1	The distribution of Flux is the same across categories of Storm Stage.	Independent-Samples Kruskal-Wallis Test	.124	Retain the null hypothesis.

a. The significance level is .050.

b. Asymptotic significance is displayed.

Independent-Samples Kruskal-Wallis Test Summary

Total N	2784
Test Statistic	4.169[a]
Degree Of Freedom	2
Asymptotic Sig.(2-sided test)	.124

a. The test statistic is adjusted for ties.

Pairwise Comparisons of Storm Stage

Sample 1-Sample 2	Test Statistic	Std. Error	Std. Test Statistic	Sig.	Adj. Sig.[a]
1-3	-56.155	31.008	-1.811	.070	.210
1-2	-106.835	84.919	-1.258	.208	.625
3-2	50.680	84.919	.597	.551	1.000

Each row tests the null hypothesis that the Sample 1 and Sample 2 distributions are the same.

Asymptotic significances (2-sided tests) are displayed. The significance level is .050.

a. Significance values have been adjusted by the Bonferroni correction for multiple tests.

2 Week KW SPSS Output - Concentration

Hypothesis Test Summary

	Null Hypothesis	Test	Sig.[a,b]	Decision
1	The distribution of TWC1 CO_2 is the same across categories of storm stage.	Independent-Samples Kruskal-Wallis Test	.000	Reject the null hypothesis.

a. The significance level is .050.

b. Asymptotic significance is displayed.

Independent-Samples Kruskal-Wallis Test Summary

Total N	2784
Test Statistic	1582.416[a]
Degree Of Freedom	2
Asymptotic Sig.(2-sided test)	.000

a. The test statistic is adjusted for ties.

Pairwise Comparisons of storm stage

Sample 1-Sample 2	Test Statistic	Std. Error	Std. Test Statistic	Sig.	Adj. Sig.[a]
2-3	-253.548	84.919	-2.986	.003	.008
2-1	1445.972	84.919	17.028	.000	.000
3-1	1192.424	31.008	38.456	.000	.000

Each row tests the null hypothesis that the Sample 1 and Sample 2 distributions are the same.

Asymptotic significances (2-sided tests) are displayed. The significance level is .050.

a. Significance values have been adjusted by the Bonferroni correction for multiple tests.

1Week KW SPSS Output - Flux

Hypothesis Test Summary

	Null Hypothesis	Test	Sig.[a,b]	Decision
1	The distribution of Flux is the same across categories of Storm Stage.	Independent-Samples Kruskal-Wallis Test	.066	Retain the null hypothesis.

a. The significance level is .050.

b. Asymptotic significance is displayed.

Independent-Samples Kruskal-Wallis Test Summary

Total N	1440
Test Statistic	5.428[a]
Degree Of Freedom	2
Asymptotic Sig.(2-sided test)	.066

a. The test statistic is adjusted for ties.

Pairwise Comparisons of Storm Stage

Sample 1-Sample 2	Test Statistic	Std. Error	Std. Test Statistic	Sig.	Adj. Sig.[a]
1-3	-49.531	22.686	-2.183	.029	.087
1-2	-60.491	45.371	-1.333	.182	.547
3-2	10.960	45.371	.242	.809	1.000

Each row tests the null hypothesis that the Sample 1 and Sample 2 distributions are the same.

Asymptotic significances (2-sided tests) are displayed. The significance level is .050.

a. Significance values have been adjusted by the Bonferroni correction for multiple tests.

1Week KW SPSS Output - Concentration

Hypothesis Test Summary

	Null Hypothesis	Test	Sig.[a,b]	Decision
1	The distribution of TWC1 CO2 is the same across categories of storm stage.	Independent-Samples Kruskal-Wallis Test	.000	Reject the null hypothesis.

a. The significance level is .050.

b. Asymptotic significance is displayed.

Independent-Samples Kruskal-Wallis Test Summary

Total N	1440
Test Statistic	723.453[a]
Degree Of Freedom	2
Asymptotic Sig.(2-sided test)	.000

a. The test statistic is adjusted for ties.

Pairwise Comparisons of storm stage

Sample 1-Sample 2	Test Statistic	Std. Error	Std. Test Statistic	Sig.	Adj. Sig.[a]
2-3	-89.818	45.371	-1.980	.048	.143
2-1	667.793	45.371	14.718	.000	.000
3-1	577.975	22.686	25.477	.000	.000

Each row tests the null hypothesis that the Sample 1 and Sample 2 distributions are the same.

Asymptotic significances (2-sided tests) are displayed. The significance level is .050.

a. Significance values have been adjusted by the Bonferroni correction for multiple tests.

72 Hour KW SPSS Output - Flux

Hypothesis Test Summary

	Null Hypothesis	Test	Sig.[a,b]	Decision
1	The distribution of Flux is the same across categories of Storm Stage.	Independent-Samples Kruskal-Wallis Test	.581	Retain the null hypothesis.

a. The significance level is .050.

b. Asymptotic significance is displayed.

Independent-Samples Kruskal-Wallis Test Summary

Total N	672
Test Statistic	1.085[a]
Degree Of Freedom	2
Asymptotic Sig.(2-sided test)	.581

a. The test statistic is adjusted for ties.

Pairwise Comparisons of Storm Stage

Sample 1-Sample 2	Test Statistic	Std. Error	Std. Test Statistic	Sig.	Adj. Sig.[a]
1-3	-12.080	16.178	-.747	.455	1.000
1-2	-21.583	22.879	-.943	.345	1.000
3-2	9.503	22.879	.415	.678	1.000

Each row tests the null hypothesis that the Sample 1 and Sample 2 distributions are the same.

Asymptotic significances (2-sided tests) are displayed. The significance level is .050.

a. Significance values have been adjusted by the Bonferroni correction for multiple tests.

72 Hour KW SPSS Output - Concentration

Hypothesis Test Summary

	Null Hypothesis	Test	Sig.[a,b]	Decision
1	The distribution of TWC1 CO2 is the same across categories of storm stage.	Independent-Samples Kruskal-Wallis Test	.000	Reject the null hypothesis.

a. The significance level is .050.

b. Asymptotic significance is displayed.

Independent-Samples Kruskal-Wallis Test Summary

Total N	672
Test Statistic	237.419[a]
Degree Of Freedom	2
Asymptotic Sig.(2-sided test)	.000

a. The test statistic is adjusted for ties.

Pairwise Comparisons of storm stage

Sample 1-Sample 2	Test Statistic	Std. Error	Std. Test Statistic	Sig.	Adj. Sig.[a]
2-3	-40.413	22.879	-1.766	.077	.232
2-1	261.948	22.879	11.449	.000	.000
3-1	221.535	16.178	13.694	.000	.000

Each row tests the null hypothesis that the Sample 1 and Sample 2 distributions are the same.

Asymptotic significances (2-sided tests) are displayed. The significance level is .050.

a. Significance values have been adjusted by the Bonferroni correction for multiple tests.

48 Hour KW SPSS Output - Flux

Hypothesis Test Summary

	Null Hypothesis	Test	Sig.[a,b]	Decision
1	The distribution of Flux is the same across categories of Storm Stage.	Independent-Samples Kruskal-Wallis Test	.138	Retain the null hypothesis.

a. The significance level is .050.

b. Asymptotic significance is displayed.

Independent-Samples Kruskal-Wallis Test Summary

Total N	480
Test Statistic	3.960[a]
Degree Of Freedom	2
Asymptotic Sig.(2-sided test)	.138

a. The test statistic is adjusted for ties.

Pairwise Comparisons of Storm Stage

Sample 1-Sample 2	Test Statistic	Std. Error	Std. Test Statistic	Sig.	Adj. Sig.[a]
1-3	-24.443	14.157	-1.727	.084	.253
1-2	-27.885	17.339	-1.608	.108	.323
3-2	3.443	17.339	.199	.843	1.000

Each row tests the null hypothesis that the Sample 1 and Sample 2 distributions are the same.

Asymptotic significances (2-sided tests) are displayed. The significance level is .050.

a. Significance values have been adjusted by the Bonferroni correction for multiple tests.

48 Hour KW SPSS Output - Concentration

Hypothesis Test Summary

	Null Hypothesis	Test	Sig.[a,b]	Decision
1	The distribution of TWC1 CO_2 is the same across categories of storm stage.	Independent-Samples Kruskal-Wallis Test	.000	Reject the null hypothesis.

a. The significance level is .050.

b. Asymptotic significance is displayed.

Independent-Samples Kruskal-Wallis Test Summary

Total N	480
Test Statistic	109.300[a]
Degree Of Freedom	2
Asymptotic Sig.(2-sided test)	.000

a. The test statistic is adjusted for ties.

Pairwise Comparisons of storm stage

Sample 1-Sample 2	Test Statistic	Std. Error	Std. Test Statistic	Sig.	Adj. Sig.[a]
2-3	-26.609	17.339	-1.535	.125	.375
2-1	151.385	17.339	8.731	.000	.000
3-1	124.776	14.157	8.814	.000	.000

Each row tests the null hypothesis that the Sample 1 and Sample 2 distributions are the same.

Asymptotic significances (2-sided tests) are displayed. The significance level is .050.

a. Significance values have been adjusted by the Bonferroni correction for multiple tests.

24 Hour KW SPSS Output - Flux

Hypothesis Test Summary

	Null Hypothesis	Test	Sig.[a,b]	Decision
1	The distribution of Flux is the same across categories of Storm Stage.	Independent-Samples Kruskal-Wallis Test	.672	Retain the null hypothesis.

a. The significance level is .050.

b. Asymptotic significance is displayed.

Independent-Samples Kruskal-Wallis Test Summary

Total N	288
Test Statistic	.796[a]
Degree Of Freedom	2
Asymptotic Sig.(2-sided test)	.672

a. The test statistic is adjusted for ties.

Pairwise Comparisons of Storm Stage

Sample 1-Sample 2	Test Statistic	Std. Error	Std. Test Statistic	Sig.	Adj. Sig.[a]
1-2	-8.333	12.021	-.693	.488	1.000
1-3	-10.010	12.021	-.833	.405	1.000
2-3	-1.677	12.021	-.140	.889	1.000

Each row tests the null hypothesis that the Sample 1 and Sample 2 distributions are the same.

Asymptotic significances (2-sided tests) are displayed. The significance level is .050.

a. Significance values have been adjusted by the Bonferroni correction for multiple tests.

24 Hour KW SPSS Output - Concentration

Hypothesis Test Summary

	Null Hypothesis	Test	Sig.[a,b]	Decision
1	The distribution of TWC1 CO_2 is the same across categories of storm stage.	Independent-Samples Kruskal-Wallis Test	.001	Reject the null hypothesis.

a. The significance level is .050.

b. Asymptotic significance is displayed.

Independent-Samples Kruskal-Wallis Test Summary

Total N	288
Test Statistic	13.322[a]
Degree Of Freedom	2
Asymptotic Sig.(2-sided test)	.001

a. The test statistic is adjusted for ties.

Pairwise Comparisons of storm stage

Sample 1-Sample 2	Test Statistic	Std. Error	Std. Test Statistic	Sig.	Adj. Sig.[a]
2-3	-14.510	12.021	-1.207	.227	.682
2-1	43.115	12.021	3.587	<.001	.001
3-1	28.604	12.021	2.380	.017	.052

Each row tests the null hypothesis that the Sample 1 and Sample 2 distributions are the same.

Asymptotic significances (2-sided tests) are displayed. The significance level is .050.

a. Significance values have been adjusted by the Bonferroni correction for multiple tests.

APPENDIX D

Sediment Core Images

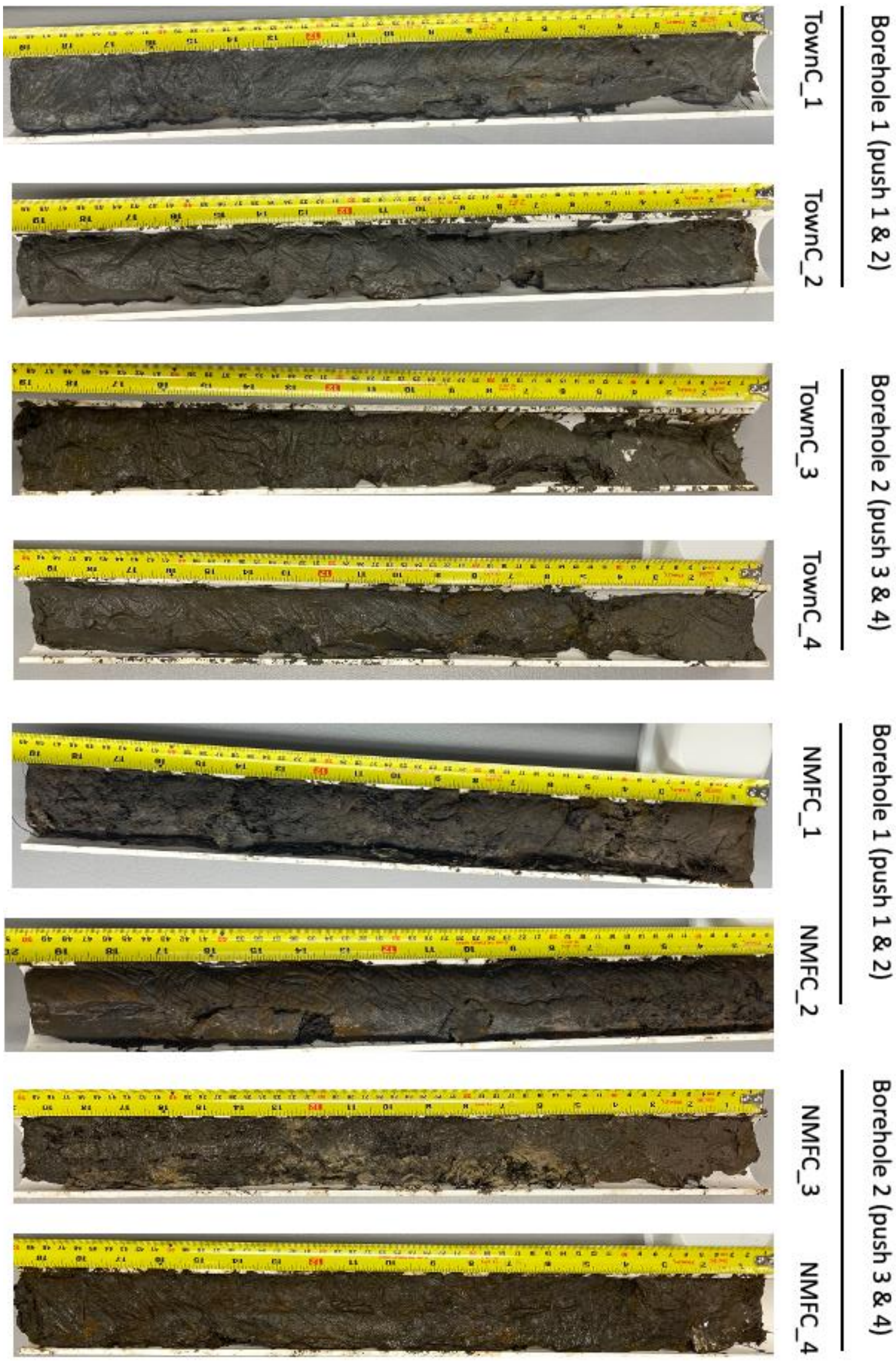

% Carbon						
Sample ID	Sample Weight	Total Sample Weight	%Carbon	C (g)	Check Standard and Dup/Trip Calculations	
TownC_1_22_1	2.5	4.4	2.89	0.13		
TownC_1_22_2	2.53	4.7	3.55	0.17		
TownC_1_22_3	2.06	6.4	3.89	0.25		
TownC_1_22_4	2.4	9.0	3.64	0.33		
TownC_1_22_5	1.78	8.1	3.12	0.25		
TownC_1_22_6	2.45	8.7	4.35	0.38		
TownC_1_22_7	1.16	8.2	2.78	0.23		
TownC_1_22_8	1.55	10.3	2.21	0.23		
TownC_1_22_9	1.57	20.0	1.93	0.39		
TownC_1_22_10	1.62	12.6	1.65	0.21		
TownC_1_22_10DUP	2.96		3.82		Error	
TownC_1_22_10TRIP	1.8		2.85		26.21	RPD
STND7	0.97		73.14		0.0082	PE
TownC_1_22_11	1.9	8.0	3.96	0.32		
TownC_1_22_12	2.18	11.6	3.08	0.36		
TownC_1_22_13	2.49	12.2	2.35	0.29		
TownC_1_22_14	3.02	8.9	2.49	0.22		
TownC_1_22_15	2.45	9.6	3.23	0.31		
TownC_1_22_16	2.68	7.3	3.17	0.23		
TownC_1_22_17	2.72	7.2	3.41	0.25		
TownC_1_22_18	2.17	6.7	4.45	0.30		
TownC_1_22_19	3.19	9.0	2.28	0.20		
TownC_1_22_20	2.17	8.0	7.53	0.60		
TownC_1_22_20DUP	2.09		2.65		Error	
TownC_1_22_20TRIP	2.22		2.84		3.03	RPD
STND8	1.12		72.38		0.0022	PE
TownC_1_22_21	2.03	7.1	3.53	0.25		
TownC_1_22_22	2.04	8.2	3.46	0.28		
TownC_1_22_23	3.18	8.6	3.24	0.28		
TownC_1_22_24	2.24	8.1	2.33	0.19		
TownC_1_22_25	2.29	7.7	13.81	1.06		
TownC_2_22_26	3.41	7.5	1.82	0.14		
TownC_2_22_27	1.99	8.6	2.95	0.25		
TownC_2_22_28	2.73	7.9	4.11	0.32		
TownC_2_22_29	1.82	7.2	4.05	0.29		
TownC_2_22_30	2.99	7.5	3.26	0.25		
TownC_2_22_30DUP	3.05		2.90		Error	
TownC_2_22_30TRIP	2.88		2.86		2.86	RPD
STND9	1.2		72.47		0.0009	PE
TownC_2_22_31	2.95	8.2	3.53	0.29		
TownC_2_22_32	2.24	7.4	3.15	0.23		

Sample ID	Sample Weight	Total Sample Weight	%Carbon	C (g)	Check Standard and Dup/Trip Calculations	Sample ID
TownC_2_22_33	2.19	7.9	3.15	0.25		
TownC_2_22_34	2.47	5.0	3.52	0.18		
TownC_2_22_35	2.07	7.2	3.08	0.22		
TownC_2_22_36	2.99	8.4	3.55	0.30		
TownC_2_22_37	2.45	8.2	3.11	0.25		
TownC_2_22_38	2.67	9.3	3.07	0.29		
TownC_2_22_39	2.63	8.5	2.86	0.24		
TownC_2_22_40	2.09	11.7	2.35	0.28		
TownC_2_22_40DUP	2.18		1.76		Error	
TownC_2_22_40TRIP	2.07		1.81		16.62	RPD
STND10	0.94		72.56		0.0002	PE
TownC_2_22_41	3.88	10.7	2.56	0.27		
TownC_2_22_42	3.48	13.3	2.31	0.31		
TownC_2_22_43	2.23	10.0	2.30	0.23		
TownC_2_22_44	2.79	9.0	1.52	0.14		
TownC_2_22_45	1.97	9.0	2.36	0.21		
TownC_2_22_46	2.12	10.0	2.18	0.22		
TownC_2_22_47	2.13	12.1	1.42	0.17		
TownC_2_22_48	2.31	11.5	1.95	0.22		
TownC_2_22_49	1.67	10.5	1.99	0.21		
TownC_2_22_50	1.72	5.3	1.83	0.10		
TownC_2_22_50DUP	1.97		1.83		Error	
TownC_2_22_50TRIP	1.65		2.16		9.97	RPD
STND11	1.1		72.19		0.0047	PE

% Carbon						
Sample ID	Sample Weight	Total Sample Weight	%Carbon	C (g)	Check Standard and Dup/Trip Calculations	
NMFC_1_22_1	2.44	8.98	6.09	0.55		
NMFC_1_22_2	2.21	6.31	11.17	0.71		
NMFC_1_22_3	2.81	4.66	10.27	0.48		
NMFC_1_22_4	2.3	3.90	11.55	0.45		
NMFC_1_22_5	2.59	4.04	11.77	0.48		
NMFC_1_22_6	2.14	5.48	15.06	0.83		
NMFC_1_22_7	3.57	4.11	9.30	0.38		
NMFC_1_22_8	2.72	5.75	10.26	0.59		
NMFC_1_22_9	2.63	5.80	8.82	0.51		
NMFC_1_22_10	3.25	4.05	14.88	0.60		
NMFC_1_22_10DUP	3.09		12.86		Error	
NMFC_1_22_10TRIP	3.19		11.17		14.35	RSD
STND12	1.43		72.20		0.0046	PE
NMFC_1_22_11	2.21	4.81	10.48	0.50		
NMFC_1_22_12	2.45	5.29	9.66	0.51		
NMFC_1_22_13	3.04	4.40	15.82	0.70		
NMFC_1_22_14	2.83	3.85	13.75	0.53		
NMFC_1_22_15	2.09	4.56	10.69	0.49		
NMFC_1_22_16	2.34	5.48	9.65	0.53		
NMFC_1_22_17	2.38	4.63	10.42	0.48		
NMFC_1_22_18	2.09	3.78	10.62	0.40		
NMFC_1_22_19	2.16	3.87	12.68	0.49		
NMFC_1_22_20	1.84	4.09	11.70	0.48		
NMFC_1_22_20DUP	1.99		12.54		Error	
NMFC_2_22_20TRIP	1.92		12.21		3.49	RPD
STND13	0.82		72.26		0.0038	PE
NMFC_1_22_21	3.1	2.76	13.81	0.38		
NMFC_1_22_22	2.24	2.61	19.97	0.52		
NMFC_1_22_23	2.17	3.57	15.00	0.54		
NMFC_1_22_24	2.08	3.55	11.05	0.39		
NMFC_1_22_25	2.19	4.64	10.00	0.46		
NMFC_2_22_26	2.81	3.14	10.76	0.34		
NMFC_2_22_27	2.16	3.89	15.77	0.61		
NMFC_2_22_28	2.26	3.83	16.58	0.64		
NMFC_2_22_29	2.82	4.43	14.85	0.66		
NMFC_2_22_30	2.6	4.43	11.61	0.52		
NMFC_2_22_30DUP	2.49		11.82		Error	
NMFC_2_22_30TRIP	2.8		11.15		3.01	RPD
STND14	1.08		72.57		0.0003	PE
NMFC_2_22_31	2.35	4.86	10.47	0.51		
NMFC_2_22_32	2.26	5.19	10.80	0.56		

Sample ID	Sample Weight	Total Sample Weight	%Carbon	C (g)	Check Standard and Dup/Trip Calculations	Sample ID
NMFC_2_22_33	2.34	6.15	13.44	0.83		
NMFC_2_22_34	2.83	5.82	10.20	0.59		
NMFC_2_22_35	2.47	6.85	7.86	0.54		
NMFC_2_22_36	2.24	5.27	9.34	0.49		
NMFC_2_22_37	2.26	5.32	8.64	0.46		
NMFC_2_22_38	2.63	6.59	9.200	0.61		
NMFC_2_22_39	2.56	5.39	10.92	0.59		
NMFC_2_22_40	2.48	4.96	7.23	0.36	Error	
NMFC_2_22_40DUP	2.49		7.22		4.79	RPD
NMFC_2_22_40TRIP	2.57		6.64		0.010	PE
STND15	1.58		71.78			
NMFC_2_22_41	2.97	6.45	6.16	0.40		
NMFC_2_22_42	2.61	6.27	6.78	0.43		
NMFC_2_22_43	2.63	4.99	7.95	0.40		
NMFC_2_22_44	2.67	5.73	10.38	0.60		
NMFC_2_22_45	2.93	5.30	10.70	0.57		
NMFC_2_22_46	2.68	5.62	10.77	0.61		
NMFC_2_22_47	2.57	7.26	9.06	0.66		
NMFC_2_22_48	2.25	7.78	4.85	0.38		
NMFC_2_22_49	2.17	6.61	4.60	0.30		
NMFC_2_22_50	2.32	3.81	4.11	0.16		
NMFC_2_22_50DUP	2.38		4.15	0.40	Error	
NMFC_2_22_50TRIP	2.43		4.22	0.43	1.40	RPD
STND16	1.04		73.00	0.40	0.0063	PE

Grain Size Analysis				
Location	Sample #	sample depth	<90%	Avg. relative % error
TownC_1_22	1	0-2	76.27	
TownC_1_22	2	2-4	205.8	
TownC_1_22	3	4-6	227.5	
TownC_1_22	4	6-8	229.9	
TownC_1_22	5	8-10	244.7	
TownC_1_22	5DUP	8-10	376.1	42.3
TownC_1_22	6	10-12	428.4	
TownC_1_22	7	12-14	207.4	
TownC_1_22	8	14-16	224.8	
TownC_1_22	9	16-18	349.4	
TownC_1_22	10	18-20	230.2	
TownC_1_22	10DUP	18-20	269.7	15.8
TownC_1_22	11	20-22	430.5	
TownC_1_22	11DUP	20-22	316.6	
TownC_1_22	12	22-24	237.5	
TownC_1_22	13	24-26	331.2	
TownC_1_22	14	26-28	229.2	
TownC_1_22	15	28-30	160.3	
TownC_1_22	15DUP	28-30	177.1	10.0
TownC_1_22	16	30-32	171.6	
TownC_1_22	17	32-34	141.9	
TownC_1_22	18	34-36	144.2	
TownC_1_22	19	36-38	329.8	
TownC_1_22	20	38-40	411.7	
TownC_1_22	20DUP	38-40	367.6	11.3
TownC_1_22	21	40-42	242.9	
TownC_1_22	22	42-44	240.7	
TownC_1_22	23	44-46	404.6	
TownC_1_22	24	46-48	519.2	
TownC_1_22	25	48-50	522.2	
TownC_1_22	25DUP	48-50	489.1	7.0
TownC_2_22	26	50-52	246.6	
TownC_2_22	27	52-54	239.5	
TownC_2_22	28	54-56	491	
TownC_2_22	29	56-58	411.4	
TownC_2_22	30	58-60	380.3	
TownC_2_22	30DUP	58-60	341.5	10.8
TownC_2_22	31	60-62	232.6	
TownC_2_22	32	62-64	205.6	
TownC_2_22	33	64-66	469.4	
TownC_2_22	34	66-68	186.7	
TownC_2_22	35	68-70	154.4	

Location	Sample #	sample depth	<90%	Avg. relative % error
TownC_2_22	35DUP	68-70	181.4	16.1
TownC_2_22	36	70-72	140.3	
TownC_2_22	37	72-74	857.7	
TownC_2_22	38	74-76	211.6	
TownC_2_22	39	76-78	179.8	
TownC_2_22	40	78-80	164	9.2
TownC_2_22	40DUP	78-80	163.1	
TownC_2_22	41	80-82	163.4	
TownC_2_22	42	82-84	151.2	
TownC_2_22	43	84-86	182.7	
TownC_2_22	44	86-88	149.2	
TownC_2_22	45	88-90	177.1	
TownC_2_22	45DUP	88-90	165.4	6.8
TownC_2_22	46	90-92	175	
TownC_2_22	47	92-94	186.7	
TownC_2_22	48	94-96	178.6	
TownC_2_22	49	96-98	163.6	
TownC_2_22	50	98-100	146.1	
TownC_2_22	50DUP	98-100	136.5	6.8

Grain Size Analysis				
Location	Sample #	sample depth	<90%	Avg. relative % error
NMFC_1_22	1	0-2	230.8	
NMFC_1_22	2	2-4	181	
NMFC_1_22	3	4-6	208.4	
NMFC_1_22	4	6-8	231.5	
NMFC_1_22	5	8-10	186.6	
NMFC_1_22	5DUP	8-10	198.9	6.4
NMFC_1_22	6	10-12	173.8	
NMFC_1_22	7	12-14	152.8	
NMFC_1_22	8	14-16	194.5	
NMFC_1_22	9	16-18	244.5	
NMFC_1_22	10	18-20	268.9	
NMFC_1_22	10DUP	18-20	193.4	32.6
NMFC_1_22	11	20-22	213.1	
NMFC_1_22	12	22-24	183	
NMFC_1_22	13	24-26	292.8	
NMFC_1_22	14	26-28	224.3	
NMFC_1_22	15	28-30	392.8	
NMFC_1_22	15DUP	28-30	401.5	2.2
NMFC_1_22	16	30-32	453.2	
NMFC_1_22	17	32-34	325.6	
NMFC_1_22	18	34-36	215.4	
NMFC_1_22	19	36-38	285.5	
NMFC_1_22	20	38-40	375.5	
NMFC_1_22	20DUP	38-40	435.5	14.8
NMFC_1_22	21	40-42	268.6	
NMFC_1_22	22	42-44	252.1	
NMFC_1_22	23	44-46	213.8	
NMFC_1_22	24	46-48	339.3	
NMFC_1_22	25	48-50	436.5	
NMFC_1_22	25DUP	48-50	493.7	12.3
NMFC_2_22	26	50-52	215.1	
NMFC_2_22	27	52-54	328.5	
NMFC_2_22	28	54-56	218.3	
NMFC_2_22	29	56-58	257.3	
NMFC_2_22	30	58-60	215	
NMFC_2_22	30DUP	58-60	210.1	2.3
NMFC_2_22	31	60-62	355.6	
NMFC_2_22	32	62-64	188.4	
NMFC_2_22	33	64-66	295.4	
NMFC_2_22	34	66-68	183.1	
NMFC_2_22	35	68-70	370.6	
NMFC_2_22	35DUP	68-70	379	2.2

Location	Sample #	sample depth	<90%	Avg. relative % error
NMFC_2_22	36	70-72	313.8	
NMFC_2_22	37	72-74	290.1	
NMFC_2_22	38	74-76	348.5	
NMFC_2_22	39	76-78	289.9	
NMFC_2_22	40	78-80	228.7	
NMFC_2_22	40DUP	78-80	312.9	31.1
NMFC_2_22	41	80-82	488.2	
NMFC_2_22	42	82-84	321.1	
NMFC_2_22	43	84-86	429.5	
NMFC_2_22	44	86-88	488.7	
NMFC_2_22	45	88-90	184.2	
NMFC_2_22	45DUP	88-90	193.6	5.0
NMFC_2_22	46	90-92	205.5	
NMFC_2_22	47	92-94	253.6	
NMFC_2_22	48	94-96	340.9	
NMFC_2_22	49	96-98	170.6	
NMFC_2_22	50	98-100	116.7	
NMFC_2_22	50DUP	98-100	120.6	3.3

Isotopic Analysis

Core Information					Net Peak Area (cps)					Activites					Age	
Core ID	Depth	Sample ID		Dry weight (g)	Count time (s)	Pb-210 46.5 KeV	Ra-226 186 KeV	Pb-214 295 KeV	Pb-214 325 KeV	SUP Pb-210	Ra-226	Pb-214 295 KeV	Pb-214 352 KeV	UNSUP Pb-210	SUP Age	UNSUP AGE
TownC_3_22	0-2	1	2	2.503	86400	202	217	277.42	875.2	0.220	-0.037	-0.017	0.046	0.205	0.000	0.000
TownC_3_23	4-6	3	6	5.003	86400	342.25	119.87			0.154	-0.012				11.362	
TownC_3_22	8-10	5	10	5	86400	304.5	186	279.14	948.5	0.132	-0.035	0.018	0.031	0.107	16.334	20.731
RownC_3_22	12-14	7	14	5.004	86400	208.25	203.25			0.075	0.037				34.341	
TownC_3_22	18-20	10	20	5.005	86400	148.5	252.87	425.59	757.31	0.040	0.066	0.046	0.010	0.012	54.487	90.129
TownC_3_22	26-28	15	28	10.009	86400	195.5	584	606.61	1269.2	0.030	0.100	0.012	0.069	-0.011	64.462	
TownC_3_22	38-40	20	40	5.007	86400	131.25	181	358.61	902.13	0.030	0.024	0.033	0.026	0.001	63.817	188.626
TownC_3_22	48-50	25	50	10.006	86400	199.5	278			0.030	0.040				63.460	

Core Information					Net Peak Area (cps)					Activites					Age	
Core ID	Depth		Sample ID	Dry weight (g)	Count time (s)	Pb-210 46.5 KeV	Ra-226 186 KeV	Pb-214 295 KeV	Pb-214 352 KeV	SUP Pb-210	Ra-226	Pb-124 295 keV	Pb-214 352 KeV	UNSUP Pb-210	SUP Pb-210	UNSUP Pb-210
NMFC_3_22	0-2	0	1	2.502	86400	324.25	181.5	330.54	776.5	0.3526042	-0.0755775	0.0031949	0.0247237	0.3386449	0	0
NMFC_3_23	4-6	6	3	2.501	86400	279.5	182.25			0.3040625	-0.0747918				4.756551513	
NMFC_3_22	8-10	10	5	5.006	86400	251.25	278.87	421.38	964.28	0.100597	0.0812823	0.045031	0.0325637	0.0617996	40.27864016	54.628364
NMFC_3_22	12-14	14	7	2.506	86400	116.5	223.87			0.1264852	-0.0294553				32.92434851	
NMFC_3_22	18-20	20	10	2.505	86400	159.5	212.5	566.4	809.34	0.1732398	-0.0418165	0.0913242	0.0318732	0.1116411	22.82270975	35.636131
NMFC_3_22	28-30	30	15	2.502	86400	97.25	210	307.29	862.15	0.1057541	-0.0445853	-0.0055032	0.04347	0.0622841	38.67310869	54.37756
NMFC_3_22	38-40	40	20	2.508	86400	130.25	323.62	446.46	985.17	0.1413009	0.0787814	0.0464509	0.0702271	0.0829619	29.36714521	45.171155
NMFC_3_22	48-50	50	25	5.004	86400	152	250.87			0.0423117	0.0648603				68.09159026	

Lead-210 Spiked Standard - CETL							
Mass	Known Activty (nCi)	Known Activty (nCi)	Count Time	cps	Area (cps)	G/d Pb-210	Efficencey
2.5g	1850	50	3600	7.87	28331.25	0.0425	0.1000927
5g	1850	50	3600	17.29	26216.25	0.0425	0.0926088
10g	1850	50	3600	9.25	33287	0.0425	0.1175911

Lead -210 Blank Standard - CETL							
Mass	Known Activty	Count Time	Area Lead-210	Area Ra-226	G/d Pb-210	Efficencey Pb-210	E R-226
2.5g		86400	0	251		0	0.0029051
5g		86400	80	140.5		0.0009259	0.0016262
10g		86400	68	150.75		0.000787	0.0017448

Eu-152 Spiked Standard - CETL							
Mass	Known Activty (Beq)	Known Activty (nCi)	Count Time	cps	Area (cps)	G/d Pb-210	Efficencey
244.43	762.2	20.6	3600	5.72	15463.65	0.0755	0.0746438
344.11	762.2	20.6	3600	13.88	46564.81	0.2659	0.0638171
443.74	762.2	20.6	3600	1.85	4186.91	0.03125	0.0487953

Blank Standard - Rich							
Mass		Count Time	Area 295	Area 352		Background 295	Background 352
2.5g		86400	322	663.54		0.0037269	0.0076799
5g		86400	180.55	666.6		0.0020897	0.0077153
10g		86400	474.3	864.21		0.0054896	0.0100024

Radiographic HU Density					
TownC_1			TownC_2		
Line of radiographic measurement	Density (HU)	Standard D (HU)	Line of radiographic measurement	Density (HU)	Standard D (HU)
1	990	384	1	670	299
2	1363	476	2	1924	603
3	1597	587	3	2230	711
4	1687	472	4	2098	646
5	1715	454	5	2222	579
6	1538	572	6	2291	786
7	1487	504	7	2382	861
8	1517	438	8	2296	761
9	1551	410	9	2202	801
10	1673	417	10	1916	649
11	1570	432	11	1886	664
12	1593	437	12	2128	712
13	1575	507	13	1999	719
14	1534	487	14	1963	684
15	1513	473	15	2018	683
16	1423	409	16	1701	626
17	1383	539	17	1936	604
18	1377	476	18	1940	653
19	1236	532	19	1700	679
20	1250	576	20	1717	756
21	917	594	21	1692	663
22	979	622	22	1915	698
23	1058	677	23	1773	700
24	1099	702	24	1981	493
25	1104	711	25	1796	530
26	1131	701	26	1748	733
27	1402	688	27	1724	637
28	1362	607	28	1819	664
29	1420	558	29	1513	555
30	1462	571	30	1481	479
31	1531	489	31	1408	610
32	1587	418	32	1762	618
33	1508	459	33	1864	584
34	1621	494	34	1937	603
35	1638	438	35	2028	568
36	1547	516	36	1980	741
37	1534	456	37	1930	623
38	1541	450	38	1960	532
39	1565	341	39	2027	631

TownC_1			TownC_2		
Line of radiographic measurement	Density (HU)	Line of radiographic measurement	Density (HU)	Line of radiographic measurement	Density (HU)
40	1452	445	40	1919	601
41	1392	467	41	1937	484
42	1297	480	42	1798	415
43	1346	489	43	1678	509
44	1401	492	44	1468	535
45	1465	500	45	1953	521
46	1459	424	46	1962	534
47	1389	519	47	1959	546
48	1465	589	48	2074	532
49	1605	510	49	2044	780
50	1484	523	50	1910	803
51	1433	596	51	2189	572
52	1418	562	52	2018	501
53	1444	534	53	1952	436
54	1381	499	54	1867	422
55	1355	499	55	1903	408
56	1219	509	56	1926	401
57	1192	456	57	1931	526
58	1345	597	58	1832	542
59	1397	506	59	1757	354
60	1489	499	60	1544	455
61	1583	501	61	1761	867
62	1470	548	62	1936	680
63	1584	411	63	1981	623
64	1230	542	64	1913	500
65	1009	259	65	1976	541
66	1378	502	66	1906	738
67	1404	511	67	1975	657
68	1420	478	68	2038	552
69	1399	538	69	1932	573
70	1578	483	70	2199	604
71	1504	524	71	2054	569
72	1608	411	72	2138	493
73	1516	409	73	2181	575
74	1500	355	74	2166	587
75	1489	485	75	2114	547
76	1495	542	76	2184	627
77	1379	579	77	2126	540
78	1396	550	78	2070	600
79	1329	536	79	1853	727
80	1303	620	80	1758	633

TownC_1			TownC_2		
Line of radiographic measurement	Density (HU)	Line of radiographic measurement	Density (HU)	Line of radiographic measurement	Density (HU)
81	1438	614	81	2066	514
82	1431	514	82	1600	940
83	1431	541	83	1296	783
84	1542	509	84	1226	851
85	1694	610	85	1242	1005
86	1669	522	86	1275	1028
87	1661	594	87	1608	837
88	1594	517	88	1538	672
89	1670	452	89	1666	781
90	1681	339	90	1943	806
91	1435	544	91	1803	725
92	1351	427	92	1882	798
93	1304	493	93	1964	814
94	1377	556	94	1809	955
95	1563	437	95	2033	924
96	1573	536	96	2154	919
97	1514	475	97	2259	896
98	1395	556	98	1981	955
99	1167	502	99	1716	1130
100	1054	570	100	1818	962
101	988	542	101	2061	823
102	1009	522	102	2239	675
103	993	491	103	2332	736
104	999	542	104	2000	931
105	1009	567	105	2157	890
106	1130	583	106	1910	941
107	1088	620	107	1986	853
108	1079	636	108	1616	988
109	1204	544	109	1696	1004
110	1216	477	110	1574	1056
111	1216	518	111	1281	973
112	1325	513	112	1798	829
113	1281	445	113	1779	797
114	1208	473	114	1866	773
115	1206	556	115	1682	561
116	1056	605	116	2030	549
117	1074	576	117	1929	486
118	1208	470	118	1961	526
119	1405	385	119	1981	643
120	1354	469	120	1865	510
121	1458	458	121	1889	379

TownC_1			TownC_2		
Line of radiographic measurement	Density (HU)	Line of radiographic measurement	Density (HU)	Line of radiographic measurement	Density (HU)
122	1469	459	122	2104	352
123	1461	393	123	2032	383
124	1427	555	124	2035	362
125	1527	599	125	1749	598
126	1338	613	126	1674	680
127	1262	553	127	1683	790
128	1174	459	128	1776	793
129	1246	409	129	1847	676
130	1282	415	130	1833	628
131	1275	411	131	1753	591
132	1226	575	132	1798	660
133	1346	561	133	1625	722
134	1231	649	134	1502	764
135	1222	628	135	1425	753
136	1115	630	136	1329	756
137	1115	576	137	1396	823
138	1088	533	138	1898	571
139	1150	534	139	1873	394
140	1363	451	140	1896	525
141	1276	444	141	2284	604
142	1276	440	142	2053	715
143	1217	543	143	2106	718
144	1223	583	144	2421	717
145	1167	587	145	2461	575
146	1077	644	146	2448	525
147	1321	653	147	2408	481
148	1347	595	148	2544	538
149	1311	614	149	2290	668
150	1351	567	150	1913	871
151	1283	557	151	1752	798
152	1309	586	152	1839	816
153	1284	580	153	2138	770
154	1301	530	154	2306	702
155	1199	553	155	2151	758
156	1150	518	156	2024	783
157	1247	464	157	1749	998
158	1257	458	158	1714	1092
159	1182	541	159	2399	637
160	1204	552	160	2412	539
161	1093	492	161	2336	664
162	1031	450	162	2145	852

TownC_1			TownC_2		
Line of radiographic measurement	Density (HU)	Line of radiographic measurement	Density (HU)	Line of radiographic measurement	Density (HU)
163	1034	465	163	2044	1047
164	1024	470	164	1649	1141
165	993	460	165	1664	1121
166	1011	514	166	1737	1149
167	1018	509	167	1546	1155
168	1046	510	168	1581	936
169	1023	544	169	1634	706
170	1137	599	170	1728	636
171	1222	645	171	1624	706
172	1158	614	172	1603	719
173	1207	631	173	1633	643
174	1181	620	174	1866	623
175	1203	606	175	1697	781
176	1141	575	176	1674	804
177	1165	520	177	1774	684
178	1169	542	178	1641	891
179	1217	503	179	1419	933
180	1281	511	180	1453	880
181	1241	494	181	1372	800
182	1322	416	182	1501	869
183	1418	425	183	1687	836
184	1510	383	184	1814	814
185	1372	474	185	1755	611
186	1301	340	186	1708	608
187	1362	415	187	1678	599
188	1390	347	188	1804	602
189	1392	464	189	1697	504
190	1363	529	190	1736	588
191	1496	518	191	1843	492
192	1506	571	192	1787	629
193	1515	543	193	1814	579
194	1426	570	194	1851	619
195	1382	656	195	1939	497
196	1381	705	196	1874	560
197	1316	660	197	1833	696
198	1280	635	198	1841	622
199	1182	538	199	1899	737
200	1171	602	200	1959	727
201	1258	526	201	2008	681
202	1244	635	202	1846	772
203	1213	615	203	1767	929

TownC_1			TownC_2		
Line of radiographic measurement	Density (HU)	Line of radiographic measurement	Density (HU)	Line of radiographic measurement	Density (HU)
204	1124	543	204	1873	810
205	1199	490	205	1982	788
206	1143	480	206	1879	838
207	996	497	207	1768	881
208	1201	493	208	1682	882
209	1217	525	209	1726	786
210	1204	521	210	1911	868
211	1229	496	211	1908	829
212	1325	545	212	1837	874
213	1510	552	213	2011	802
214	1678	365	214	2189	728
215	1623	394	215	2006	809
216	1456	308	216	1997	939
217	1398	364	217	1904	923
218	1187	600	218	1664	897
219	1244	381	219	1785	945
220	1391	478	220	1846	874
221	1350	569	221	1763	825
222	1468	579	222	1839	829
223	1411	597	223	1785	754
224	1316	499	224	1787	780
225	1186	408	225	1722	860
226	1397	423	226	1759	834
227	1472	419	227	1845	733
228	1464	347	228	1825	741
229	1441	450	229	1949	766
230	1494	509	230	2045	764
231	1423	540	231	2015	700
232	1443	534	232	2033	681
233	1411	478	233	1993	769
234	1496	486	234	2057	796
235	1496	411	235	2031	772
236	1532	416	236	2039	676
237	1503	427	237	2109	695
238	1569	449	238	2251	835
239	1498	437	239	2398	742
240	1435	361	240	2477	515
241	1407	400	241	2254	689
242	1466	381	242	2210	506
243	1417	405	243	2247	569
244	1479	469	244	2713	541

TownC_1			TownC_2		
Line of radiographic measurement	Density (HU)	Line of radiographic measurement	Density (HU)	Line of radiographic measurement	Density (HU)
245	1748	357	245	3040	428
246	1674	434	246	2947	724
247	1687	348	247	1326	589
248	1491	353			
249	1547	311			
250	1546	356			
251	1422	430			
252	1434	483			
253	1390	501			
254	1371	509			
255	1405	570			
256	1564	567			
257	1704	551			
258	1885	488			
259	1955	428			
260	2136	384			
261	1550	211			

Radiographic HU Density					
NMFC_1			NMFC_2		
Line of radiographic measurement	Density (HU)	Standard D (HU)	Line of radiographic measurement	Density (HU)	Standard D (HU)
1	561	194	1	1497	359
2	971	539	2	1939	531
3	2134	638	3	1935	468
4	2665	272	4	1849	653
5	2639	328	5	1706	636
6	2271	464	6	2012	582
7	2116	402	7	2300	644
8	2187	292	8	2344	591
9	2048	319	9	2024	496
10	1991	374	10	2070	628
11	1937	506	11	2236	753
12	1844	603	12	1829	826
13	1819	638	13	1957	792
14	1905	625	14	1340	653
15	1865	730	15	1447	669
16	1798	661	16	1410	582
17	1632	663	17	1389	493
18	1571	591	18	1481	528
19	1558	729	19	1618	505
20	1541	738	20	1582	719
21	1518	740	21	1599	709
22	1459	857	22	1624	655
23	1397	801	23	1488	632
24	1188	823	24	1471	623
25	1206	817	25	1427	645
26	1256	773	26	1340	555
27	1309	820	27	1214	547
28	1321	852	28	970	458
29	1364	881	29	1138	620
30	1166	791	30	1144	637
31	1405	721	31	1155	604
32	1244	728	32	1312	661
33	1425	706	33	1343	640
34	1315	700	34	1282	770
35	1232	608	35	1181	760
36	1059	569	36	1191	703
37	1198	484	37	1263	648
38	1310	612	38	1415	744
39	1412	572	39	1668	710

NMFC_1			NMFC_2		
Line of radiographic measurement	Density (HU)	Line of radiographic measurement	Density (HU)	Line of radiographic measurement	Density (HU)
40	1453	679	40	1593	687
41	1495	618	41	1536	553
42	1446	819	42	1469	419
43	1538	760	43	1454	463
44	1317	727	44	1555	483
45	1595	806	45	1554	538
46	1848	684	46	1442	597
47	1969	697	47	1639	698
48	1727	809	48	1754	681
49	1396	780	49	1724	588
50	1371	615	50	1672	645
51	1386	579	51	1493	508
52	1327	592	52	1468	491
53	1301	575	53	1456	679
54	1218	643	54	1517	668
55	1258	674	55	1513	615
56	1630	722	56	1482	516
57	1763	622	57	1586	576
58	1930	588	58	1467	605
59	1981	672	59	1672	588
60	2058	720	60	1647	645
61	1957	677	61	1624	683
62	1533	532	62	1576	696
63	1402	661	63	1557	694
64	1536	755	64	1507	623
65	1494	872	65	1436	574
66	1255	784	66	1484	605
67	1661	825	67	1421	629
68	1618	682	68	1330	646
69	1675	708	69	1372	711
70	1518	650	70	1435	762
71	1539	674	71	1426	695
72	1662	627	72	1530	678
73	1671	684	73	1569	621
74	1734	714	74	1669	656
75	1842	665	75	1630	715
76	1755	578	76	1555	683
77	1629	569	77	1670	675
78	1712	560	78	1720	653
79	1711	674	79	1594	677
80	1807	614	80	1653	638

NMFC_1			NMFC_2		
Line of radiographic measurement	Density (HU)	Line of radiographic measurement	Density (HU)	Line of radiographic measurement	Density (HU)
81	1986	658	81	1667	637
82	1853	696	82	1608	643
83	1836	560	83	1552	562
84	1949	515	84	1447	606
85	1798	582	85	1521	638
86	1529	647	86	1532	694
87	1548	579	87	1563	700
88	1421	595	88	1712	580
89	1465	645	89	1502	679
90	1521	537	90	1435	721
91	1385	493	91	1429	711
92	1547	442	92	1247	651
93	1713	703	93	1254	736
94	1652	701	94	1429	761
95	1560	618	95	1362	731
96	1601	578	96	1444	668
97	1578	578	97	1442	653
98	1481	750	98	1442	662
99	1536	799	99	1677	763
100	1709	671	100	1552	730
101	1721	758	101	1563	749
102	1712	687	102	1486	736
103	1738	785	103	1440	797
104	1429	685	104	1369	682
105	1321	722	105	1408	574
106	1147	722	106	1406	608
107	1174	570	107	1425	592
108	1067	669	108	1495	767
109	1236	759	109	1409	597
110	1264	839	110	1463	542
111	1266	720	111	1573	623
112	1065	578	112	1704	655
113	1405	539	113	1613	633
114	1614	764	114	1579	718
115	1803	833	115	1528	656
116	1768	853	116	1517	727
117	1720	655	117	1657	784
118	1855	745	118	1705	685
119	1900	786	119	1570	651
120	1774	465	120	1370	696
121	1651	565	121	1449	538

NMFC_1			NMFC_2		
Line of radiographic measurement	Density (HU)	Line of radiographic measurement	Density (HU)	Line of radiographic measurement	Density (HU)
122	1950	679	122	1393	678
123	1820	652	123	1342	627
124	1568	628	124	1417	569
125	1510	659	125	1306	574
126	1431	693	126	1143	661
127	1482	474	127	1049	652
128	1457	411	128	1200	794
129	1326	471	129	1264	730
130	1352	656	130	1285	610
131	1401	672	131	1466	650
132	1624	536	132	1286	753
133	1468	602	133	1293	702
134	1656	723	134	1354	682
135	1727	834	135	1382	696
136	1624	789	136	1323	797
137	1698	849	137	1350	917
138	1575	842	138	1449	837
139	1606	761	139	1465	863
140	1584	768	140	1671	663
141	1406	879	141	1645	547
142	1575	996	142	1104	664
143	1557	925	143	1245	640
144	1508	932	144	1292	780
145	1750	803	145	1351	709
146	1745	692	146	1285	707
147	1846	531	147	1461	759
148	1814	671	148	1508	743
149	1775	674	149	1506	695
150	1795	625	150	1473	661
151	1691	637	151	1440	691
152	1739	539	152	1548	755
153	1415	567	153	1364	564
154	1618	620	154	1362	737
155	1729	575	155	1460	763
156	1420	564	156	1424	754
157	1580	720	157	1554	673
158	1597	806	158	1777	560
159	1680	670	159	1656	648
160	1464	630	160	1634	622
161	1654	631	161	1490	641
162	1644	684	162	1538	559

NMFC_1			NMFC_2		
Line of radiographic measurement	Density (HU)	Line of radiographic measurement	Density (HU)	Line of radiographic measurement	Density (HU)
163	1538	636	163	1523	674
164	1682	448	164	1438	724
165	1617	435	165	1499	705
166	1703	647	166	1652	651
167	1689	596	167	1764	635
168	1478	491	168	1716	646
169	1594	556	169	1550	714
170	1557	598	170	1729	676
171	1566	698	171	1549	560
172	1424	720	172	1698	639
173	1136	678	173	1885	807
174	1251	718	174	1969	712
175	1104	618	175	1935	706
176	1239	441	176	1730	643
177	1466	574	177	1515	662
178	1404	568	178	1280	752
179	1300	549	179	1439	876
180	1275	580	180	1470	888
181	1496	719	181	1826	743
182	1413	597	182	1767	640
183	1321	586	183	1628	610
184	1318	577	184	1566	632
185	1420	653	185	1628	752
186	1342	646	186	1584	562
187	1425	810	187	1498	650
188	1392	766	188	1486	675
189	1396	635	189	1441	797
190	1383	733	190	1650	643
191	1594	786	191	1560	625
192	1549	721	192	1703	688
193	1553	740	193	1654	646
194	1343	752	194	1363	642
195	1335	778	195	1450	696
196	1348	756	196	1621	604
197	1363	694	197	1564	601
198	1358	651	198	1773	527
199	1475	653	199	1900	552
200	1462	661	200	1819	555
201	1332	631	201	1793	563
202	1310	608	202	1699	557
203	1367	757	203	1754	488

NMFC_1			NMFC_2		
Line of radiographic measurement	Density (HU)	Line of radiographic measurement	Density (HU)	Line of radiographic measurement	Density (HU)
204	1363	738	204	1748	477
205	1230	692	205	1695	516
206	1386	765	206	1651	528
207	1340	802	207	1647	593
208	1361	853	208	1621	600
209	1408	793	209	1575	645
210	1459	869	210	1540	660
211	1553	733	211	1665	624
212	1366	606	212	2104	321
213	1442	646	213	1963	322
214	1433	600	214	1744	373
215	1505	580	215	1766	538
216	1461	561	216	1558	600
217	1318	514	217	1553	666
218	1343	414	218	1615	849
219	1354	463	219	1605	811
220	1470	556	220	1366	649
221	1417	574	221	1246	691
222	1219	510	222	1420	709
223	1351	374	223	1553	619
224	1459	499	224	1665	655
225	1359	561	225	1621	776
226	1260	692	226	1701	797
227	1116	620	227	1611	806
228	1237	553	228	1563	819
229	1369	581	229	1768	681
230	1909	592	230	1785	671
231	2001	636	231	1907	684
232	1872	663	232	1921	660
233	1873	737	233	1902	716
234	1774	647	234	1984	693
235	1583	490	235	1990	685
236	1685	465	236	2012	684
237	1708	418	237	2043	681
238	1565	493	238	1965	689
239	1457	541	239	1987	668
240	1442	572	240	1914	660
241	1476	484	241	1944	586
242	1462	535	242	1915	634
243	1520	567	243	1868	661
244	1624	504	244	1800	703

NMFC_1			NMFC_2		
Line of radiographic measurement	Density (HU)	Line of radiographic measurement	Density (HU)	Line of radiographic measurement	Density (HU)
245	1490	667	245	1830	700
246	1437	726	246	1875	684
247	1473	805	247	1879	729
248	1572	749	248	1837	706
249	1676	771	249	1922	727
250	1822	832	250	1946	719
251	2024	988	251	2017	657
252	1894	989	252	1916	689
253	1830	1037	253	1933	690
254	1178	558	254	2002	712
			255	2073	682
			256	2107	664
			257	2142	679
			258	2312	599
			259	2391	626
			260	2539	556
			261	2565	570
			262	2456	470
			263	2657	373
			264	2229	488
			265	1904	380